

Advanced dynamics of optically trapped nanowire waveguides

Author:

Toe, Wen Jun

Publication Date:

2016

DOI:

<https://doi.org/10.26190/unsworks/18907>

License:

<https://creativecommons.org/licenses/by-nc-nd/3.0/au/>

Link to license to see what you are allowed to do with this resource.

Downloaded from <http://hdl.handle.net/1959.4/55850> in <https://unsworks.unsw.edu.au> on 2024-04-30

THE UNIVERSITY OF NEW SOUTH WALES
Thesis/Dissertation Sheet

Surname or Family name: **Toe**

First name: **Wen Jun**

Other name/s: -

Abbreviation for degree as given in the University calendar: **PhD**

School: **School of Physics**

Faculty: **Faculty of Science**

Title: **Advanced dynamics of optically trapped nanowire waveguides**

Abstract 350 words maximum:

In this thesis I describe a number of studies to examine some high order effects of advanced trapping dynamics beyond the standard single gradient force optical trap. Our interests lay primarily on low symmetry particles, specifically on high refractive index, high aspect ratio nanowires. We examine higher order dynamics due to coupling between rotational and translational degrees of freedom when a single high aspect ratio nanowire is trapped. We also study the coupling of the trapping laser into the waveguiding modes of the trapped nanowire, as well as the coupling interactions between multiple trapped nanowires.

On single optically trapped nanowires, we show calculations beyond the standard power spectral analysis to demonstrate the emergence of resonance behaviour in overdamped systems due to the coupling between rotational and translational degrees of freedom. We also experimentally demonstrate the effects of such coupling which shows up in the form of resonance peaks in the power spectrum when single nanowires are trapped in optical tweezers.

Next we examine the coupling of light into the waveguide modes of high refractive index nanowires by calculating the field profiles, dispersion and group velocity. We then investigate the optical coupling between multiple high refractive index nanowires in close proximity. In particular, we calculate the field profiles, dispersion and optical force of coupled nanowire waveguides with the Coupled Mode Theory and Perturbation Theory. The optical forces between coupled waveguides is also calculated and compared to results obtained from Maxwell's Stress Tensor calculations.

In the final results chapter, we explore various experimental approaches to experimentally measure the coupled nanowire system that was calculated in the previous chapter. We propose time-shared optical tweezers with interferometric particle tracking as a means of physically measuring the coupling between nanowires and investigate the feasibility of this measurement technique for our system.

In summary, we conducted theoretical analysis and experiments that aid in the further understanding of the advanced dynamics of high refractive index, high aspect ratio nanowires within the optical trapping domain.

Declaration relating to disposition of project thesis/dissertation

I hereby grant to the University of New South Wales or its agents the right to archive and to make available my thesis or dissertation in whole or in part in the University libraries in all forms of media, now or here after known, subject to the provisions of the Copyright Act 1968. I retain all property rights, such as patent rights. I also retain the right to use in future works (such as articles or books) all or part of this thesis or dissertation.

I also authorise University Microfilms to use the 350 word abstract of my thesis in Dissertation Abstracts International (this is applicable to doctoral theses only).

.....
Signature

 witness*

.....
Date

14.02.2016

The University recognises that there may be exceptional circumstances requiring restrictions on copying or conditions on use. Requests for restriction for a period of up to 2 years must be made in writing. Requests for a longer period of restriction may be considered in exceptional circumstances and require the approval of the Dean of Graduate Research.

FOR OFFICE USE ONLY

Date of completion of requirements for Award:

DOCTORAL THESIS

Advanced Dynamics of Optically Trapped Nanowire Waveguides

Author:

Wen Jun TOE

Supervisor:

Dr. Peter REECE

A thesis submitted in fulfilment of the requirements for the degree of
Doctor of Philosophy



UNSW
A U S T R A L I A

School of Physics, Faculty of Science
The University of New South Wales

February 2016

“Success is a journey, not a destination. The doing is often more important than the outcome.”

Arthur Robert Ashe, Jr.

Contents

Contents	v
Originality Statement	ix
Copyright Statement	xi
Authenticity Statement	xiii
Abstract	xv
Publications	xvii
Acknowledgements	xix
List of Figures	xxi
Abbreviations	xxv
Symbols	xxvii
1 Introduction	1
1.1 Brief history of optomechanics	2
1.2 Optical trapping of non-spherical particles	4
1.3 Optical binding and interactions	7
1.4 Objectives and outline	8
1.5 References	9
2 Construction of the Research Optical Tweezers	17
2.1 Introduction	18
2.2 Basic optical tweezers	18
2.3 Sample mount and sample preparation	20
2.4 Beam steering optics	21
2.5 Acousto-Optic Deflectors (AOD)	22
2.5.1 Beam Steering and Trap Multiplexing by AOD	23
2.5.2 Calibration of AOD input frequency against distance in the image plane	25
2.5.3 Trap Power Attenuation by AOD	28
2.6 Spatial light modulator (SLM)	29

2.6.1	Phase mask or hologram generation	31
2.6.2	Zernike polynomials for aberration corrections	31
2.7	Vibration isolation	33
2.8	Particle tracking and measurements	34
2.8.1	Interferometric particle tracking	34
2.8.2	Calibration of QPD response to particle displacement	36
2.9	Trapping and tracking of a particle using optical tweezers	41
2.10	References	43
3	Optical Trapping of InP Nanowires	47
3.1	Introduction	49
3.2	Theoretical considerations of the optical trapping of nanowires	51
3.3	InP nanowire trapping experiments	54
3.3.1	InP nanowire preparation	54
3.3.2	Trapping a single InP nanowire	55
3.3.3	Calibration of detector response of a trapped nanowire	56
3.3.4	Length measurements of nanowires	58
3.3.5	Trap stiffness of optically trapped nanowires	60
3.4	Length dependence of nanowire trapping	61
3.5	Stable axial trapping position	64
3.6	Resonant behaviour of optically trapped nanowires	68
3.7	Winding number analysis	73
3.7.1	Introduction to the winding number analysis	73
3.7.2	Application of the winding number analysis on optically trapped nanowire trajectory	75
3.8	Height dependence of nanowire resonance	76
3.9	Expansion of the power spectral analysis method	79
3.10	Power dependence of nanowire resonance	82
3.11	Length dependence of resonance peaks	88
3.12	Conclusion	89
3.13	References	90
4	Waveguiding Properties and Coupling of Indium Phosphide (InP) Nanowire Waveguides	95
4.1	Introduction	96
4.2	Waveguiding properties of single InP nanowire waveguides	98
4.3	Poynting vectors for InP nanowire waveguides	108
4.4	Dispersion and group velocity of InP nanowire waveguides	111
4.5	Coupling between two InP nanowire waveguides	113
4.5.1	Conditions for weak coupling	114
4.6	Coupling constant of coupled InP nanowire waveguides	114
4.7	Mode profiles of coupled InP nanowire waveguides	117
4.8	Optical force calculations from Maxwell's Stress Tensor	123
4.9	Power transfer between coupled nanowires and beat length	126

4.10	Group velocities of coupled nanowire waveguides	129
4.11	Dispersion relation of coupled nanowire waveguides	130
4.12	Optical forces from eigenmode analysis	132
4.13	Conclusion	136
4.14	References	137
5	Measurement of Forces by Time Shared Optical Tweezers	143
5.1	Introduction	144
5.2	Trap multiplexing and multiple particle tracking methods	145
5.2.1	Orthogonally polarised dual beam optical tweezers	145
5.2.2	Trap multiplexing and tracking by holographic optical tweezers	147
5.2.3	Fast tracking by time-shared trap multiplexing	151
5.3	Limits of tracking by time-shared optical tweezers	152
5.4	Hydrodynamic coupling interactions	155
5.5	Tracking of multiple polystyrene particles by time-shared traps	157
5.6	Tracking of multiple gold nanoparticles by time-shared traps	161
5.7	Applicability of time-shared optical tweezers in trapping and tracking two interacting InP nanowires	163
5.8	Conclusion	164
5.9	References	166
6	Conclusion	169
6.1	References	171
A	Derivation of force in terms of Maxwell's Stress Tensor and Poynting Vector	173
A.1	References	177

Originality Statement

'I hereby declare that this submission is my own work and to the best of my knowledge it contains no materials previously published or written by another person, or substantial proportions of material which have been accepted for the award of any other degree or diploma at UNSW or any other educational institution, except where due acknowledgement is made in the thesis. Any contribution made to the research by others, which whom I have worked at UNSW or elsewhere, is explicitly acknowledged in the thesis. I also declare that the intellectual content of this thesis is the product of my own work, except to the extent that assistance from others in the project's design and conception in style, presentation and linguistic expression is acknowledged.'

Signed:

Date:

14.02.2016

Copyright Statement

'I hereby grant the University of New South Wales or its agents the right to archive and to make available my thesis or dissertation in whole or part in the University libraries in all forms or media, now or here after known, subject to the provisions of the Copyright Act 1968. I retain all proprietary rights, such as patent rights. I also retain the right to use in future works (such as articles or books) all or part of this thesis or dissertation.

I also authorise the University Microfilms to use the 350 word abstract of my thesis in Dissertation Abstract International (this is applicable to doctoral theses only).

I have either used no substantial portions of copyright material in my thesis or I have obtained permission to use copyright material; where permission has not been granted I have applied/will apply for a partial restriction of the digital copy of my thesis or dissertation.'

Signed:

Date:

14.02.2016

Authenticity Statement

'I certify that the Library deposit digital copy is a direct equivalent of the final officially approved version of my thesis. No emendation of content has occurred and if there are any minor variations in formatting, they are the result of the conversion to digital format'

Signed:

Date:

14.02.2016

Abstract

Advanced Dynamics of Optically Trapped Nanowire Waveguides

by Wen Jun TOE

In this thesis I describe a number of studies to examine some high order effects of advanced trapping dynamics beyond the standard single gradient force optical trap. Our interests lay primarily on low symmetry particles, specifically on high refractive index, high aspect ratio nanowires. We examine higher order dynamics due to coupling between rotational and translational degrees of freedom when a single high aspect ratio nanowire is trapped. We also study the coupling of the trapping laser into the waveguiding modes of the trapped nanowire, as well as the coupling interactions between multiple trapped nanowires.

On single optically trapped nanowires, we show calculations beyond the standard power spectral analysis to demonstrate the emergence of resonance behaviour in over-damped systems due to the coupling between rotational and translational degrees of freedom. We also experimentally demonstrate the effects of such coupling which shows up in the form of resonance peaks in the power spectrum when single nanowires are trapped in optical tweezers.

Next we examine the coupling of light into the waveguide modes of high refractive index nanowires by calculating the field profiles, dispersion and group velocity. We then investigate the optical coupling between multiple high refractive index nanowires in close proximity. In particular, we calculate the field profiles, dispersion and optical force of coupled nanowire waveguides with the Coupled Mode Theory and Perturbation Theory. The optical forces between coupled waveguides is also calculated and compared to results obtained from Maxwell's Stress Tensor calculations.

In the final results chapter, we explore various experimental approaches to experimentally measure the coupled nanowire system that was calculated in the previous chapter. We propose time-shared optical tweezers with interferometric particle tracking as a means of physically measuring the coupling between nanowires and investigate the feasibility of this measurement technique for our system.

In summary, we conducted theoretical analysis and experiments that aid in the further understanding of the advanced dynamics of high refractive index, high aspect ratio nanowires within the optical trapping domain.

Publications

Peer-Reviewed Publications

P. J. Reece, **W. J. Toe**, F. Wang, S. Paiman, Q. Gao, H. H. Tan, and C. Jagadish, "Characterization of Semiconductor Nanowires Using Optical Tweezers," *Nano Lett* **11** (6), 2375-2381 (2011).

F. Wang, **W. J. Toe**, W. M. Lee, D. McGloin, Q. Gao, H. H. Tan, C. Jagadish, and P. J. Reece, "Resolving Stable Axial Trapping Points of Nanowires in an Optical Tweezers Using Photoluminescence Mapping," *Nano Lett* **13** (3), 1185-1191 (2013).

W. J. Toe, I. O. Piwonka, C. Angstmann, Q. Gao, H. H. Tan, C. Jagadish, B. Henry, and P. J. Reece, "Anomalous Dynamic Behavior of Optically Trapped High Aspect Ratio Nanowires," *ArXiv e-prints*, arXiv:1508.03072, August 2015.

W. J. Toe, I. O. Piwonka, C. Angstmann, Q. Gao, H. H. Tan, C. Jagadish, B. Henry, and P. J. Reece, "Nonconservative Dynamics of Optically Trapped High-aspect-ratio Nanowires," *Physical Review E*, 2016.

Conference Proceedings

W. J. Toe, I. O. Piwonka, A. Andres-Arroyo, Q. Gao, H. H. Tan, C. Jagadish, B. Henry, C. Angstmann, and P. J. Reece, "Anomalous Dynamic Behaviour of Optically Trapped High Aspect Ratio Nanowires," *Optical Trapping and Optical Micromanipulation XI* **9164** (2014). (**Accepted as Oral Presentation**)

W. J. Toe, P. J. Reece, and A. Andres-Arroyo, "Measurement of Hydrodynamic Coupling by Time-shared Optical Tweezers," in Optics in the Life Sciences, OSA Technical Digest (online) (Optical Society of America, 2015), paper OtM2E.2. **(Accepted as Oral Presentation)**

Conference Presentations

W. J. Toe, K. Pearce, F. Wang, and P. J. Reece, "Dark Field Optical Tweezers for Studying Nanoparticle Dynamics," The 20th Australian Institute of Physics Congress 2012 (AIP 2012). **(Accepted as Oral Presentation)**

W. J. Toe, F. Wang, Q. Gao, H. H. Tan, C. Jagadish, and P. J. Reece, "Axial Photoluminescence Mapping of Optically Trapped Semiconductor Nanowires," International Conference of Nanoscience and Nanotechnology 2014 (ICONN 2014). **(Accepted as Oral Presentation)**

W. J. Toe, I. O. Piwonka, F. Wang, A. Andres-Arroyo, H. H. Tan, C. Jagadish, C. Angstmann, B. Henry, and P. J. Reece, "Optical Trapping and Spectroscopic Characterisation of Single Semiconductor Nanowires," The Australian Nanotechnology Network Nanotechnology Entrepreneurship Workshop for Early Career Researchers (2015). **(Accepted as Poster Presentation)**

Acknowledgements

I would like to take a moment to express my most sincere gratitude to Dr. Peter Reece, who has continually offered me guidance right from the beginning. As my supervisor, Peter has had to put up with the headstrong-yet-clueless-and-easily-distracted PhD student with average work ethics that is yours truly (Sorry Peter!). And yet, he has been endlessly patient in nudging me (sometimes even hauling my a**) in the right direction, up until the end when this thesis is finally written, and possibly even more after that. Coming from a hard science background, academic writing has never been my strongest suit; more than once in the duration of my candidacy Peter has had to overhaul my entire piece of written work, and then provide me with a generous stream of suggestions for improvements. On top of his busy schedule, Peter has never failed in finding the time to discuss my progress, be it experimental or written (especially written!) works. Needless to say, Peter has been one of the most significant, if not the most important person that I owe my thanks to for the completion of this work. Thank you Peter!

Next up, I have my lab mates Fan (now Dr. Wang) and Ana to acknowledge. Fan and I worked together on the experimental aspects of the optical tweezers before he graduated from his PhD. Much of the construction of the optical tweezers and data collection is done with him by my side, figuring out the technical details and quirks of the experimental setup with me when my own ideas were exhausted. As for Ana, I owe her tremendously for her amazing organisational skills and prowess in Matlab programming. Ana has been generous in getting my Matlab and LaTeX proficiency up to scratch and in lending her assistance in these areas whenever I needed it. This thesis would have been much harder to accomplish without her initial coaching, her LaTeX thesis template, as well as her occasional rant at me to be more organised. So here I would like to say thank you to you both. I couldn't have asked for better lab mates than you guys.

Of course I will not forget all the people I have collaborated with in the duration of this thesis. To Ignacio, Dr. Chris Angstmann and Prof. Bruce Henry from the School of Mathematics, I would like to convey my appreciation for your help in the mathematical modelling and explanation of the nanowire rotation dynamics. To Dr. Gao, Prof. Tan and Prof. Jagadish from the Department of

Electronic Materials Engineering in ANU, I am indebted to you for your continuous supply of InP nanowires which are central to this research.

Last but not least, I would like to thank all my friends, family and colleagues for your support in my journey. Honourable mentions are Mr Pat MacMillan, who is always available for a chat, or for lessons (sometimes long lectures) in physics, chemistry and life alike. Friday lunch at the park is always a nice wind down for a hectic week. Also to Hannah, who is half way across the world in person but is still always available for mental support, especially in the final few months leading up to the completion of this thesis. Finally to my mom, who shows her support by dropping me random encouraging text messages and is always offering to help me financially if everything goes to shit. It is often said that the journey is more important than the destination; from where I stand, having all of you along the way is the true testament to this quote!

List of Figures

1	Introduction	1
1.1	Optically trapped KNbO ₃ nanowire as a tunable light emitting scanning probe	6
2	Construction of the Research Optical Tweezers	17
2.1	Ray optics picture of a spherical particle in optical tweezers	19
2.2	Telescope setup of beam expanding optics	20
2.3	Sample slide preparation and mounting	21
2.4	Placement of steering mirror	22
2.5	Acousto-optic deflector (AOD)	23
2.6	Beam steering and trap multiplexing by two AOD crystals	24
2.7	Time-shared optical tweezers in action	25
2.8	Stage micrometer	26
2.9	Two time-shared traps	27
2.10	Calibration of AOD input frequency against distance in the image plane	27
2.11	Calibration of AOD input voltage against trapping power	29
2.12	Configuration of spatial light modulator (SLM) in optical tweezers	30
2.13	Kinoform applied to SLM for aberration correction	32
2.14	Configuration of spatial light modulator (SLM) in optical tweezers	33
2.15	Comparison of power spectra with and without vibration isolation	34
2.16	Configuration of quadrant photodiode (QPD) in optical tweezers	36
2.17	Calibration of QPD	38
2.18	Detector response curve of a trapped 1 μm sphere	40
2.19	Schematic diagram of our optical tweezers setup	41
2.20	Trajectory of an optically trapped 1 μm sphere	42
3	Optical Trapping of InP Nanowires	47
3.1	Probes	50
3.2	Optical tweezers scanning probe	51
3.3	Nanowire bright field images	55
3.4	Failed nanowire trapping	57

3.5	Successful nanowire trapping	57
3.6	Calibration curves	58
3.7	Nanowire bright field image on coverslip	59
3.8	Power spectrum of single nanowire	61
3.9	Trap stiffness vs. nanowire length	62
3.10	Corner frequency vs. nanowire length	63
3.11	Calibration curves	64
3.12	Trapping orientation of elongated objects	65
3.13	Nanowires with tapering	66
3.14	Trapping orientation of elongated objects	67
3.15	μ -PL mapping of trapped nanowire	67
3.16	Resonance peak in power spectrum of trapped nanowire	69
3.17	Autocorrelation function in the trajectory of a trapped nanowire	70
3.18	Intensity of trap focus with aberrations	71
3.19	Translational distribution of optically trapped nanowires	72
3.20	Example trajectory for winding number calculation	75
3.21	Winding number for nanowire trajectory	76
3.22	Winding number for nanowire trajectory at different trapping heights	77
3.23	Resonance versus trapping height	79
3.24	Resonance peak in power spectrum of trapped nanowire with fit	81
3.25	Resonance peak in power spectrum of trapped nanowire for different powers	83
3.26	Fitting parameters of the power spectral density for different trapping powers	84
3.27	Peak frequency versus trapping power	85
3.28	Winding numbers and winding rate of nanowires for different trapping powers	86
3.29	Translational distribution of nanowire for different trapping powers	87
3.30	Projections of the translational distribution of a trapped nanowire at different trapping powers	88
3.31	Resonance peak versus nanowire length	89

4 Waveguiding Properties and Coupling of Indium Phosphide (InP)

Nanowire Waveguides		95
4.1	Illustration of single nanowire waveguide	100
4.2	Electric field components of InP nanowire waveguides for different radii	103
4.3	Electric field intensity in 150 nm InP nanowires	104
4.4	FDTD results for electric field intensity in 150 nm InP nanowires	105
4.5	Evanescence field trapping	106
4.6	Evanescence field trapping - experimental observation	106
4.7	Poynting vector of 150 nm InP nanowire waveguide	109
4.8	Poynting vector of 300 nm InP nanowire waveguide	110
4.9	Dispersion relation of InP nanowire waveguide	111
4.10	Group velocity v_g of InP nanowire waveguide	112

4.11	Illustration of two coupled nanowire waveguides	113
4.12	Coupling constant of two identical InP nanowire waveguides (3-D plot)	115
4.13	Coupling constant of two identical InP nanowire waveguides	116
4.14	Electric field of the symmetric and anti-symmetric modes in coupled 150 nm InP nanowires separated at 500 nm	118
4.15	Magnetic field of the symmetric and anti-symmetric modes in coupled 150 nm InP nanowires separated at 500 nm	118
4.16	Electric field of the symmetric and anti-symmetric modes in coupled 150 nm InP nanowires separated at 300 nm	119
4.17	Magnetic field of the symmetric and anti-symmetric modes in coupled 150 nm InP nanowires separated at 300 nm	119
4.18	Electric field of the symmetric and anti-symmetric modes in coupled 200 nm InP nanowires separated at 500 nm	120
4.19	Magnetic field of the symmetric and anti-symmetric modes in coupled 200 nm InP nanowires separated at 500 nm	120
4.20	Electric field of the symmetric and anti-symmetric modes in coupled 200 nm InP nanowires separated at 300 nm	121
4.21	Magnetic field of the symmetric and anti-symmetric modes in coupled 200 nm InP nanowires separated at 300 nm	121
4.22	Comparison of electric field intensity in coupled 150 nm InP nanowires separated at 300 nm between analytical calculations and FDTD simulations	122
4.23	Optical forces from symmetric and antisymmetric modes of coupled InP nanowires	125
4.24	Electric field of the anti-symmetric mode in coupled 200 nm InP nanowires separated at 300 nm	128
4.25	Group velocity for the isolated, symmetric and antisymmetric modes of coupled 100 nm InP nanowires separated at 300 nm	130
4.26	Dispersion relation for the unperturbed, symmetric and antisymmetric modes of coupled 100 nm InP nanowires separated at 250 nm	131
4.27	Dispersion relation for the unperturbed, symmetric and antisymmetric modes of coupled 100 nm InP nanowires separated at 300 nm	131
4.28	Dispersion relation for the unperturbed, symmetric and antisymmetric modes of coupled 100 nm InP nanowires separated at 500 nm	132
4.29	Optical forces from symmetric and antisymmetric modes of coupled InP nanowires	134
4.30	Comparison of optical forces calculated by Maxwell's Stress Tensor with the eigenmode analysis	135
5	Measurement of Forces by Time Shared Optical Tweezers	143
5.1	Trap multiplexing by orthogonal polarisation	145
5.2	Rotation of polarisation for lenses of different NA	146
5.3	Tracking signal separation by spatial filtering	149
5.4	Simultaneous tracking of multi-trap optical tweezers using signal separation by spatial filtering	150

5.5	Simultaneous trapping and tracking of multiple objects by time-shared optical tweezers and QPD	152
5.6	Illustration of two trapped spheres	158
5.7	Longitudinal cross correlation functions of two optically trapped 1 μm polystyrene spheres	159
5.8	Transverse cross correlation functions of two optically trapped 1 μm polystyrene spheres	160
5.9	Depth of the minimum in the cross correlation functions versus ratio of radius a and separation d	161
5.10	Cross correlation between two 100 nm spherical gold nanoparticles	162
6	Conclusion	169

Abbreviations

2-D	Two-Dimensional
3-D	Three-Dimensional
AOD	Acousto-Optic Deflector
AFM	Atomic Force Microscope
BFP	Back Focal Plane
CCD	Charge Coupled Device
CMT	Coupled Mode Theory
DFS	Digital Frequency Synthesizer
DH-PSF	Double Helix Point Spread Function
FDTD	Finite-Difference Time-Domain
FPGA	Field Programmable Gate Array
InP	Indium Phosphide
MOCVD	Metal Organic Chemical Vapour Deposition
NA	Numerical Aperture
PL	Photo Luminescence
QPD	Quadrant Photo Diode
RF	Radio Frequency
SEM	Scanning Electron Microscopy
SHG	Second Harmonic Generation
SLM	Spatial Light Modulator
μ-PL	Micro-Photo Luminescence

Symbols

a	radius
d	separation
f_c	corner frequency
k_0	free-space wavenumber
n	refractive index
n_c	core refractive index
n_m	medium refractive index
r	radial displacement
t	time
v_g	group velocity
x, y	displacements
C	coupling constant
F	force
K	stiffness matrix
L	length
L_0	beat length
N	number (of particles/traps)
P	power
T	temperature
β	propagation constant
λ	wavelength
γ	drag coefficient

ω	frequency
κ	trap stiffness
τ	characteristic time
η	shear viscosity
ξ	noise strength

Chapter 1

Introduction

1.1	Brief history of optomechanics	2
1.2	Optical trapping of non-spherical particles	4
1.3	Optical binding and interactions	7
1.4	Objectives and outline	8
1.5	References	9

1.1 Brief history of optomechanics

Optomechanics is the study of the interaction between electromagnetic radiation and mechanical systems via radiation pressure. The understanding of these interactions is of fundamental interest in science with a long-standing history. The first observation of the manifestation of radiation pressure was made by Johannes Kepler in 1691, where he put forward the concept to explain the observation that a tail of a comet always points away from the Sun. It wasn't until 1862 before James Clerk Maxwell showed theoretically that electromagnetic radiation carries momentum and thus exerts a pressure upon any surface exposed to it, resulting in radiation pressure which is the key to opto-mechanical interactions.

The road towards experimental demonstration of radiation pressure is less straight forward, the most notable failure being the Crookes radiometer invented in 1873 by the chemist, Sir William Crookes. The radiometer is made of a rotor with several vertical lightweight metal vanes, polished white on one side and black on the other. The vanes are spaced equally around the axis on a low friction spindle within a glass bulb from which much of the air has been removed to form a partial vacuum. When exposed to light, the vanes turn with no other source of power except for the light incident upon it, and was thus believed to be a demonstration of radiation pressure. This explanation proved to be incorrect however, as it was later discovered that the rotation was caused by a temperature gradient causing pressure differences between the vanes, rather than simple radiation pressure [1].

The search for experimental verification of radiation pressure carried on until 1901, when Ernest Fox Nichols and Gordon Ferrie Hull constructed the Nichols radiometer, which consists of two glass vanes suspended on a very fine glass fibre [2, 3]. Convection effects were minimised by coating one side of the vanes with a highly reflective silver mirror to reduce absorption and to reduce the air pressure within the radiometer [2]. The apparatus was able to measure radiation pressures as small as 10^{-4} dyne to within about 0.6% agreement with values predicted by Maxwell. Further experiments by Richard Beth

in 1936 measured the torque exerted by the change in angular momentum in circularly polarised light [4].

The invention of the laser in the 1950's revolutionised the field of optomechanics due to its capability of generating high intensities of light. In particular, this led to the emergence of optical trapping in 1969 when Arthur Ashkin first observed the acceleration of freely suspended particles by forces of radiation pressure from a laser [5]. One of the more surprising discoveries from this study was that particles were drawn towards the centre of the propagation axis of the laser, rather than away from it, effectively achieving particle confinement in two dimensions. Ashkin then used two counter propagating beams and managed to demonstrate the first instance of a three dimensional optical trap. A variation of this was the optical levitation trap, where gravity was used in place of a second laser beam to confine the particle in the axial direction [6].

The single-beam gradient force radiation pressure particle trap more commonly known today as the optical tweezers wasn't invented until 1985 [1]. Ashkin recognised the role of gradient forces in optical traps, and designed the optical tweezers with a large numerical aperture objective lens such that a large intensity gradient in the axial direction can be achieved to generate a large enough gradient force to counteract scattering forces. With this setup, Ashkin successfully demonstrated stable 3-dimensional optical trapping of dielectric spheres with diameters ranging from 10 μm down to 25 nm. Since its invention, the gradient force optical tweezers has had profound impact in various fields of research, including colloidal hydrodynamics [7–13], molecular biology [14–16] and nanotechnology [17–32]. One of the most notable achievements of optical tweezers in biology is the precise position detection over time and the measurement of pico-Newton forces in the action of single molecule motors such as Kinesin [15] and Myosin [16].

The invention of the optical tweezers also brought about broader researches into fields related to optical forces. An example of this is the discovery and demonstration of optical binding by Michael Burns in 1989 [33]. Optical binding is a phenomenon where intense light field induces significant forces between microscopic particles due to the interaction between a particle and the scattered light fields from nearby particles. In Burns' experiment, microbeads pushed against the surface of the sample cell due

to radiation pressure from a laser source reorganised themselves into ordered structures forming two-dimensional ‘optical crystals’ [34]. Tatarkova and colleagues further showed the optical binding of multiple colloidal particles in a one-dimensional array far from any surface using counter propagating Gaussian optical traps [35]. In this study, up to seven $3\ \mu\text{m}$ spheres arranged themselves within the counter propagating trap forming a linear array with constant interparticle spacing, thereby demonstrating the ability to experimentally recreate optical binding and coupling between micro-particles.

1.2 Optical trapping of non-spherical particles

Optical trapping of spherical particles is very well understood and has been extensively studied and documented in the literature, both experimentally and theoretically [1, 36–39]. The same cannot be said for non-spherical particles due to the significant increase in complexity exhibited by non-spherical particles compared to spherical particles, such as the inclusion of angular degrees of freedom and the lack of analytical solutions [40]. These non-spherical particles include spheroidal and ellipsoidal particles [41, 42], nano and micro rods [43–45], nanowires [29, 30, 45] as well as more complex structures such as red blood cells [46, 47] and engineered micro structures [48–54].

Spheroidal particles are considered to be one of the simplest non-spherical particles, as it is formed by a slight deformation of a sphere [40, 41]. A prolate spheroid tends to align its symmetry axis with the beam axis while an oblate spheroid orients itself so that its symmetry axis is perpendicular to the beam axis, because in both cases the overlap between the particles and the optical trap is maximised and potential energy is minimised [41]. Cylinders and disks are symmetrically similar to spheroids, except with right-angled edges. This leads to the observation of oblique trapping in cylinders, where the symmetry axis is oriented neither parallel nor perpendicular to the beam axis, but somewhere in between [55–57]. The advanced dynamics of non-spherical particle trapping can have many applications. In one study by Phillip *et al.*, it is found that some desirable features of a force field that can be introduced by modifying the particle shape or dielectric structure beyond that of a simple homogeneous sphere [51]. In particular,

it is discovered that tapered cylinders have a 'force plateau' in the restoring force, resulting in a constant lateral force that serves to draw the particle into the beam when displaced. Phillip *et al.* further demonstrated this effect by designing and fabricating a passive force clamp based on a tapered cylinder which is capable of applying a constant force over several micrometres [51].

One particular class of non-spherical elongated particles, namely high aspect ratio (< 100) nanowires, is gaining increasing interest because of its high shape anisotropy and unique physical properties. Numerous attempts have been made to understand the trapping properties of high aspect ratio nanowires through simulations and numerical calculations; these include Borghese *et al.*'s studies on the rotation and torque of optically trapped nanowires by modelling them as linear chains composed of identical spheres [58], as well as Cao *et al.*'s simulations on the equilibrium orientations of nanowires and nanorods of various dimensions and aspect ratios [55]. Simpson and Hanna have also calculated the trapping stability of nanowires [59] and microrods [44] due to variations in size and refractive indices [44]. There have also been experimental studies into the trapping dynamics of various kinds of nanowires, such as Irrera *et al.*'s study on silicon nanowires [30], Neves *et al.*'s study on tilted polymer nanofibres [24], Marago *et al.*'s work on carbon nanotubes [22], Pauzauskie *et al.*'s optical trapping and integration of nanowire assemblies from various semiconducting material [26], as well as our own work in the characterisation of optically trapped Indium Phosphide (InP) nanowires [29].

Understanding the trapping dynamics of optically trapped nanowires is highly beneficial and has many potential applications because recent developments in fabrication technologies have enabled the fabrication of high quality semiconductor nanowires, which have shown great promise in various electronics and photonics applications including optical waveguides [60], field effect transistors [61], single electron transistors [62], nanolasers [63], photodetectors [64] and integrated microprocessors [65, 66]. In fact, there has been developments in microscopy, photonics and chemistry based on the optical trapping of semiconductor nanowires. For example, Pauzauskie *et al.* has optically trapped nanowires of various semiconductor material and cross-sectional geometries and then manipulated them to construct nanowire junctions and assemblies [26] while Smith

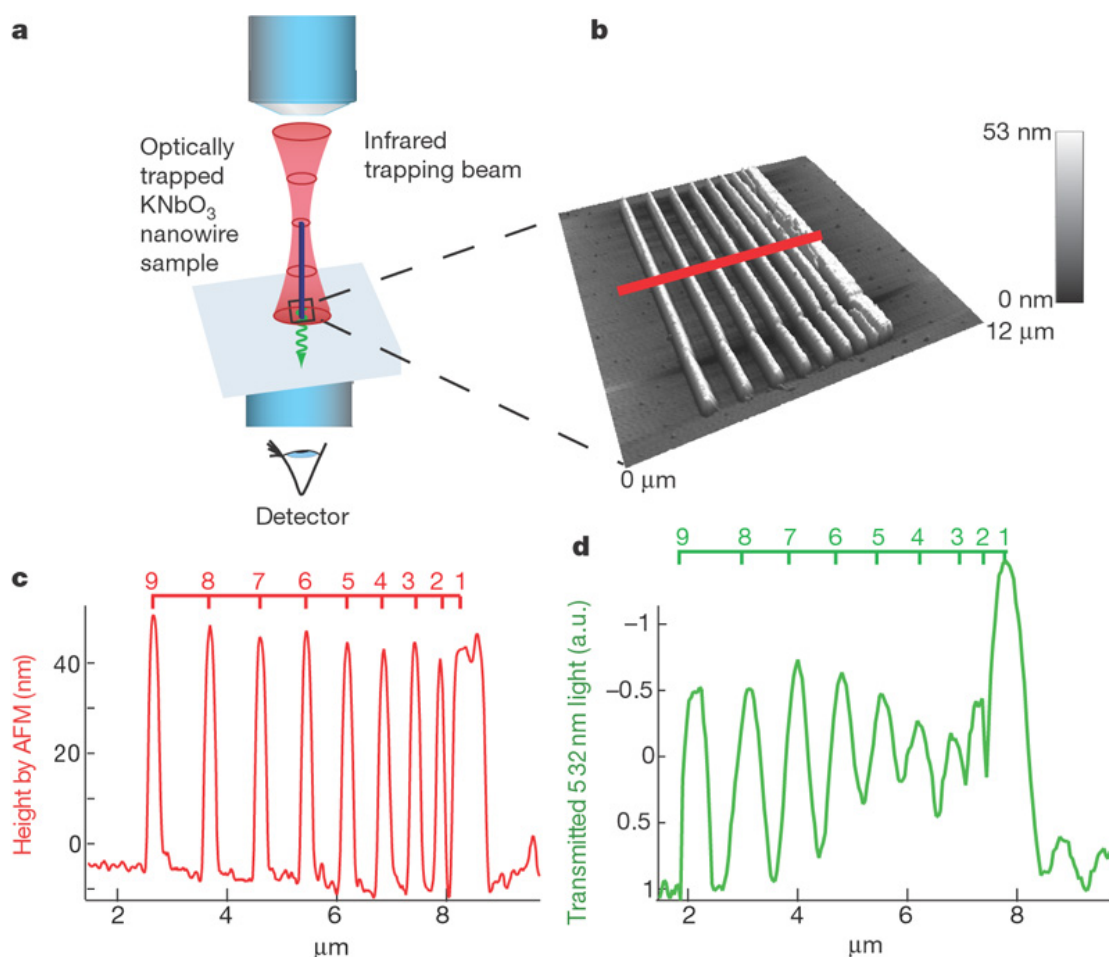


Figure 1.1: (a) Schematic of inverted optical scanning configuration. (b) AFM topographic image of thermally evaporated pattern of gold stripes on a glass coverslip. (c) AFM line scan from region indicated in (b). (d) Optical transmission profile captured by scanning a single KNbO₃ nanowire over the metallic surface structure. The nanowire used to create the transmission line scan was measured by AFM to have these dimensions: width=122 nm, length=1.4 mm and height=53 nm. Figure from [27]. Reprinted by permission from Macmillan Publishers Ltd: Nature [27], copyright 2007.

et al. demonstrated the generation of singlet oxygen from optically trapped silicon and gold nanowires using near infrared wavelengths, which has potential applications in photodynamic therapy [67]. Furthermore, by examining the Brownian motion of silicon nanowires within optical traps Roder *et al.* managed to examine photothermal heating effects on these nanowires [68]. In scanning probe microscopy, optically trapped high aspect ratio nanowires have been used as scanning probes due to the ability of achieving very fine tips with a small spatial footprint and a smaller force constant. Nakayama *et al.* used optically trapped Potassium Niobate (KNbO₃) nanowire as a tunable light

emitting probe to image a test pattern consisting a series of 200-nm-wide, 50-nm-thick gold lines spaced between 200 nm and 1000 nm apart (Figure 1.1) [27]. Marago *et al.* managed to show that optically trapped single-wall carbon nanotubes can achieve force sensitivities down to femtonewtons in the axial direction [22].

1.3 Optical binding and interactions

Optical binding is another avenue where optomechanics is applied. Optical binding forces arise from the scattering of light between several objects [69]. This phenomena was first observed in a line shaped optical trap created using a cylindrical lens [33], and has since been studied theoretically [70, 71] and demonstrated in other forms of optical traps such as counter propagating traps [35, 72] and evanescent field traps [73]. The optical binding energy landscape between two particles is known to be a series of roughly equally spaced energy minima at particle-particle separations approximately equal to integer multiples of the wavelength of the interacting light [74], and particle-pairs have been shown to maintain discrete interparticle separations by staying in the nearest energy minimum or 'hopping' into other energy minima [33, 35, 75]. This effect has been shown to occur in both the direction of light propagation i.e. longitudinal optical binding [35], and the direction perpendicular to light propagation i.e. transverse optical binding [76].

Optical binding forces have a wide range of applications, from forming the basis for self-assembly to precision particle sorting and transport [77]. Grzegorzczuk *et al.* recently demonstrated the assembly of an optical mirror with only a single layer of 3 μm spherical polystyrene particles [78]. On a separate study, Grzegorzczuk *et al.* also demonstrated the passive guiding and sorting of small particles based on the equilibrium between optical scattering and binding forces [77]. Optical binding forces also leads to the formation of optical matter, a contactless but rigid particle formation held together by optical binding forces. Yan *et al.* showed the self assembly of silver nanoparticles into dimers, chains and closed-packed 'photonic clusters' induced by optical binding forces [79].

1.4 Objectives and outline

In this thesis I aim to examine some advanced trapping dynamics beyond the standard single gradient force optical trap, particularly on the trapping dynamics of single and multiple high refractive index, high aspect ratio nanowires. In Chapter 3 we examine higher order dynamics due to coupling between rotational and translational degrees of freedom when a single high aspect ratio nanowire is trapped. In Chapter 4 we study the coupling of the trapping laser into the waveguiding modes of the trapped nanowire, as well as the coupling interactions between multiple trapped nanowires. Finally in Chapter 5 we discuss various experimental approaches and propose a novel technique to experimentally measure these dynamics due to coupling interactions.

1.5 References

- [1] A. Ashkin, J. M. Dziedzic, J. E. Bjorkholm, and Steven Chu. Observation of a single-beam gradient force optical trap for dielectric particles. *Opt. Lett.*, 11:288–290, 1986.
- [2] E. F. Nichols and G. F. Hull. A preliminary communication on the pressure of heat and light radiation. *Physical Review*, 13(5):307–320, 1901. V23if Times Cited:66 Cited References Count:16.
- [3] E. F. Nichols and G. F. Hull. The pressure due to radiation. *Astrophysical Journal*, 17(5):315–351, 1903. V6513 Times Cited:17 Cited References Count:39.
- [4] R. A. Beth. Mechanical detection and measurement of the angular momentum of light. *Physical Review*, 50(2):115–125, 1936. V22ia Times Cited:464 Cited References Count:15.
- [5] A. Ashkin. Acceleration and trapping of particles by radiation pressure. *Phys. Rev. Lett.*, 24:156–159, Jan 1970.
- [6] A. Ashkin and J. M. Dziedzic. Optical levitation by radiation pressure. *Appl. Phys. Lett.*, 19:283, 1971.
- [7] M. Polin, D. G. Grier, and S. R. Quake. Anomalous vibrational dispersion in holographically trapped colloidal arrays. *Physical Review Letters*, 96(8), 2006. 018AX Times Cited:49 Cited References Count:22.
- [8] J. C. Meiners and S. R. Quake. Direct measurement of hydrodynamic cross correlations between two particles in an external potential. *Physical Review Letters*, 82(10):2211–2214, 1999. 173AX Times Cited:140 Cited References Count:14.
- [9] A. Curran, M. P. Lee, M. J. Padgett, J. M. Cooper, and R. Di Leonardo. Partial synchronization of stochastic oscillators through hydrodynamic coupling. *Physical Review Letters*, 108(24), 2012. 958RK Times Cited:11 Cited References Count:20.
- [10] J. Kotar, L. Debono, N. Bruot, S. Box, D. Phillips, S. Simpson, S. Hanna, and P. Cicuta. Optimal hydrodynamic synchronization of colloidal rotors. *Physical Review Letters*, 111(22), 2013. 265HM Times Cited:12 Cited References Count:32.
- [11] R. Di Leonardo, S. Keen, J. Leach, C. D. Saunter, G. D. Love, G. Ruocco, and M. J. Padgett. Eigenmodes of a hydrodynamically coupled micron-size multiple-particle ring. *Physical Review E*, 76(6), 2007. Part 1 246CR Times Cited:23 Cited References Count:28.
- [12] R. Di Leonardo, S. Keen, F. Ianni, J. Leach, M. J. Padgett, and G. Ruocco. Hydrodynamic interactions in two dimensions. *Physical Review E*, 78(3), 2008. 1 355BD Times Cited:20 Cited References Count:20.
- [13] R. Di Leonardo, A. Buzas, L. Kelemen, G. Vizsnyiczai, L. Oroszi, and P. Ormos. Hydrodynamic synchronization of light driven microrotors. *Physical Review Letters*, 109(3), 2012. 974WA Times Cited:26 Cited References Count:22.

- [14] K. Svoboda, C. F. Schmidt, B. J. Schnapp, and S. M. Block. Direct observation of kinesin stepping by optical trapping interferometry. *Nature*, 365(6448):721–727, 1993. Mc812 Times Cited:1199 Cited References Count:49.
- [15] K. Svoboda and S. M. Block. Force and velocity measured for single kinesin molecules. *Cell*, 77(5):773–784, 1994. Nq123 Times Cited:525 Cited References Count:44.
- [16] J. E. Molloy, J. E. Burns, J. Kendrickjones, R. T. Tregear, and D. C. S. White. Movement and force produced by a single myosin head. *Nature*, 378(6553):209–212, 1995. Td759 Times Cited:400 Cited References Count:14.
- [17] Karel Svoboda and Steven M. Block. Optical trapping of metallic rayleigh particles. *Optics Letters*, 19(13):930–932, 1994.
- [18] P. M. Hansen, V. K. Bhatia, N. Harrit, and L. Oddershede. Expanding the optical trapping range of gold nanoparticles. *Nano Letters*, 5(10):1937–1942, 2005.
- [19] L. Bosanac, T. Aabo, P. M. Bendix, and L. B. Oddershede. Efficient optical trapping and visualization of silver nanoparticles. *Nano Letters*, 8(5):1486–1491, 2008. 301OV Times Cited:63 Cited References Count:18.
- [20] F. Hajizadeh and S. N. S. Reihani. Optimized optical trapping of gold nanoparticles. *Optics Express*, 18(2):551–559, 2010.
- [21] L. Jauffred, A. C. Richardson, and L. B. Oddershede. Three-dimensional optical control of individual quantum dots. *Nano Letters*, 8(10):3376–3380, 2008. 358HD Times Cited:51 Cited References Count:19.
- [22] O. M. Marago, P. H. Jones, F. Bonaccorso, V. Scardaci, P. G. Gucciardi, A. G. Rozhin, and A. C. Ferrari. Femtonewton force sensing with optically trapped nanotubes. *Nano Letters*, 8(10):3211–3216, 2008. 358HD Times Cited:51 Cited References Count:33.
- [23] P. J. Pauzauskie, A. Jamshidi, J. K. Valley, J. H. Satcher, and M. C. Wu. Parallel trapping of multiwalled carbon nanotubes with optoelectronic tweezers. *Applied Physics Letters*, 95(11), 2009. 497XC Times Cited:15 Cited References Count:29.
- [24] A. A. R. Neves, A. Camposeo, S. Pagliara, R. Saija, F. Borghese, P. Denti, M. A. Iati, R. Cingolani, O. M. Marago, and D. Pisignano. Rotational dynamics of optically trapped nanofibers. *Optics Express*, 18(2):822–830, 2010. 547BP Times Cited:30 Cited References Count:46.
- [25] R. Agarwal, K. Ladavac, Y. Roichman, G. H. Yu, C. M. Lieber, and D. G. Grier. Manipulation and assembly of nanowires with holographic optical traps. *Optics Express*, 13(22):8906–8912, 2005. 979XE Times Cited:147 Cited References Count:29.
- [26] P. J. Pauzauskie, A. Radenovic, E. Trepagnier, H. Shroff, P. D. Yang, and J. Liphardt. Optical trapping and integration of semiconductor nanowire assemblies in water. *Nature Materials*, 5(2):97–101, 2006. 008SC Times Cited:175 Cited References Count:29.

- [27] Y. Nakayama, P. J. Pauzauskie, A. Radenovic, R. M. Onorato, R. J. Saykally, J. Liphardt, and P. D. Yang. Tunable nanowire nonlinear optical probe. *Nature*, 447(7148):1098–U8, 2007. 183HT Times Cited:187 Cited References Count:30.
- [28] P. J. Reece, S. Paiman, O. Abdul-Nabi, Q. Gao, M. Gal, H. H. Tan, and C. Jagadish. Combined optical trapping and microphotoluminescence of single inp nanowires. *Applied Physics Letters*, 95(10), 2009. 493GM Times Cited:9 Cited References Count:20.
- [29] P. J. Reece, W. J. Toe, F. Wang, S. Paiman, Q. Gao, H. H. Tan, and C. Jagadish. Characterization of semiconductor nanowires using optical tweezers. *Nano Letters*, 11(6):2375–2381, 2011. 773QJ Times Cited:26 Cited References Count:25.
- [30] A. Irrera, P. Artoni, R. Saija, P. G. Gucciardi, M. A. Iati, F. Borghese, P. Denti, F. Iacona, F. Priolo, and O. M. Marago. Size-scaling in optical trapping of silicon nanowires. *Nano Letters*, 11(11):4879–4884, 2011. 843MA Times Cited:25 Cited References Count:41.
- [31] F. Wang, P. J. Reece, S. Paiman, Q. Gao, H. H. Tan, and C. Jagadish. Nonlinear optical processes in optically trapped inp nanowires. *Nano Letters*, 11(10):4149–4153, 2011. 830OT Times Cited:5 Cited References Count:28.
- [32] F. Wang, W. J. Toe, W. M. Lee, D. McGloin, Q. Gao, H. H. Tan, C. Jagadish, and P. J. Reece. Resolving stable axial trapping points of nanowires in an optical tweezers using photoluminescence mapping. *Nano Letters*, 13(3):1185–1191, 2013. 107TN Times Cited:4 Cited References Count:31.
- [33] M. M. Burns, J. M. Fournier, and J. A. Golovchenko. Optical binding. *Physical Review Letters*, 63(12):1233–1236, 1989. Aq052 Times Cited:243 Cited References Count:11.
- [34] M. M. Burns, J. M. Fournier, and J. A. Golovchenko. Optical matter - crystallization and binding in intense optical-fields. *Science*, 249(4970):749–754, 1990. Dv088 Times Cited:334 Cited References Count:35.
- [35] S. A. Tatarkova, A. E. Carruthers, and K. Dholakia. One-dimensional optically bound arrays of microscopic particles. *Physical Review Letters*, 89(28), 2002. 634AM Times Cited:158 Cited References Count:24.
- [36] Keir C. Neuman and Steven M. Block. Optical trapping. *Review of Scientific Instruments*, 75:2787, 2004.
- [37] R. W. Bowman and M. J. Padgett. Optical trapping and binding. *Reports on Progress in Physics*, 76(2), 2013. 086PI Times Cited:43 Cited References Count:250.
- [38] A. Ashkin. Forces of a single-beam gradient laser trap on a dielectric sphere in the ray optics regime. *Biophysical Journal*, 61(2):569–582, 1992. Hc778 Times Cited:853 Cited References Count:36.

- [39] T. A. Nieminen, V. L. Y. Loke, A. B. Stilgoe, G. Knoner, A. M. Branczyk, N. R. Heckenberg, and H. Rubinsztein-Dunlop. Optical tweezers computational toolbox. *Journal of Optics a-Pure and Applied Optics*, 9(8):S196–S203, 2007. Sp. Iss. SI 203CV Times Cited:132 Cited References Count:77.
- [40] S. H. Simpson. Inhomogeneous and anisotropic particles in optical traps: Physical behaviour and applications. *Journal of Quantitative Spectroscopy & Radiative Transfer*, 146:81–99, 2014. Sp. Iss. SI Am2ra Times Cited:6 Cited References Count:206.
- [41] S. H. Simpson and S. Hanna. Optical trapping of spheroidal particles in gaussian beams. *Journal of the Optical Society of America a-Optics Image Science and Vision*, 24(2):430–443, 2007. 126MS Times Cited:40 Cited References Count:36.
- [42] S. H. Simpson and S. Hanna. Computational study of the optical trapping of ellipsoidal particles. *Physical Review A*, 84(5), 2011. 843EP Times Cited:12 Cited References Count:46.
- [43] C. Selhuber-Unkel, I. Zins, O. Schubert, C. S?nnichsen, and L. B. Oddershede. Quantitative optical trapping of single gold nanorods. *Nano Letters*, 8(9):2998–3003, 2008.
- [44] S. H. Simpson and S. Hanna. Optical trapping of microrods: variation with size and refractive index. *Journal of the Optical Society of America a-Optics Image Science and Vision*, 28(5):850–858, 2011. 756PD Times Cited:13 Cited References Count:42.
- [45] S. H. Simpson and S. Hanna. Holographic optical trapping of microrods and nanowires. *Journal of the Optical Society of America a-Optics Image Science and Vision*, 27(6):1255–1264, 2010. 602DC Times Cited:31 Cited References Count:48.
- [46] S. Rancourt-Grenier, M. T. Wei, J. J. Bai, A. Chiou, P. P. Bareil, P. L. Duval, and Y. L. Sheng. Dynamic deformation of red blood cell in dual-trap optical tweezers. *Optics Express*, 18(10):10462–10472, 2010. 594TD Times Cited:22 Cited References Count:15.
- [47] M. C. Zhong, X. B. Wei, J. H. Zhou, Z. Q. Wang, and Y. M. Li. Trapping red blood cells in living animals using optical tweezers. *Nature Communications*, 4, 2013. 143MR Times Cited:21 Cited References Count:31.
- [48] D. B. Phillips, J. A. Grieve, S. N. Olof, S. J. Kocher, R. Bowman, M. J. Padgett, M. J. Miles, and D. M. Carberry. Surface imaging using holographic optical tweezers. *Nanotechnology*, 22(28), 2011. 775NX Times Cited:16 Cited References Count:28.
- [49] D. B. Phillips, S. H. Simpson, J. A. Grieve, G. M. Gibson, R. Bowman, M. J. Padgett, M. J. Miles, and D. M. Carberry. Position clamping of optically trapped microscopic non-spherical probes. *Optics Express*, 19(21):20622–20627, 2011. 835VV Times Cited:23 Cited References Count:16.

-
- [50] D. B. Phillips, G. M. Gibson, R. Bowman, M. J. Padgett, S. Hanna, D. M. Carberry, M. J. Miles, and S. H. Simpson. An optically actuated surface scanning probe. *Optics Express*, 20(28):29679–29693, 2012. 089MK Times Cited:21 Cited References Count:33.
- [51] D. B. Phillips, M. J. Padgett, S. Hanna, Y. L. D. Ho, D. M. Carberry, M. J. Miles, and S. H. Simpson. Shape-induced force fields in optical trapping. *Nature Photonics*, 8(5):400–405, 2014. Af9cc Times Cited:17 Cited References Count:42.
- [52] V. L. Y. Loke, T. Asavei, A. B. Stilgoe, T. A. Nieminen, and H. Rubinsztein-Dunlop. Driving corrugated donut rotors with laguerre-gauss beams. *Optics Express*, 22(16), 2014. An6ol Times Cited:1 Cited References Count:34.
- [53] T. Asavei, T. A. Nieminen, V. L. Y. Loke, A. B. Stilgoe, R. Bowman, D. Preece, M. J. Padgett, N. R. Heckenberg, and H. Rubinsztein-Dunlop. Optically trapped and driven paddle-wheel. *New Journal of Physics*, 15, 2013. 163BI Times Cited:8 Cited References Count:32.
- [54] T. Asavei, V. L. Y. Loke, M. Barbieri, T. A. Nieminen, N. R. Heckenberg, and H. Rubinsztein-Dunlop. Optical angular momentum transfer to microrotors fabricated by two-photon photopolymerization. *New Journal of Physics*, 11, 2009. 494NB Times Cited:22 Cited References Count:46.
- [55] Y. Y. Cao, A. B. Stilgoe, L. X. Chen, T. A. Nieminen, and H. Rubinsztein-Dunlop. Equilibrium orientations and positions of non-spherical particles in optical traps. *Optics Express*, 20(12):12987–12996, 2012. 961KP Times Cited:9 Cited References Count:37.
- [56] R. C. Gauthier. Theoretical investigation of the optical trapping force and torque on cylindrical micro-objects. *Journal of the Optical Society of America B-Optical Physics*, 14(12):3323–3333, 1997. Ym873 Times Cited:73 Cited References Count:21.
- [57] R. C. Gauthier, M. Ashman, and C. P. Grover. Experimental confirmation of the optical-trapping properties of cylindrical objects. *Applied Optics*, 38(22):4861–4869, 1999. 224MC Times Cited:51 Cited References Count:28.
- [58] F. Borghese, P. Denti, R. Saija, M. A. Iati, and O. M. Marago. Radiation torque and force on optically trapped linear nanostructures. *Physical Review Letters*, 100(16), 2008. 295EK Times Cited:53 Cited References Count:29.
- [59] S. H. Simpson and S. Hanna. Stability analysis and thermal motion of optically trapped nanowires. *Nanotechnology*, 23(20), 2012. 935PJ Times Cited:7 Cited References Count:34.
- [60] L. M. Tong, J. Y. Lou, and E. Mazur. Single-mode guiding properties of subwavelength-diameter silica and silicon wire waveguides. *Optics Express*, 12(6):1025–1035, 2004. 808UU Times Cited:286 Cited References Count:23.
- [61] Y. Huang, X. F. Duan, Y. Cui, L. J. Lauhon, K. H. Kim, and C. M. Lieber. Logic gates and computation from assembled nanowire building blocks. *Science*, 294(5545):1313–1317, 2001. 491VF Times Cited:1418 Cited References Count:22.
-

- [62] C. Thelander, T. Martensson, M. T. Bjork, B. J. Ohlsson, M. W. Larsson, L. R. Wallenberg, and L. Samuelson. Single-electron transistors in heterostructure nanowires. *Applied Physics Letters*, 83(10):2052–2054, 2003. 717LJ Times Cited:294 Cited References Count:14.
- [63] X. F. Duan, Y. Huang, R. Agarwal, and C. M. Lieber. Single-nanowire electrically driven lasers. *Nature*, 421(6920):241–245, 2003. 635KG Times Cited:1578 Cited References Count:25.
- [64] J. F. Wang, M. S. Gudixsen, X. F. Duan, Y. Cui, and C. M. Lieber. Highly polarized photoluminescence and photodetection from single indium phosphide nanowires. *Science*, 293(5534):1455–1457, 2001. 465XV Times Cited:1135 Cited References Count:17.
- [65] C. M. Lieber. Design, synthesis and properties of programmable nanowire transistors for nanoscale circuits and processors. *Abstracts of Papers of the American Chemical Society*, 243, 2012. 219JX 1039-INOR Times Cited:0 Cited References Count:0.
- [66] H. Yan, H. S. Choe, S. W. Nam, Y. J. Hu, S. Das, J. F. Klemic, J. C. Ellenbogen, and C. M. Lieber. Programmable nanowire circuits for nanoprocessors. *Nature*, 470(7333):240–244, 2011. 718RQ Times Cited:222 Cited References Count:21.
- [67] B. E. Smith, P. B. Roder, J. L. Hanson, S. Manandhar, A. Devaraj, D. E. Perea, W. J. Kim, A. L. D. Kilcoyne, and P. J. Pauzauskie. Singlet-oxygen generation from individual semiconducting and metallic nanostructures during near-infrared laser trapping. *Acs Photonics*, 2(4):559–564, 2015. Cg3mt Times Cited:0 Cited References Count:39.
- [68] P. B. Roder, B. E. Smith, E. J. Davis, and P. J. Pauzauskie. Photothermal heating of nanowires. *Journal of Physical Chemistry C*, 118(3):1407–1416, 2014. 297JV Times Cited:3 Cited References Count:38.
- [69] O. M. Marago, P. H. Jones, P. G. Gucciardi, G. Volpe, and A. C. Ferrari. Optical trapping and manipulation of nanostructures. *Nature Nanotechnology*, 8(11):807–819, 2013.
- [70] V. Karasek and P. Zemanek. Analytical description of longitudinal optical binding of two spherical nanoparticles. *Journal of Optics a-Pure and Applied Optics*, 9(8):S215–S220, 2007. Sp. Iss. SI 203CV Times Cited:26 Cited References Count:30.
- [71] F. Depasse and J. M. Vigoureux. Optical binding force between 2 rayleigh particles. *Journal of Physics D-Applied Physics*, 27(5):914–919, 1994. Nn440 Times Cited:34 Cited References Count:16.
- [72] W. Singer, M. Frick, S. Bernet, and M. Ritsch-Marte. Self-organized array of regularly spaced microbeads in a fiber-optical trap. *Journal of the Optical Society of America B-Optical Physics*, 20(7):1568–1574, 2003. 701MW Times Cited:93 Cited References Count:34.

- [73] M. C. Frawley, I. Gusachenko, V. G. Truong, M. Sergides, and S. N. Chormaic. Selective particle trapping and optical binding in the evanescent field of an optical nanofiber. *Optics Express*, 22(13):16322–16334, 2014. Aj9tn Times Cited:4 Cited References Count:25.
- [74] J. Rodriguez, L. C. Davila Romero, and D. L. Andrews. Optical binding in nanoparticle assembly: Potential energy landscapes. *Physical Review A*, 78(4), 2008. 367SY Times Cited:15 Cited References Count:38.
- [75] S. K. Mohanty, J. T. Andrews, and P. K. Gupta. Optical binding between dielectric particles. *Optics Express*, 12(12):2746–2753, 2004. 829GR Times Cited:36 Cited References Count:7.
- [76] V. Demergis and E. L. Florin. Ultrastrong optical binding of metallic nanoparticles. *Nano Letters*, 12(11):5756–5760, 2012. 039KJ Times Cited:15 Cited References Count:39.
- [77] T. M. Grzegorzcyk, B. A. Kemp, and J. A. Kong. Passive guiding and sorting of small particles with optical binding forces. *Optics Letters*, 31(22):3378–3380, 2006. 102GT Times Cited:18 Cited References Count:31.
- [78] T. M. Grzegorzcyk, J. Rohner, and J. M. Fournier. Optical mirror from laser-trapped mesoscopic particles. *Physical Review Letters*, 112(2), 2014. Ab6zy Times Cited:2 Cited References Count:22.
- [79] Z. J. Yan, R. A. Shah, G. Chado, S. K. Gray, M. Pelton, and N. F. Scherer. Guiding spatial arrangements of silver nanoparticles by optical binding interactions in shaped light fields. *Acs Nano*, 7(2):1790–1802, 2013. 099KA Times Cited:16 Cited References Count:39.

Chapter 2

Construction of the Research Optical Tweezers

2.1	Introduction	18
2.2	Basic optical tweezers	18
2.3	Sample mount and sample preparation	20
2.4	Beam steering optics	21
2.5	Acousto-Optic Deflectors (AOD)	22
2.5.1	Beam Steering and Trap Multiplexing by AOD	23
2.5.2	Calibration of AOD input frequency against distance in the image plane	25
2.5.3	Trap Power Attenuation by AOD	28
2.6	Spatial light modulator (SLM)	29
2.6.1	Phase mask or hologram generation	31
2.6.2	Zernike polynomials for aberration corrections	31
2.7	Vibration isolation	33
2.8	Particle tracking and measurements	34
2.8.1	Interferometric particle tracking	34
2.8.2	Calibration of QPD response to particle displacement	36
2.9	Trapping and tracking of a particle using optical tweezers	41
2.10	References	43

2.1 Introduction

A key component in this research is the optical tweezers used throughout the duration of this study. While there are a number of good papers in the literature which describe in detail the various components of an optical tweezers setup [1–4], I will use this chapter to reiterate or highlight a few key points in the design consideration of the optical tweezers used in our studies. I will also introduce some aspects of the optical tweezers which are unique to our setup. The construction and modification of this optical tweezers is an ongoing process, with new components or modifications constantly added to suit different experiments. In terms of trapping, our tweezers is capable of manual and electronic beam steering, both holographic and time-shared trap multiplexing, as well as the trapping of nanoparticles and nanowires. As for measurements, our tweezers can perform video tracking from bright and dark field illumination, fast particle tracking via back focal plane interferometry, and photoluminescence spectroscopy. In this chapter I will address the different components of the tweezers setup which enables these various capabilities and provide detailed information including the operating principles, construction and calibration of each one of them.

2.2 Basic optical tweezers

An optical tweezers is an optical trap created by a tightly focused laser beam using a high numerical aperture (NA) microscope objective lens. It functions by trapping a particle at the centre of the tightly focused beam [1, 5]. A particle near the optical trap is acted upon by two forces, namely the scattering force which pushes the particle away from the focal region and the gradient force which pulls the particle towards the region [1, 3]. These forces result from the transfer of momentum from the scattering and refraction of incident photons [1, 3]. An optical trap is stable in three dimensions when the scattering force and the gradient force counteract and balance each other. As a classic example, the source of these gradient forces and scattering forces can be modelled using dielectric spheres and ray optics, as shown in the Figure 2.1 below.

The simplest optical tweezers can be built by simply passing a laser through a beam expander and a high NA objective lens. A high NA objective ($NA > 1.2$) is chosen due to its ability to generate a tight diffraction limited focal spot thus maximizing the intensity gradient at the focus. This creates a gradient force large enough to counter the scattering force thereby creating a stable trap in 3D. A beam expander is used to

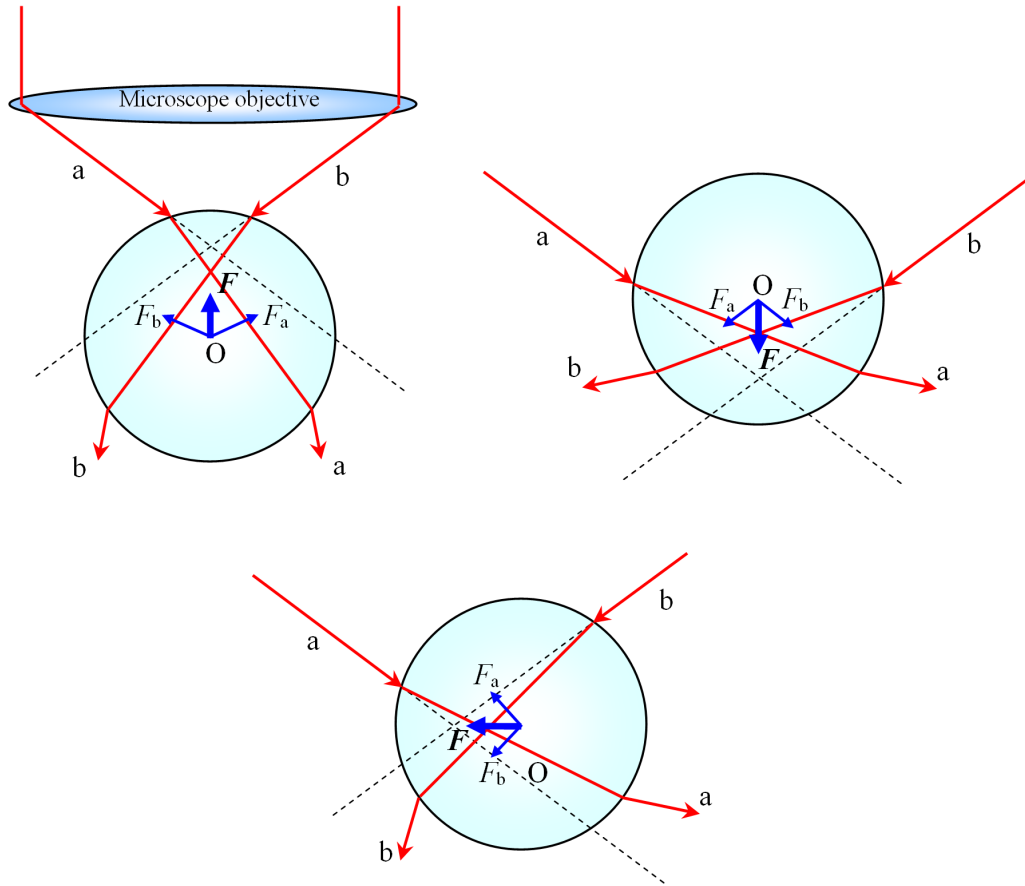


Figure 2.1: Ray optics diagram showing the refraction of light rays through a dielectric sphere with refractive index greater than the surrounding medium. (Top left figure) The centre of the sphere is slightly displaced below the paraxial focus further away from the microscope objective (O denotes the centre of the sphere). Consider ray ‘a’, its change in direction from refraction imparts a force F_a in the dielectric sphere. The same happens for ray ‘b’, and every other ray in between. The net result is a net force F , pointing towards the paraxial focus, shown as a bold arrow in the diagram. (Top right figure) The centre of the sphere is displaced slightly above the paraxial focus closer to the microscope objective, and the net force is pointing towards the paraxial focus and away from the objective. (Bottom figure) The light rays are refracted through a dielectric sphere slightly displaced in the lateral direction from the paraxial focus. The net force (shown in bold) points in the direction opposing the direction of displacement towards the paraxial focus [6].

expand the laser beam to overfill the back aperture of the objective lens to increase the ratio of gradient to scattering force, which results in higher trapping efficiency [1, 6].

In our setup, the optical trap is generated using a diode pumped Nd:YAG laser at 1064nm and 3W maximum power (Laser Quantum Ventus 1064). It is chosen for its pointing stability and low absorption by biological materials in the infrared, with enough optical power to generate a stable trap. The beam is passed through a high pass filter at 800 nm to remove the pump source laser and a half wave plate to orient the polarisation in the preferred direction for the following optics. A telescope system of two lenses is used as a beam expander while a 100x oil immersion microscope objective lens with a numerical aperture (NA) of 1.25 (Nikon E Plan Achromat 100x 1.25NA) is used to focus the laser into an optical trap. The focal lengths of the lenses and their placements are chosen for the right magnification to expand the beam to just overfill the back aperture of the objective. For example, the diameter of the diode laser output is 3 mm while the back aperture of the objective lens is 8 mm, so a magnification factor of 3 is required to achieve a beam diameter which will overfill the back aperture. To achieve this we pick two lenses with focal length f and $3f$ respectively and place them a distance of $4f$ apart, shown in Figure 2.2 below.

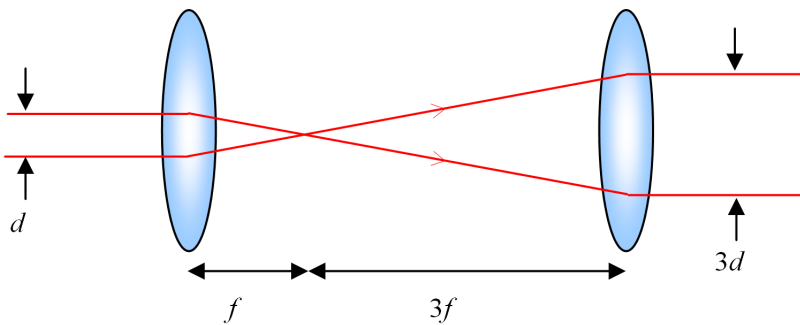


Figure 2.2: Telescope setup of beam expanding optics for achieving a magnification of 3. To achieve this we pick two lenses with focal length f and $3f$ respectively and place them a distance of $4f$ apart.

2.3 Sample mount and sample preparation

Our samples are contained within water in a sealed chamber formed by a thin cover slip (grade 0), a glass slide, and an annular sticky tape as shown in the figure below. Water is chosen as a medium because it is a good representation of most biological systems. To reduce imaging aberrations, immersion oil ($n = 1.56$) is used between the

objective lens and the cover slip which minimizes refractive index mismatch between layers. The sample slide containing the sample chamber is mounted onto a sample stage with manual controls in all 3 directions and motorised controls in 2 directions within the horizontal plane to enable navigation of the sample chamber relative to the optical trap. In our setup, we use a Newport 562-XYZ ULTRAlign sample stage with 3 vernier micrometer actuators capable of $1\ \mu\text{m}$ increments. These are mounted on two Thorlabs MT1 Translation stages with Z812B motorised actuators capable of a minimum incremental movement of $0.2\ \mu\text{m}$.

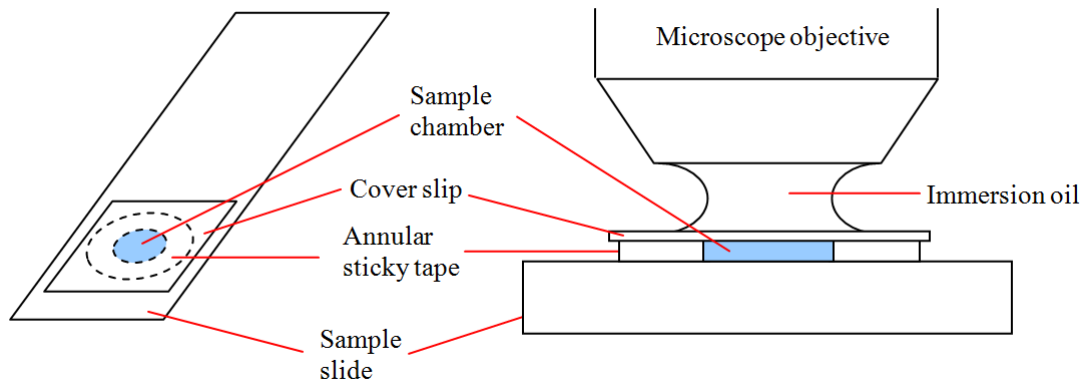


Figure 2.3: (Left) Top view of a sample slide containing a sample chamber formed by an annular sticky tape and covered by a thin cover slip. (Right) Cross section of the sample slide with oil immersion microscope objective.

2.4 Beam steering optics

The steering of the optical trap can be achieved by changing the angle of the laser beam entering the back aperture of the objective lens which translates into a lateral displacement of the focal point in the image plane. The simplest way to achieve this is by placing a moving mirror in the Fourier plane of the sample i.e. the back focal plane, as tilting the angle of the mirror placed on the back focal plane changes the angle of the laser entering the objective but conserves the position of the beam on the back aperture of the lens. Details about the principles behind this structure can be understood in terms of Fourier Optics [7]. In our setup, manual beam steering capability is added on to the optical tweezers by adding a relay telescope system which projects the back focal plane of the microscope objective onto the moving mirror, shown in Figure 2.4. Using the same mechanism, beam steering can be done using an acousto-optic deflector (AOD) or a spatial light modulator (SLM), which will be discussed in later sections.

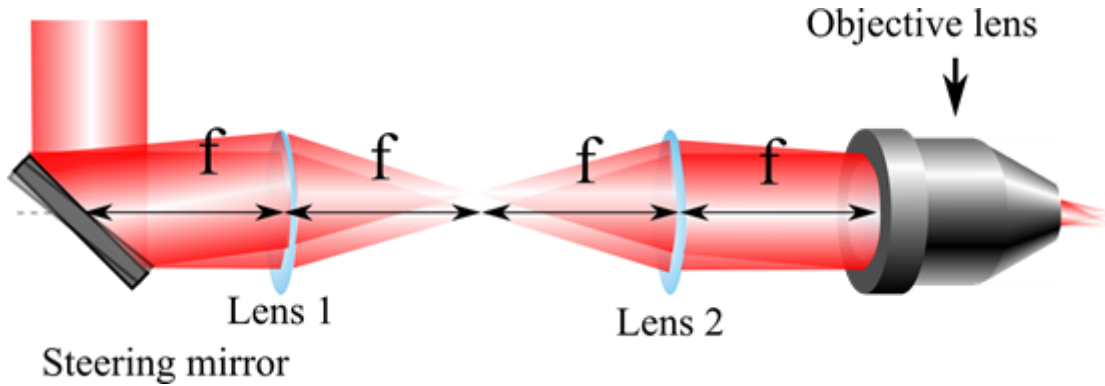


Figure 2.4: The steering mirror placed in the back focal plane is capable of translating the focal spot in the trapping plane without displacing the beam path from the centre of the back aperture of the objective lens.

2.5 Acousto-Optic Deflectors (AOD)

The acousto-optic deflectors (AOD) serve a number of purposes on our optical tweezers setup, namely trap attenuating, electronic beam steering and time-shared trap multiplexing [1, 8]. An AOD consists of a transparent paratellurite (TeO_2) crystal attached to a piezo-electric transducer which is able to generate a sound wave within the crystal when driven by a radio frequency (RF) synthesizer. The compressive nature of sound waves causes the molecules in the crystal to vibrate around their equilibrium position, which in turn leads to a perturbation of the refractive index in local regions of the crystal. As the sound wave propagates in the crystal, alternating regions of high and low refractive indices are formed where the spacing between successive regions of high (or low) refractive indices corresponds to the wavelength of the sound wave in the crystal. When the angle between the incoming laser and the interface between high and low refractive indices satisfies the Bragg condition for constructive interference, Bragg diffraction occurs where most of the energy from the laser beam is diffracted away from the initial beam by twice the Bragg angle. Furthermore, tuning the frequency input of the RF synthesizer allows us to change the frequency of the sound wave generated in the crystal. Since the velocity of sound is constant within the crystal, tuning the frequency of the RF synthesizer changes the wavelength of the sound wave, thereby changing the spacing of the diffraction grating and the diffraction angle of the incoming laser beam.

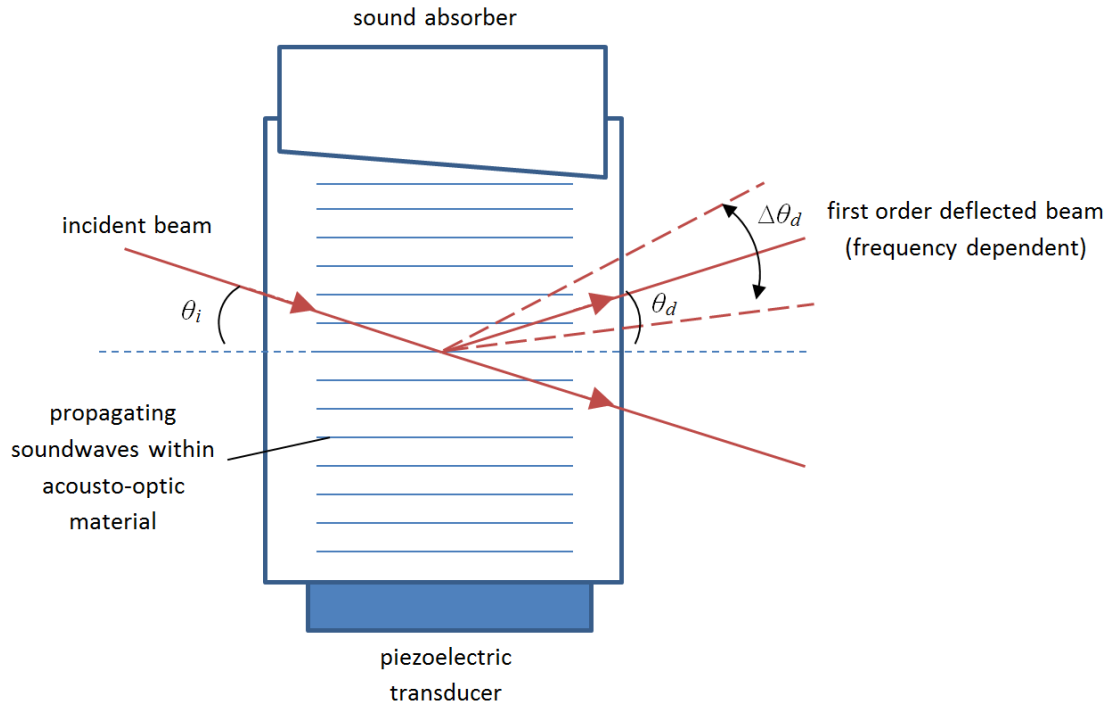


Figure 2.5: The acousto-optic deflector (AOD) deflects the incoming beam by Bragg diffraction. The deflection angle of the deflected beam depends on the frequency of the acoustic wave within the acousto-optic crystal, because a change in the frequency of the sound waves changes the spacing between successive high and low refractive index layers within the crystal thereby changing the angle for constructive interference.

2.5.1 Beam Steering and Trap Multiplexing by AOD

As explained in the previous section on beam steering, the displacement of the trap within the trapping plane can be changed by changing the angle of the laser beam entering the back aperture of the objective lens. Rather than using a moving mirror, the same can be achieved electronically using the AOD by placing the AOD crystal on the back focal plane (or any phase conjugated plane relative to the back focal plane) of the objective lens. Tuning the input RF frequency into the crystal changes the spacing of the generated grating which then changes the deflected angle of the laser passing through the crystal. There are advantages in using non-mechanical beam steering methods, such as the much higher scan rate achievable and the lack of inertia in moving parts [3, 9].

For beam steering in both x and y directions in the image plane, a set of two AOD crystals are used such that they deflect the laser beam in orthogonal directions.

To optimize the diffraction efficiency, the input beam is linearly polarized and the crystal rotated to the Bragg angle with respect to the incident laser beam.

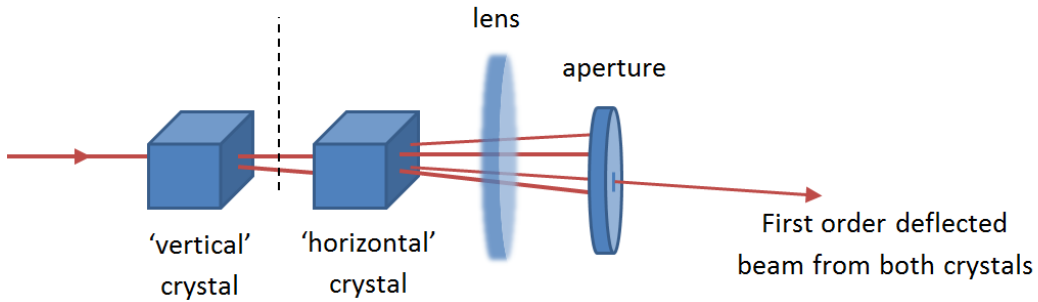


Figure 2.6: Two AOD crystals placed in the back focal plane is capable of translating the focal spot in the trapping plane without displacing the beam path from the centre of the back aperture of the objective lens.

In our setup, we use two AOD's (Gooch and Housego Model 45035-3-6.5DEG-1.060XY) driven by two digital frequency synthesizers (Gooch and Housego (R)64020-250-1ADMDFS-A) capable of a variable RF output up to 1W. The digital frequency synthesizers take in digital input from a field programmable gate array (FPGA) (National Instruments PCIe-7852R) card, which is programmed using LabView. The AOD's have an operating frequency between 25 and 45 MHz specified by the manufacturer, so we pick 35 MHz to be the centre frequency and align the first order deflected beam at 35 MHz from both crystals down the centre of the optical path. The undeflected beams are terminated by placing an aperture after the two AOD's, as shown in Figure 2.6. Beam steering is simply achieved by adjusting the input frequency to both crystals using the digital frequency synthesizer.

The AOD's can also be used to generate multiple traps from a single laser source by time-sharing the optical trap [1, 9]. This is done by steering the trap between a few locations at high frequency. If the switching of the trap is much faster than the diffusion time of the trapped object, the trapped object effectively does not 'see' this switching, and the trapping power is simply averaged over the number of traps that is being generated by time sharing. The rise time for these AOD's is specified by the manufacturer to be $4.5 \mu\text{s}$, so we pick $50 \mu\text{s}$ as our switching time between traps so that it is much larger than the rise time. For two traps this results in a switching rate of 10 kHz per trap with a duty cycle of 50%. A duty cycle of 50% means the trapping beam acts on each particle 50% of the time, which is a result of sharing the trap between two locations. We will examine the limits of time shared trap multiplexing in Chapter

5.2.3, but for now it is sufficient to say that a switching frequency of 10 kHz between two locations is sufficient to create two time-shared traps. It should also be noted that the latching of both frequency synthesizers has to be synchronous. This means both frequency synthesizers must be switched at the same time. Multiple traps can similarly be generated by steering the trap through multiple locations provided enough trapping laser power is provided and the condition of switching faster than the diffusion time of the trapped object is fulfilled. In our setup, we demonstrate up to four individual traps generated by time sharing (Figure 2.7).

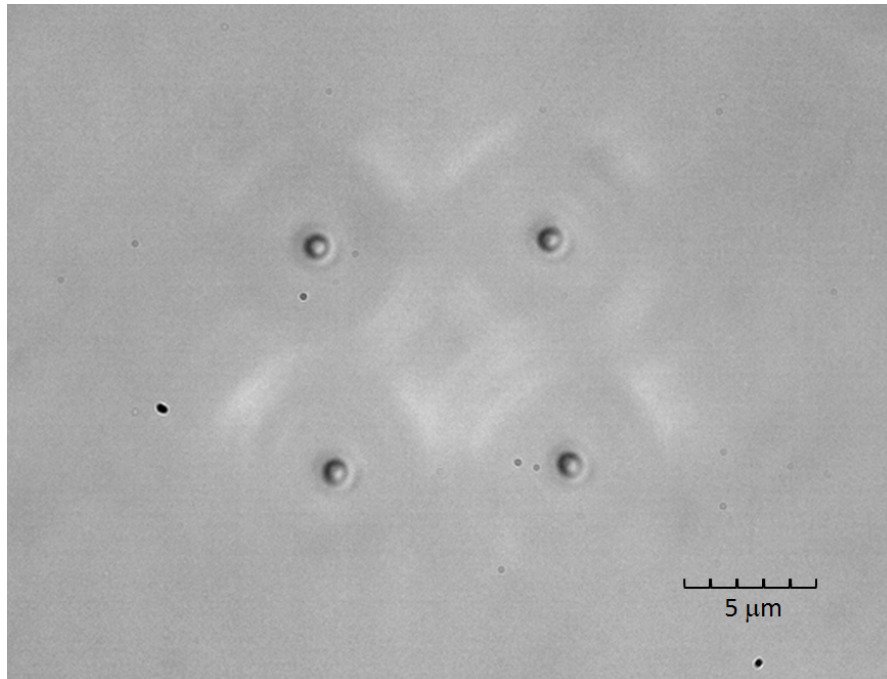


Figure 2.7: A photo captured from the video camera showing four time-shared traps holding one $1\ \mu\text{m}$ spheres in each trap.

2.5.2 Calibration of AOD input frequency against distance in the image plane

As mentioned previously, the Gooch and Housego AOD which is used in our setup has an operating frequency of 25 to 45 MHz. According to the manufacturer's data sheet, the difference in diffraction angle between these two limits of the operating frequency is only 32 milliradians (mrad) for lasers at 1064 nm. Given our choice of the centre frequency at 35 MHz, there will only be a maximum deflection angle of 16 mrad on either side from the centre. At this small angle, the relationship between the change in

frequency and the lateral displacement of the beam in the image plane is linear to a very good approximation. This is quantified experimentally in the following paragraphs.

The procedure for calibrating the input frequency of the AOD against the absolute displacement from the centre in the image plane is as follows. Firstly, a stage micrometer is photographed using a camera with square pixels. The resulting image allows us to find the number of pixels per μm (Figure 2.8). Then, images of two traps at different frequencies (Figure 2.9) are captured and the number of pixels between the two traps is measured. The number of pixels can then be converted into absolute distance and a graph of distance versus frequency is plotted. From the slope of the graph we find the displacement per frequency change. The same procedure is carried out for each of the two AOD crystals to obtain the calibration factor for both x and y axes.

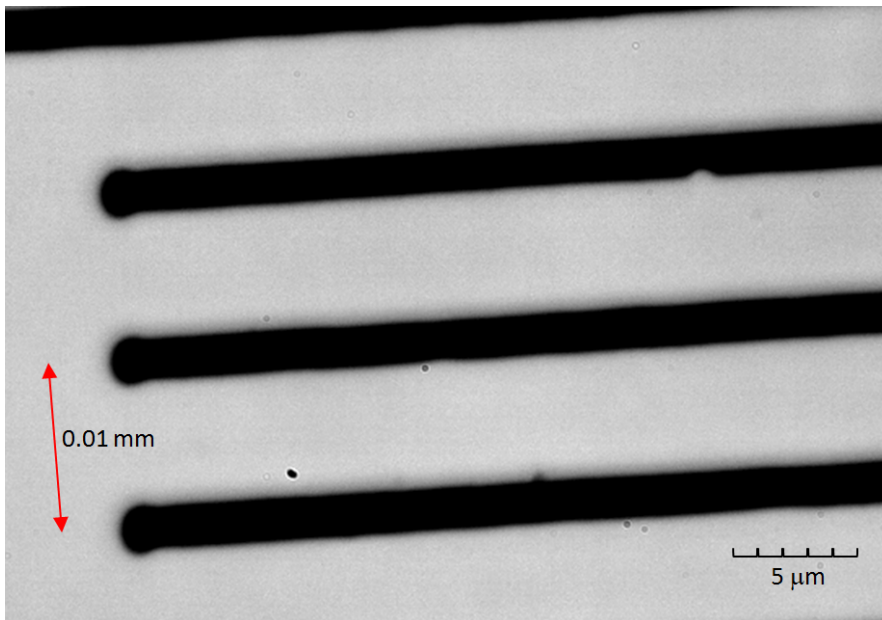


Figure 2.8: Image of stage micrometer on the image plane. The scale of the micrometer is 0.01 mm, as indicated by the red arrow.

From the photo of the stage micrometer we find that the scale on the photographs is 10.33 pixels per μm , using an image processing software ImageJ. This is used to calculate the absolute distance between two traps and a graph of distance versus frequency change is plotted (Figure 2.10). Finally from the slope of the graphs we find that conversion factor from changing frequency to distance in the image plane is $0.68 \pm 0.01\mu\text{m}$ per MHz in the x axis and $0.70 \pm 0.01\mu\text{m}$ per MHz in the y axis. Since the AOD's have an operating frequency of 35 ± 10 MHz, this translates to roughly $\pm 7 \mu\text{m}$ of maximum displacement on the trapping plane on both axes from the centre of the trap.

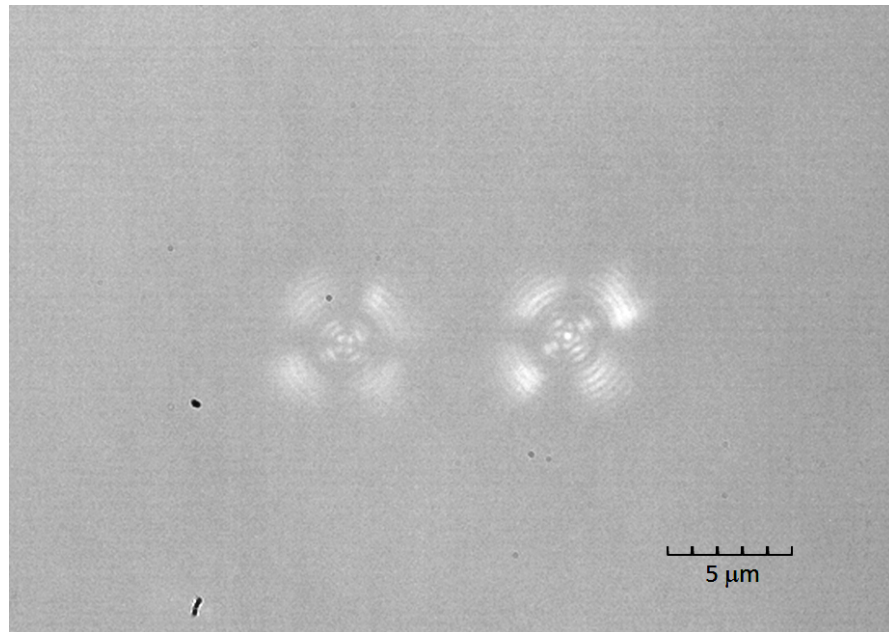


Figure 2.9: An image of two empty traps with the AOD set at 30 and 40 MHz in the x axis. The number of pixels on the image between the centre of each trap is measured.

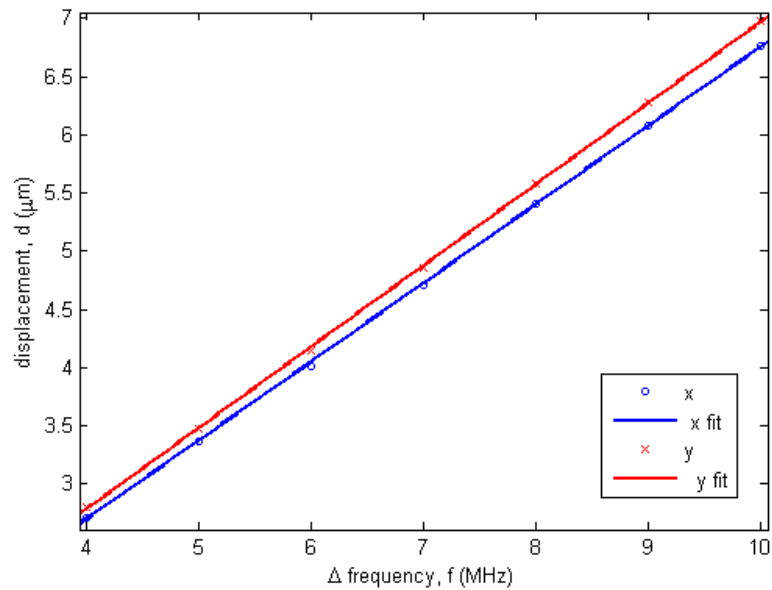


Figure 2.10: Displacement on image plane versus frequency change of AOD input frequency.

2.5.3 Trap Power Attenuation by AOD

By changing the input voltage of the RF synthesizer, we tune the amplitude of the RF signal generated for the AOD crystals. This changes the diffraction efficiency of the AOD crystals, giving us a way of controlling the optical power of the laser output from the AOD and by extension the strength of the optical trap. Changing the RF input changes the diffraction efficiency because diffraction efficiency is related to the difference in refractive index between the compressed and decompressed regions within the AOD crystal. A larger RF input (below saturation) generates stronger compression and decompression within the crystal, leading to a larger change in refractive index. This in turn leads to a larger refractive index difference between the compressed and decompressed regions, resulting in a higher diffraction efficiency. It should be noted that the diffraction efficiency is not a linear function of the input voltage of the RF synthesizer. Hence, a calibration curve is experimentally obtained to map input voltage to the optical power of the trapping laser at the trap focus. The calibration curve in Figure 2.11 shows the optical power at the exit aperture of the AOD (shown in blue). The percentage optical loss from the remaining optics in the optical path is measured and subtracted to obtain the optical power of the trapping laser at the trap focus (shown in red). We note that power transmission through the oil immersion objective is measured using the dual-objective method [10].

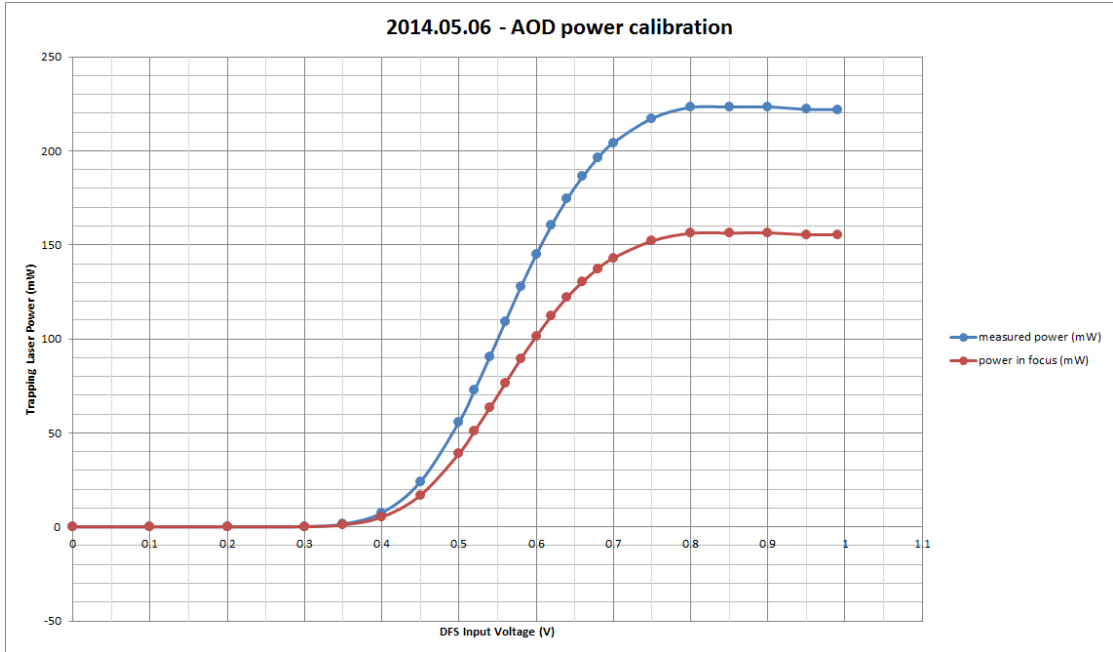


Figure 2.11: Trapping power of a single trap at the trap focus versus input voltage of DFS. The optical power at the exit aperture of the AOD is shown in blue while the optical power of the trapping laser at the trap focus with all losses taken into account is shown in red.

2.6 Spatial light modulator (SLM)

An additional piece of equipment added to our optical tweezers setup is the spatial light modulator (SLM). The SLM works by modulating the phase of the input beam to create the desired beam shape at the focus. This allows it to generate a variety of beam profiles on the trapping focus such as a Bessel beam and a Laguerre-Gaussian beam [11]. SLM's were first used with optical tweezers as a method for non-mechanical optical manipulation in 1999 [12, 13] and has since been used in holographic tweezers to steer optical traps in 3D or to generate multiple traps [14–16]. The capabilities of an SLM is not limited to only these applications; as SLM's can display arbitrary phase patterns, it is possible to use them to correct for aberrations in the optical trap [17–19].

However, there are some drawbacks in using a SLM as a mechanism for beam steering and trap multiplexing compared to an AOD. Firstly, the SLM has a much lower modulated efficiency at 30-50% [20] compared to the AOD which easily achieve 80% efficiency in our setup. Second and more importantly, the refresh rate of an SLM is typically only around 100 Hz, which is orders of magnitude lower than that of the AOD which is in the order of tens of kHz.

In our setup, an SLM is used for beam steering in the axial direction and for aberration correction of the optical traps. Aberration correction is necessary as it is known that the introduction of AOD's into the system causes significant aberrations from the non-flat wave front entering and exiting the AOD crystals, as well as the refractive index mismatch between crystal and air [21]. Apart from that, the refractive index mismatch between immersion oil, cover slip and water within trapping chamber leads to some aberrations as well [22, 23]. The SLM used in our setup is the Hamamatsu LCOS-SLM x10468-03 SLM, which is a phase only reflection SLM with dielectric mirror for 1064 nm wavelength light. Just like the AOD's, the SLM is placed in the Fourier plane (or any equivalent conjugate planes) of the trapping plane. The incident light is expanded to fully fill the entire SLM to maximise resolution, and linearly polarised in the horizontal direction to match the orientation of the liquid crystals in the SLM as specified by the manufacturer. To achieve a high modulation efficiency, the incident angle upon the SLM has to be small ($< 10^\circ$); in our setup the incident beam is set at 7.5° from normal incidence. The first order deflection of the beam reflected off the SLM is aligned down the optical path and used as the trapping beam while the zero-th order reflected beam is terminated since it cannot be fully modulated.

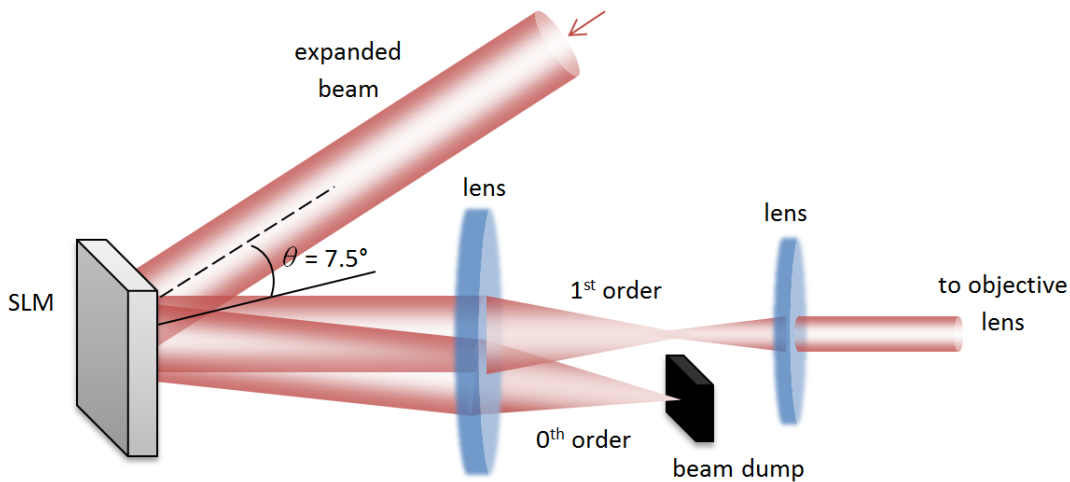


Figure 2.12: The configuration of the spatial light modulator (SLM) in the optical tweezers setup. The incident beam is expanded to fully fill the active area of the SLM; the first order reflection is used as the trapping beam while the zero order is terminated.

2.6.1 Phase mask or hologram generation

To understand how a SLM shapes the beam at the focus of the objective lens i.e. the optical trap, one must understand Fourier Optics, which I will not go into details here. A phase only SLM, which is the type used in our setup shapes the wavefront of light by changing the phase of the incident light. This is done by a phase mask or hologram on the SLM.

2.6.2 Zernike polynomials for aberration corrections

The SLM in our setup is used for aberration corrections, and to describe the aberrations we use a set of orthogonal Zernike's circle polynomials [24]. By combining different modes of these polynomials, any aberration can be described. The Zernike polynomials are as follows

$$Z_1 = 2r \cos \theta \quad (2.1a)$$

$$Z_2 = 2r \sin \theta \quad (2.1b)$$

$$Z_3 = \sqrt{3} (2r^2 - 1) \quad (2.1c)$$

$$Z_4 = \sqrt{6} r^2 \cos 2\theta \quad (2.1d)$$

$$Z_5 = \sqrt{6} r^2 \sin 2\theta \quad (2.1e)$$

$$Z_6 = \sqrt{8} (3r^3 - 2r) \cos \theta \quad (2.1f)$$

$$Z_7 = \sqrt{8} (3r^3 - 2r) \sin \theta \quad (2.1g)$$

$$Z_8 = \sqrt{5} (6r^4 - 6r^2 + 1) \quad (2.1h)$$

$$Z_9 = \sqrt{8} r^3 \sin 3\theta \quad (2.1i)$$

$$Z_{10} = \sqrt{8} r^3 \cos 3\theta \quad (2.1j)$$

$$Z_{11} = (20r^6 - 30r^4 + 12r^2 - 1) \quad (2.1k)$$

Here Z_1 and Z_2 stand for tilting in x and y respectively which controls the lateral displacement of the trap. Z_3 represents defocusing, where a Fresnel lens is applied to change the position of the trap focus axial direction. Z_4 and Z_5 describe the astigmatisms in x and y . Z_6 and Z_7 are coma in x and y . Z_8 and Z_{11} describe primary and secondary spherical aberrations while Z_9 and Z_{10} denote trefoils in x and y .

To find the optimal aberration corrections for our system, we need to find the correct amplitude for each Zernike Mode to be applied to our system to exactly cancel existing aberrations. This is done by the following protocol. A red dyed labelled $1\ \mu\text{m}$ microsphere is optically trapped using our optical tweezers. The laser from the optical trap causes nonlinear excitation on the fluorescent dye on the microsphere, and strong two-photon absorption and re-emission can be detected from the trapped sphere. This emission is collected using an avalanche photodiode which is wired to a lock-in amplifier to amplify the signal. Since two-photon absorption induced photoluminescence has a quadratic dependence on the peak intensity of the excitation source, the higher emission intensity correlates with a superior trapping spot with less aberration. Thus by scanning each Zernike mode and collecting the resulting emission intensity from an optically trapped red microsphere, we find the optimal amplitude for each Zernike mode which results in the strongest optical trap (with least aberration).

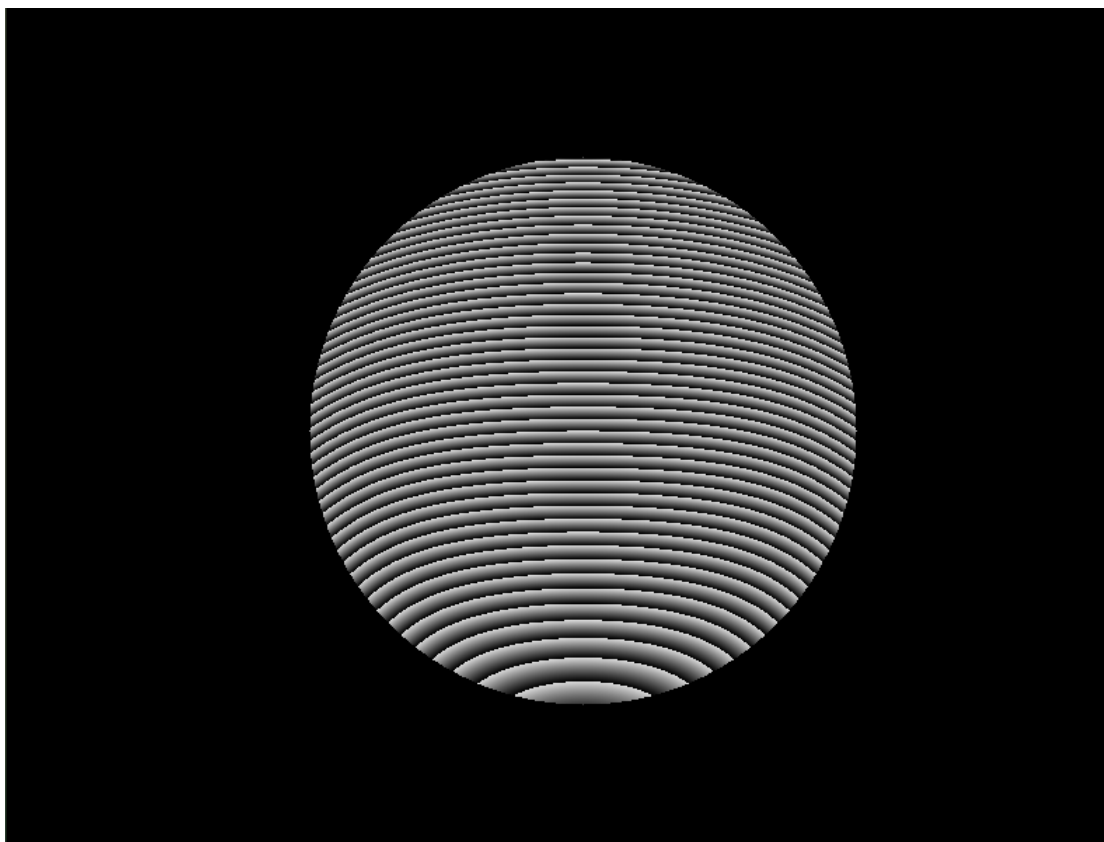


Figure 2.13: The resulting kinoform that is used for aberration correction in our optical tweezers.

Through optimising our system from aberrations, we found that the main contribution of aberrations in our system are from spherical aberrations. This is expected

as our system comprises of multiple interfaces where refractive index mismatch occurs, namely the interface between objective lens, immersion oil, glass cover slip and deionised water in which the optically trapped particles are suspended. Figure 2.13 shows the resulting kinoform that we use for our experiments, while Figure 2.14 shows a comparison between corrected and uncorrected beam profiles at the trapping focus.

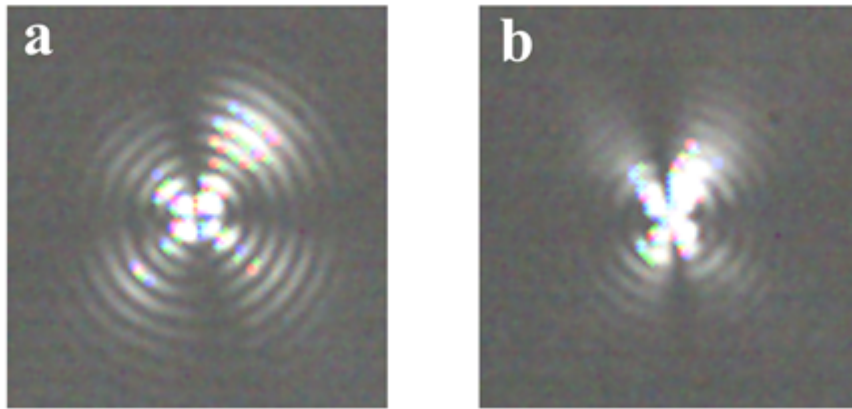


Figure 2.14: Images of the beam focus (a) with and (b) without the Zernike mask, measured by a CCD camera.

2.7 Vibration isolation

Without isolation from external vibration, the optical tweezers are susceptible to external noise, especially when high precision measurements are made. Pneumatic isolation mounts (Newport Pneumatic Isolation Mount Type XL-A) are used to isolate the optical bench and our optical tweezers setup from external vibration. These mounts are capable of damping vibrations above 10 Hz by more than 95%. Prior to the incorporation of vibration isolation, we systematically measure 100 Hz spikes in our power spectra of the trajectories of trapped particles that were independent of our experimental variables (Figure 2.15). Upon incorporation of vibration isolation, cleaner power spectra without spikes due to external vibration were obtained (Figure 2.15).

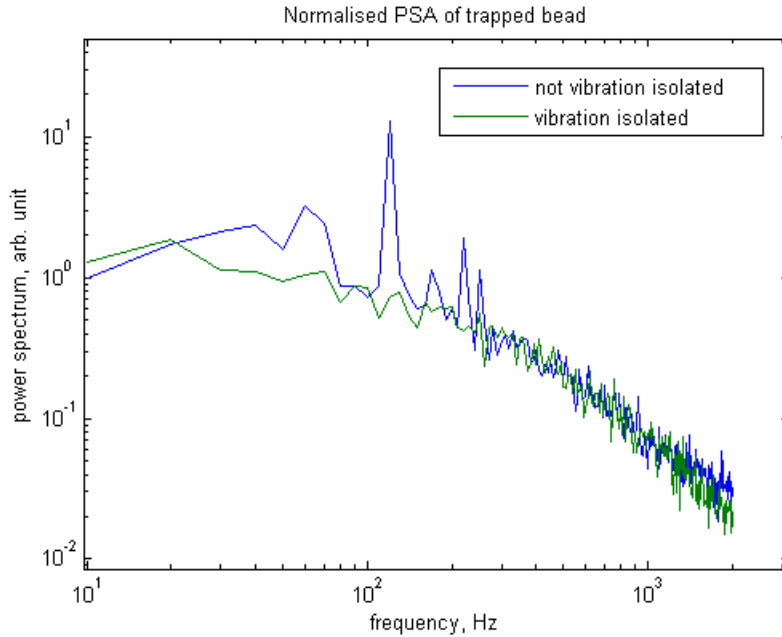


Figure 2.15: Power spectra of an optically trapped $1\ \mu\text{m}$ polystyrene sphere when pneumatic isolation mounts are turned off (blue) and on (green). Low frequency vibrations, particularly the spike at 100 Hz, are visibly removed when vibration isolation is incorporated.

2.8 Particle tracking and measurements

There are currently two major techniques for tracking particle displacements within an optical trap, namely interferometric particle tracking and video particle tracking [1, 3]. In this work we perform particle tracking primarily using interferometric methods due to its superior bandwidth over video tracking, as well as its compatibility with multiple time-shared traps as explained in Chapter 5.

2.8.1 Interferometric particle tracking

The displacement of a trapped particle within an optical trap can be accurately determined by back focal plane interferometry. This technique was first demonstrated for optical tweezers by Gittes and Schmidt [25]. Back focal plane interferometry relies on the interference between forward scattered laser light from the trapped particle and the unscattered laser light. A detector, usually a quadrant photodiode (QPD) is placed in the back focal plane of the condenser lens to record the intensity pattern caused by this interference. The intensity of this interference pattern in the back focal plane does not

depend on the absolute location of the trapped particle, only its displacement relative to the centre of the optical trap. This pattern represents the angular intensity distribution of the light that has passed through the focus and is described by Equation 2.2 [25]. For a particle with radius a displaced by some distance x ,

$$\frac{\delta I(x)}{I_{\text{tot}}} = \frac{2k^3\alpha}{\pi r^2} e^{(-x^2/w_0^2)} \times \sin(kx \sin \theta \cos \phi) e^{(-k^2 w_0^2 \theta^2 / 4)} \quad (2.2)$$

where δI is the change in intensity at any point in the back focal plane (θ, ϕ) due to a particle displacement x . Here w_0 is the $1/e$ radius of the focus, $k = 2\pi n_m / \lambda = k_0 n_m$; n_m is the refractive index of the medium and λ is the wavelength of the trapping laser. α is given as

$$\alpha = a^3 \frac{n_r^2 - 1}{n_r^2 + 2} \quad (2.3)$$

where $n_r = n/n_m$ is the relative refractive index of the particle to the medium.

If a split photodiode is used to monitor the interference pattern in the back focal plane, the detector response can be obtained by integrating Equation 2.2 over all points on the back focal plane, giving Equation 2.4a

$$\frac{I_+ - I_-}{I_+ + I_-} \approx \frac{16}{\sqrt{\pi}} \frac{k\alpha}{w_0^2} G(x/w_0) \quad (2.4a)$$

$$G(u) = e^{(-2u^2)} \int_0^u e^{(v^2)} dv \quad (2.4b)$$

where I_+ is the intensity hitting half of the split photodiode and I_- is the intensity hitting the other half of the split photodiode. For measuring displacements in both x and y directions, a QPD which is essentially a split diode in two directions is used instead. This is explained in Figure 2.16.

In our experimental setup, we use a 0.65 NA condenser lens (Olympus S Plan Fluor 40x 0.65NA ELWD) to collect tracking signals, which is expanded by a telescope relay to slightly overfill a Hamamatsu G6849 InGaAs QPD. The intensity incident upon the QPD is proportional to the output voltage of the QPD, which is wired to an FPGA card (National Instruments PCIe-7852R) for data acquisition.

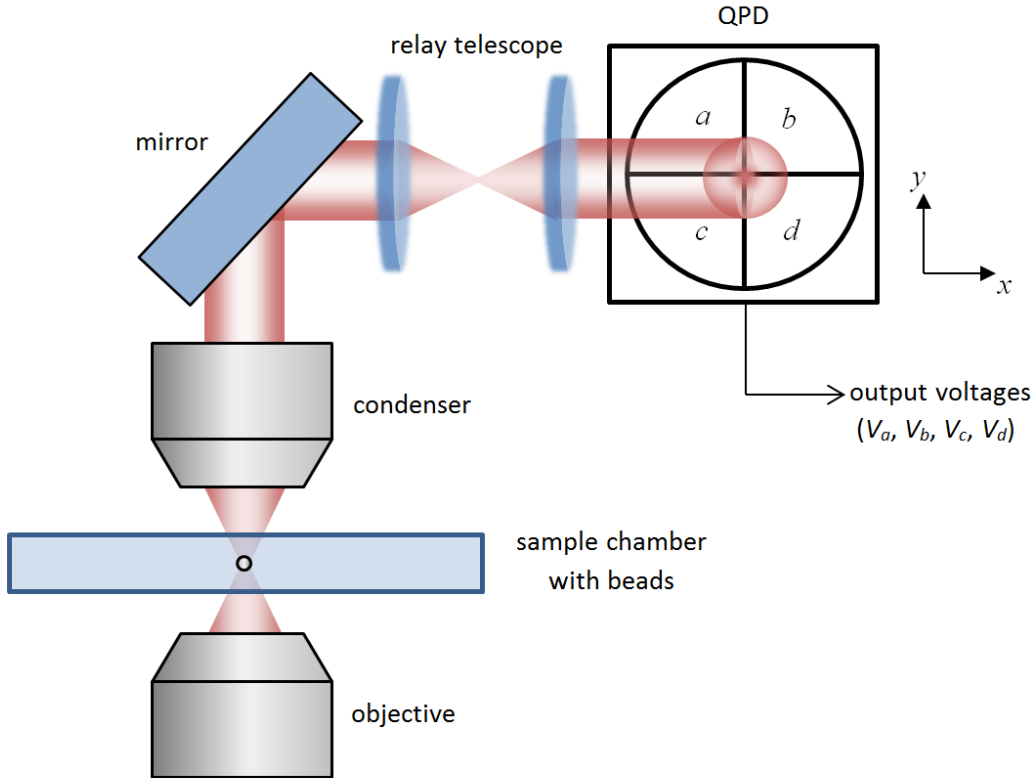


Figure 2.16: The configuration of the quadrant photodiode (QPD) in the optical tweezers setup. The QPD has four quadrants a , b , c , and d with output voltage V_a, V_b, V_c and V_d . For particle displacements in the x direction, $I_+ \propto V_a + V_c$ and $I_- \propto V_b + V_d$ hence the detector response for x displacements is $[(V_a + V_c) - (V_b + V_d)] / (V_a + V_b + V_c + V_d)$. The detector response for y displacements can be worked out using a similar fashion, $[(V_a + V_b) - (V_c + V_d)] / (V_a + V_b + V_c + V_d)$.

2.8.2 Calibration of QPD response to particle displacement

To be able to measure the actual displacement of the particle from the trap centre using the QPD, we have to calibrate the QPD response against particles located at known distances from the trap centre. There are numerous calibration methods for calibrating detector responses to displacements of trapped particles, and the most popular one is the 'stuck-particle method' where a bead is stuck on a nano-positioning stage which is scanned through the optical tweezers [4]. As the nano-positioning stage has precise control over displacements in 3-D, the voltage signal of the forward-scattered interference patterns can be mapped onto a high precision position grid. There are a number of disadvantages in this method. Firstly, it requires a 'sacrificial particle' for the calibration which is stuck and can no longer be used for measurements. This also means that

the particle that is being measured is not necessarily the same particle that is being calibrated, and will result in a slightly different detector response. This is problematic when particle samples within a solution has a large size dispersion. A solution to this problem is to calibrate the trap post-measurements, but this means post processing of the data is necessary and real time results acquisition is not possible. Secondly, the detector response from stuck particles may include scattering from the surface where the particle is stuck onto leading to slightly inaccurate detector responses. Third and most importantly, the stuck particle calibration method does not work for non-symmetric particles, as there is no control over the orientation of the stuck particle to be the same as its orientation while being trapped.

For our setup, we address some of the weaknesses of the stuck-particle calibration method by a different calibration method utilizing the AOD. The explanation of our calibration protocol will be done in reference to Figure 2.17 above. In order to calibrate a trap centred at some point, call it Point O, we must first move the particle a known distance away from Point O. This is done by moving the trap with the trapped particle within it to the new position using the AOD, and refer to this position as Point A. Since the AOD has been calibrated with respect to actual distance (see Section 2.5.2), the distance between Point O and Point A, Δx , is known exactly. Next, the laser is switched back to the trap centre (Point O) and the scattered signal from the particle is measured by the QPD. It is important to note that the beam at Point A is kept at a much longer interval than the beam at Point O, such that the particle stays at Point A; in our experiments, we keep the beam for $500 \mu\text{s}$ at Point A and $50 \mu\text{s}$ at Point O. It is also critical that the QPD measurement is taken exactly when the beam is at Point O. The QPD response is thus a measurement of the particle being displaced by Δx from a trap centered on Point O. This calibration procedure is repeated at least 2000 times for each known displacement Δx to improve accuracy, and the same is done for a few different particle displacements to build up a detector response calibration curve (Figure 2.18).

From Figure 2.18a, we see that the detector response curve for a trapped $1 \mu\text{m}$ polystyrene sphere demonstrate the distinct features of a typical detector response curves [25, 26], as predicted by Equation 2.4a also shown in the Figure. This reaffirms the validity of our calibration method. Since the normal displacement due to Brownian motion of an optically trapped particle falls well within the linear region of the detector response curve, we can directly map the detector response to particle displacement through linear interpolation (Figure 2.18b). If the output voltages from each quadrant

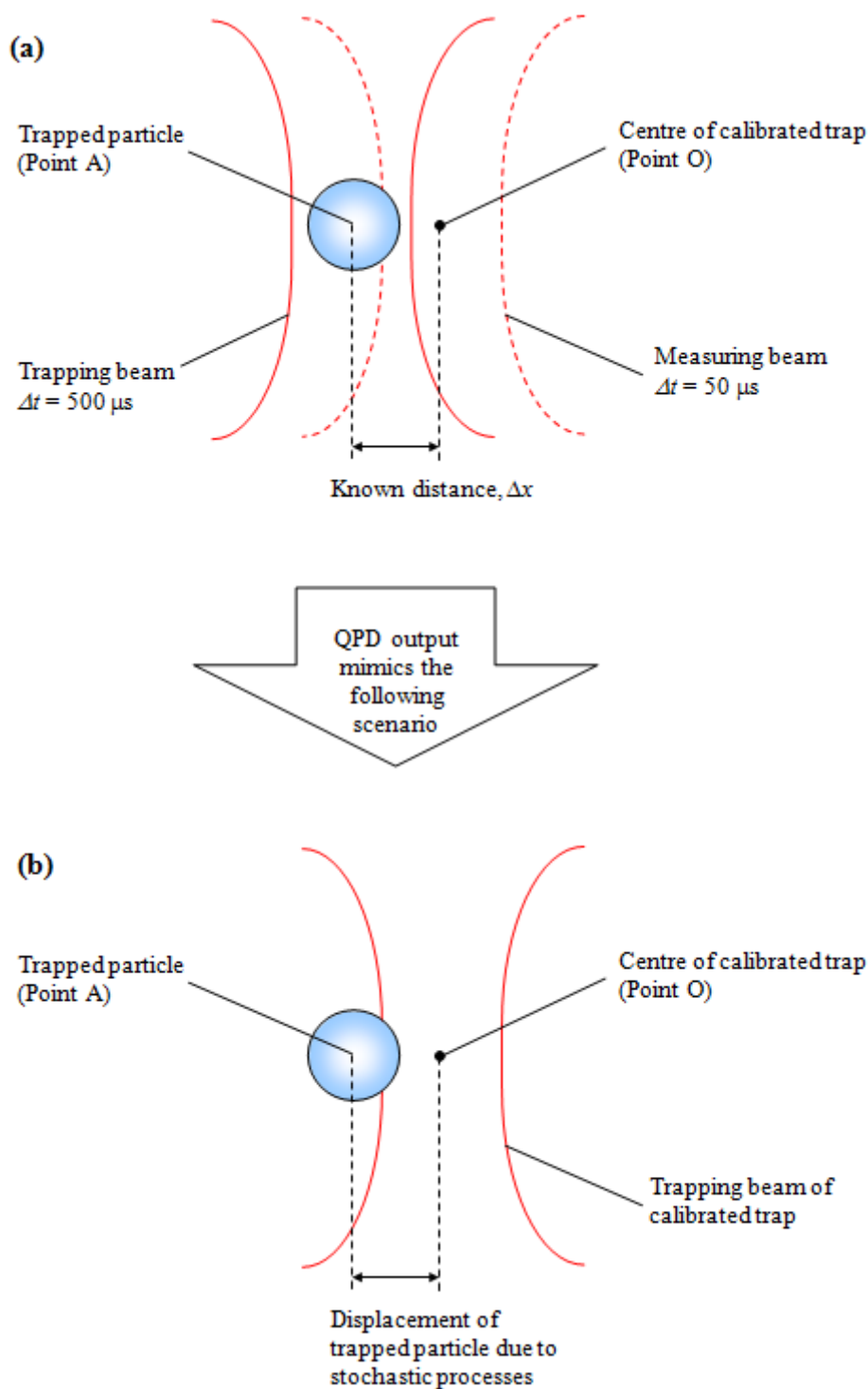


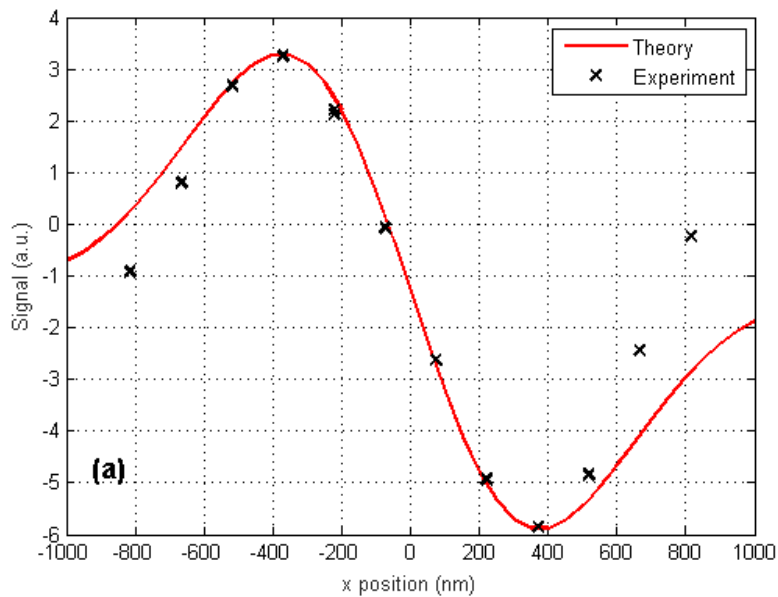
Figure 2.17: (a) The trap is calibrated by trapping the particle at Point A and then measuring the scattering from the particle when the laser is at Point O. To achieve this, the laser spends most of the time holding the particle at Point A ($500 \mu\text{s}$), and switches over to Point O in short intervals to take measurements ($50 \mu\text{s}$). (b) The QPD readout from measuring at Point O in the top diagram mimics the QPD readout from the scenario when a particle is displaced from the trap centre of the calibrated trap. This therefore allows us to find the actual displacement of the particle from the trap centre, Δx by looking at the QPD readout.

of the QPD are V_a, V_b, V_c and V_d , then the x and y displacements of an optically trapped particle are given as

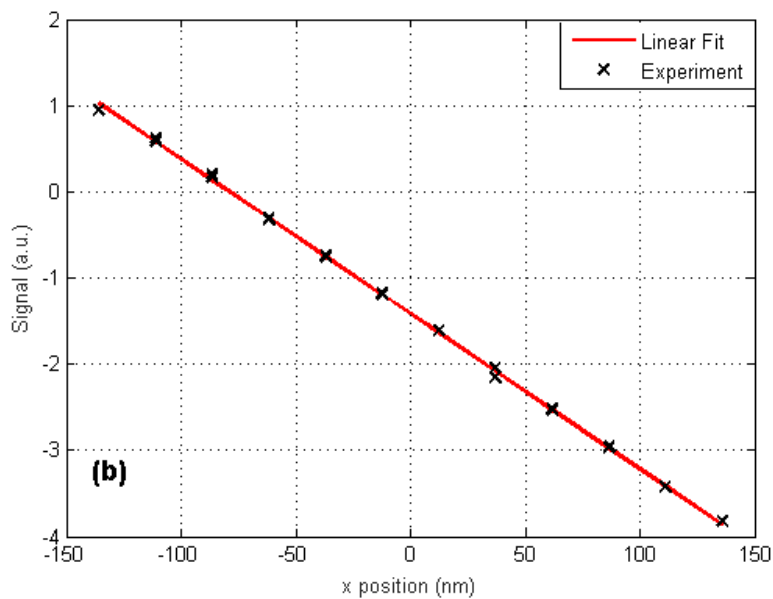
$$\Delta x = C_x \frac{(V_a + V_c) - (V_b + V_d)}{(V_a + V_b + V_c + V_d)} \quad (2.5a)$$

$$\Delta y = C_y \frac{(V_a + V_b) - (V_c + V_d)}{(V_a + V_b + V_c + V_d)} \quad (2.5b)$$

where C_x and C_y are the calibration constants which are the gradients obtained from the linear fits of the QPD detector response curves (Figure 2.18b).



(a) QPD detector response curve of a trapped $1 \mu\text{m}$ spheres over $\pm 1 \mu\text{m}$ from the trap centre, denoted by the black crosses. The red curve is a scaled plot of Equation 2.4a.



(b) Linear region of the QPD detector response curve with a linear fit.

Figure 2.18: QPD detector response curve of a trapped $1 \mu\text{m}$ spheres.

2.9 Trapping and tracking of a particle using optical tweezers

Figure 2.19 shows the schematic of our optical tweezers setup that is used for all experimental work presented in this thesis.

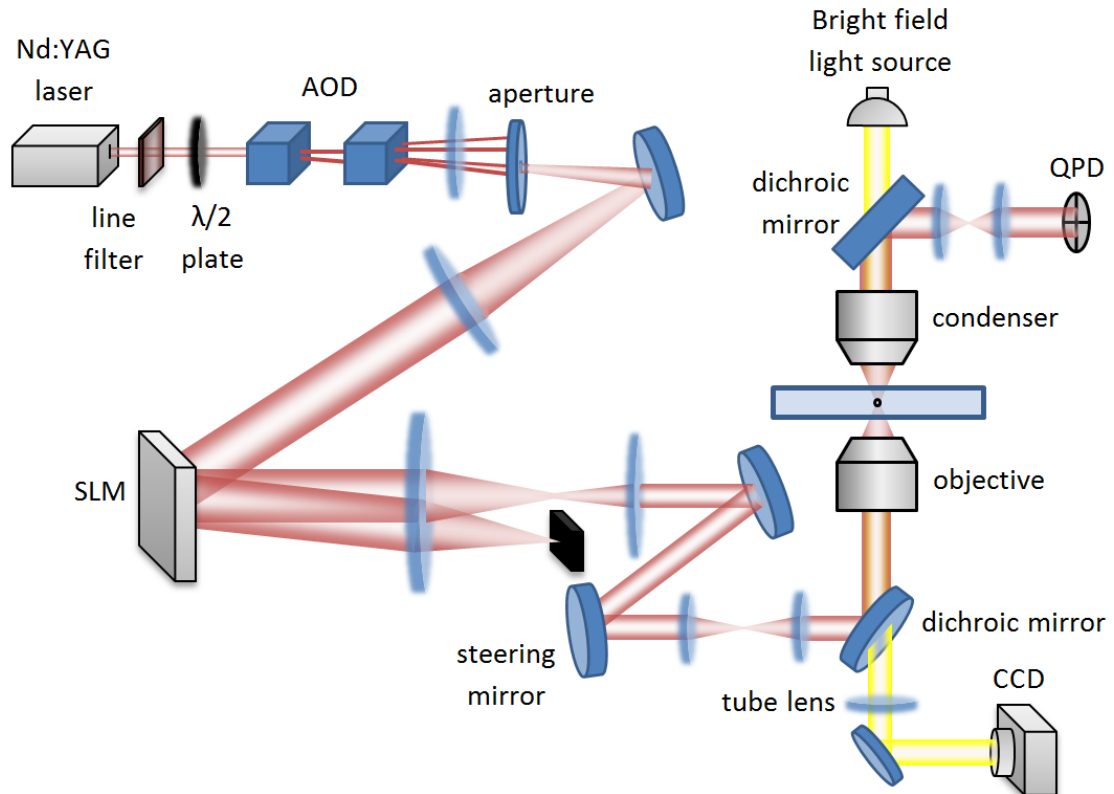


Figure 2.19: A schematic diagram of the optical tweezers setup used in this study.

The trapping and tracking of a particle using our optical tweezers setup can be summarised as the following:

1. Optimise the trap from aberrations using the SLM (Section 2.6.2). This step is only done every few months or when a full system realignment is necessary.
2. Calibrate the output power (Section 2.5.3) and displacement (Section 2.5.2) of the AOD. This step is only necessary if the SLM is reconfigured.
3. Vibration isolation is turned on (Section 2.7).

4. Samples are prepared and mounted onto the optical tweezers setup. Both the manual and motorised stage controls can be used to browse within the sample chamber to find suitable particles for optical trapping (Section 2.3).
5. Once a suitable particle is found, it is trapped using the trapping beam of the optical tweezers (Section 2.2).
6. The QPD detector response for the trapped particle is calibrated (Section 2.8.2).
7. Once calibrated, the particle is tracked by back focal plane interferometry using the QPD (Section 2.8.1).

For all of our experiments unless otherwise specified, the trapped particle is tracked for 2 seconds with a sampling rate of 10 kHz and 5 sets of 2-second trajectories are recorded. An example set of particle trajectory for an optically trapped $1\ \mu\text{m}$ polystyrene sphere is shown in Figure 2.20.

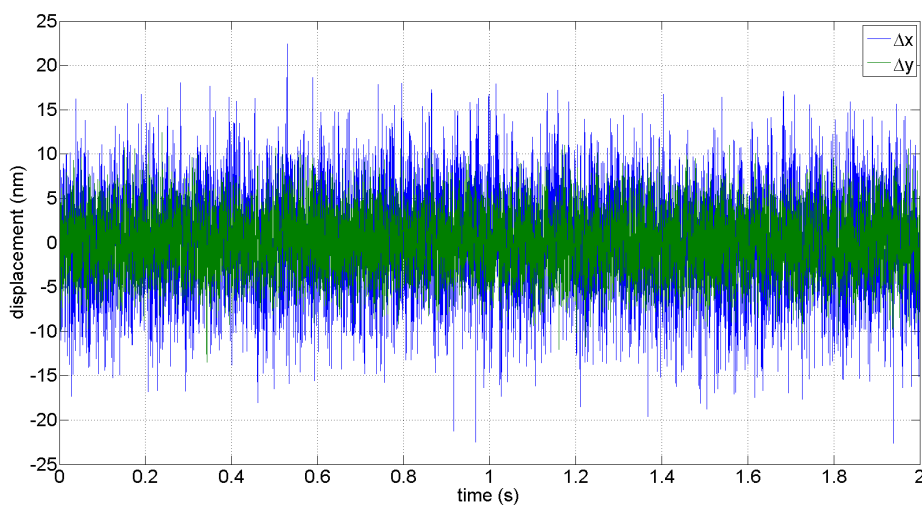


Figure 2.20: The trajectory of an optically trapped $1\ \mu\text{m}$ polystyrene sphere. The blue curve denotes displacements in the x direction while the green curve denotes displacements in the y direction.

2.10 References

- [1] Keir C. Neuman and Steven M. Block. Optical trapping. *Review of Scientific Instruments*, 75:2787, 2004.
- [2] Kishan Dholakia, Peter Reece, and Min Gu. Optical micromanipulation. *Chem. Soc. Rev.*, 37:42–55, 2008.
- [3] R. W. Bowman and M. J. Padgett. Optical trapping and binding. *Reports on Progress in Physics*, 76(2), 2013. 086PI Times Cited:43 Cited References Count:250.
- [4] W. M. Lee, P. J. Reece, R. F. Marchington, N. K. Metzger, and K. Dholakia. Construction and calibration of an optical trap on a fluorescence optical microscope. *Nature Protocols*, 2(12):3226–3238, 2007. 262HS Times Cited:36 Cited References Count:32.
- [5] A. Ashkin, J. M. Dziedzic, J. E. Bjorkholm, and Steven Chu. Observation of a single-beam gradient force optical trap for dielectric particles. *Opt. Lett.*, 11:288–290, 1986.
- [6] A. Ashkin. Forces of a single-beam gradient laser trap on a dielectric sphere in the ray optics regime. *Biophysical Journal*, 61(2):569–582, 1992. Hc778 Times Cited:853 Cited References Count:36.
- [7] Joseph W. Goodman. *Introduction to Fourier optics*. Fourier optics. Englewood, Colo. : Roberts & Co. Publishers, Englewood, Colo., 3rd ed. edition, 2005. Includes bibliographical references (p. 465-479) and index.
- [8] A. H. Mack, M. K. Trias, and S. G. J. Mochrie. Precision optical trapping via a programmable direct-digital-synthesis-based controller for acousto-optic deflectors. *Review of Scientific Instruments*, 80(1), 2009. 401TT Times Cited:4 Cited References Count:18.
- [9] K. Visscher, S. P. Gross, and S. M. Block. Construction of multiple-beam optical traps with nanometer-resolution position sensing. *Ieee Journal of Selected Topics in Quantum Electronics*, 2(4):1066–1076, 1996. Xd616 Times Cited:262 Cited References Count:32.
- [10] N. B. Viana, M. S. Rocha, O. N. Mesquita, A. Mazolli, and P. A. M. Neto. Characterization of objective transmittance for optical tweezers. *Applied Optics*, 45(18):4263–4269, 2006. 054he Times Cited:24 Cited References Count:10.
- [11] H. Rubinsztein-Dunlop, T. A. Nieminen, M. E. J. Friese, and N. R. Heckenberg. Optical trapping of absorbing particles. *Advances in Quantum Chemistry, Vol 30*, 30:469–492, 1998. Bk92r Times Cited:39 Cited References Count:50 Advances in Quantum Chemistry.
- [12] Y. Hayasaki, M. Itoh, T. Yatagai, and N. Nishida. Nonmechanical optical manipulation of microparticle using spatial light modulator. *Optical Review*, 6(1):24–27, 1999. 182UA Times Cited:41 Cited References Count:13.

- [13] M. Reicherter, T. Haist, E. U. Wagemann, and H. J. Tiziani. Optical particle trapping with computer-generated holograms written on a liquid-crystal display. *Optics Letters*, 24(9):608–610, 1999. 192JC Times Cited:263 Cited References Count:9.
- [14] J. E. Curtis, B. A. Koss, and D. G. Grier. Dynamic holographic optical tweezers. *Optics Communications*, 207(1-6):169–175, 2002. 569WQ Times Cited:669 Cited References Count:22.
- [15] J. Liesener, M. Reicherter, T. Haist, and H. J. Tiziani. Multi-functional optical tweezers using computer-generated holograms. *Optics Communications*, 185(1-3):77–82, 2000. 371JL Times Cited:248 Cited References Count:11.
- [16] D. G. Grier. A revolution in optical manipulation. *Nature*, 424(6950):810–816, 2003. 711HQ Times Cited:1817 Cited References Count:85.
- [17] T. Cizmar, M. Mazilu, and K. Dholakia. In situ wavefront correction and its application to micromanipulation. *Nature Photonics*, 4(6):388–394, 2010. 606JV Times Cited:155 Cited References Count:41.
- [18] C. Lopez-Quesada, J. Andilla, and E. Martin-Badosa. Correction of aberration in holographic optical tweezers using a shack-hartmann sensor. *Applied Optics*, 48(6):1084–1090, 2009. 421VV Times Cited:17 Cited References Count:33.
- [19] K. D. Wulff, D. G. Cole, R. L. Clark, R. DiLeonardo, J. Leach, J. Cooper, G. Gibson, and M. J. Padgett. Aberration correction in holographic optical tweezers. *Optics Express*, 14(9):4169–4174, 2006. 039HI Times Cited:67 Cited References Count:22.
- [20] E. Martin-Badosa, M. Montes-Usategui, A. Carnicer, J. Andilla, E. Pleguezuelos, and I. Juvells. Design strategies for optimizing holographic optical tweezers setups. *Journal of Optics a-Pure and Applied Optics*, 9(8):S267–S277, 2007. Sp. Iss. SI 203CV Times Cited:35 Cited References Count:33.
- [21] T. Cizmar, H. I. C. Dalgarno, P. C. Ashok, F. J. Gunn-Moore, and K. Dholakia. Optical aberration compensation in a multiplexed optical trapping system. *Journal of Optics*, 13(4), 2011. Sp. Iss. SI 781JH Times Cited:3 Cited References Count:19.
- [22] P. Török, P. Varga, Z. Laczik, and G. R. Booker. Electromagnetic diffraction of light focused through a planar interface between materials of mismatched refractive indices: an integral representation. *J. Opt. Soc. Am. A*, 12(2):325–332, 1995.
- [23] M. J. Booth and T. Wilson. Refractive-index-mismatch induced aberrations in single-photon and two-photon microscopy and the use of aberration correction. *Journal of Biomedical Optics*, 6(3):266–272, 2001. 462DR Times Cited:50 Cited References Count:17.
- [24] Born Max, Wolf Emil, and Reviewer Eugene Hecht. Principles of optics: Electromagnetic theory of propagation, interference and diffraction of light. *Physics Today*, 53:77, 2000.
- [25] Frederick Gittes and Christoph F. Schmidt. Interference model for back-focal-plane displacement detection in optical tweezers. *Opt. Lett.*, 23(1):7–9, Jan 1998.

- [26] A. Rohrbach, H. Kress, and E. H. K. Stelzer. Three-dimensional tracking of small spheres in focused laser beams: influence of the detection angular aperture. *Optics Letters*, 28(6):411–413, 2003. 652ZT Times Cited:47 Cited References Count:9.

Chapter 3

Optical Trapping of InP Nanowires

3.1	Introduction	49
3.2	Theoretical considerations of the optical trapping of nanowires	51
3.3	InP nanowire trapping experiments	54
3.3.1	InP nanowire preparation	54
3.3.2	Trapping a single InP nanowire	55
3.3.3	Calibration of detector response of a trapped nanowire	56
3.3.4	Length measurements of nanowires	58
3.3.5	Trap stiffness of optically trapped nanowires	60
3.4	Length dependence of nanowire trapping	61
3.5	Stable axial trapping position	64
3.6	Resonant behaviour of optically trapped nanowires	68
3.7	Winding number analysis	73
3.7.1	Introduction to the winding number analysis	73
3.7.2	Application of the winding number analysis on optically trapped nanowire trajectory	75
3.8	Height dependence of nanowire resonance	76
3.9	Expansion of the power spectral analysis method	79
3.10	Power dependence of nanowire resonance	82
3.11	Length dependence of resonance peaks	88

3.12 Conclusion	89
3.13 References	90

3.1 Introduction

There has been growing interest in the optical trapping of micron-sized objects as potential probe tips in high-resolution scanning probe microscopy [1]. The appeal in using optically trapped probe tips is the capability of achieving very fine tips with a small spatial footprint and a smaller force constant. This potentially increases the maximum achievable spatial resolution and sensitivity, which in turn enables the interrogation of surfaces that are otherwise inaccessible to conventional scanning probe techniques [2–4]. Furthermore, the advancement in two-photon polymerization technology has led to the ability to fabricate complex 3 dimensional objects that can be tailored to meet specific dimensions which optimizes the probing capability of such optically trapped scanning probes [2, 3, 5, 6]. Examples of this are the probes designed and fabricated by Phillips *et al.* [3, 5–7] which consist of conical handles where optical forces are applied, and spherical markers as tracking points, shown in Figure 3.1 below. Some of these probes are capable of achieving a lateral resolution of 200 nm (due to the tip diameter) and a depth resolution of about 10 nm [6] as shown in Figure 3.2.

Another class of potential candidates for optically trapped scanning probes are semiconductor nanowires. The development of nanoscale fabrication technology has enabled the production of high quality nanoscale structures; advanced fabrication methods allow the composition and dimensions of these nanostructures to be controlled with very high purity and accuracy [8–11]. Among the various types of nanostructures, semiconductor nanowires have attracted considerable interest due to its potential in nano-scale electronic and photonic applications, including optical waveguides [12], field effect transistors [13], single electron transistors [14], nanolasers [15], photodetectors [16] and integrated microprocessors [17, 18]. Nanowires have also been optically manipulated to assemble more complex nanostructures [19, 20].

In addition to having diameters as small as 50nm, nanowires typically have an aspect ratio well above 50 making them excellent candidates as scanning probe tips. On top of that, semiconductor nanowires are typically composed of optically active materials that exhibit room temperature photoluminescence as well as strong second harmonic generation [15, 21]. These additional functionalities open up new possibilities in terms of probing methods, such as the use of guided light within a nanowire to probe surface features [1]. Indium phosphide (InP) nanowires are chosen for this study due to their excellent optical and electrical properties. InP nanowires have been shown to have photoluminescence and photodetection capabilities [16]. They have also been used

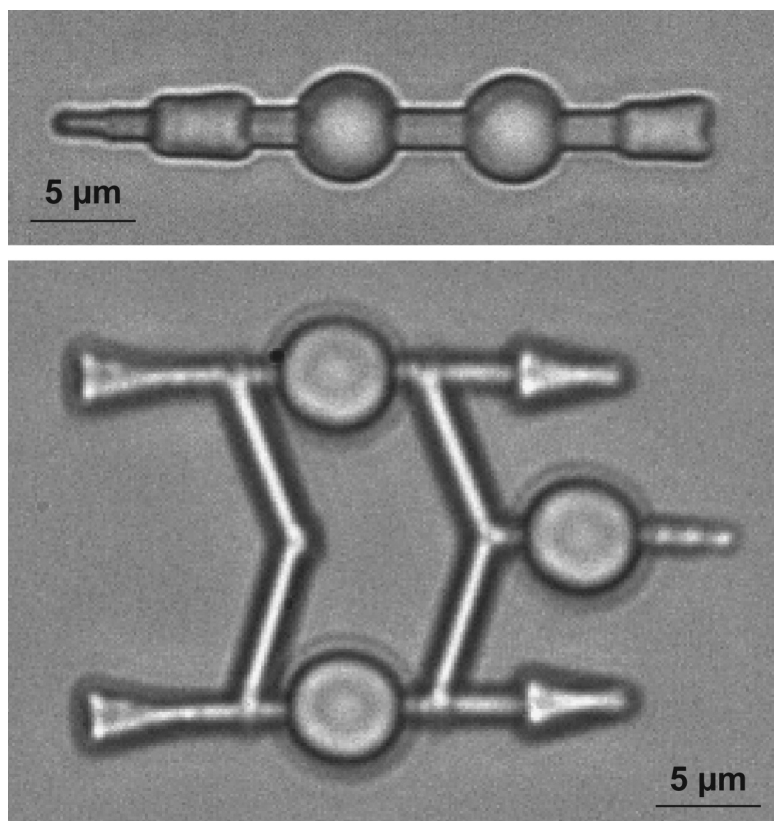


Figure 3.1: Probes consisting of conical sections through which the object is trapped and spheres to provide tracking points for high-speed video stereomicroscopy. The three-dimensional coordinates of each sphere can be recovered to an accuracy of $\leq 5\text{nm}$ at rates of up to 1 kHz, from which the position and orientation of the extended particle can be determined. Image adopted from Simpson *et al* [7]. Reprinted from [7], copyright 2013, with permission from Elsevier.

as single electron transistors [14]. Our group has also demonstrated second harmonic generation (SHG) of 532nm photons from a 1064nm pump source via a single optically trapped nanowire [21]. Due to these qualities, it is therefore desirable to fully characterise and thoroughly understand the trapping behaviour of single InP nanowires.

In this chapter, I aim to study the behaviour of a single InP nanowire within an optical trap. This is an important step before we examine the interaction of multiple trapped nanowires. In this chapter I will discuss the trapping and tracking of single InP nanowires. The trap stiffness of optically trapped InP nanowires will be measured, and the dependence on nanowire length and trapping power is examined. Finally, I will also examine some dynamic behaviour in the optical trapping of these nanowires that arises due to their shape asymmetry.

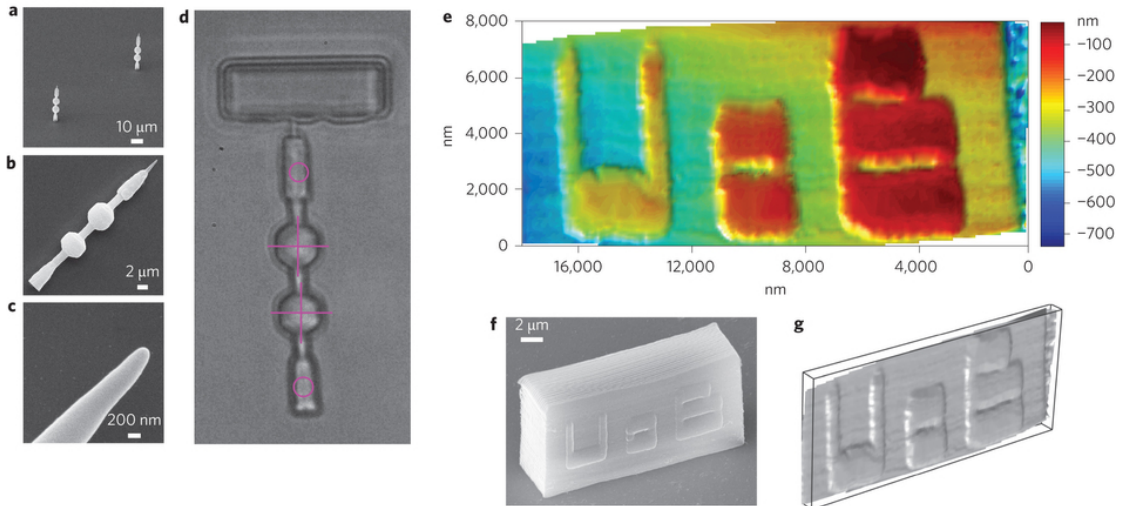


Figure 3.2: (a) Scanning electron microscope (SEM) image of two newly fabricated probes still attached to the substrate. (b) SEM image of a single probe dislodged from the substrate and lying on its side. (c) Close-up SEM image of the probe tip from the probe in (b). (d) Optical image of a probe as it is scanned along the side of a calibration sample. Circles indicate the location of the optical traps; crosses mark the tracked points of the probe. (e) Surface topography of the side of the calibration sample recorded with this probe. (f) SEM image showing the side of the calibration sample that was scanned with the probe. (g) Same data as in (e), viewed as a three-dimensional reconstruction for comparison with (f). All figures adopted from Phillips *et al* [6]. Reprinted by permission from Macmillan Publishers Ltd: Nature Photonics [6], copyright 2014.

3.2 Theoretical considerations of the optical trapping of nanowires

Optically trapped microscopic objects emulate the motion of an over-damped harmonic oscillator driven by stochastic thermal fluctuations. Such motion can be described by diffusive Brownian motion modulated by translational restoring forces, as described by Einstein-Ornstein-Uhlenbeck theory [22]. For small displacements, the restoring force acting on an optically trapped object is proportional to its displacement from the trapping centre. For a trapped particle within an aqueous medium, the system can be described as a highly overdamped harmonic oscillator for the three translation coordinates [23, 24]. Using the Einstein-Ornstein-Uhlenbeck theory of Brownian motion, the motion of the trapped particle can be described by a Langevin equation in the following form [25]:

$$m \frac{\partial^2 x}{\partial t^2} + \gamma_0 \frac{\partial x}{\partial t} + \kappa x = (2k_B T \gamma_0)^{1/2} \eta(t) \quad (3.1)$$

Where m is the mass of the particle, $x(t)$ is the trajectory of the particle, κ is the trap stiffness, γ_0 is the Stoke's drag of the particle, T is the temperature, and $\eta(t)$ denotes the stochastic process of the Brownian motion of the trapped particle, with $\langle \eta(t) \rangle = 0$ and $\langle \eta(t) \eta(t') \rangle = \delta(t - t')$. In Equation 3.1, the first term on the left is the inertial term, the second is the viscous damping or Stokes drag, and the third term is the optical restoring force. The term on right-hand side denotes the Brownian forces at absolute temperature T . As the characteristic time for momentum relaxation through viscous damping, $t_p \equiv m/\gamma_0$ is very small (i.e., low Reynolds number environment) the inertial term may be neglected.

Following from Berg-Sorensen and Flyvbjerg [22], the above equation may be approximated by

$$\frac{\partial x}{\partial t} + 2\pi f_c x = (2D)^{1/2} \eta(t) \quad (3.2)$$

Where we have defined the corner frequency, $f_c \equiv \kappa/2\pi\gamma_0$, and $D = k_B T/\gamma_0$ is the Einstein equation for diffusion of particles through a fluid medium. By taking the Fourier transformation of 3.2 we find that the power spectrum, S , is given by the Lorentzian equation

$$S \equiv \left\langle \frac{|\tilde{x}|^2}{T} \right\rangle = \frac{D/2\pi^2}{f_c^2 + f^2} \quad (3.3)$$

Where $|\tilde{x}|$ is the Fourier transform of $x(t)$. Hence we can obtain the value of f_c by fitting a Lorentzian to our experimental data, and then calculate the trap stiffness κ .

In the case of optically trapped nanowires, the elongated shape introduces two additional angular degrees of freedom, rotation and tilt. The stochastic motion of the nanowires within an optical trap can therefore be described by a set of uncoupled Langevin equations in terms of translational x_i and angular θ_j coordinates [26] (with the inertial terms removed due to reasons explained above):

$$\partial_t x_i(t) = -\omega_i x_i(t) + \xi_i(t) \quad (3.4a)$$

$$\partial_t \theta_j(t) = -\Omega_j \theta_j(t) + \xi_j(t) \quad (3.4b)$$

Where $\omega_i = \kappa_i/\gamma_i$ and $\Omega_j = \tau_j/\gamma_j$ are relaxation constants related to the force and torque constants and drag coefficients. $\xi_i(t)$ represents the noise term with zero mean and variance, $\langle \xi_i(t) \xi_i(t + \tau) \rangle = 2k_B T \gamma_i \eta(\tau)$. The trap stiffness and torque constants for each degree of freedom can be extracted by performing a power spectrum analysis on the Langevin equations.

Note that in order to accurately predict the trap stiffness parameter, we need to know the form of drag coefficient for the objects of interest. For spherical particles such as colloidal microspheres this is a well-known analytical expression; however for more complex shapes, such as elongated cylinders, no analytical expression is available. Here we model the nanowires as rigid cylinders and compute the Stokes' drag for cylindrical objects based on computational models developed by Tirado and Torre [27, 28]. The viscous drag of cylindrical objects, γ_i is described by an anisotropic hydrodynamic mobility tensor [26, 28].

$$\gamma_{\perp} = \frac{4\pi\eta_0 L}{\ln(L/2a) + \delta_{\perp}} \quad (3.5a)$$

$$\gamma_{\parallel} = \frac{2\pi\eta_0 L}{\ln(L/2a) + \delta_{\parallel}} \quad (3.5b)$$

$$\gamma_{\theta} = \frac{\pi\eta_0 L^3}{3(\ln(L/2a) + \delta_{\theta})} \quad (3.5c)$$

Where γ_{\perp} and γ_{\parallel} are the drag coefficients perpendicular and parallel to the symmetry axis of the cylinder, while γ_{θ} is the rotational drag coefficient for reorientation of the cylinder. η_0 is the viscosity of water while δ_{\perp} , δ_{\parallel} and δ_{θ} are correction factors accounting for the ends of the cylinder which depends on the aspect ratio of the cylinder, $L/2a$, and was calculated by Tirado [27]. A power spectrum analysis of this system yields a characteristic Lorentzian dependence for each degree of freedom with corner frequencies given by $f_{ci} = \kappa_i/2\pi\gamma_i$, from which the trap stiffness for each degree of freedom κ_i can be extracted.

This simple approximation provides an accurate description for a large class of optical trapping experiments, such as the case in nanowires when the coupling between rotational and translational motions are weak, or when the rotational motions are heavily suppressed. The above approximation breaks down however, when there are significant angular motions strongly coupled to translational motions, as shown in some of our experiments in a later section in this chapter.

3.3 InP nanowire trapping experiments

3.3.1 InP nanowire preparation

InP nanowires used in the following studies were epitaxially grown on an InP (111)B substrate by metal organic chemical vapour deposition (MOCVD) [9]. The semiconductor substrates were initially immersed in poly-L-lysine solution and treated with gold colloid solution containing gold nanoparticles of 30 nm in diameter. The nanowires were then grown in the MOCVD reactor using trimethylindium (TMIn) and phosphine (PH₃) precursors, with the gold nanoparticles acting as seeds for the growth via the vapour liquid solid (VLS) mechanism [9, 29]. During growth, pressure was kept at 100 mbar while the temperature was set at 490 °C, the V/III ratio was set at 44, and the growth time was approximately 20 min. These growth conditions produced nanowires of very uniform cylindrical geometry of dimensions 30±6 nm in diameter and up to 15 μm in length. The nanowires had a predominantly wurtzite (WZ) crystal structure, which was confirmed by high-resolution transmission electron and scanning electron microscopy measurements [9].

Individual InP nanowires were transferred into liquid medium and onto a sample slide that can be mounted on the optical tweezers setup by the following procedures: a 3 mm by 3 mm InP substrate (only approximate, as substrate is cleaved along its crystal planes) with grown nanowires is added into a 10 ml vial with 1 ml of deionised water. The surface of the substrate containing nanowires is placed facing upwards in the vial so that the nanowires may freely diffuse into the solution during sonication. The vial is sealed and sonicated in a water bath for 2 minutes. The resulting solution is diluted 10 to 50 times depending on the yield of the nanowires from sonication. This set of procedures produces a solution containing nanowires with lengths up to 15 μm.

For optical trapping experiments, the diluted solution containing nanowires is then prepared onto a sample slide as described in the sample preparation section of Chapter 2 Section 2.3 and mounted onto the optical tweezers setup shown in Figure 2.3. It should be noted that the resulting solution from sonication will also contain some contaminants due to broken nanowires or broken bits of substrate. If the concentration of contaminants is too high in a sample, further dilution is necessary.

3.3.2 Trapping a single InP nanowire

Once the sample slide containing the nanowires is mounted onto the sample stage, we navigate through the sample to look for nanowires to trap by raster scanning the sample chamber using motorised sample stage controls. Trapping of nanowires is slightly more difficult than trapping spheres, as the non-spherical shape of the nanowires means that the initial orientation of the nanowire is critical to successfully capture it.

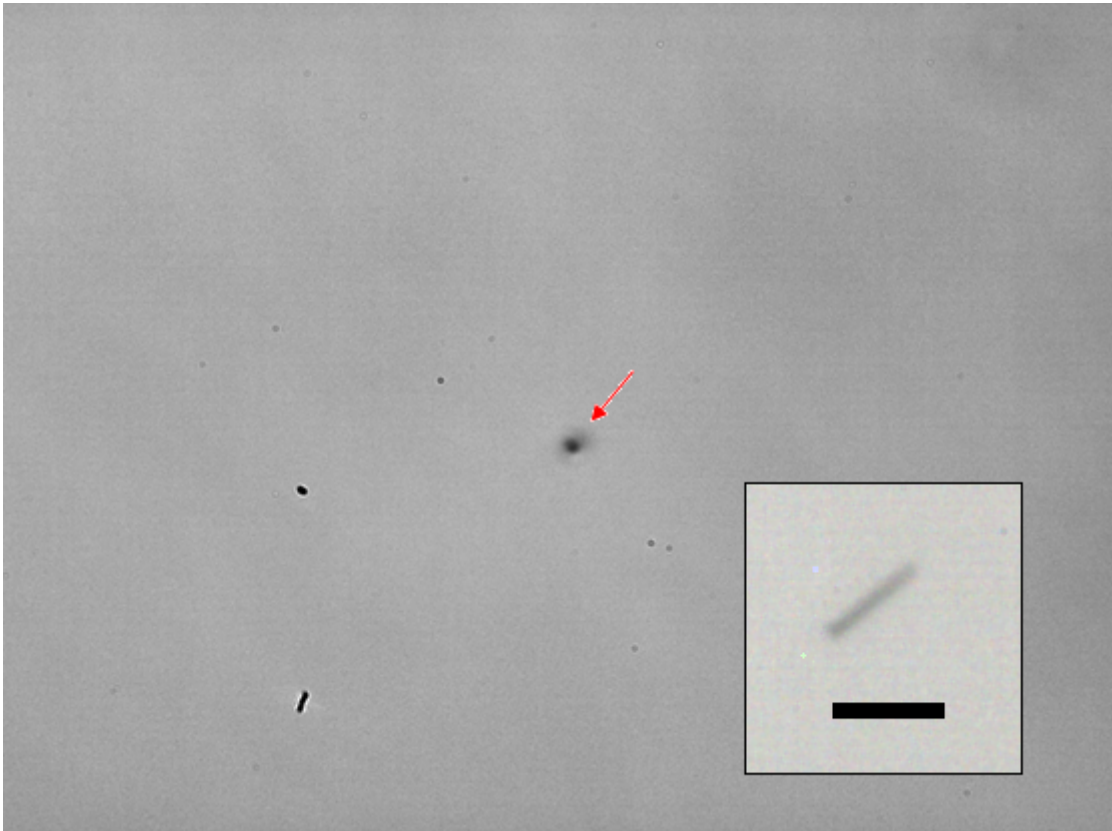


Figure 3.3: A photograph of the image plane showing a trapped nanowire in the optical tweezers (indicated by the red arrow). The nanowire is aligned to the optical axis, which is perpendicular to the image plane. (Insert) A photograph of an untrapped nanowire on its side. The black scale bar indicates $5 \mu\text{m}$. Both pictures are at the same scale.

Through our trapping experiments we found that we are able to trap nanowires between $3 \mu\text{m}$ and $15 \mu\text{m}$. When trapped, these nanowires align themselves to the optical axis of the trap which is perpendicular to the image plane, as can be seen in Figure 3.3. Hence in order to trap a nanowire, it must be slightly tilted towards the vertical direction while the optical trap is positioned above for it to enter the trap smoothly into the stable trapping position, as shown in Figure 3.5. If the nanowire enters the trap horizontally

such as that shown in Figure 3.4, a large cross sectional area of the nanowire will be exposed to the laser beam resulting in a large scattering force pushing the nanowire away from the trap along the beam propagation direction.

3.3.3 Calibration of detector response of a trapped nanowire

Tracking of the optically trapped nanowire is done using back focal plane interferometry with a quadrant photodiode (QPD) as described in the methods chapter. This method is chosen over video tracking methods for its unparalleled temporal and spatial resolution. The calibration procedure and the measurement of a detector response curve are also the same as that for spheres as described in Section 2.8.2 in Chapter 2.

Figure 3.6 is a set of detector response curves for nanowires of different lengths which exhibit a form characteristic of trapped spherical objects [30] and includes a linear region near the trapping origin and a strongly nonlinear region at larger displacement, thus validating the applicability of this method of tracking to our system. From the curves it can be seen that the detector response is linear with respect to the displacement of the nanowires from the centre of the trap up to ± 200 nm; typical Brownian fluctuation of the nanowires within the trap is an order of magnitude smaller than these limits.

The relative invariance of the detector response curves between different lengths of nanowire can be attributed to the fact that the scattering cross section of the nanowires with the same diameter within the optical trap remains constant irrespective of the lengths of the nanowires. This is because the lengths of these nanowires extend beyond the depth of focus of the optical trap, resulting in the same interaction volume with the optical trap regardless of nanowire length. This will be examined further in Section 3.4, on the length dependence of trap stiffness of nanowires. It should also be noted that the calibration is only valid for conditions where the nanowire maintains its orientation with the long axis directed along the propagation direction, which is the case for high refractive index nanowires of length greatly exceeding the focal depth of the tweezers.

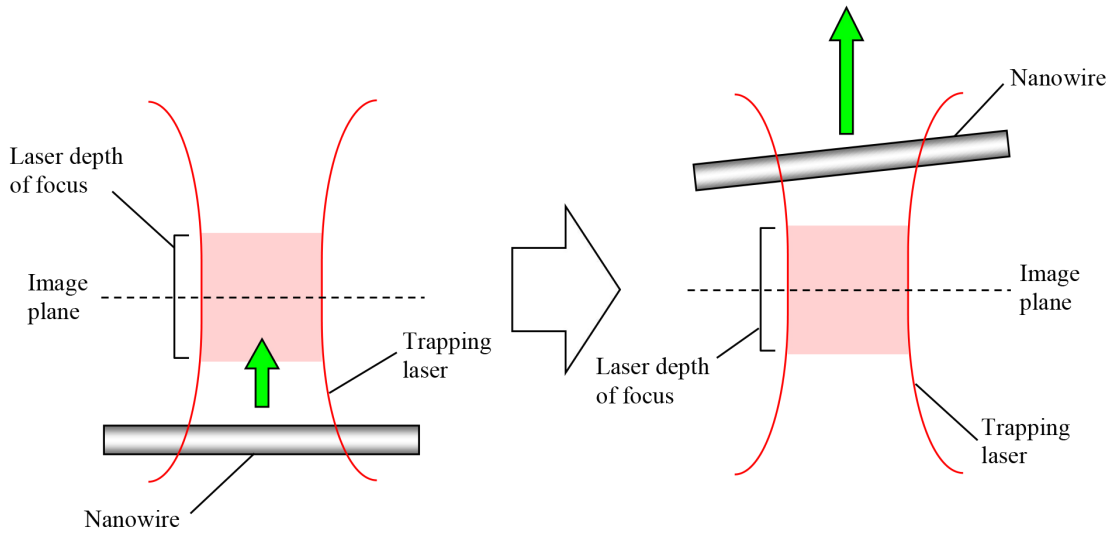


Figure 3.4: Failed attempt to trap a nanowire. (Left) If the wire is not tilted enough when the trap is moved over it, the nanowire will experience an attractive potential towards the trap centre. (Right) It will then experience a huge acceleration as it passes through the depth of focus of the laser and is therefore ‘kicked’ away from the trap.

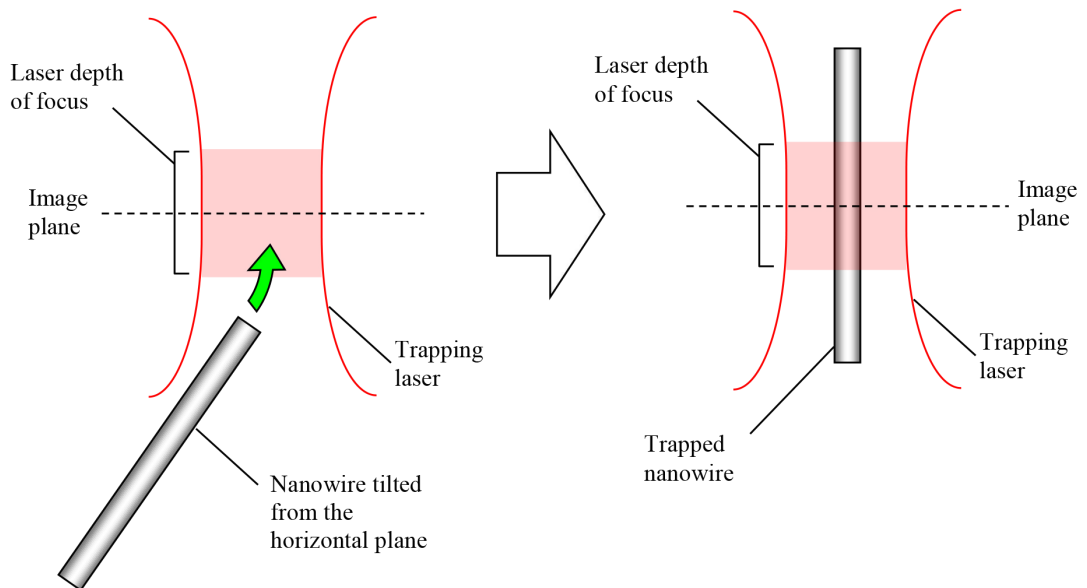


Figure 3.5: Successful trapping of nanowires using optical tweezers. (Left) The trap is moved above a slightly tilted nanowire. The attractive potential of the trap will pull the wire towards it, and at the same time align the nanowire vertically. (Right) The nanowire is trapped in the optical trap. The depth of focus is where the tweezers is ‘holding’ the nanowire.

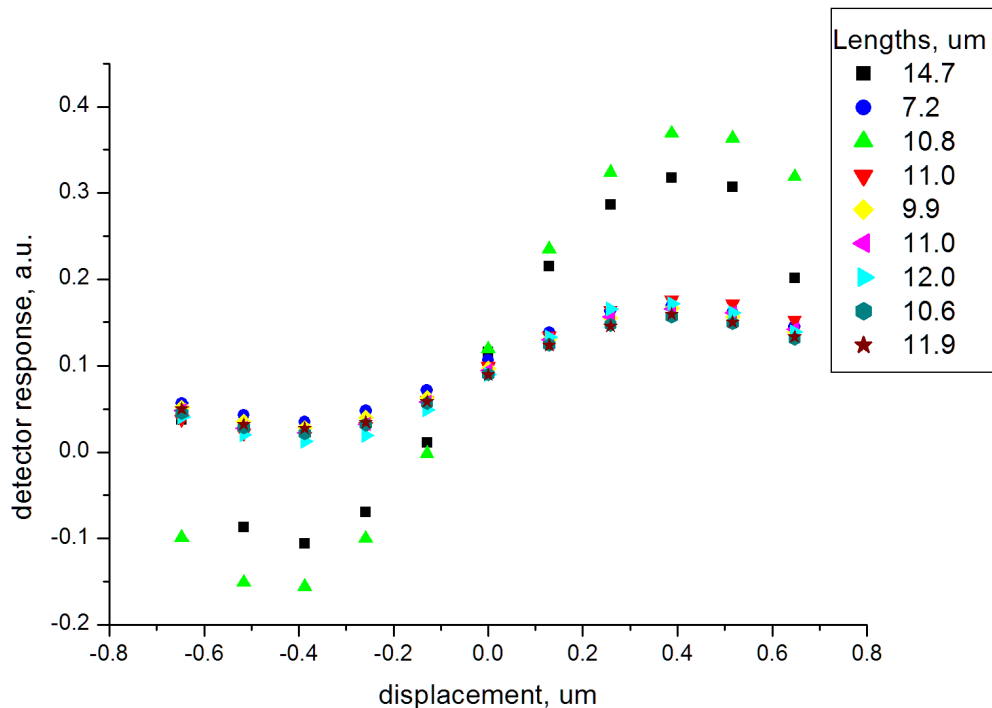


Figure 3.6: QPD response for the lateral displacement of nine nanowires of different lengths within an optical trap. The curves have a linear response for small perturbations and a strongly nonlinear response for larger displacements. All but two of the nanowires has almost identical calibration curves; this suggest that the two nanowires have a different interaction volume with the optical trap compared to the other nanowires, probably because they have different diameters (see Section 3.4).

3.3.4 Length measurements of nanowires

The lengths of individual optically trapped nanowires are of interest in various length dependence studies. As such, the lengths of the same nanowires that we have tracked have to be measured and matched to the tracking data that were taken. This is done by pushing a previously tracked nanowire against the cover slip of the sample chamber using the optical tweezers until the nanowire is flat on the image plane, and then capturing an image of it as shown in Figure 3.7. The apparent lengths of the nanowires in the pictures are then measured in units of pixels using image processing software. Multiple photographs are captured for each nanowire to make repeated measurements. Finally the apparent lengths of the nanowires are converted into actual lengths using the conversion factor obtained from the image of a stage micrometer as described in Chapter 2 Section 2.5.2 (Figure 2.8).

Here I will show an example of measuring the length of a typical nanowire. All nanowire lengths in experimental results presented in this thesis are measured using the same method unless otherwise stated. From Figure 3.7 we found that the length of the nanowire is 150.8 pixels. Using the conversion factor 10.33 pixels per μm obtained from the stage micrometer (Section 2.5.2), we find the length of the nanowire, L .

$$L = \frac{150.8 \text{ pixels}}{10.33 \text{ pixels}/\mu\text{m}} = 14.6 \pm 0.3 \mu\text{m} \quad (3.6)$$

The error of these measurements comes mainly from how accurately one can pinpoint the ends of the nanowires, which is a consequence of the resolution of the camera. From the pictures, the edges of the nanowires are blurry up to 3 pixels, which give an error of $\pm 0.3 \mu\text{m}$.

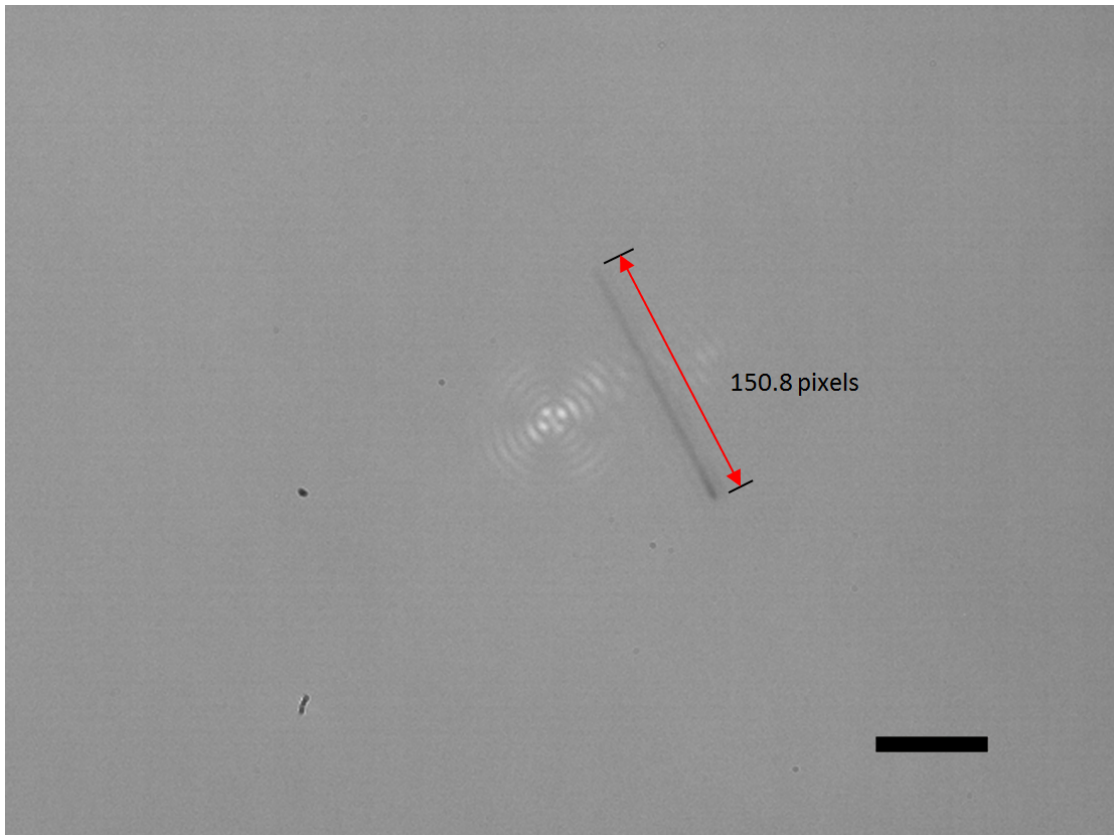


Figure 3.7: A photograph of a nanowire pushed against the cover slip of the sample slide. We know we are imaging the cover slip plane because we can see the scattering of the trapping laser off the cover slip. We then measure the length of the nanowire from the picture in pixels and convert it to real length. The black scale bar indicates $5 \mu\text{m}$.

3.3.5 Trap stiffness of optically trapped nanowires

Here I show an example of how the trap stiffness of a nanowire is measured and calculated. The trajectory of the trapped nanowire is measured using a QPD as described in Chapter 2 Section 2.9. To briefly recap, a nanowire is trapped and a detector response curve is measured. The nanowire is then tracked for 2 seconds with a sampling rate of 10 kHz. 5 sets of 2-second trajectories are recorded. After that, the nanowire is pushed to the cover slip of the sample chamber and a photo is taken so that the length of the nanowire can be measured. A power spectrum analysis [22] is performed on all the measured trajectories and averaged. The averaged power spectrum is then fitted to the equation

$$S \equiv \left\langle \frac{|\tilde{x}|^2}{T} \right\rangle = \frac{D/2\pi^2}{f_c^2 + f^2} \quad (3.7)$$

Figure 3.8 shows the power spectrum of a nanowire of length 4.8 μm . The dashed line represents the fit using Equation 3.7. The deviation of the experimental data from the fit at higher frequencies is due to the finite sampling rate of the detector. From the fit, we found the corner frequency, f_c to be 894 ± 9 Hz with 94 mW of trapping power. We can then use this to calculate the trap stiffness using the equation

$$\kappa_i = 2\pi\gamma_{\perp}f_c \quad (3.8)$$

where $\gamma_{\perp} = \frac{4\pi\eta_0L}{\ln(L/2a) + \delta_{\perp}}$ is the Stoke's drag for nanowires perpendicular to the trap axis

Hence, the trap stiffness of this nanowire with 94 mW of trapping power is found to be $\kappa = 55.7 \pm 2.4$ pN/ μm . Normalizing with respect to power gives us a normalized trap stiffness of 0.60 ± 0.10 pN $\mu\text{m}^{-1}\text{mW}^{-1}$.

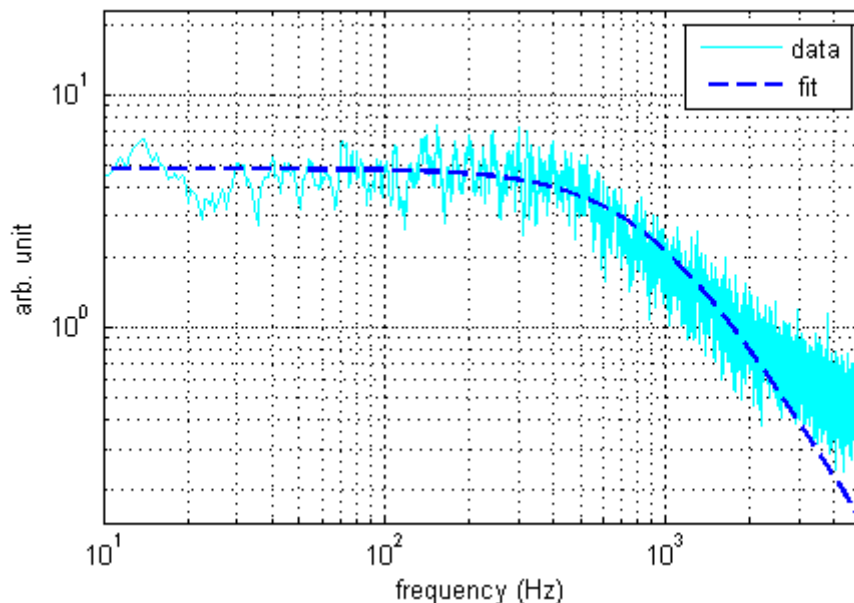


Figure 3.8: The power spectrum of a $4.8 \mu\text{m}$ nanowire in the trapped with 94 mW of optical power. The solid line represents experimental data while the dashed line corresponds to a Lorentzian curve which is fit to the data points. From the graph it can be seen that the equation fits the experimental data from 10 Hz to 2 kHz . The discrepancies at frequencies greater than 2 kHz are artefacts in the experimental data due to a finite sampling rate. This is a known effect as discussed in Berg-Sørensen and Flyvbjergs' work [22].

3.4 Length dependence of nanowire trapping

In this section I will talk about our study on how the trapping properties of optically trapped nanowires depend on their lengths. To do this study, we trap and measure the trap stiffness of nanowires as well as their lengths as explained in the previous section, and repeat for as many nanowires as can be found in the sample chamber. The results are shown in Figure 3.9.

From the plots of trap stiffness versus nanowire length we can see that the trap stiffness values falls into two distinct bands of different values. The average value for the points in the lower band is $0.71 \pm 0.24 \text{ pN}\mu\text{m}^{-1}\text{mW}^{-1}$, while the average of the points in the upper band is $2.02 \pm 0.20 \text{ pN}\mu\text{m}^{-1}\text{mW}^{-1}$. Furthermore, we see that within each band the trap stiffness of the nanowires is independent of the length of the nanowires. Recall that $\kappa_i = 2\pi\gamma_{\perp}f_c$ and $\gamma_{\perp} = 4\pi\eta_0L/\ln(L/2a) + \delta_{\perp}$, it follows that if κ_i is independent of length, f_c must be inversely proportional to length. This is exactly

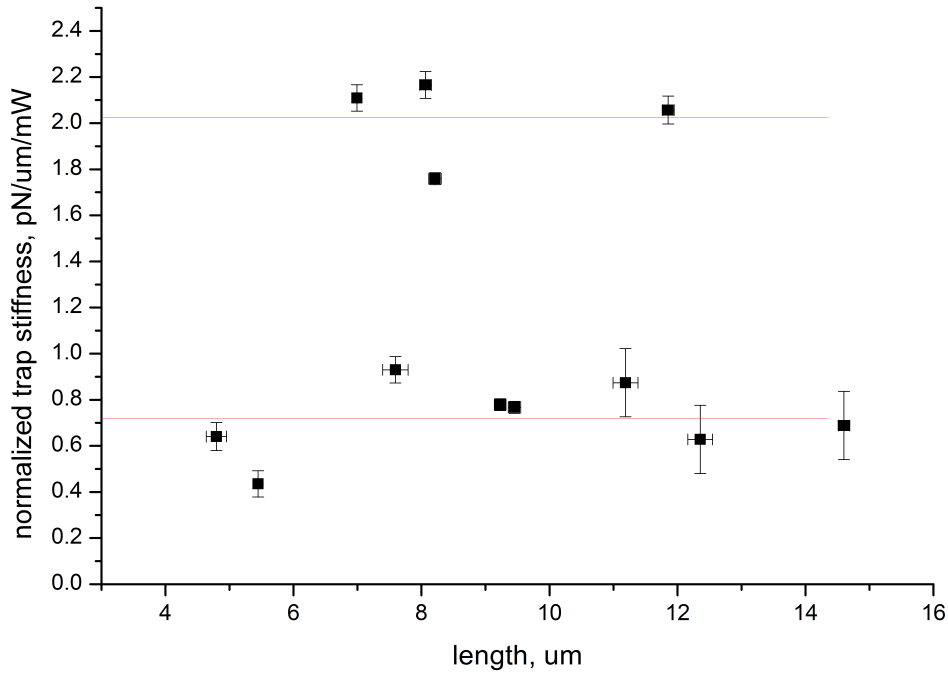


Figure 3.9: Plot of normalized trap stiffness versus nanowire length. We can see clearly that the trap stiffness values falls into two distinct bands. The red lines are the average values of the data points in the corresponding bands. The four points on the upper band corresponds to the nanowires with larger slopes in the calibration curves shown in Figure 3.11.

what we obtain from the experimental measurement of the corner frequency, f_c as shown in Figure 3.10 below.

Intuitively, one would expect that for a given trapping laser power, the trap stiffness of the optical trap would depend on the length of the trapped nanowires. However, the observed length independence may be rationalized by considering the depth of focus of the optical tweezers. As the length of the nanowires extends far beyond the depth of focus of the microscope objective ($\sim 1.0 \mu\text{m}$), but with the gradient forces only dominate within the depth of focus, any extension on the nanowire length which protrudes several wavelengths from the focus in the axial direction will have a minimal contribution to increases in trapping forces.

To understand why there are two distinct bands of trap stiffness values, we went back and examined the detector response curves for these nanowires shown in Figure 3.11. From the plot, we see that the curves are linear over $\pm 80 \text{ nm}$ from the trap centre as expected. The curves can also be resolved into two discrete groups of similar

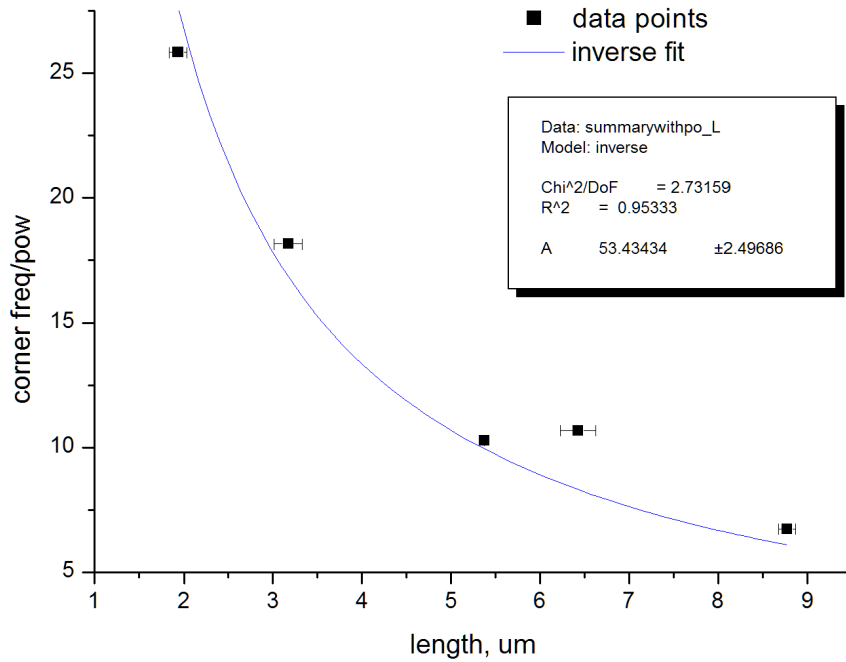


Figure 3.10: The plot of corner frequency per trapping versus nanowire length. The dots represent the data points and the solid line is an inverse fit.

gradients with an average gradient of $1.2 \pm 0.2 \text{ nm}^{-1}$ and $0.3 \pm 0.1 \text{ nm}^{-1}$ respectively. These groupings appear to be independent of the lengths of the nanowires. One possible explanation of this grouping is that different numbers of nanowires are simultaneously trapped in the optical tweezers, causing a different interaction volume with the optical trap leading to a different detector response. Furthermore, the detector response curves which fall into the group of a larger gradient correspond to the nanowires with trap stiffness on the upper band in Figure 3.9.

Thus we conclude that the bands in trap stiffness values are due to a different number of nanowires within the optical trap. When there is more than one nanowire in the optical trap, the interaction volume with the optical trap increases causing a larger gradient in the detector response curve and larger trap stiffness. However, within each band of constant trap stiffness the interaction volume between the nanowire and the optical trap remains constant regardless of nanowire length; hence the detector response curves and trap stiffness are independent from the lengths of the nanowires.

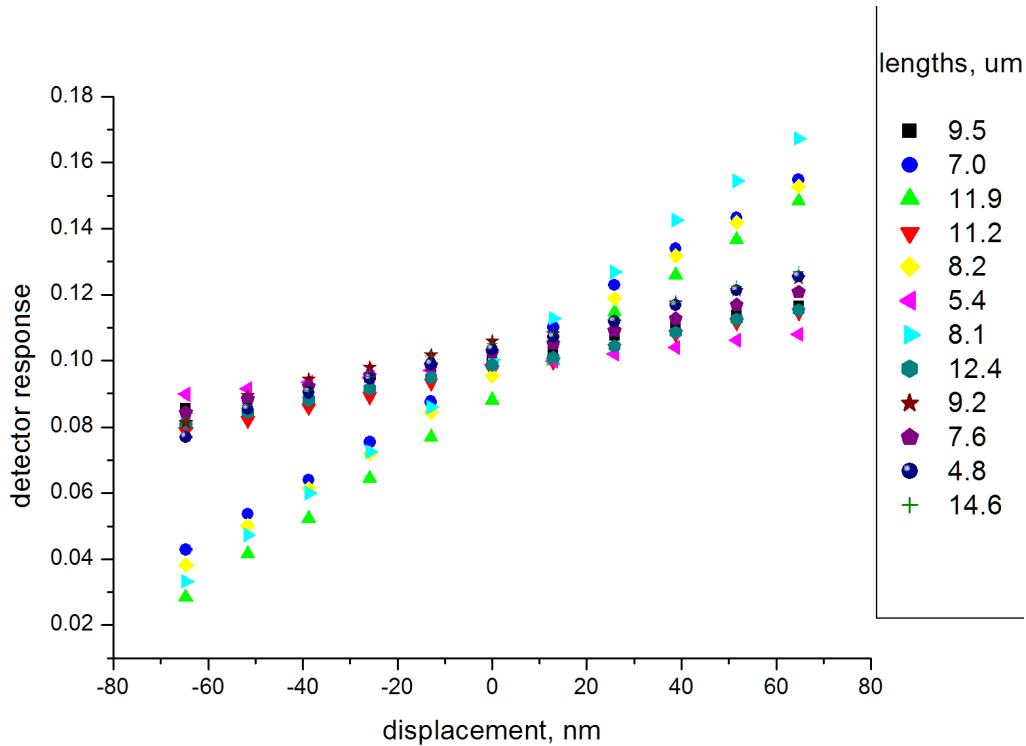


Figure 3.11: Calibration curves of a set of nanowires of different length. We can see clearly that the slopes of the calibration curves falls into to distinct groups of different slopes.

3.5 Stable axial trapping position

Unlike spherical objects, the elongated axial dimension of nanowires leads to some interesting trapping properties. Cao *et al.* [31] numerically calculated the preferred orientation of optically trapped micro cylinders and nanowires with a range of different radii and lengths, for both linearly and circularly polarised traps (Figure 3.12). Elongated objects of lengths smaller than the depth of focus of the trapping objective tend to align along the polarization of the optical field due to higher polarizability along the symmetry axis [31], while longer nanowires tend to align to the optical axis to maximize the overlap between the trapped particle and the incident field for minimizing potential energy [31, 32]. The preferred trapping orientations lead to a restricted range of possible trapping scenarios, beyond which stable trapping is not possible.

Additionally, simulations [3, 7] and experiments [3] done by Simpson *et al.* show that optically trapped cylinders with zero tapering are very weakly confined along the axis of the cylinder except for the two ends of the cylinder, as indicated by the red solid

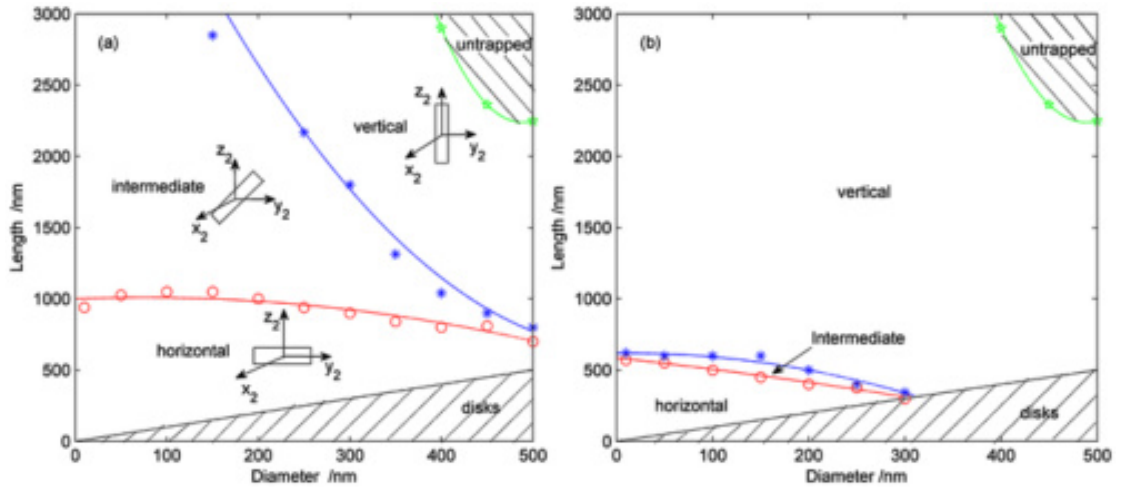


Figure 3.12: Orientations landscapes of nanowires and micro cylinders in (a) linearly polarized and (b) circularly polarized beams. The coordinate system is Cartesian coordinate system centred at cylinder position. The rectangular shapes in (a) show the orientations of cylinders in each region. Four regimes in the orientation landscapes are the untrapped region, vertical region, horizontal region, and the intermediate region between the vertical and horizontal regions. The red circles mark the longest nanowire or micro cylinder trapped horizontally for each diameter. The blue asterisks represent the shortest nanowire or micro cylinder trapped vertically for each diameter. The green points indicate the longest nanowire or micro cylinder for each diameter that can be trapped (vertically). Figure adopted from Cao *et al* [31].

curves in Figure 3.14. The rise in axial force at two points along the curve indicated by the maxima (and minima in the opposite direction) is due to the tips of the cylinder intersecting the high intensity part of the trapping beam. However, the addition of a tapering angle on the cylinders introduces an axial force that tends to drive the equilibrium trapping point towards the base of the conical cylinder (where the radius is larger) [3, 7] as shown in Figure 3.13. The effects of a range of tapering angle on the axial force is also calculated by Simpson *et al.* [7] and shown in Figure 3.14.

Based on previous study done by our group, the equilibrium trapping position of indium phosphide (InP) nanowires have been determined to be near one end, with the major segment of the length sitting below the trap far from their centre of mass [33]. This is measured by the micro-photoluminescence (μ -PL) mapping of the axial profile of the nanowire. A trapped nanowire is axially scanned across a fixed 514nm excitation source and the resulting PL is collected by a spectrometer and CCD camera. When the tip of the nanowire is scanned past the excitation source, the PL intensity decreases and eventually drops to zero when the nanowire tip is beyond the excitation source (Figure 3.15).

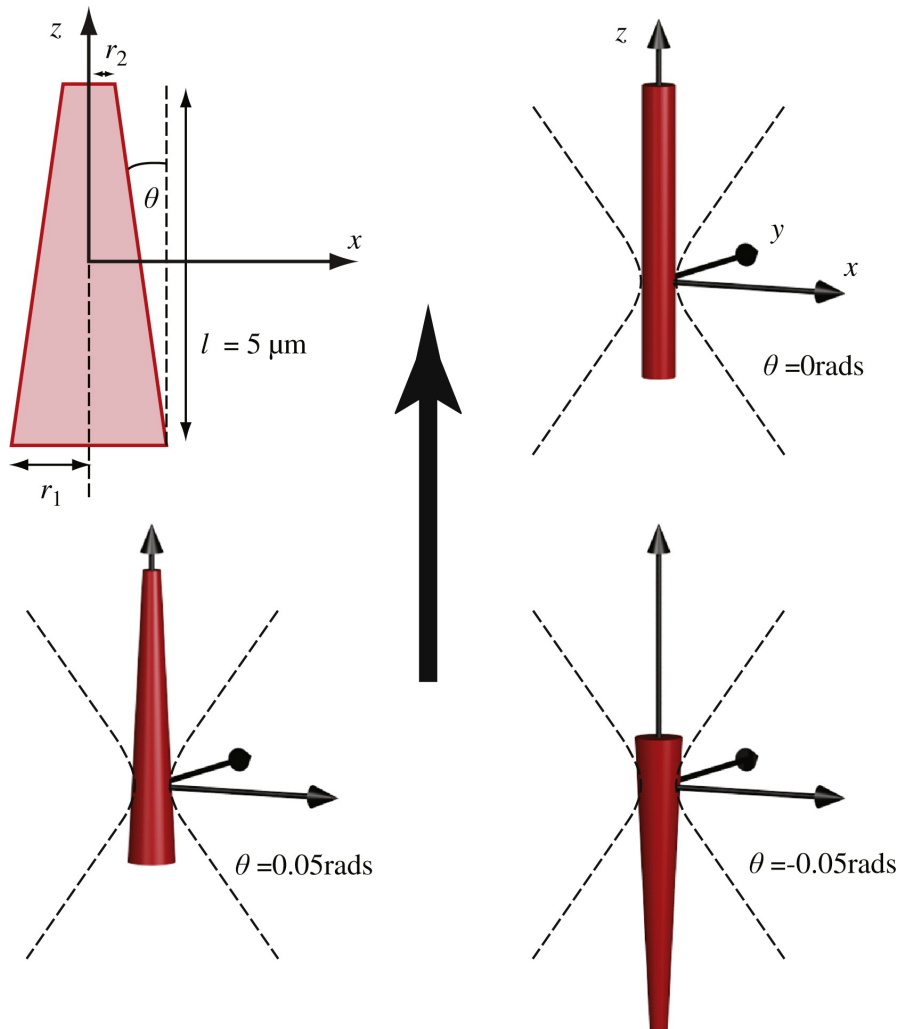


Figure 3.13: The trapping geometry of a vertically trapped cylinder with tapering. Figure adopted from Simpson *et al* [7]. Reprinted from [7], copyright 2013, with permission from Elsevier.

This allows us to work out the distance between the equilibrium trapping point and the tips of the nanowire. Furthermore, we also found that optically trapped nanowires are aligned closely to the optical axis of the tweezers and experience small perturbations from the equilibrium point. These experimental results from the measurement of our indium phosphide (InP) nanowires are qualitatively consistent with the theoretical predictions discussed above, despite differences in a few modelling parameters such as refractive index and taper angle. We believe the fact that these nanowires being trapped vertically near one of the tips will have implications on the resonant behaviour addressed in the next section.

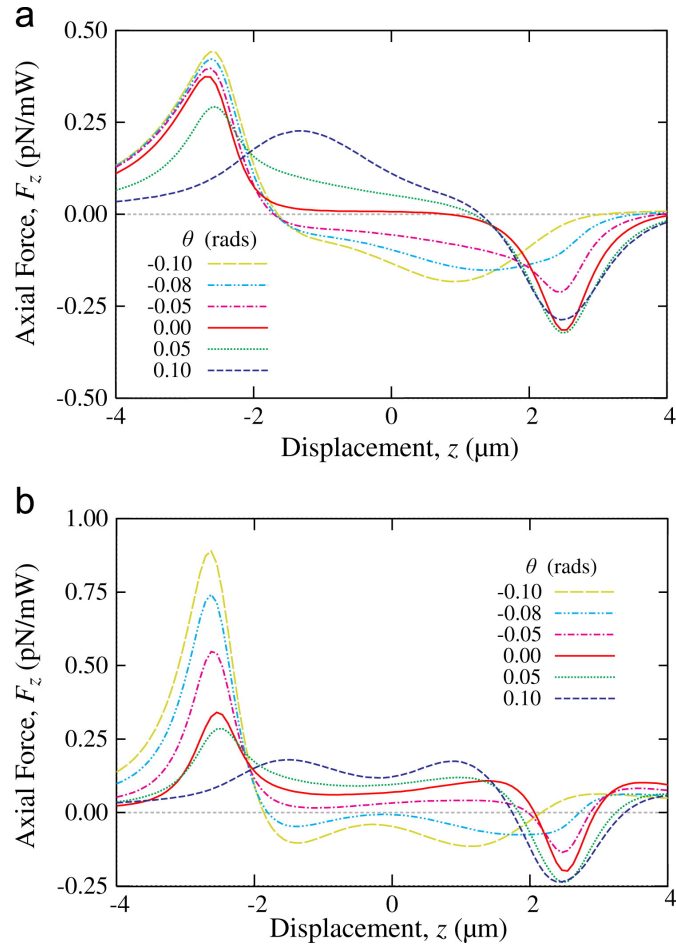


Figure 3.14: The variation in axial force, F_z with vertical position, z for tapers with different opening angle, θ , and two refractive indices. The relative refractive index for (a) and (b) are 1.1 and 1.2 respectively. Figure adopted from Simpson *et al* [7]. Reprinted from [7], copyright 2013, with permission from Elsevier.

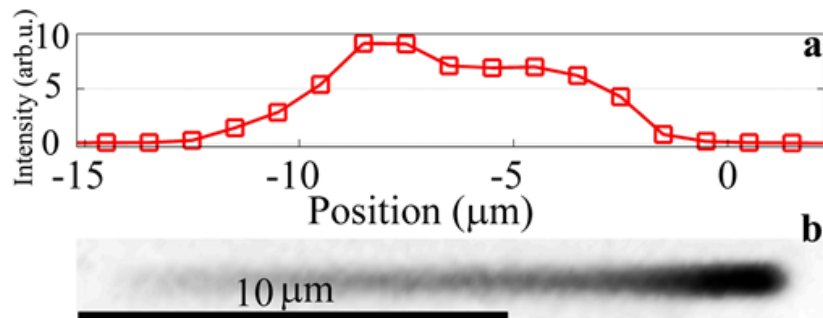


Figure 3.15: (a) The micro-photoluminescence intensity distribution from a trapped nanowire along the axial direction. The origin of the x-axis is defined by the fixed position of the focus of the 514nm excitation laser. Positive values indicate the length of nanowire from the excitation laser focus in the direction of propagation of the trapping laser. (b) Bright field image of the nanowire.

3.6 Resonant behaviour of optically trapped nanowires

Whilst the simple approximation of treating any optically trapped object as a simple overdamped harmonic oscillator provides an accurate description for a large class of optical trapping experiments, it also masks a more complex optical potential that includes both conservative and non-conservative components. The introduction of more complex hydrodynamic interactions, trap geometry, and particle geometry leads to new dynamic behaviour. For example, spherical objects can exhibit resonance behaviour when the trap is underdamped [34–36] with emergence of a resonant peak as the trapping conditions transition from over- to underdamped oscillations [35]. In terms of trap geometry, rotation of the trapped particle may also be caused by manipulating the angular momentum of the trapping laser such as the use of the Laguerre-Gaussian beam [37, 38]. As for particle geometry, it has been shown that birefringence in particle shape, form or composition leads to optical torque driven rotation [39, 40]. It has also been shown that a combination of two or more of the above factors will lead to anomalous trapping dynamics as well, such as Arita’s [41] demonstration of rotational motion (up to 5MHz) of a trapped birefringent particle in an underdamped environment using circularly polarized light, where rotational and translation modes become coupled.

Objects with high aspect ratios ($>100:1$) such as nanowires represent a specific case of complex particle geometry amongst optically trapped objects. There have been a number of optical trapping experiments [1, 42] and calculations [31, 42–44] on high aspect ratio elongated objects. It is established that an elongated object within an optical field is sensitive to the polarization and intensity gradient of the incident optical field [31, 32, 45]. In the context of Brownian dynamics, the asymmetry of elongated objects leads to complex dynamical behaviour: in addition to three translational degrees of freedom, a trapped nanowire or nanorod may also undergo angular fluctuations [26]. The rotational dynamics may be sufficiently weak to lead to uncoupled Brownian motion, however under certain conditions coupling between degrees of freedom may lead to anomalous behaviour. For instance, Simpson and Hanna showed through calculations the emergence of cyclic motion due to the non-conservative nature of optical forces when non-spherical particles are trapped within a linearly polarized Gaussian beam trap [45]. This is seen experimentally in Pauzauskis’s demonstration of oscillations in optically trapped SnO_2 ribbons [19] and Neves’s demonstration of low frequency rotation at high tilt angle of trapped polymer nanofibres in linearly polarized Gaussian beam optical traps [42].

Our interests lie in experimental investigations of optically trapped InP nanowires, which are weakly tapered cylindrical nanowires of uniform composition and refractive index profile, held in a linearly polarized, gradient force optical tweezers. Detailed description of the measurement procedures are previously presented in Chapter 2 Section 2.9. To briefly recap, a nanowire is trapped and a detector response curve is measured. The nanowire is then tracked for 2 seconds with a sampling rate of 10 kHz. 5 sets of 2-second trajectories are recorded. After that, the nanowire is pushed to the cover slip of the sample chamber and a photo is taken so that the length of the nanowire can be measured. The power spectrum of the trajectory of a nanowire exhibiting resonant behaviour is shown by the blue curve in Figure 3.16. On the same plot is a power spectrum of a nanowire without a pronounced resonant behaviour and a fit to Equation 3.7 for comparison.

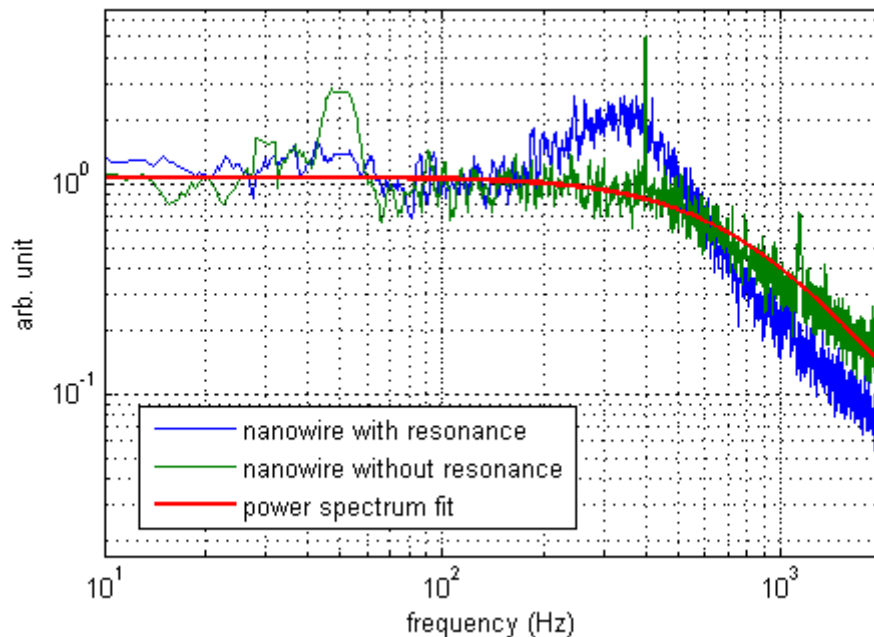


Figure 3.16: The blue curve represents the power spectrum of a trapped nanowire showing resonant oscillations, the green curve shows the power spectrum of the same trapped nanowire without resonance and the red curve is a Lorentzian fit to the green curve. The resonance peak is only observed when the nanowire is trapped at $50\ \mu\text{m}$ from the cover slip, while trapping at distances greater or less than $50\ \mu\text{m}$ only result in power spectrum curves without resonance peaks.

In particular, a broad resonant peak in the power spectrum is observed at around 500 Hz, and only persists as the nanowire is trapped at a critical distance of about $50\ \mu\text{m}$ from the cover slip. We note that the trapped nanowire is observed on the video camera

(see section 3.3.2 above in this chapter) throughout the duration of measurement and is observed to remain vertically trapped with minimal tilt throughout the measurement duration. The effect of changing trap height on the resonance peak will be examined in the next section. This resonance behaviour is also reflected in the autocorrelation function of the nanowire trajectory, where a fluctuation between positive and negative correlation can be seen in Figure 3.17. Also shown in Figure 3.17 is the autocorrelation function of the same nanowire when the resonance behaviour is suppressed; the resulting curve is an exponential decay as expected.

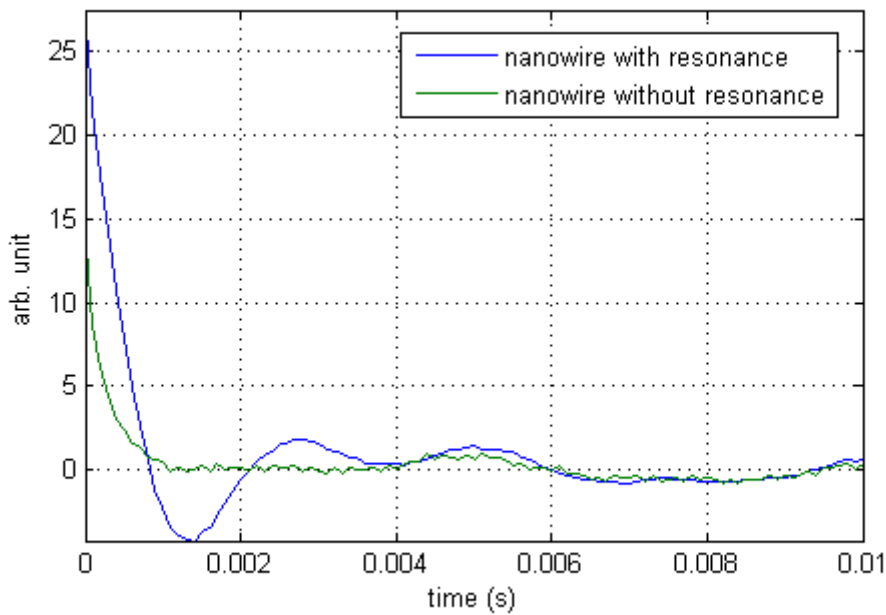


Figure 3.17: Autocorrelation function of the same nanowire presented in Figure 3.16.

The emergence of this resonant peak cannot be accounted for in the conventional power spectrum analysis method for optical tweezers, hence a more detailed analysis is required to understand our results. Furthermore, our system is unique in comparison to Pauzauskis's [19] and Neves's [42] demonstration of nanofibre rotations because in our system a linearly polarised Gaussian beam is used to generate oscillating behaviour of up to hundreds of Hz, while the tilt angle of the oscillating nanowire remained small. The refractive index of our InP nanowires are also much greater than the refractive index of the nanofibres used in either case.

Although the shape of the curves is quite characteristic of underdamped motion as seen in Di Leonardo's experiments involving the trapping of aerosols [35], we rule out the underdamped Langevin equation and any theories involving inertial effects because our experiments are performed in a low Reynolds number environment where inertial effects are heavily suppressed.

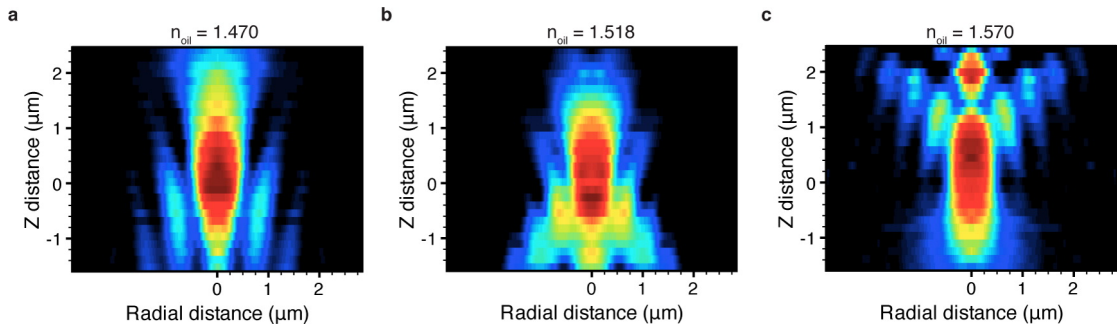
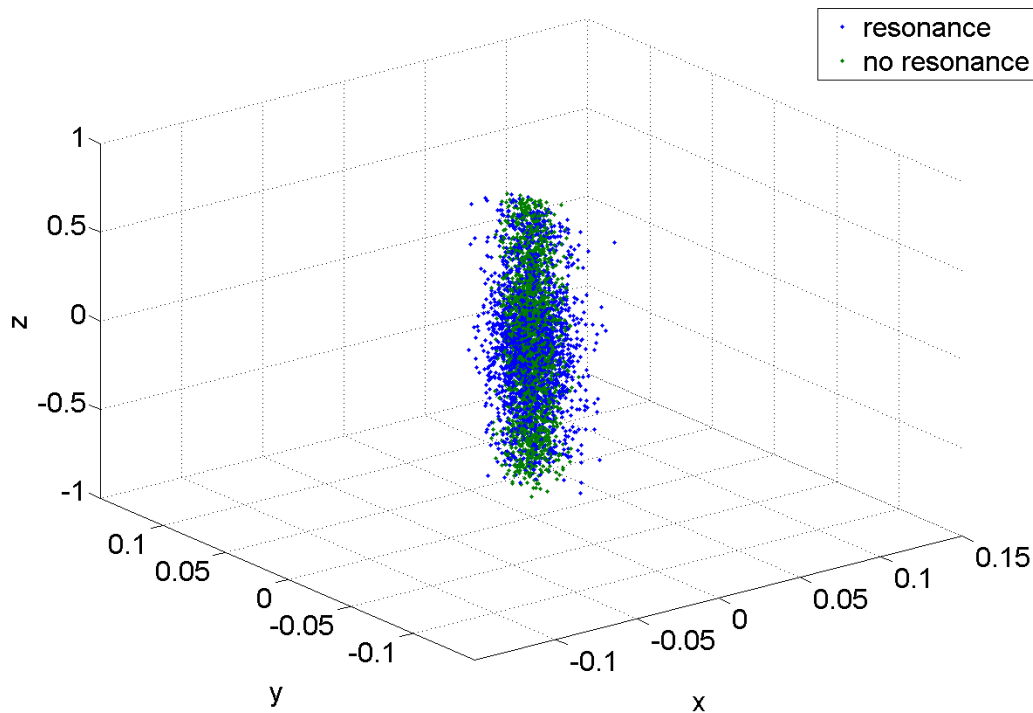


Figure 3.18: Mappings of focal intensity above the coverslip surface via a 1.4NA oil immersion objective and immersion media with different refractive indices. In all cases, there exist regions of local intensity maxima where optical trapping can occur. Figure adopted from [46]. Reprinted with permission from [46], copyright 2013 American Chemical Society.

Recently, Kyrsting *et al.* mapped the 3D focal intensity of optical tweezers and found that spherical aberrations due to refractive index mismatch between immersion oil and trapping medium affects the focal intensity distribution, which leads to regions of local maxima outside the main focal point where trapping can occur [46] (Figure 3.18). The nanowire experiencing Kramer's hopping between these regions of high laser intensity might lead to resonant behaviours. For this to be true, we would expect the position distribution of the nanowire within the trap to be clustered into multiple discrete regions where the laser intensity is a local maxima and the nanowire can be stably trapped. However, this possible explanation is shown to be false on the basis of one smooth Gaussian distribution over all translational displacements of the trapped nanowire, shown in Figure 3.19.



(a) 3-D plot

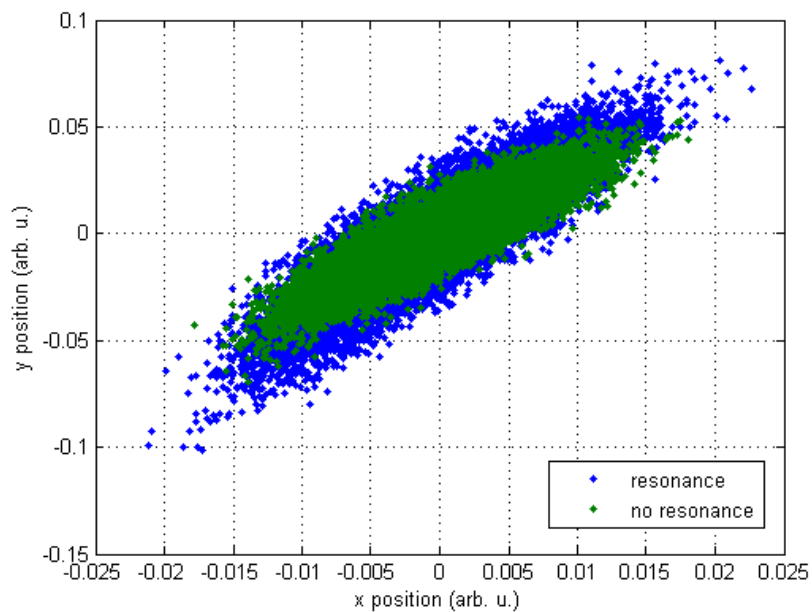
(b) xy projection

Figure 3.19: (a) A 3-D plot and (b) an xy projection of the trajectory of an optically trapped nanowire with resonant (blue) and no resonant (green) behaviours. From the plots it can be seen that the distribution of the trapped particle varies smoothly indicating a single trapping site. It should also be noted that the nanowire fluctuates in larger amplitudes when it is under resonance.

3.7 Winding number analysis

To further understand the resonant behaviour observed in optically trapped nanowires, we perform a winding number analysis on the trajectory of these nanowires.

3.7.1 Introduction to the winding number analysis

The winding number, ω of a closed-loop trajectory is the number of counter-clockwise turns the path travels around a reference point on a plane. From a mathematical stand point, if the trajectory is defined by a parametric equation in polar coordinates, $(r(t), \theta(t))$ for $0 \leq t \leq 1$, then the winding number, ω is an integer number given as

$$\omega = \frac{\theta(1) - \theta(0)}{2\pi} \quad (3.9)$$

This is because the angular coordinate, $\theta(t)$, must differ by an integer multiple of 2π between $t = 0$ and $t = 1$ if the trajectory is closed.

Experimentally, given a set of measured coordinates $\{x_i, y_i\}$ where $i = 0, 1, \dots, N$ for N measurement points, the easiest way to obtain the winding number (around the origin) is by considering the crossings of the positive x axis. If the trajectory crosses the x axis from negative y to positive y then add one to the winding number; if it crosses from positive y to negative y then take one away from the winding number. Given a set of data points, the first order interpolation of the trajectory is found by simply joining the points with straight lines. Then, we need to find the point of intersection between the x axis and the trajectory. Given any two points (x_i, y_i) , and (x_{i+1}, y_{i+1}) , the equation of the line joining the points is

$$y = y_i + \frac{(y_{i+1} - y_i)}{(x_{i+1} - x_i)}(x - x_i) \quad (3.10)$$

Hence, the line will intersect the x axis at

$$x_i^* = x_i - \frac{(x_{i+1} - x_i)}{(y_{i+1} - y_i)}(y_i) \quad (3.11)$$

To avoid the case when $y_{i+1} - y_i = 0$, we multiply through by $(y_{i+1} - y_i)^2$ to obtain

$$x_i^* (y_{i+1} - y_i)^2 = x_i (y_{i+1} - y_i)^2 - (x_{i+1} - x_i) (y_{i+1} - y_i) (y_i) \quad (3.12)$$

Where if $x_i^* > 0$, then $x_i^* (y_{i+1} - y_i)^2 > 0$ as well.

```
Set count = 0
for i = 1..n-1,
    if x(i)*(y(i+1) - y(i))^2 - y(i)*(x(i+1) - x(i))*(y(i+1) - y(i)) > 0 then
        if y(i) < 0 and y(i+1) > 0 then
            count(i+1) = count(i) + 1

        else if y(i) > 0 and y(i+1) < 0 then
            count(i+1) = count(i) - 1
    else
        count(i+1) = count(i)
    end if

Winding Number = count(n)
```

A pseudo code for calculating the winding number can be written as shown above while an example trajectory is plotted in Figure 3.20 below, where the starting point is circled in red. In this example, the trajectory crosses the positive x axis twice in the counter-clockwise direction so the winding number is 2.

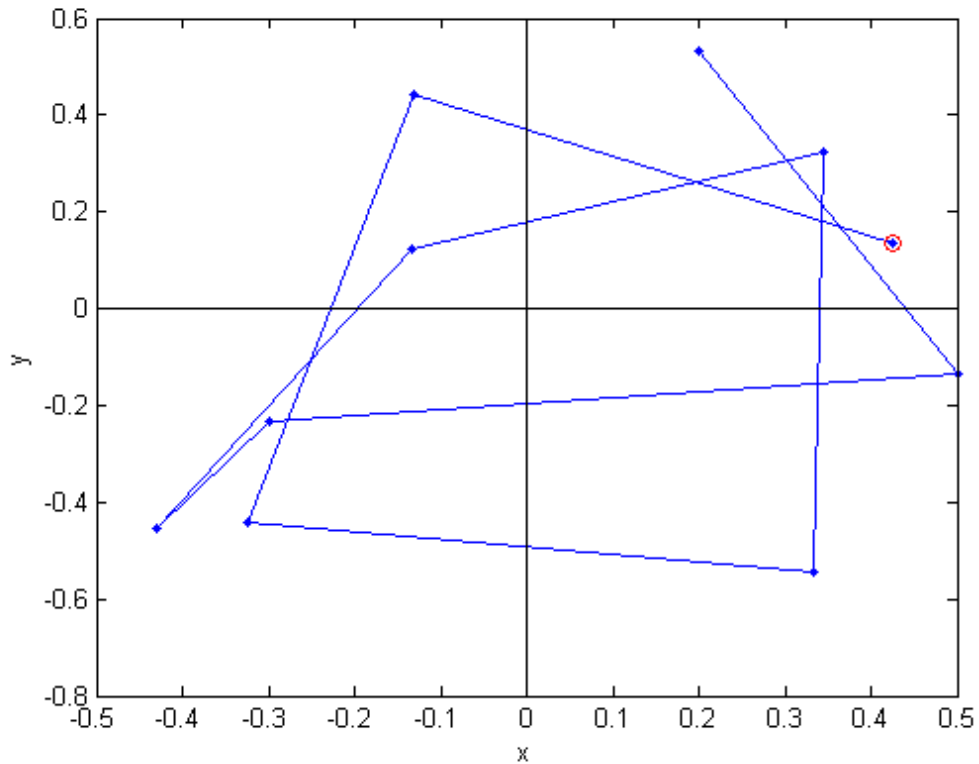


Figure 3.20: Example trajectory with a winding number of 2. From the plot we can see that the trajectory (starting from the point circled red) crosses the positive x axis twice in the counter clockwise direction.

3.7.2 Application of the winding number analysis on optically trapped nanowire trajectory

The winding number analysis is applied to the same set of trajectory data of nanowires presented in Figure 3.16, 3.17, and 3.19 and the resulting plot is shown in Figure 3.21. From the plot, it can be seen that although there are some fluctuations in the winding number, the net effect is an increase in the number of turns in one direction over time. An explanation for these results is that the net increase in winding number implies that there is a bias towards cyclic motion, while fluctuations in the winding number indicate that this cyclic motion is modulated by Brownian fluctuations. The winding number has a larger rate of increase in the case when a resonant peak is observed, implying a higher number of turns and stronger rotational motion.

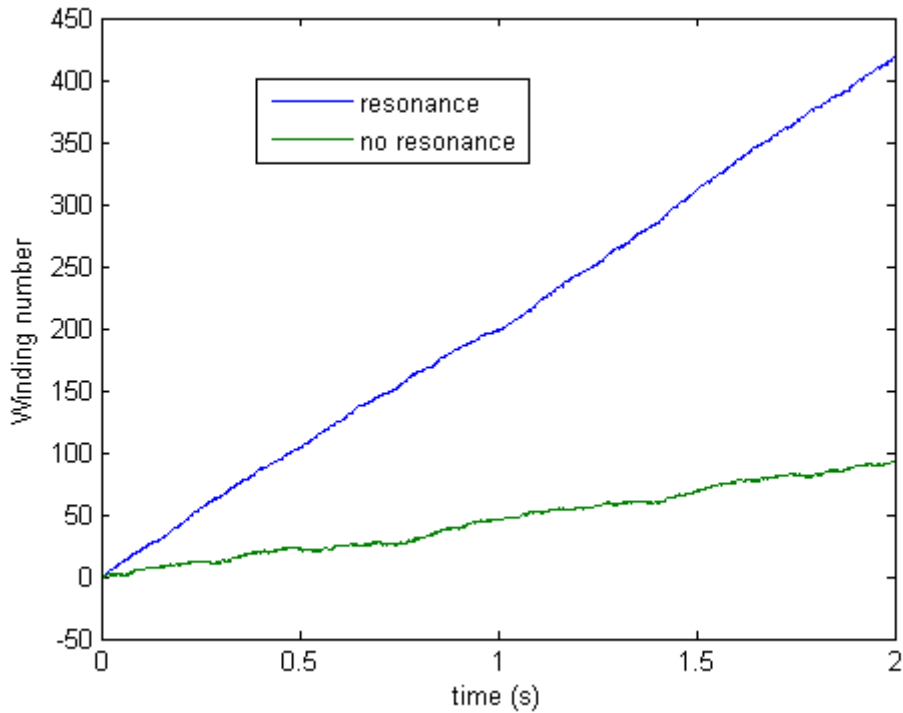


Figure 3.21: The winding number of the same set of trajectory data of nanowires presented in Figure 3.16, 3.17, and 3.19. The nanowire with a resonance peak in the power spectrum shows a larger rate of increase in winding number compared to the nanowire without a resonance peak. The increasing winding number for both cases implies that the nanowire is undergoing cyclic motion within the trap, while a larger increase in winding number for the nanowire under resonance indicates that the cyclic motion occurs in a higher frequency than when it is non-resonant.

3.8 Height dependence of nanowire resonance

For this study, a nanowire of $5\ \mu\text{m}$ is trapped at $10\ \mu\text{m}$ away from the coverslip and the trajectory measured using a QPD as explained in Section 3.3.5. We then measured the trajectory of the same nanowire at up to $80\ \mu\text{m}$ from the cover slip in steps of $10\ \mu\text{m}$. We then move the nanowire back to $50\ \mu\text{m}$ in steps of $10\ \mu\text{m}$, and measured the trajectory at every $10\ \mu\text{m}$ decrease. We then perform a power spectrum analysis and winding number analysis on all trajectory data and the results are presented in Figure 3.23 and Figure 3.22 below.

From Figure 3.23 we can see that a resonance peak at $350\ \text{Hz}$ is visible in all 3 axes at trapping height $50\ \mu\text{m}$ and $60\ \mu\text{m}$, but vanishes when the nanowire is trapped at heights far above or below $50\ \mu\text{m}$. We note that changing the height of the trap will

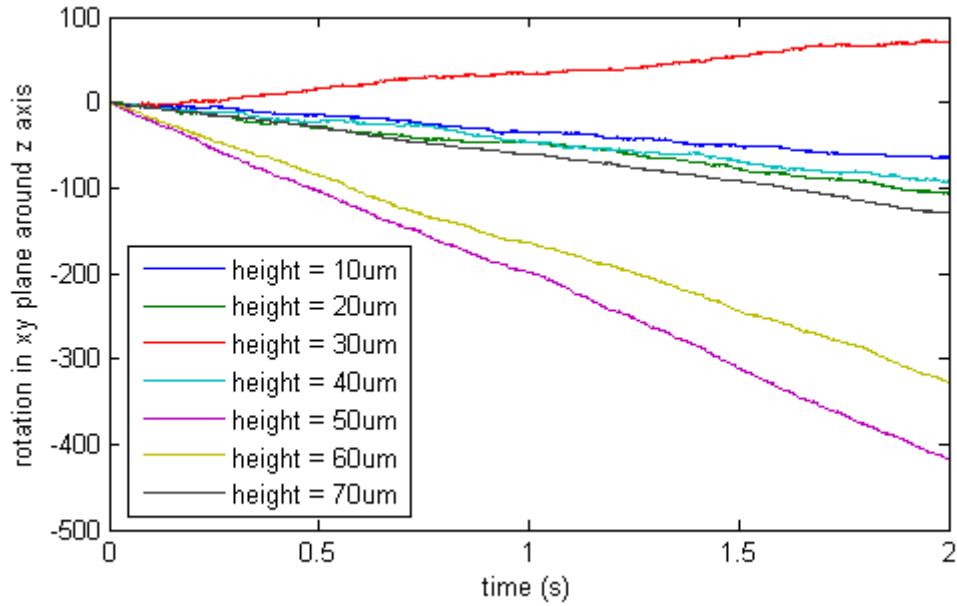
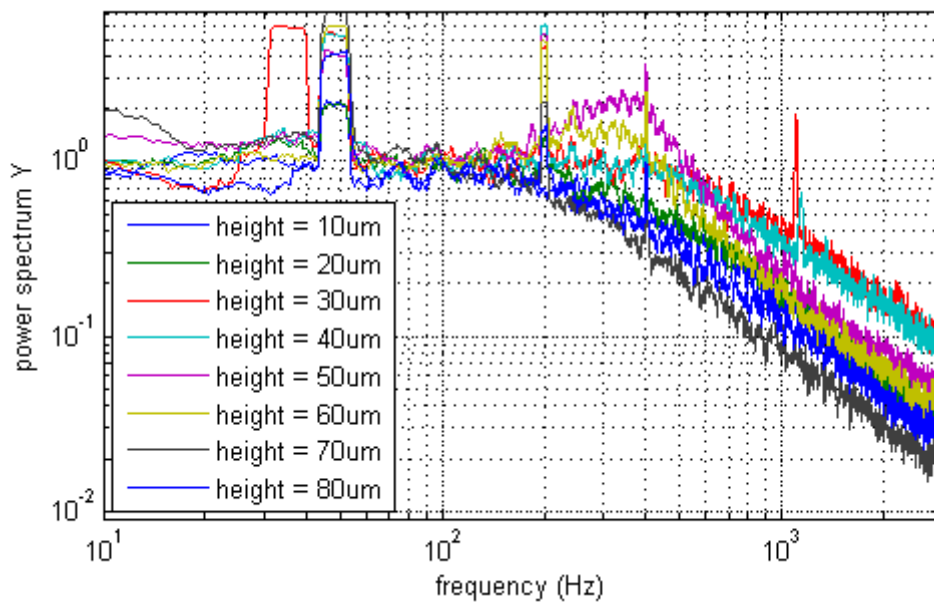
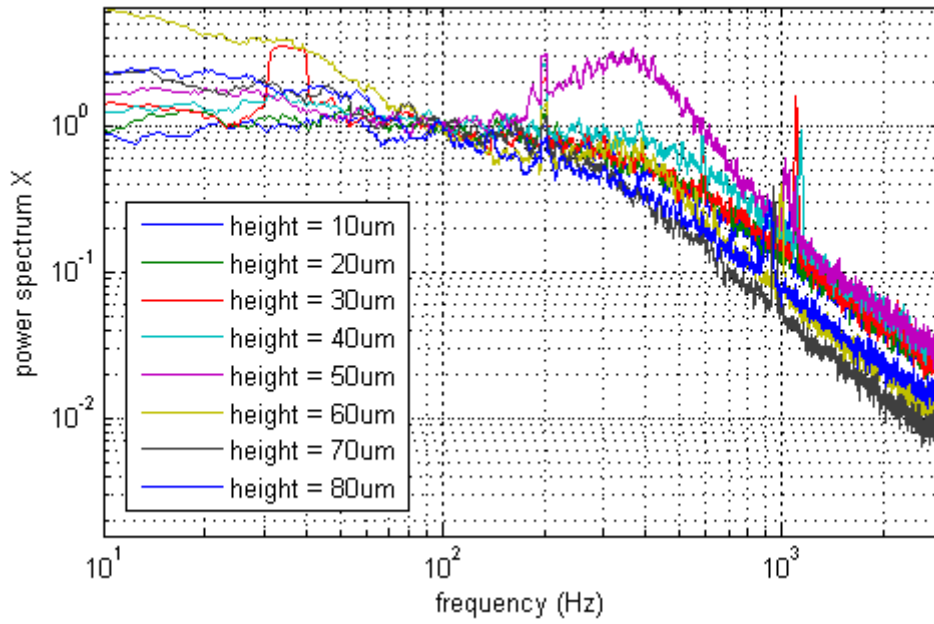


Figure 3.22: The winding number of the trajectories data of a nanowire trapped at $10 \mu\text{m}$ - $80 \mu\text{m}$ away from the cover slip. The winding number has the largest amplitude when the nanowire is trapped at $50 \mu\text{m}$ when the resonance peak is the greatest.

induce spherical aberrations and accentuate other aberrations already present within the trap. Increased aberrations will change the relative contributions from gradient and scattering forces for a given fixed input power, and we hypothesise that this is the origin of the height dependence of the resonance. However, the emergence of the resonant peak itself cannot be accounted for in the conventional power spectrum analysis method for optical tweezers, and to understand this phenomenon we develop a more detailed analysis in the next section (Section 3.9).



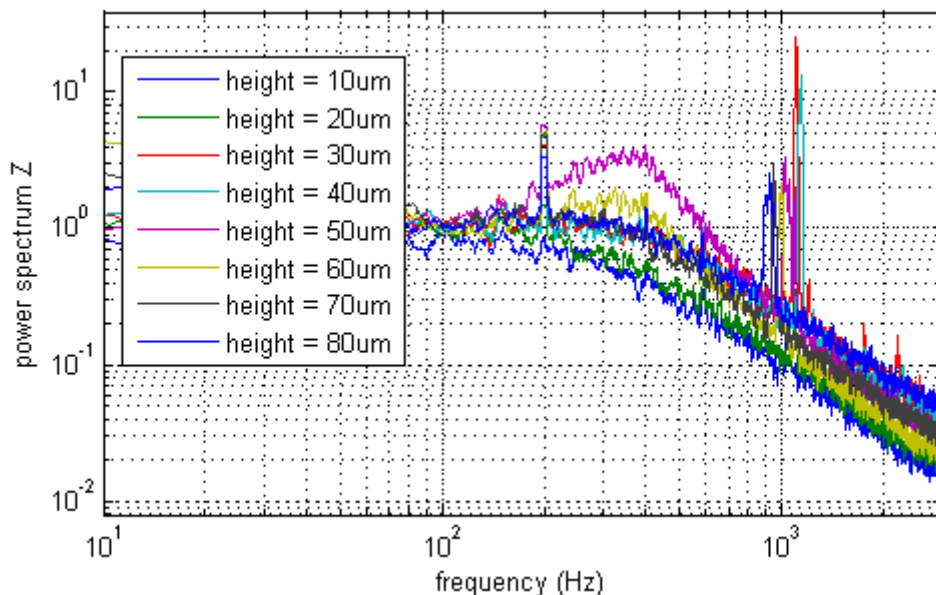


Figure 3.23: Power spectra of the trajectories of a nanowire trapped at $10\ \mu\text{m}$ - $80\ \mu\text{m}$ away from the cover slip in the (a) x -axis, (b) y -axis and (c) z -axis. A resonance peak at $350\ \text{Hz}$ is visible in all 3 axes at trapping height $50\ \mu\text{m}$ and $60\ \mu\text{m}$. When the nanowire is trapped at heights far above or below $50\ \mu\text{m}$, the resonance peak vanishes.

3.9 Expansion of the power spectral analysis method

Simpson and Hanna predicted the emergence of cyclic motion in optically trapped rods due to the interaction of non-conservative optical scattering forces which induces coupling between translations perpendicular to the long axis and rotation about axes perpendicular to both the long axis and translation direction [45]. In this study, it is shown that the occurrence of non-conservative motion depends on the symmetry of the stiffness matrix K ; if K is non-symmetric, the motion is non-conservative and there will be a bias toward cyclic motion between coupled coordinates. This is a shape induced effect which is only observable in low symmetry particles.

Recall from Section 3.2 we have treated the translational and rotational degrees of freedom separately, but this is insufficient for our system as it does not predict the resonance peaks that we measured. In order to account for the emergence of the resonant peak observed in our experiments we consider a more general form of the equations of motion which include cross-coupling terms and a non-symmetric stiffness matrix, K .

The dynamical equations in an over-damped environment can be written as a single 5-coordinate vector equation in terms of the generalized forces (neglecting rotation around the z -axis due to symmetry):

$$-\Gamma \dot{\vec{q}} + \vec{\zeta}(t) - K\vec{q} = \vec{0} \quad (3.13)$$

Where $\vec{q} = (x, \theta_y, y, \theta_x, z)$ are the generalised coordinates, Γ is the hydrodynamic drag matrix, $\vec{\zeta}(t)$ is the generalised noise term with $\langle \zeta_i(t) \zeta_i(t + \tau) \rangle = 2k_b T \gamma_i \eta(\tau)$ where γ_i is given in Equation 3.5 and K is the trap stiffness matrix given by:

$$K = \begin{pmatrix} K_{x,x} & K_{x,\theta_y} & 0 & 0 & 0 \\ K_{\theta_y,x} & K_{\theta_y,\theta_y} & 0 & 0 & 0 \\ 0 & 0 & K_{y,y} & K_{y,\theta_x} & 0 \\ 0 & 0 & K_{\theta_x,y} & K_{\theta_x,\theta_x} & 0 \\ 0 & 0 & 0 & 0 & K_{z,z} \end{pmatrix} \quad (3.14)$$

In this construction, we only include off diagonal terms that couple between translation and rotation within a plane, i.e. a translation in x will induce a rotation in the xz plane. This is justified as the non-conservative forces driving the coupling are principally directed along the z -axis and thus should induce rotation around the orthogonal axis. The above-mentioned approximations leads to two coupled equations of motion that retain the non-conservative effects, and that can be treated independently. An analysis of the two-coordinate stochastic equations leads to a power spectral density for each coupled coordinate (e.g. $i = x, \theta_y$) that has the form [47]

$$S_i(\omega) = \frac{\eta_i \omega^2 + \alpha_i}{2\pi \left((\omega^2 - \epsilon)^2 + (\mu\omega)^2 \right)} \quad (3.15)$$

where μ and ϵ are the respective trace and determinant of the matrix $M = \Gamma^{-1}K$, and η_i is associated with the noise strength. The term $\alpha_x = \eta_x m_{\theta_y}^2 + \eta_{\theta_y} m_{x\theta_y}^2$ is related to the cross-coupling matrix elements in M . In interpreting the solution in terms of the experimental system we note that if the coupling relates to the non-conservative scattering force, the off-axis components of the stiffness matrix should be non-symmetric, e.g. $K_{\theta_y,x} \neq K_{x,\theta_y}$. The form of the power spectral density is similar to that of an underdamped harmonic oscillator, such as is observed in aerosol tweezing experiments

[35, 36]. This is to be expected as both represent coupled first order differential equations; in the case of the underdamped oscillator coupling is between restoring and inertial terms, whilst in the present case it is between translation and rotation.

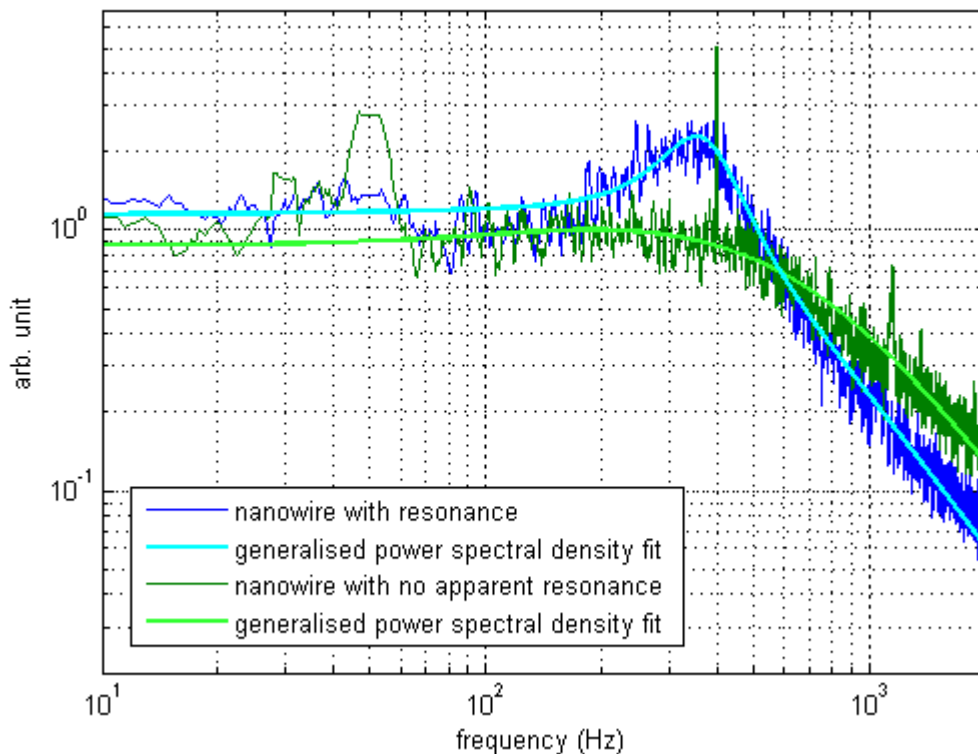


Figure 3.24: The blue curve represents the power spectrum of a trapped nanowire showing resonant oscillations while the dark green curve shows the power spectrum of the same trapped nanowire with no apparent resonance. Both the light blue and light green curves are fits using the generalised power spectral density equation, Equation 3.15. The fit on the data with no apparent resonance indicates a strongly suppressed peak at a similar frequency.

A fit of the power spectrum presenting the resonant peak in Figure 3.24 using Equation 3.15 (blue curves) shows excellent agreement with the experimental data presented in Figure 3.16. In fitting the data we apply an additional offset to account for detector noise. Indeed a fit of the data taken at the lower trapping height also reveals a strongly suppressed peak at a similar frequency (green curves).

The main features of the fitting function include the resonance peak frequency squared (ϵ) and peak frequency width (μ), the low frequency plateau given by $\alpha/2\pi\epsilon^2$, and a peak amplitude, $(\eta\epsilon^2 + \alpha)/2\pi\mu^2\epsilon^2$. From the fits, we extract $\mu = 366 \pm 5$ Hz, $\epsilon = (1.46 \pm 0.25) \times 10^5$ Hz² and the peak frequency is $f_{\text{peak}} = \sqrt{\epsilon} = 382 \pm 5$ Hz

for the case when the resonance peak is strongly present. On inspecting the fitting parameters between the different trapping heights we make the important empirical observation that a non-zero resonance peak is only observed under conditions where one of the cross-coupling terms is negative. Such a scenario is ensured in this system as the trapping point is far from the centre of rotation - the action of rotation under Brownian motion induces a translation at the trapping point which is in the opposite direction to the associated restoring force.

3.10 Power dependence of nanowire resonance

We further investigated the power dependence of the resonance effect on trapped nanowires by tuning the trapping power of our optical trap. A $4.6 \mu\text{m}$ nanowire is trapped at a height of $50 \mu\text{m}$ from the cover slip so that the resonance peak is maximised. Then, the trajectory of the trapped nanowire is measured as described in Section 3.3.5. The trapping power is adjusted by tuning the voltage amplitude of the RF signal fed into the acousto-optic deflectors. The actual power in milliwatts at the trapping focus is obtained via the power calibration curve shown in Figure 2.11 (Chapter 2 Section 2.5.3). For each trapping power, the trajectory of the trapped nanowire is measured followed by a power spectrum analysis, and then fitted with Equation 3.15. Resulting power spectra and the associated fits are shown in Figure 3.25; again we note exceptional agreements between experimental results and the model.

Qualitatively we see that the peak position of the resonance is blue shifted from 200 Hz to 1800 Hz with increasing trapping power together with a reduction of the amplitude of the fluctuations. The parameters associated with the fits are given in Figure 3.26. We observe that ϵ increases quadratically with trapping power, whilst μ increases linearly. As the trap stiffness is proportional to trapping power and $\mu = \text{tr}(M)$ is proportional to the trap stiffness because $M = \Gamma^{-1}K$, we should expect a linear increase in this parameter. Similarly, ϵ is the determinant of M and should therefore be proportional to the square of the matrix elements, and hence proportional to the square of the power. Since the peak frequency $f_{\text{peak}} = \sqrt{\epsilon}$, we expect it to increase linearly with trapping power as can be seen in Figure 3.27.

From Figure 3.26(b) we see that the noise strength parameter η is roughly constant at across all trapping powers, which indicates that there is no obvious heating across the different trapping powers. Finally, we note that whilst the trapping power dictates

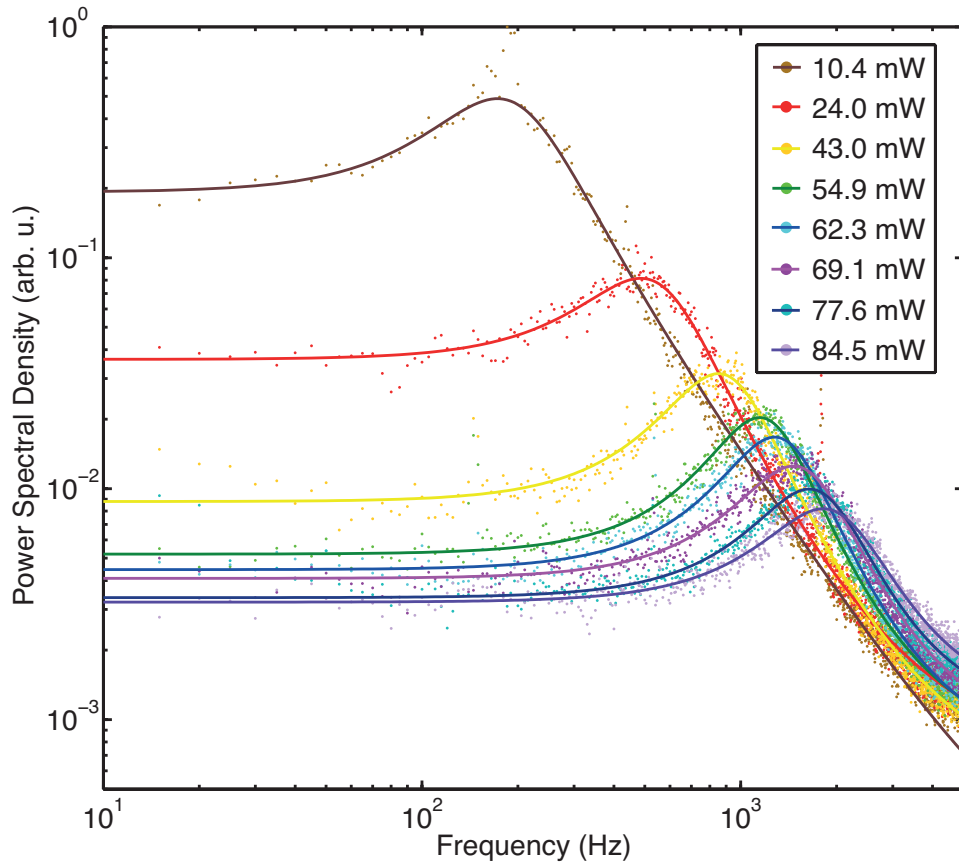


Figure 3.25: Power spectra of nanowires at different trapping powers, trapped at $50 \mu\text{m}$ height from the cover slip. Each power spectrum is fitted with the generalised power spectral density equation (Equation 3.15) and the peak frequency extracted and then plotted in Figure 3.27.

the relative strengths of the trap stiffness (conservative) and radiation pressure (non-conservative), it should not modify the ratio of the two competing forces under conditions where the harmonic approximation for the trap stiffness is valid.

In addition to the characteristic power spectrum described above, another important property of this system is its penchant to produce a continuous cycling of the position/orientation under steady state conditions. In order to discern the presence of cyclic motion a winding number analysis of the nanowire trajectories is performed. In our case the winding events are denoted when the nanowire trajectory moves around the centre of the trap in either a clockwise (negative) or anticlockwise (positive) motion. In an unbiased system the rates of cycling in either direction is balanced leading to an average of zero winding. The results presented for different powers in Figure 3.28(a),

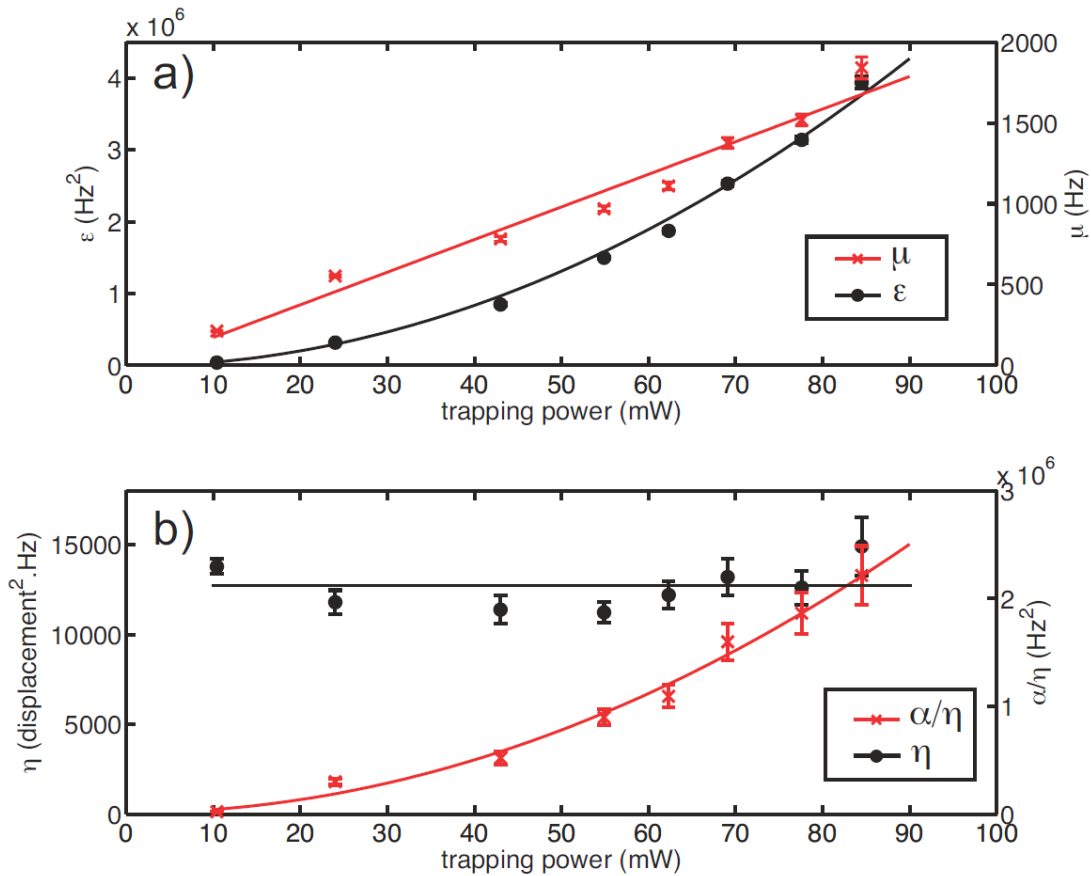


Figure 3.26: Fitting parameters of the power spectral density data presented in Figure 3.25. (a) ϵ increase quadratically and μ linearly with trapping power, which corresponds to linear increase in both the peak frequency and width. (b) The noise strength, η , shows no clear dependence on trapping power indicating a constant temperature, whilst α increases quadratic with trapping power. All dependencies are consistent with a trap stiffness that is linearly proportional to the trapping intensity in the presence of asymmetric coupling.

indicate that nanowires do indeed have a tendency to persistently cycle around a central point within the trap in a particular sense; short timescale fluctuations correspond to Brownian fluctuations in the trend. The winding behaviour is persistent over many seconds and is reproducible for each individually trapped wire. The sense of the cycling tends to be in a particular sense, suggesting an underlying bias within the trapping geometry, however winding in the opposite sense is also observed for some trapping events. We find that for different powers the rate of winding increases before plateauing at higher powers above 60 mW; this is clearly observed in a plot of the gradient of the winding number with trapping power, shown in Figure 3.28(b).

The winding property is dissipative in nature and is sustained only by the action of

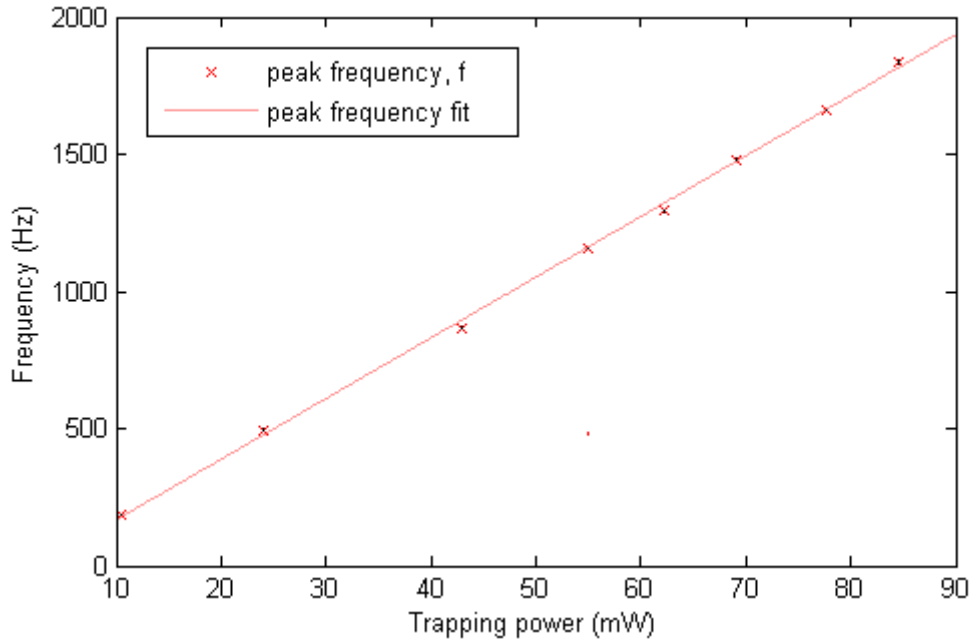


Figure 3.27: The peak frequency and peak width for each trapping power is extracted from the fits in Figure 3.25. From the plots it can be seen that peak frequency and peak width increases linearly with trapping power.

the non-conservative scattering forces. We may understand the process most intuitively by considering the following: when the nanowire is tilted with respect to the direction of the scattering force (along the z -axis) it will experience a greater pushing force. If the nanowire position lies below the focus it will be pushed through the focus to a position that is balanced by the axial restoring force. The additional lift force will only be alleviated when the tilt is reduced leading to a rotation back to the equilibrium position. The nanowire is then free to drop below the equilibrium position along the z -axis.

We also examined the effects of trapping power on the translational distribution of the trapped nanowire, which is plotted in Figure 3.29, and projected onto orthogonal planes in Figure 3.30a, 3.30b, and 3.30c. In the plots, the trapping laser is directed towards the z direction while the trapping laser is linearly polarised in the x direction. From the plots, we see that the trajectory of the nanowire in the translational direction is more strongly confined as the trapping power is increased. However, the opposite appears to be true for motions in the axial direction – as trapping power is increased, motions in the axial directions appear to spread further from the centre of the trap. We believe this is also a manifestation of the winding effects mentioned before. As trapping power

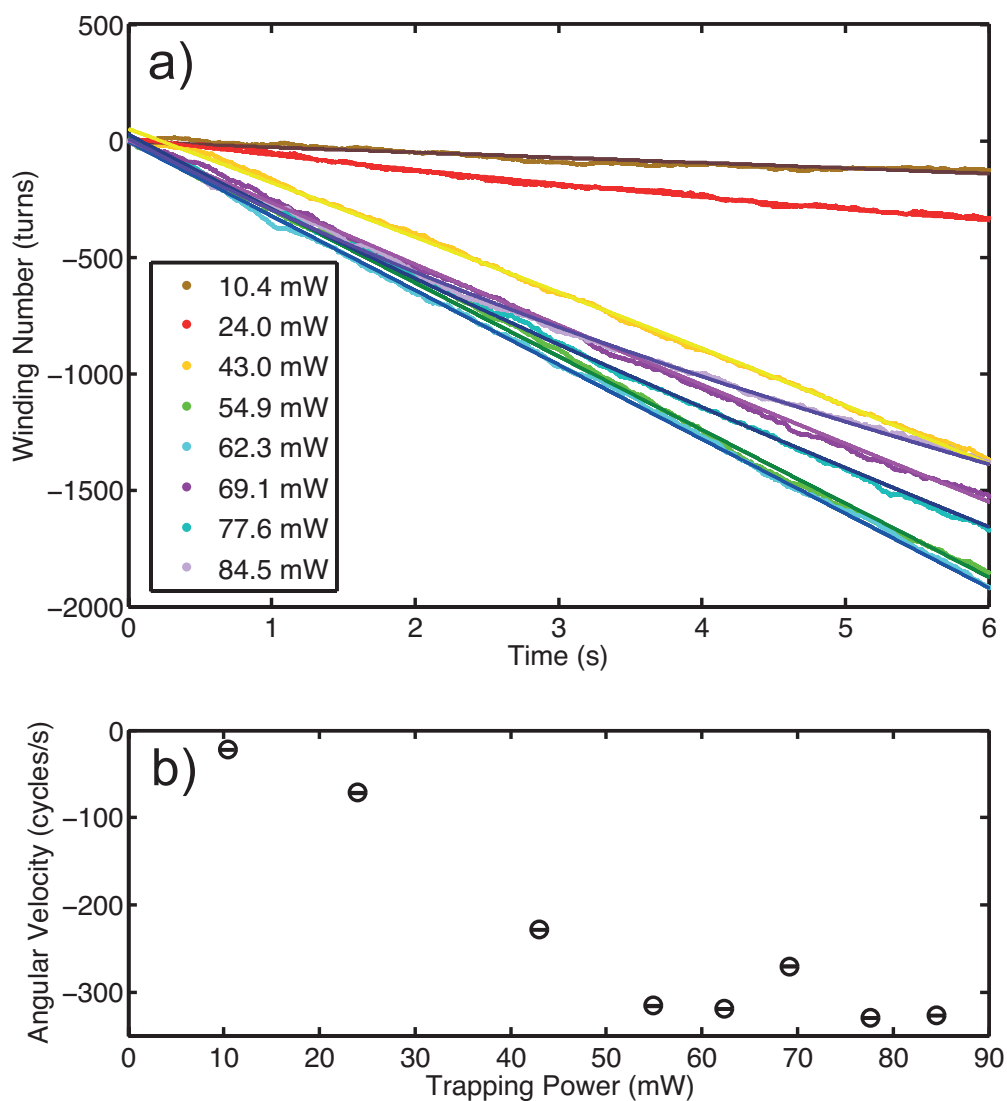


Figure 3.28: (a) A winding number plot of the nanowire motion for different trapping powers. Small timescale fluctuations in the winding decorate a clear monotonic increase with time, indicating persistent cycling in one direction. (b) The rate of winding, given by the gradient of the winding plots, is observed to increase approximately trapping power for lower powers and plateau at higher powers. The winding also takes on a distinctly non-linear trend at very high trapping frequencies.

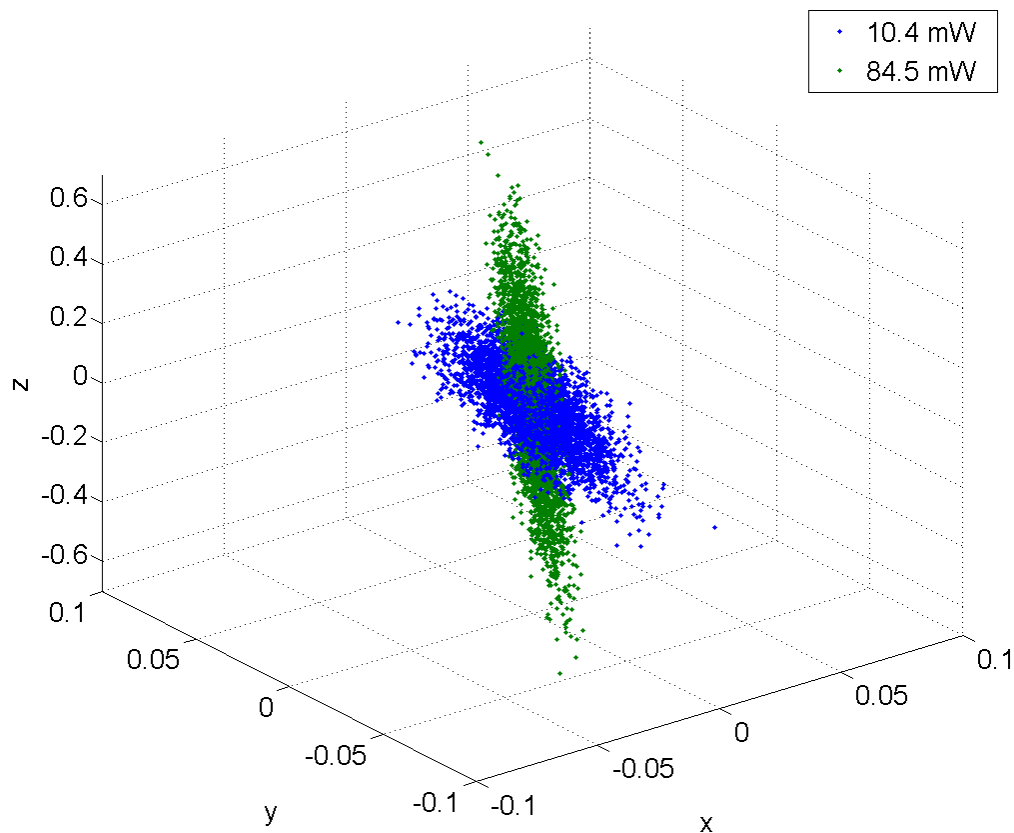


Figure 3.29: Translational distribution of a trapped nanowire under two different trapping powers – 10.4mW (blue) and 84.5mW (green). Results show stronger confinement in the horizontal plane and weaker confinement in the axial direction as trapping power is increased.

increase, the non-conservative scattering forces also increase; the nanowire experiences greater pushing and restoring forces in the axial direction resulting in a greater amplitude of the cyclic motion.

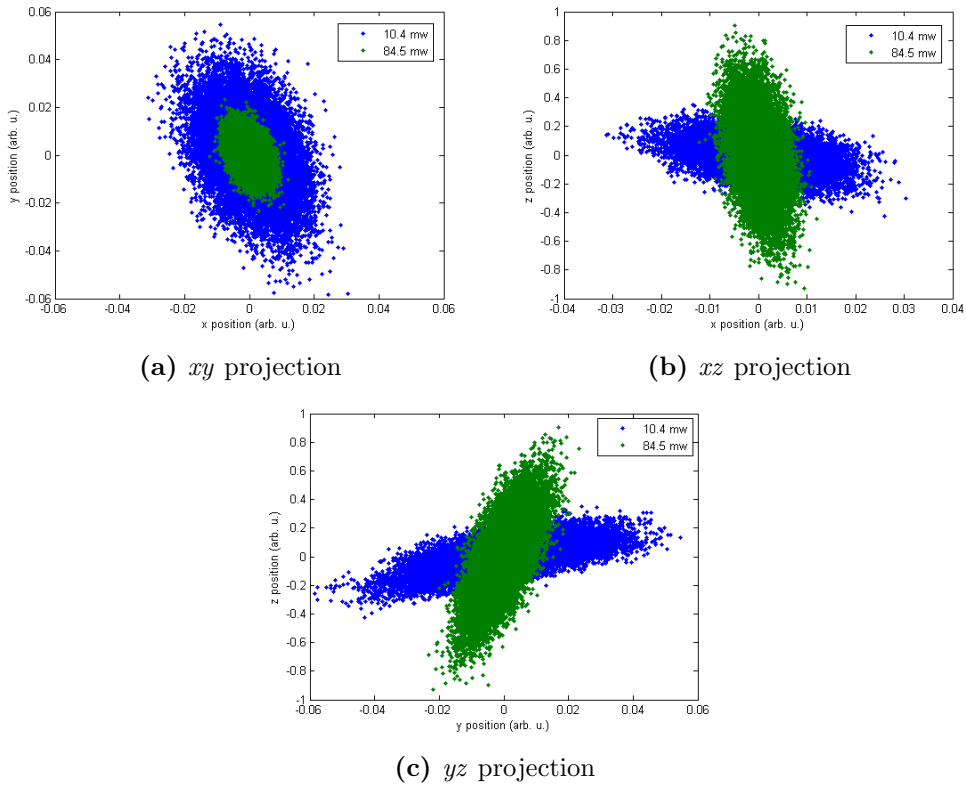


Figure 3.30: Projection of the translational distribution of a trapped nanowire shown in Figure 3.29 on to the xy , xz and yz planes.

3.11 Length dependence of resonance peaks

In this section I will present our study on how the resonant behaviour of optically trapped nanowires depends on their lengths. To do this study, we measure the trajectory and power spectrum of nanowires as they are trapped at a height of $50 \mu\text{m}$ from the cover slip so that the resonance peak is maximised, as explained in the previous section. We also measure their lengths and repeat for as many nanowires as can be found in the sample chamber. The tabulated results are shown in Figure 3.31.

Results show that resonance frequency decrease linearly with length. Although our model does not explicitly account for this behaviour, we believe this is a manifestation of the (approximately) linearly increasing hydrodynamic drag of nanowires, γ_{\perp} with increasing length.

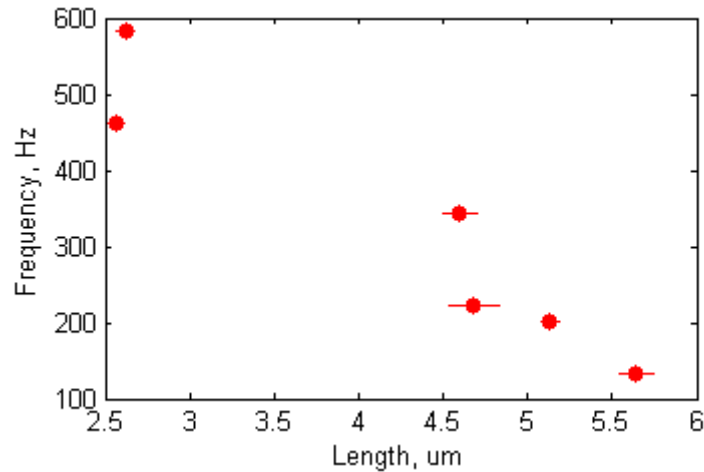


Figure 3.31: Length dependence of the resonance peak in the power spectrum of optically trapped nanowires under resonance.

3.12 Conclusion

In summary, we have characterised the trapping properties of single trapped InP nanowires. We have shown in Section 3.4 that the trap stiffness of optically trapped nanowires is independent of the length of the nanowires. We have also examined higher order dynamics due to coupling between rotational and translational degrees of freedom when a single high aspect ratio nanowire is trapped. Section 3.9 and 3.10 provided clear experimental and theoretical evidence for the influence of non-conservative coupling between translation and rotational modes in optically trapped nanowires beyond the standard single trapped spherical particle picture. We see experimentally that this leads to a distinct resonance peak in the power spectrum and an accompanying winding of the particle trajectories, which suggests that the trapped nanowires undergo cyclic motion. This model system provides exciting new opportunities to study complex dynamic behaviour involving non-conservative forces and may lead to exciting new insights into analogous biophysical systems. Further investigations into the dependence of this effect on polarization and nanowire dimensions will be carried out to better understand this phenomenon, but these are beyond the scope of this work.

3.13 References

- [1] Y. Nakayama, P. J. Pauzauskie, A. Radenovic, R. M. Onorato, R. J. Saykally, J. Liphardt, and P. D. Yang. Tunable nanowire nonlinear optical probe. *Nature*, 447(7148):1098–U8, 2007. 183HT Times Cited:187 Cited References Count:30.
- [2] D. B. Phillips, J. A. Grieve, S. N. Olof, S. J. Kocher, R. Bowman, M. J. Padgett, M. J. Miles, and D. M. Carberry. Surface imaging using holographic optical tweezers. *Nanotechnology*, 22(28), 2011. 775NX Times Cited:16 Cited References Count:28.
- [3] D. B. Phillips, S. H. Simpson, J. A. Grieve, G. M. Gibson, R. Bowman, M. J. Padgett, M. J. Miles, and D. M. Carberry. Position clamping of optically trapped microscopic non-spherical probes. *Optics Express*, 19(21):20622–20627, 2011. 835VV Times Cited:23 Cited References Count:16.
- [4] S. N. Olof, J. A. Grieve, D. B. Phillips, H. Rosenkranz, M. L. Yallop, M. J. Miles, A. J. Patil, S. Mann, and D. M. Carberry. Measuring nanoscale forces with living probes. *Nano Letters*, 12(11):6018–6023, 2012. 039KJ Times Cited:14 Cited References Count:20.
- [5] D. B. Phillips, G. M. Gibson, R. Bowman, M. J. Padgett, S. Hanna, D. M. Carberry, M. J. Miles, and S. H. Simpson. An optically actuated surface scanning probe. *Optics Express*, 20(28):29679–29693, 2012. 089MK Times Cited:21 Cited References Count:33.
- [6] D. B. Phillips, M. J. Padgett, S. Hanna, Y. L. D. Ho, D. M. Carberry, M. J. Miles, and S. H. Simpson. Shape-induced force fields in optical trapping. *Nature Photonics*, 8(5):400–405, 2014. Af9cc Times Cited:17 Cited References Count:42.
- [7] S. H. Simpson, D. B. Phillips, D. M. Carberry, and S. Hanna. Bespoke optical springs and passive force clamps from shaped dielectric particles. *Journal of Quantitative Spectroscopy & Radiative Transfer*, 126:91–98, 2013. Sp. Iss. SI 196US Times Cited:11 Cited References Count:34.
- [8] Y. S. Kim, N. Y. Lee, J. R. Lim, M. J. Lee, and S. Park. Nanofeature-patterned polymer mold fabrication toward precisely defined nanostructure replication. *Chemistry of Materials*, 17(23):5867–5870, 2005. 983WG Times Cited:44 Cited References Count:22.
- [9] S. Paiman, Q. Gao, H. J. Joyce, Y. Kim, H. H. Tan, C. Jagadish, X. Zhang, Y. Guo, and J. Zou. Growth temperature and v/iii ratio effects on the morphology and crystal structure of inp nanowires. *Journal of Physics D-Applied Physics*, 43(44), 2010. 668UH Times Cited:12 Cited References Count:41.
- [10] V. A. Shchukin and D. Bimberg. Spontaneous ordering of nanostructures on crystal surfaces. *Reviews of Modern Physics*, 71(4):1125–1171, 1999. 226UA Times Cited:701 Cited References Count:224.
- [11] S. H. Wu, J. Serbin, and M. Gu. Two-photon polymerisation for three-dimensional micro-fabrication. *Journal of Photochemistry and Photobiology a-Chemistry*, 181(1):1–11, 2006. 058AV Times Cited:68 Cited References Count:32.

-
- [12] L. M. Tong, J. Y. Lou, and E. Mazur. Single-mode guiding properties of subwavelength-diameter silica and silicon wire waveguides. *Optics Express*, 12(6):1025–1035, 2004. 808UU Times Cited:286 Cited References Count:23.
- [13] Y. Huang, X. F. Duan, Y. Cui, L. J. Lauhon, K. H. Kim, and C. M. Lieber. Logic gates and computation from assembled nanowire building blocks. *Science*, 294(5545):1313–1317, 2001. 491VF Times Cited:1418 Cited References Count:22.
- [14] C. Thelander, T. Martensson, M. T. Bjork, B. J. Ohlsson, M. W. Larsson, L. R. Waltenberg, and L. Samuelson. Single-electron transistors in heterostructure nanowires. *Applied Physics Letters*, 83(10):2052–2054, 2003. 717LJ Times Cited:294 Cited References Count:14.
- [15] X. F. Duan, Y. Huang, R. Agarwal, and C. M. Lieber. Single-nanowire electrically driven lasers. *Nature*, 421(6920):241–245, 2003. 635KG Times Cited:1578 Cited References Count:25.
- [16] J. F. Wang, M. S. Gudiksen, X. F. Duan, Y. Cui, and C. M. Lieber. Highly polarized photoluminescence and photodetection from single indium phosphide nanowires. *Science*, 293(5534):1455–1457, 2001. 465XV Times Cited:1135 Cited References Count:17.
- [17] C. M. Lieber. Design, synthesis and properties of programmable nanowire transistors for nanoscale circuits and processors. *Abstracts of Papers of the American Chemical Society*, 243, 2012. 219JX 1039-INOR Times Cited:0 Cited References Count:0.
- [18] H. Yan, H. S. Choe, S. W. Nam, Y. J. Hu, S. Das, J. F. Klemic, J. C. Ellenbogen, and C. M. Lieber. Programmable nanowire circuits for nanoprocessors. *Nature*, 470(7333):240–244, 2011. 718RQ Times Cited:222 Cited References Count:21.
- [19] P. J. Pauzauskie, A. Radenovic, E. Trepagnier, H. Shroff, P. D. Yang, and J. Liphardt. Optical trapping and integration of semiconductor nanowire assemblies in water. *Nature Materials*, 5(2):97–101, 2006. 008SC Times Cited:175 Cited References Count:29.
- [20] J. Li and G. Du. Manipulation and assembly of zno nanowires with single holographic optical tweezers system. *Applied Optics*, 53(3):351–355, 2014. 296GD Times Cited:0 Cited References Count:16.
- [21] F. Wang, P. J. Reece, S. Paiman, Q. Gao, H. H. Tan, and C. Jagadish. Nonlinear optical processes in optically trapped inp nanowires. *Nano Letters*, 11(10):4149–4153, 2011. 830OT Times Cited:5 Cited References Count:28.
- [22] Kirstine Berg-Sørensen and Henrik Flyvbjerg. Power spectrum analysis for optical tweezers. *Review of Scientific Instruments*, 75(3):594–612, 2004.
- [23] K. Dholakia, P. Reece, and M. Gu. Optical micromanipulation. *Chemical Society Reviews*, 37(1):42–55, 2008. 251YJ Times Cited:138 Cited References Count:59.
- [24] Keir C. Neuman and Steven M. Block. Optical trapping. *Review of Scientific Instruments*, 75:2787, 2004.
-

- [25] H. Risken and H. Risken. *The Fokker-Planck equation : methods of solution and applications*. Berlin and New York : Springer-Verlag, Berlin and New York, 2nd ed. edition, 1989. (Hannes) Bibliography: p. 448-461.
- [26] O. M. Marago, P. H. Jones, F. Bonaccorso, V. Scardaci, P. G. Gucciardi, A. G. Rozhin, and A. C. Ferrari. Femtonewton force sensing with optically trapped nanotubes. *Nano Letters*, 8(10):3211–3216, 2008. 358HD Times Cited:51 Cited References Count:33.
- [27] M. M. Tirado and J. Garcíadelatorre. Translational friction coefficients of rigid, symmetric top macromolecules - application to circular-cylinders. *Journal of Chemical Physics*, 71(6):2581–2587, 1979. H1466 Times Cited:278 Cited References Count:25.
- [28] M. M. Tirado, C. L. Martinez, and J. G. Delatorre. Comparison of theories for the translational and rotational diffusion-coefficients of rod-like macromolecules - application to short dna fragments. *Journal of Chemical Physics*, 81(4):2047–2052, 1984. Tg208 Times Cited:278 Cited References Count:28.
- [29] R. S. Wagner and W. C. Ellis. Vapor-liquid-solid mechanism of single crystal growth (new method growth catalysis from impurity whisker epitaxial + large crystals si e). *Applied Physics Letters*, 4(5):89–&, 1964. 5163A Times Cited:4240 Cited References Count:9.
- [30] A. Rohrbach, H. Kress, and E. H. K. Stelzer. Three-dimensional tracking of small spheres in focused laser beams: influence of the detection angular aperture. *Optics Letters*, 28(6):411–413, 2003. 652ZT Times Cited:47 Cited References Count:9.
- [31] Y. Y. Cao, A. B. Stilgoe, L. X. Chen, T. A. Nieminen, and H. Rubinsztein-Dunlop. Equilibrium orientations and positions of non-spherical particles in optical traps. *Optics Express*, 20(12):12987–12996, 2012. 961KP Times Cited:9 Cited References Count:37.
- [32] S. H. Simpson and S. Hanna. Optical trapping of microrods: variation with size and refractive index. *Journal of the Optical Society of America a-Optics Image Science and Vision*, 28(5):850–858, 2011. 756PD Times Cited:13 Cited References Count:42.
- [33] F. Wang, W. J. Toe, W. M. Lee, D. McGloin, Q. Gao, H. H. Tan, C. Jagadish, and P. J. Reece. Resolving stable axial trapping points of nanowires in an optical tweezers using photoluminescence mapping. *Nano Letters*, 13(3):1185–1191, 2013. 107TN Times Cited:4 Cited References Count:31.
- [34] Y. Deng, J. Bechhoefer, and N. R. Forde. Brownian motion in a modulated optical trap. *Journal of Optics a-Pure and Applied Optics*, 9(8):S256–S263, 2007. Sp. Iss. SI 203CV Times Cited:17 Cited References Count:34.
- [35] R. Di Leonardo, G. Ruocco, J. Leach, M. J. Padgett, A. J. Wright, J. M. Girkin, D. R. Burnham, and D. McGloin. Parametric resonance of optically trapped aerosols. *Physical Review Letters*, 99(1), 2007. 187AO Times Cited:37 Cited References Count:21.

-
- [36] D. R. Burnham, P. J. Reece, and D. McGloin. Parameter exploration of optically trapped liquid aerosols. *Physical Review E*, 82(5), 2010. 1 681JH Times Cited:13 Cited References Count:67.
- [37] S. H. Simpson and S. Hanna. Orbital motion of optically trapped particles in laguerre-gaussian beams. *Journal of the Optical Society of America a-Optics Image Science and Vision*, 27(9):2061–2071, 2010. 648DZ Times Cited:11 Cited References Count:35.
- [38] S. J. Parkin, T. A. Nieminen, N. R. Heckenberg, and H. Rubinsztein-Dunlop. Optical measurement of torque exerted on an elongated object by a noncircular laser beam. *Physical Review A*, 70(2), 2004. 851WO Times Cited:21 Cited References Count:28.
- [39] M. C. Zhong, J. H. Zhou, Y. X. Ren, Y. M. Li, and Z. Q. Wang. Rotation of birefringent particles in optical tweezers with spherical aberration. *Applied Optics*, 48(22):4397–4402, 2009. 490BC Times Cited:6 Cited References Count:31.
- [40] K. D. Wulff, D. G. Cole, and R. L. Clark. Controlled rotation of birefringent particles in an optical trap. *Applied Optics*, 47(34):6428–6433, 2008. 386BB Times Cited:3 Cited References Count:31.
- [41] Y. Arita, M. Mazilu, and K. Dholakia. Laser-induced rotation and cooling of a trapped microgyroscope in vacuum. *Nature Communications*, 4, 2013. 209KD Times Cited:10 Cited References Count:35.
- [42] A. A. R. Neves, A. Camposeo, S. Pagliara, R. Saija, F. Borghese, P. Denti, M. A. Iati, R. Cingolani, O. M. Marago, and D. Pisignano. Rotational dynamics of optically trapped nanofibers. *Optics Express*, 18(2):822–830, 2010. 547BP Times Cited:30 Cited References Count:46.
- [43] M. Griesshammer and A. Rohrbach. 5d-tracking of a nanorod in a focused laser beam - a theoretical concept. *Optics Express*, 22(5):6114–6132, 2014. Ad9is Times Cited:0 Cited References Count:37.
- [44] S. H. Simpson and S. Hanna. Holographic optical trapping of microrods and nanowires. *Journal of the Optical Society of America a-Optics Image Science and Vision*, 27(6):1255–1264, 2010. 602DC Times Cited:31 Cited References Count:48.
- [45] S. H. Simpson and S. Hanna. First-order nonconservative motion of optically trapped nonspherical particles. *Physical Review E*, 82(3), 2010. 1 656IT Times Cited:17 Cited References Count:39.
- [46] A. Kyrsting, P. M. Bendix, and L. B. Oddershede. Mapping 3d focal intensity exposes the stable trapping positions of single nanoparticles. *Nano Letters*, 13(1):31–35, 2013. 065IP Times Cited:12 Cited References Count:28.
- [47] C. W. Gardiner. *Handbook of stochastic methods for physics, chemistry, and the natural sciences*. Berlin New York : Springer-Verlag, Berlin New York, 2nd ed. edition, 1990. (Crispin W.) Includes bibliographical references (p. [421]-[430]) and indexes.
-

Chapter 4

Waveguiding Properties and Coupling of Indium Phosphide (InP) Nanowire Waveguides

4.1	Introduction	96
4.2	Waveguiding properties of single InP nanowire waveguides	98
4.3	Poynting vectors for InP nanowire waveguides	108
4.4	Dispersion and group velocity of InP nanowire waveguides	111
4.5	Coupling between two InP nanowire waveguides	113
4.5.1	Conditions for weak coupling	114
4.6	Coupling constant of coupled InP nanowire waveguides	114
4.7	Mode profiles of coupled InP nanowire waveguides	117
4.8	Optical force calculations from Maxwell's Stress Tensor	123
4.9	Power transfer between coupled nanowires and beat length	126
4.10	Group velocities of coupled nanowire waveguides	129
4.11	Dispersion relation of coupled nanowire waveguides	130
4.12	Optical forces from eigenmode analysis	132
4.13	Conclusion	136
4.14	References	137

4.1 Introduction

Amidst huge advances in nanotechnology and optomechanics, there has been growing interest in the use of nanophotonic waveguides as optical force mechanical actuators [1–3]. Extensive studies have been made on optomechanical systems, such as the coupling between a high-Q optical microresonator and a silica waveguide [4], the optical forces between a silicon nanowire waveguide and a substrate [5], and the interaction forces between optically coupled waveguides [6–8]. Optomechanics offer a wide range of benefits over conventional methods, most notably the ability to operate with high frequency and fidelity in the nanoscale. Optical forces are widely used to precisely control or measure the position of nanometre sized particles [2], as well as to study pico newton forces in molecular motors and DNA dynamics [9]. For example, optical forces has been used to measure the force and velocity of kinesin and myosin molecules by attaching them to mechanical handles [10–13]. In scanning probe microscopy, optomechanical probes can attain force sensitivities of several orders of magnitude greater than conventional AFM. Phillips *et al.* demonstrated optically trapped probes that are capable of achieving a lateral resolution of 200 nm (due to the tip diameter) and a depth resolution of about 10 nm [14]. Doolin *et al.* developed optomechanical cantilevers with noise floors as low as 2 fm Hz^{-1/2} and 130 aN Hz^{-1/2} force sensitivity at vacuum in room temperature, which is orders of magnitude smaller than conventional mechanical cantilevers used in AFM's [15].

In cases when the light interacting with one particle interacts with a second particle, this can give rise to interparticle forces mediated by light i.e. optical binding. One particular optical binding study relevant to our research is Simpson *et al.*'s simulation of optical binding between arrays of non-spherical particles [16]. In this study, it is predicted that optically bound rod like structures such as nanowires not only demonstrate discrete separations such as that observed in spherical particles, they also tend to acquire a parallel, side-by-side orientation such as that of the rungs of a ladder. In our study we aim to study the interactions between two optically trapped InP nanowires aligned parallel to each other. Since the optical forces involved in trapping these nanowires are relatively weak, this presents an excellent opportunity for us to observe the possible optical binding forces between InP nanowires within optical traps.

Optical coupling between waveguides has been well understood since the advent of optical fibres, but it has since been applied in the nanoscale by Huang *et al.* [17].

Furthermore, Pernice *et al.* has done theoretical investigations and numerical modelling of the optical forces generated between coupled nanowire waveguides [5, 18, 19]. The frequency dependence of optical forces between coupled waveguides has also been calculated [20]. On the other hand, Povinelli *et al.* have shown the effects of forces between two optically coupled silicon nanowire waveguides [6, 7]. In this study, both nanowire waveguides are fixed at both ends to the substrate with a free standing section in the middle which is displaced by optical coupling forces when light is passed through the nanowires. Roels *et al.* further showed that the optical interaction forces between coupled waveguides can be tuned by controlling the relative phase of the optical fields injected into the waveguides [8].

In contrast to previous studies, our system will consist of two optically trapped InP nanowire waveguides suspended in deionised water by optical tweezers. This setup is unique because the nanowires are not physically fixed, but simply held in optical tweezers with relatively low rigidity or trap stiffness, which is ideal for measuring any existing coupling forces in the order of the trap stiffness. Our system also offers the flexibility of varying the equilibrium separation of the two nanowires by displacing the optical trap.

In order to predict the behaviour of coupled InP nanowire waveguides in the system we propose, we must first quantify the wave guiding properties of single InP nanowires in our system of optical trapping within deionised water as the surrounding medium. Single nanowires as waveguides are interesting in itself, particularly because of its excellent optical and electrical properties on top of its compact size. Consequently, nanowire waveguides have great potential in nano-scale electronic and photonic applications, including optical waveguides [21], field effect transistors [22], single electron transistors [23], nanolasers [24], photodetectors [25] and integrated microprocessors [26, 27], as well as probe tips in high-resolution optical scanning probe microscopy [28]. Although nanowire waveguides have been studied extensively, most studies in the literature primarily focus on silicon and silica nanowires [4–8, 18, 19, 21]. In our studies, we are interested in using Indium Phosphide (InP) nanowires as waveguides due to their excellent optical and electrical properties. In particular, InP nanowires have been shown to demonstrate second harmonic generation (SHG) of 532 nm light when pumped with a 1064 nm source, and have a strong photoluminescence (PL) at 890 nm when pumped with an external source [29]. As such, we will focus most of our analysis of the waveguiding properties of the nanowires at 890 nm wavelength.

In this chapter, we will first examine the waveguiding properties of a single trapped InP nanowire in deionised water as the medium. We will calculate the field intensity profile, Poynting vector, dispersion relation, group velocities of guided modes and how all these quantities vary with different nanowire radii. A firm understanding of these variables is essential for the calculation of coupled nanowire waveguides, which we will examine next. The coupling constant, beat length, field profiles and optical forces will be calculated and related back to experimentally measurable quantities.

4.2 Waveguiding properties of single InP nanowire waveguides

We start by considering Maxwell's equations shown in Equation 4.1.

$$\nabla \times \mathbf{E} = i(\mu_0/\epsilon_0)^{1/2} k\mathbf{H}; \quad \nabla \times \mathbf{H} = \mathbf{J} - i(\mu_0/\epsilon_0)^{1/2} kn^2\mathbf{E} \quad (4.1a)$$

$$\nabla \cdot (n^2\mathbf{E}) = \sigma/\epsilon_0; \quad \nabla \cdot \mathbf{H} = 0 \quad (4.1b)$$

where \mathbf{E} is the electric field, \mathbf{H} is the magnetic field, \mathbf{J} is the current density, k is the wave vector in free space, n is the refractive index, σ is the electric charge density and ϵ_0, μ_0 are permittivity and permeability of free space respectively.

If the electric and magnetic waves are separable (as shown in Equation 4.2) and source free i.e. $\mathbf{J} = 0$, Maxwell's equations can be rewritten as the homogeneous vector wave equations (Equation 4.3) with propagation constant β [30].

$$\mathbf{E} = (\mathbf{e}_t + e_z\hat{\mathbf{z}}) e^{i\beta z}; \quad \mathbf{H} = (\mathbf{h}_t + h_z\hat{\mathbf{z}}) e^{i\beta z} \quad (4.2)$$

$$\{\nabla^2 + n^2k^2 - \beta^2\} \mathbf{e} = -(\nabla + i\beta\hat{\mathbf{z}}) \mathbf{e}_t \cdot \nabla \ln n^2 \quad (4.3a)$$

$$\{\nabla^2 + n^2k^2 - \beta^2\} \mathbf{h} = \{(\nabla + i\beta\hat{\mathbf{z}}) \times \mathbf{h}\} \times \nabla \ln n^2 \quad (4.3b)$$

The above equations apply for any waveguide with arbitrary shape and refractive index. For a circularly symmetric waveguide with step profile index such as that for

our InP nanowires, these equations (Equation 4.3) can be solved analytically with the following assumptions:

1. Circular cross section with radius a , radius big enough (>5 nm) such that permittivity and permeability still apply.
2. Length long enough to establish spatial steady state.
3. Uniform diameter.
4. Smooth sidewall.
5. Wire is non-dissipative and source free.
6. Wire with refractive index n_c in a uniform medium with refractive indices n_m , so can be described as follows.

$$n(r) = \begin{cases} n_c, & 0 < r < a \\ n_m, & a \leq r < \infty \end{cases} \quad (4.4)$$

A representative nanowire waveguide is illustrated in Figure 4.1. The shaded region represents the core, surrounded by the cladding which is assumed to be unbounded in extent as described by Equation 4.4. We choose cartesian axes such that the z axis coincides with the long axis of the nanowire waveguide.

Under the conditions listed above, the vector wave equation (Equation 4.3) can be reduced to the scalar wave equation shown in Equation 4.5 below at all points except the boundaries between core and cladding. This is because at all points except the boundaries, the refractive index $n(r)$ is constant and $\nabla \ln n^2 = 0$. To obtain the full solution, we solve the scalar wave equation for the core and the cladding separately and use the boundary conditions to determine the field amplitudes [30].

$$\{\nabla^2 + n^2 k^2 - \beta^2\} \mathbf{e} = 0 \quad (4.5a)$$

$$\{\nabla^2 + n^2 k^2 - \beta^2\} \mathbf{h} = 0 \quad (4.5b)$$

Where $k = 2\pi/\lambda$ and β is the propagation constant.

Following the calculations shown by Tong *et al.* [21], the eigenvalue equations of the scalar wave equation for the fundamental modes (HE_{11} modes) is given as

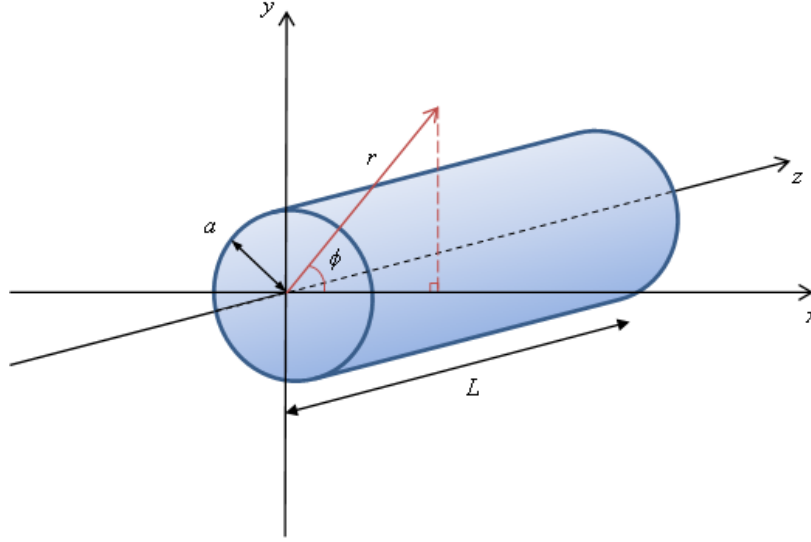


Figure 4.1: Nomenclature and coordinates for describing our nanowire waveguide. The shaded region represents the core with refractive index n_c , and is surrounded by the cladding which is assumed to be an unbounded medium with refractive index n_m .

$$\left\{ \frac{J'_1(U)}{UJ_1(U)} + \frac{K'_1(W)}{WK_1(W)} \right\} \left\{ \frac{J'_1(U)}{UJ_1(U)} + \frac{n_m^2 K'_1(W)}{n_c^2 WK_1(W)} \right\} = \left(\frac{\beta}{kn_c} \right)^2 \left(\frac{V}{UW} \right)^4 \quad (4.6)$$

Where J_i is the Bessel function of the first kind, K_i is the modified Bessel function of the second kind, $U = a(k^2 n_c^2 - \beta^2)^{1/2}$ is the core parameter, $W = a(\beta^2 - k^2 n_m^2)^{1/2}$ is the cladding parameter, and $V = ka(n_c^2 - n_m^2)^{1/2}$ is the waveguide parameter.

The electromagnetic fields of the fundamental modes can be expressed as [21, 30]

$$\Psi = (\mathbf{E}, \mathbf{H}) \quad (4.7a)$$

$$\mathbf{E}(r, \phi, z) = (e_r \hat{r} + e_\phi \hat{\phi} + e_z \hat{z}) e^{i\beta z} e^{-i\omega t} \quad (4.7b)$$

$$\mathbf{H}(r, \phi, z) = (h_r \hat{r} + h_\phi \hat{\phi} + h_z \hat{z}) e^{i\beta z} e^{-i\omega t} \quad (4.7c)$$

Inside the nanowire where $0 < r < a$,

$$e_r = -\frac{a_1 J_0(UR) + a_2 J_2(UR)}{J_1(U)} \sin(\phi) \quad (4.8a)$$

$$e_\phi = -\frac{a_1 J_0(UR) - a_2 J_2(UR)}{J_1(U)} \cos(\phi) \quad (4.8b)$$

$$e_z = \frac{-iU}{a\beta} \frac{J_1(UR)}{J_1(U)} \sin(\phi) \quad (4.8c)$$

$$h_r = \left(\frac{\epsilon_0}{\mu_0}\right)^{1/2} \frac{kn_c^2}{\beta} \frac{a_3 J_0(UR) - a_4 J_2(UR)}{J_1(U)} \cos(\phi) \quad (4.9a)$$

$$h_\phi = -\left(\frac{\epsilon_0}{\mu_0}\right)^{1/2} \frac{kn_c^2}{\beta} \frac{a_3 J_0(UR) + a_4 J_2(UR)}{J_1(U)} \sin(\phi) \quad (4.9b)$$

$$h_z = -i \left(\frac{\epsilon_0}{\mu_0}\right)^{1/2} \frac{F_2 U}{ka} \frac{J_1(UR)}{J_1(U)} \cos(\phi) \quad (4.9c)$$

Outside the nanowire where $a \leq r < \infty$,

$$e_r = -\frac{U}{W} \frac{a_1 K_0(WR) - a_2 K_2(WR)}{K_1(W)} \sin(\phi) \quad (4.10a)$$

$$e_\phi = -\frac{U}{W} \frac{a_1 K_0(WR) + a_2 K_2(WR)}{K_1(W)} \cos(\phi) \quad (4.10b)$$

$$e_z = \frac{-iU}{a\beta} \frac{K_1(WR)}{K_1(W)} \sin(\phi) \quad (4.10c)$$

$$h_r = \left(\frac{\epsilon_0}{\mu_0}\right)^{1/2} \frac{kn_c^2}{\beta} \frac{U}{W} \frac{a_5 K_0(WR) - a_6 K_2(WR)}{K_1(W)} \cos(\phi) \quad (4.11a)$$

$$h_\phi = -\left(\frac{\epsilon_0}{\mu_0}\right)^{1/2} \frac{kn_c^2}{\beta} \frac{U}{W} \frac{a_5 K_0(WR) + a_6 K_2(WR)}{K_1(W)} \sin(\phi) \quad (4.11b)$$

$$h_z = -i \left(\frac{\epsilon_0}{\mu_0}\right)^{1/2} \frac{F_2 U}{ka} \frac{K_1(WR)}{K_1(W)} \cos(\phi) \quad (4.11c)$$

where

$$R = \frac{r}{a} \quad (4.12a)$$

$$\Delta = \frac{1}{2} \left(1 - \frac{n_m^2}{n_c^2}\right) \quad (4.12b)$$

$$a_1 = \frac{F_2 - 1}{2}; a_2 = \frac{F_2 + 1}{2}; a_3 = \frac{F_1 - 1}{2}; a_4 = \frac{F_1 + 1}{2}; a_5 = \frac{F_1 - 1 + 2\Delta}{2}; a_6 = \frac{F_1 + 1 - 2\Delta}{2} \quad (4.12c)$$

$$F_1 = \left(\frac{UW}{V}\right)^2 [b_1 + (1 - 2\Delta) b_2]; F_2 = \left(\frac{V}{UW}\right)^2 \frac{1}{b_1 + b_2} \quad (4.12d)$$

$$b_1 = \frac{1}{2U} \left\{ \frac{J_0(U)}{J_1(U)} - \frac{J_2(U)}{J_1(U)} \right\}; b_2 = -\frac{1}{2W} \left\{ \frac{K_0(W)}{K_1(W)} - \frac{K_2(W)}{K_1(W)} \right\}; \quad (4.12e)$$

Using these equations we calculate the normalised electric field components for InP nanowires applicable to our experimental setup. In our optical trapping experiments, InP nanowires ($n_c = 3.457$) are submerged in deionised water ($n_m = 1.33$). We are interested in waveguiding modes for $\lambda = 890$ nm because it is the peak wavelength of the photoluminescence of these InP nanowires. The fundamental modes in cylindrical coordinates are shown in Figure 4.2. From the figures it can be seen that InP nanowires with a radius larger than 100 nm have a tight field confinement, while for nanowires with radius 75 nm and less there are significant field amplitudes extending outside the nanowire.

Figure 4.3 shows the fundamental mode for 150 nm diameter InP nanowires from our calculation, while Figure 4.4 shows results from finite-difference time-domain (FDTD) simulations. The entire simulation volume is covered by a coarse mesh and a fine mesh in the proximity of the nanowire. The fine mesh has a mesh size of 2.5 nm covering a region of $300 \text{ nm} \times 300 \text{ nm} \times 5.2 \mu\text{m}$, which covers the entire nanowire that is in the centre of this fine mesh region. Comparison between our results and FDTD simulations shows good agreement at almost all points, except for points near the boundary. We believe this is an artefact due to the discretization of the parameters used to run the FDTD simulations, especially at the interface between the nanowire core and the surrounding medium where there is a discontinuity.

From Figures 4.3 and 4.4, we see that there are significant evanescent waves outside the nanowire waveguide, which has many potential applications. We note that the field is not circularly symmetric due to polarisation. In the context of particle trapping and optomechanics, evanescent waves have been shown to generate significant gradient forces on nearby particles and is able to form an optical trap [32, 33]. Early evanescent field optical traps are generated by total internal reflection in prisms [33, 34], but later experiments involving evanescent field trapping also expanded to evanescent fields around fibre cores from optical fibres [31, 35–38]. A few notable studies include Frawley *et al.*'s demonstration of selective particle trapping and optical binding in the evanescent field of an optical nanofiber [31] and Skelton *et al.*'s experimental realisation of evanescent wave trapping and transport of micro and nano particles along tapered optical fibres of sub-micron diameters [38]. In Frawley's study, $3.13 \mu\text{m}$ SiO_2 spheres are

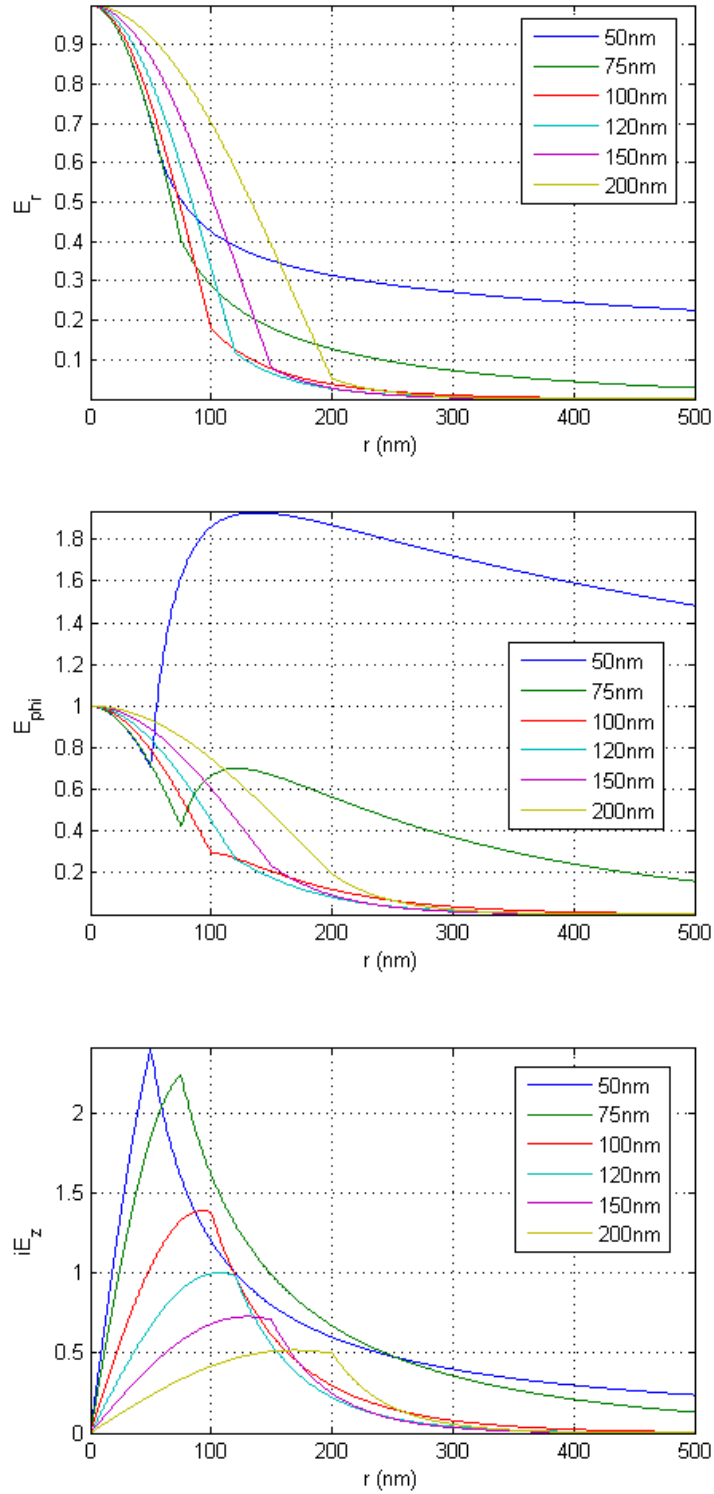


Figure 4.2: Radial, azimuthal and longitudinal components (e_r, e_ϕ, e_z) of HE_{11} modes of InP nanowires in deionised water at $\lambda = 890$ nm for different nanowire radii, shown in cylindrical coordinates. Amplitudes are normalised such that $e_r(r = 0) = 1$ and $e_\phi(r = 0) = 1$. The magnetic field components, h can be obtained similarly and is not shown here.

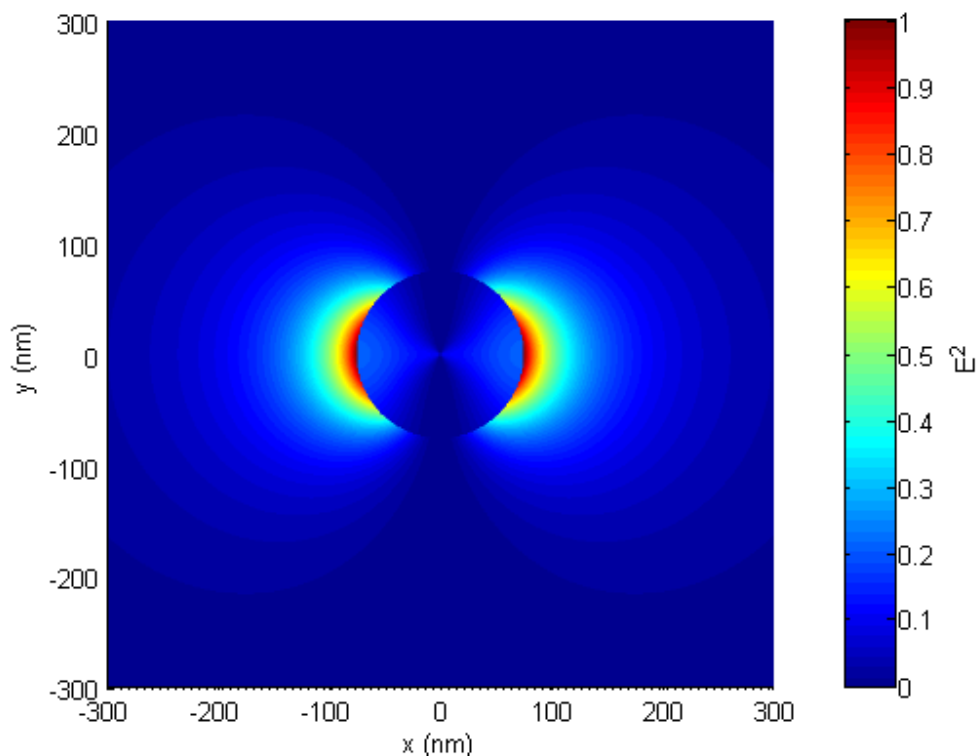


Figure 4.3: Electric field intensity of the fundamental mode at $\lambda = 890$ nm in a 150 nm diameter InP nanowire ($n_c = 3.457$) with water as surrounding medium ($n_m = 1.33$).

trapped in the evanescent field of 1064 nm wavelength light propagating down a 550 nm nanofiber (Figure 4.5), while interacting with other trapped spheres along the length of the fibre (Figure 4.6). As for Skelton’s experiment, microparticles are observed to be trapped against the fibre by the optical gradient force of the evanescent field, and propelled along it by the scattering force in the same direction as the mode propagates [38].

Despite all the potential trapping applications by evanescent fields, it remains less efficient compared to optical tweezers because evanescent fields are inherently lossy and generally only a fraction of optical power is coupled into evanescent modes. However, if evanescent field interactions are used in conjunction with conventional optical trapping, this can provide numerous advantages and it is the basis of our studies of coupled nanowire waveguides. We believe that the strong evanescent fields exhibited by single trapped InP nanowires are essential for the interaction and possible binding between multiple InP nanowires via evanescent field coupling, which will be examined in Section

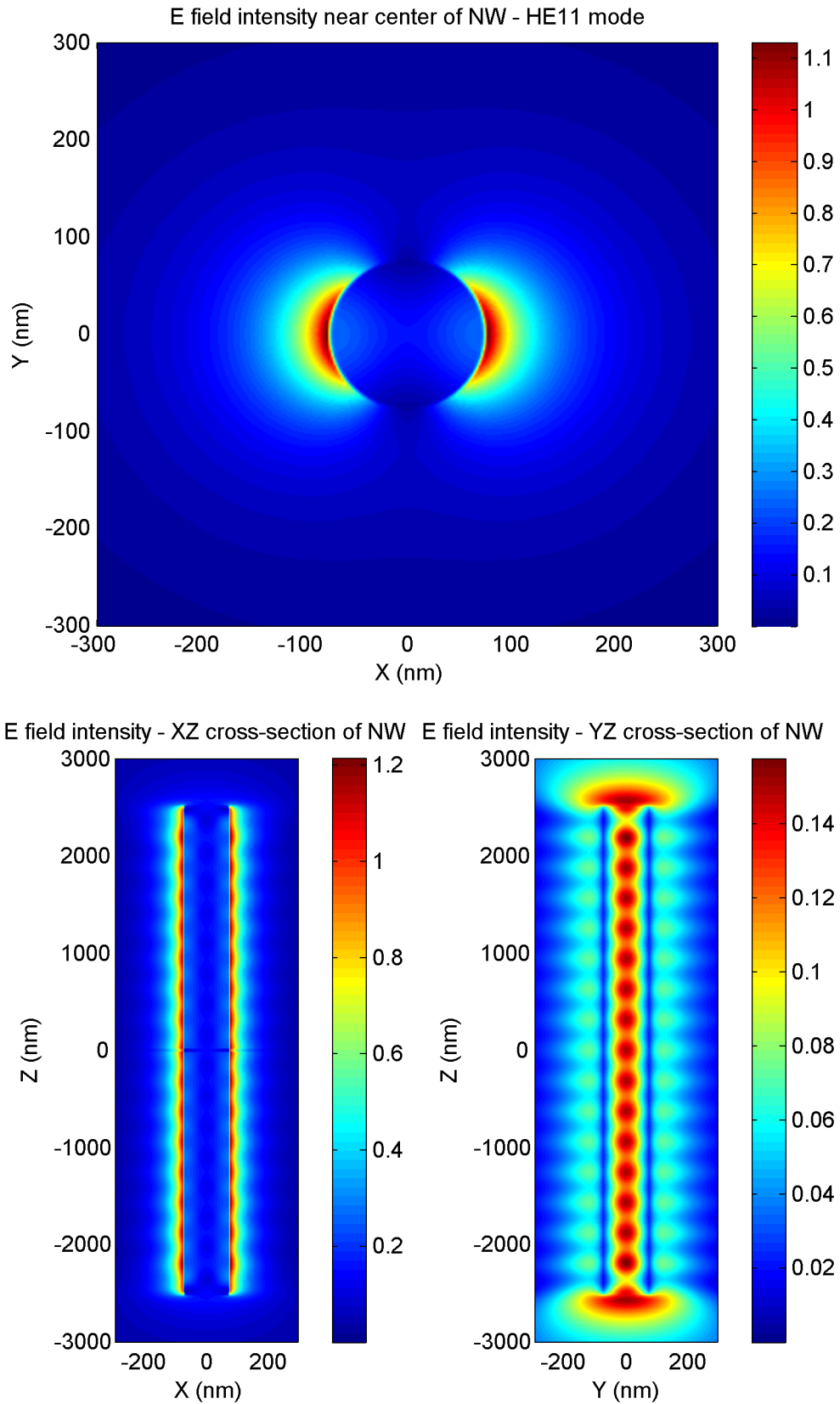


Figure 4.4: FDTD results of the electric field intensity in a 150 nm diameter InP nanowire for the same parameters presented in Figure 4.3. Figures credit: Dr. Dhruv Saxena.

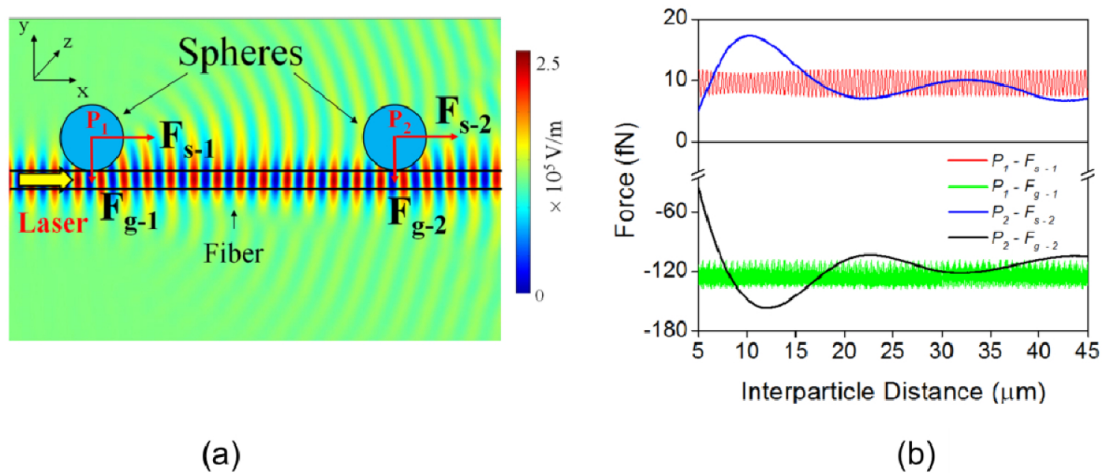


Figure 4.5: (a) Gradient forces, F_g and scattering forces, F_s on nearby particles in the nanofiber evanescent field. (b) Magnitude of gradient and scattering forces on two $3.13 \mu\text{m}$ particles in the evanescent field of a 550 nm nanofiber. Figure adapted from [31].

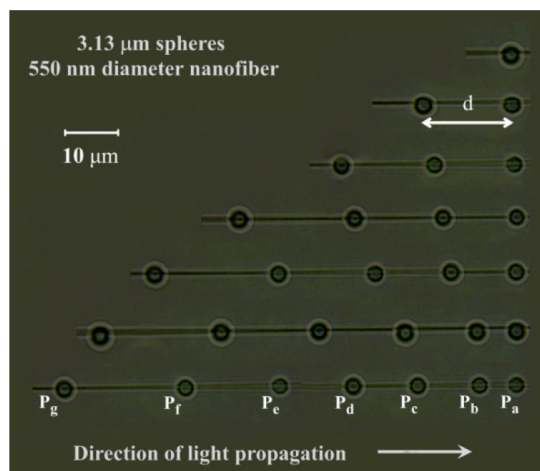


Figure 4.6: Experimental observation of SiO_2 particle chains trapped in the evanescent field of nanofiber. From top to bottom, the number of trapped particles increase from one to seven particles; the interparticle distance, d changes as new particles are added due to optical binding between trapped particles. Figure adapted from [31].

4.5 of this chapter.

4.3 Poynting vectors for InP nanowire waveguides

Apart from optical trapping, evanescent waves have also been used in sensing applications [39–41] and in these applications knowledge about the power distribution around the waveguide is critical. For our studies, we require the Poynting vector to calculate the power flow through the system in order to calculate the forces due to optical coupling for a given optical power.

In the nanowires considered in our experiments, the average energy flow in the radial and azimuthal directions are negligible so only the axial component of the Poynting vector, S_z needs to be considered [21]

Inside the nanowire where $0 < r < a$,

$$S_z = \frac{1}{2} \left(\frac{\varepsilon_0}{\mu_0} \right)^{1/2} \frac{k_0 n_c^2}{\beta J_1^2(U)} \left[a_1 a_3 J_0^2(UR) + a_2 a_4 J_2^2(UR) + \frac{1 - F_1 F_2}{2} J_0(UR) J_2(UR) \cos(2\phi) \right] \quad (4.13)$$

Outside the nanowire where $a \leq r < \infty$,

$$S_z = \frac{1}{2} \left(\frac{\varepsilon_0}{\mu_0} \right)^{1/2} \frac{k_0 n_c^2}{\beta K_1^2(W)} \frac{U^2}{W^2} \left[a_1 a_5 K_0^2(WR) + a_2 a_6 K_2^2(WR) - \frac{1 - 2\Delta - F_1 F_2}{2} K_0(WR) K_2(WR) \cos(2\phi) \right] \quad (4.14)$$

where the coordinates, R and various coefficients ($\Delta, a_1, a_2, a_3, a_4, a_5, a_6, F_1, F_2$) are defined in equation 4.12.

The profile of the Poynting vector for 150 nm diameter InP nanowires at 890 nm is shown in Figure 4.7. The mesh profile represents the propagating fields inside the nanowire, while the gradient profile represents the evanescent fields outside the nanowire in water. It can be seen from the plot that there are large evanescent fields up to two radii away from the centre of the nanowire, and extends up to 500 nm away. Compared to the Poynting vector for 300 nm diameter nanowires shown in Figure 4.8, we see that in this case most of the optical power is transmitted within the waveguide with little evanescent fields that become insignificant beyond 50 nm from the edge of the nanowire.

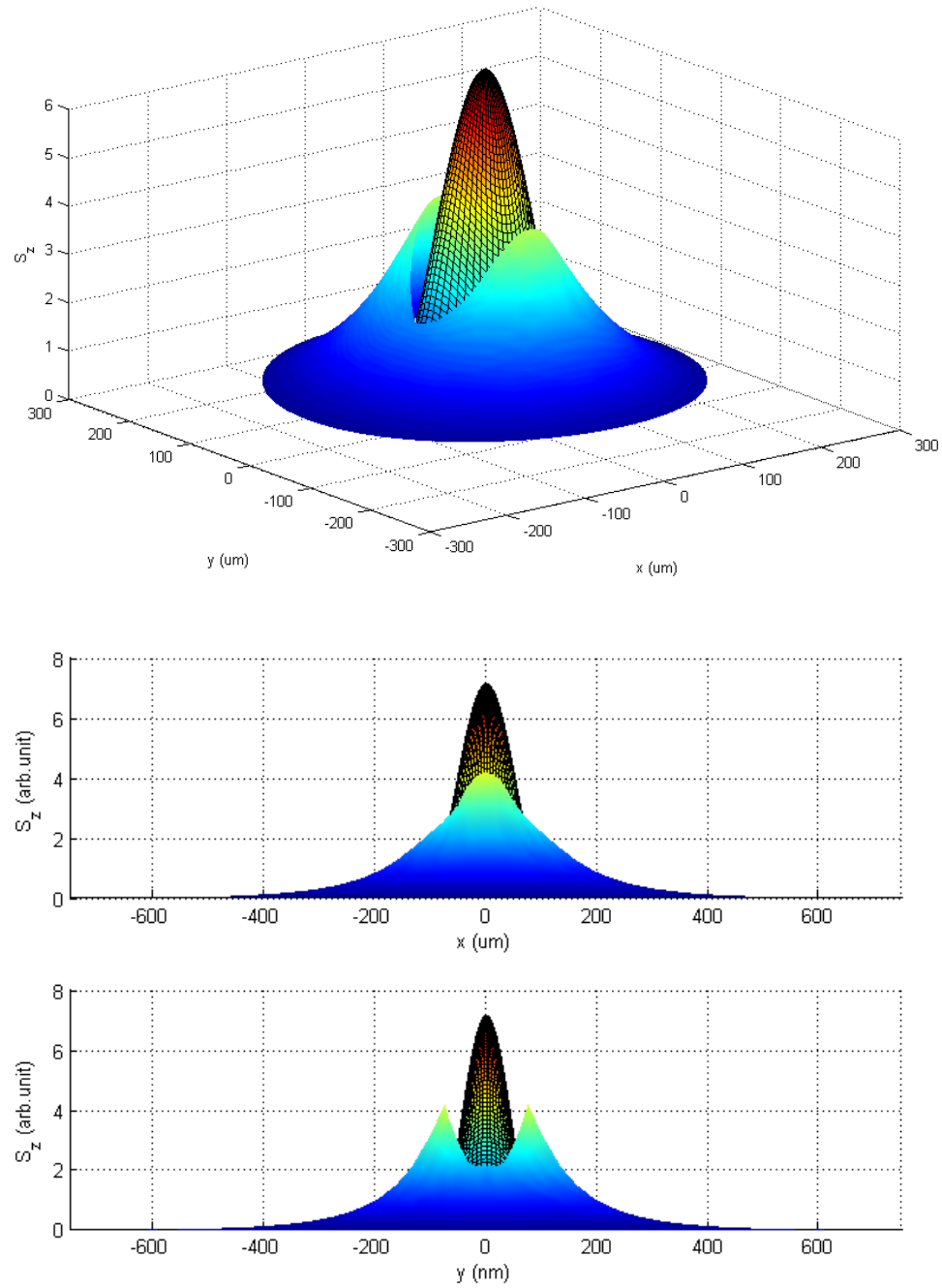


Figure 4.7: Poynting vectors of 150 nm nanowires in the axial direction. Also shown are the projections onto the xz and yz planes. From the figures it can be seen that the evanescent fields are significant within twice the radii outside the nanowire, and extend out to 500 nm.

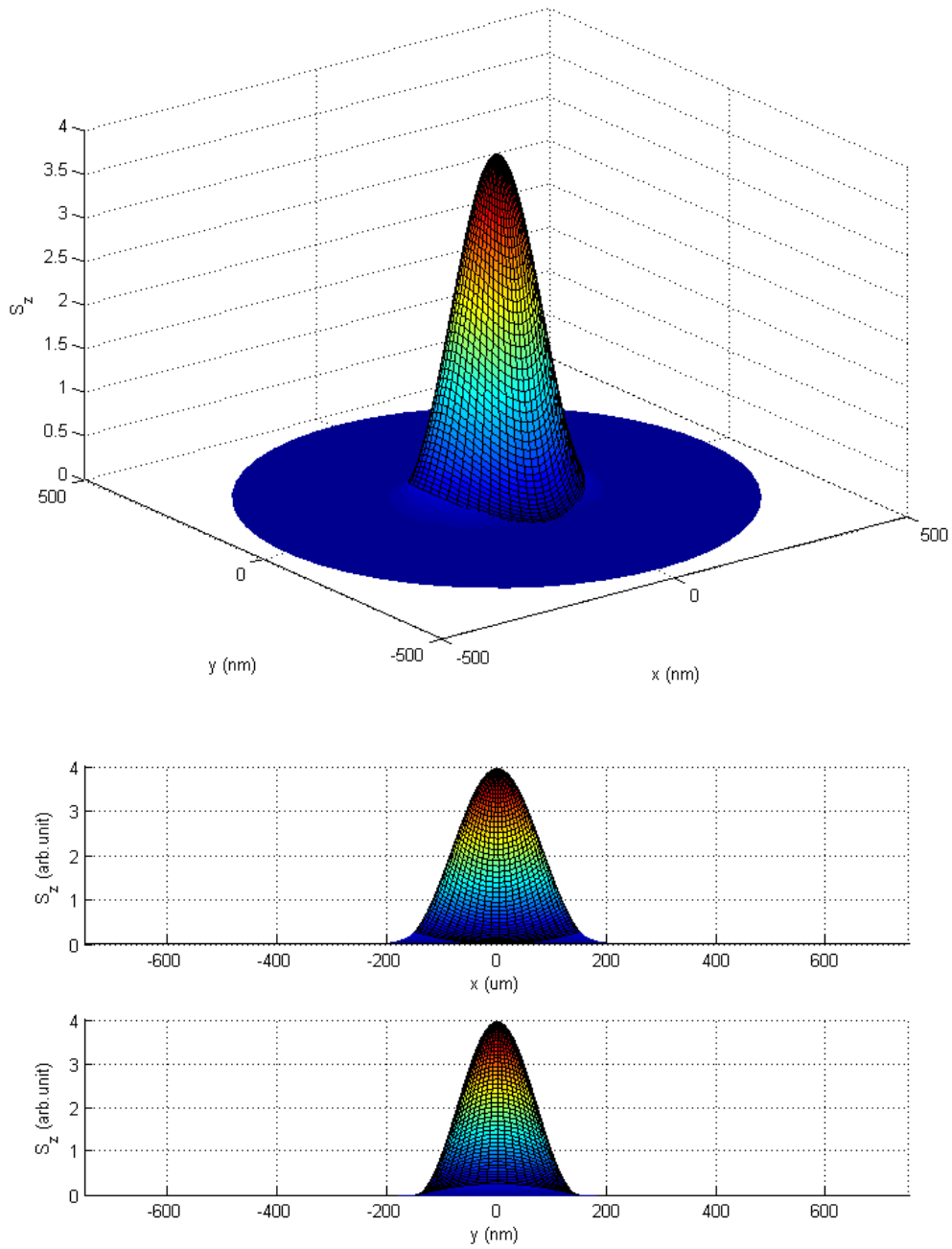


Figure 4.8: Poynting vectors of 300 nm nanowires in the axial direction. Also shown are the projections onto the xz and yz planes. From the figures it can be seen that the evanescent fields are weak and become insignificant beyond 50 nm from the nanowire.

4.4 Dispersion and group velocity of InP nanowire waveguides

The dispersion and group velocity, v_g of optical waveguides are important quantities in many applications; for our studies, the dispersion and group velocity of the guided mode is used to calculate the optical forces on coupled waveguides later in Section 4.12. By definition, the group velocity is the speed at which the power of a mode is transmitted along an optical waveguide [30]. The group velocity for the j th mode is given as

$$v_{gj} = \frac{d\omega}{d\beta_j} = \frac{-2\pi c}{\lambda^2} \frac{d\lambda}{d\beta_j} \quad (4.15)$$

where ω is the angular frequency, λ is the free space wavelength and β_j is the propagation constant of the j th mode [30].

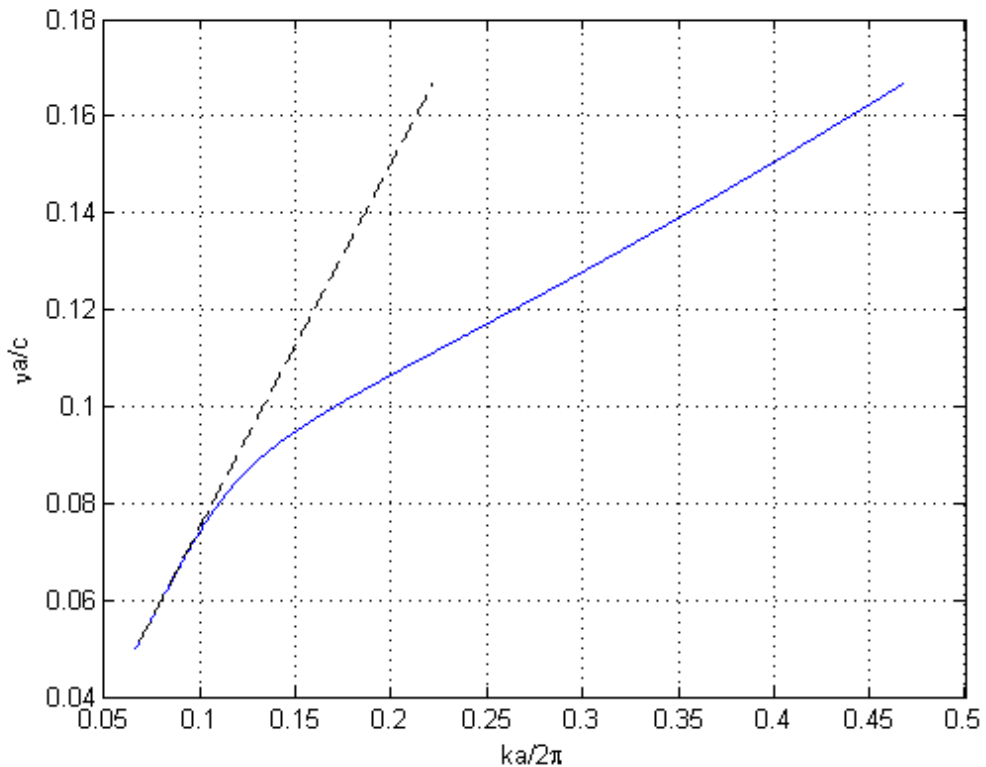


Figure 4.9: Dispersion relation of the fundamental mode in InP nanowire waveguides, normalised to nanowire radii, a . The dashed lines indicate the light cone for a plane wave in the surrounding medium i.e. deionised water.

Once again, for our studies we are interested in the waveguiding properties of optically trapped InP nanowires in deionised water. By numerically solving the scalar wave equation (Equation 4.6) for all wavelengths, we obtain the propagation constants and establish the dispersion relation for our InP nanowire waveguides, shown in Figure 4.9. We then calculated the group velocity for single mode InP nanowires of diameters 150 nm, 160 nm, 200 nm and 300 nm with the results shown in Figure 4.10 (shown as radii $a = 75$ nm, 80 nm, 100 nm, 150 nm).

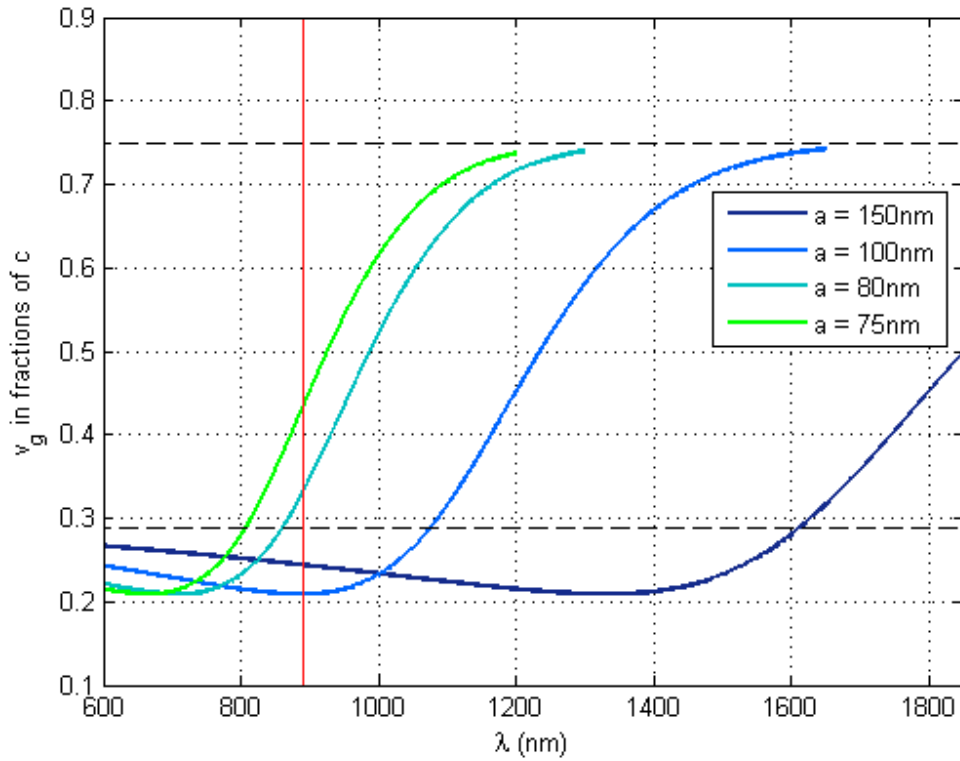


Figure 4.10: Group velocity of the fundamental mode in InP nanowires of radius, $a = 75$ nm, 80 nm, 100 nm, and 150 nm, shown as fractions of c . Two dashed horizontal lines mark the group velocity of plane waves in the surrounding medium, c/n_m and in bulk InP, c/n_c . The red vertical line marks $\lambda = 890$ nm.

From Figure 4.10 it can be seen that for a given nanowire diameter, v_g approaches the plane wave velocity in the surrounding medium c/n_m (i.e. water) as the wavelength increases to values much larger than the diameter of the nanowire. On the other hand, v_g approaches c/n_c when the wavelength is very small, with a minimum value smaller than c/n_c . We also see that for a fixed wavelength, v_g falls from c/n_m with decreasing nanowire diameter until it reaches a minimum value smaller than c/n_c before approaching c/n_c again as the diameter is further reduced.

4.5 Coupling between two InP nanowire waveguides

Consider two identical parallel nanowire waveguides separated by a distance d , illustrated in Figure 4.11. If the waveguides are optically well separated i.e. the contribution from one waveguide to the field at the centre of the second waveguide is small, and if they are also weakly guiding then the fields of the composite waveguide are well approximated by a superposition of the fields of each waveguide in isolation [30]. Since the two waveguides are identical, the symmetry of the system requires that the two fundamental solutions Ψ_+ and Ψ_- of the scalar wave equation are given by

$$\Psi_+ = \bar{\Psi}_1 + \bar{\Psi}_2 \quad (4.16a)$$

$$\Psi_- = \bar{\Psi}_1 - \bar{\Psi}_2 \quad (4.16b)$$

where $\bar{\Psi}_1$ and $\bar{\Psi}_2$ are fundamental solutions for each waveguide in isolation.

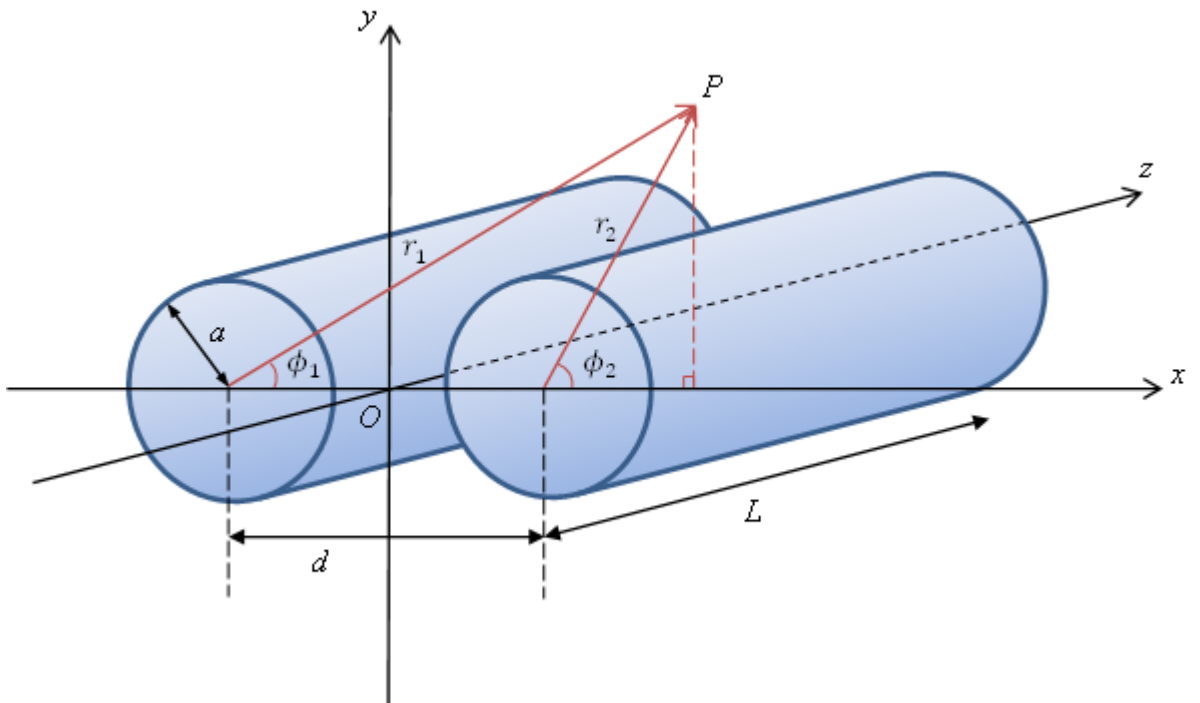


Figure 4.11: Nomenclature and coordinates for describing our system of two coupled nanowire waveguides.

4.5.1 Conditions for weak coupling

There has been extensive studies in the literature on the Coupled Mode Theory (CMT) for optical waveguides [42–52], which is generally only applicable to weakly coupling, weakly guiding waveguide pairs. Weak coupling implies the evanescent fields from one waveguide do not contribute significantly to the fields within the core of the second coupled waveguide as within the framework of the CMT, the fields from the first waveguide is not subjected to the boundary conditions at the core-cladding interface of the second waveguide [46] thus leading to a deviation from the full analytical result.

Generally, weak coupling applies when the separation between waveguides d is much larger than the radii of each individual waveguide a [46, 52], $d \gg a$. We extend that condition based on our system that since our InP nanowire waveguides have very weak guided modes in the core i.e. the field intensity is low inside the core (as seen in Section 4.2), the weak coupling condition is still applicable and the CMT remains a good approximation at separations larger than but comparable to the radius.

4.6 Coupling constant of coupled InP nanowire waveguides

For weakly coupled nanowire waveguides, we can consider one nanowire as a perturbation introduced onto the other nanowire. Thus, the propagation constants β_+ and β_- of the two fundamental solutions Ψ_+ and Ψ_- can be well approximated as a perturbation of the propagation constant of a single nanowire in isolation, β [30, 46].

$$\beta_{\pm} = \beta \pm C \quad (4.17)$$

Where C is the perturbation factor also known as the coupling constant given as

$$C = k \left\{ \int_{A_{\infty}} (n(r) - \bar{n}_{c1}) \bar{\Psi}_1 \bar{\Psi}_2 dA / \int_{A_{\infty}} \bar{\Psi}_1^2 dA \right\} \quad (4.18)$$

Here \bar{n}_{c1} is the refractive index of the first nanowire before perturbation and $\bar{\Psi}_1$, $\bar{\Psi}_2$ are the solutions to the scalar wave equation of the nanowires before perturbation [30].

For two identical step index nanowires with radius a and refractive index $n(r)$ as described in equation 4.18, C can be reduced into the following form [30]

$$C = \frac{(2\Delta)^{1/2} U^2 K_0(Wd/a)}{a V^3 K_1^2(W)} \quad (4.19)$$

The coupling constants for two identical InP nanowires at 890 nm wavelength for a range of nanowire radius, a and core to core separation, d is calculated and plotted in Figure 4.12 and Figure 4.13 below. It should be noted that in Figure 4.13, the white region in the upper left corner represents core-to-core separations less than the sum of radii of both nanowires i.e. the nanowires are intersecting, which is not allowed since our nanowires are hard solids.

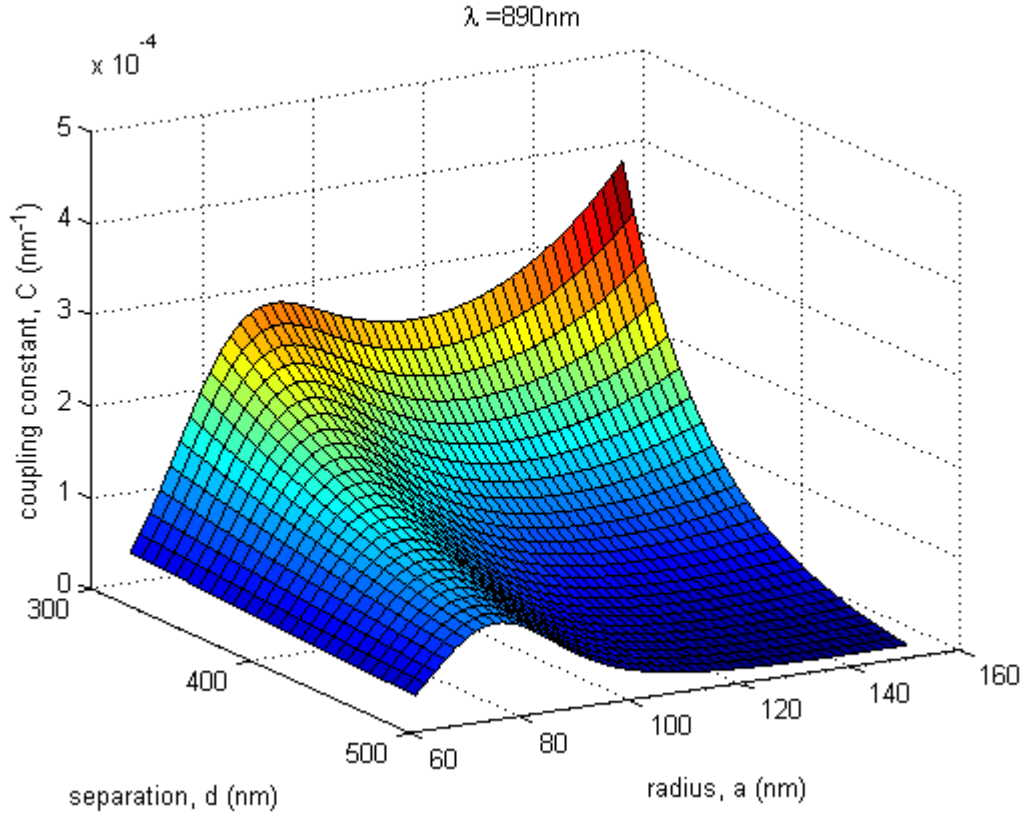


Figure 4.12: Coupling constants of two identical InP nanowires at 890 nm wavelength as a function of nanowire radius and nanowire separation.

From Figure 4.12, we see that for a fixed core-to-core separation the coupling constant reaches a local maxima when the radii a of the nanowires are between 70 and 100 nm, and reaches another maxima when the edges of the nanowires are touching.

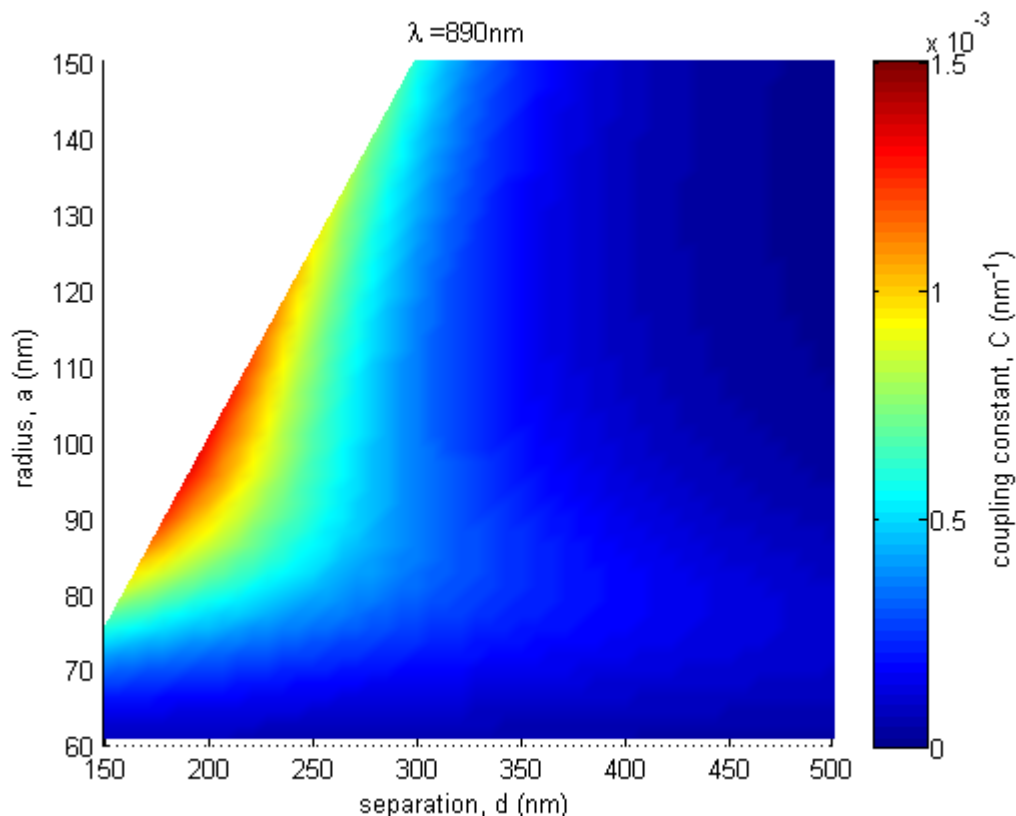


Figure 4.13: Coupling constants of two identical InP nanowires at 890 nm wavelength as a function of nanowire radius and nanowire separation, as in Figure 4.12 but also includes data for separations $d < 300$ nm. We model our nanowires as hard solids and do not intersect, so d cannot be less than twice the radius a which is depicted as the white region in the plot.

Furthermore, the coupling constant decreases with increasing separation, and the rate of decrease is higher when the radii of the nanowires are larger. From Figure 4.13 we see that the absolute maximum coupling constant is achieved if we use 100 nm radii nanowires and take the separation of these nanowires to the limit where they are touching. On the other hand, we see from Figure 4.12 that nanowires of around 75 nm appears to be better at retaining a significant coupling constant for larger separations between 300 and 500 nm. These observations can be explained by considering the mode profile of the guided modes of individual nanowires as presented in Section 4.2.

The coupling efficiency of light from one waveguide to another is a compromise between the strength of the propagation mode within the waveguide and the evanescent modes outside the waveguide. When the diameter of the waveguide is large, the guided mode is well confined within the waveguide while the evanescent field is small and decays rapidly over a short distance away from the edge of the waveguide resulting a

rapid decline in coupling efficiency as the separation between nanowires is increased. On the opposing limit when the diameter of the waveguide is small, the guided mode is weak and the evanescent field from a nearby waveguide does not couple into the guided mode efficiently.

4.7 Mode profiles of coupled InP nanowire waveguides

As mentioned in Section 4.5, the solutions of the fundamental modes for two identical coupled waveguides can be calculated from the solutions for each waveguide in isolation.

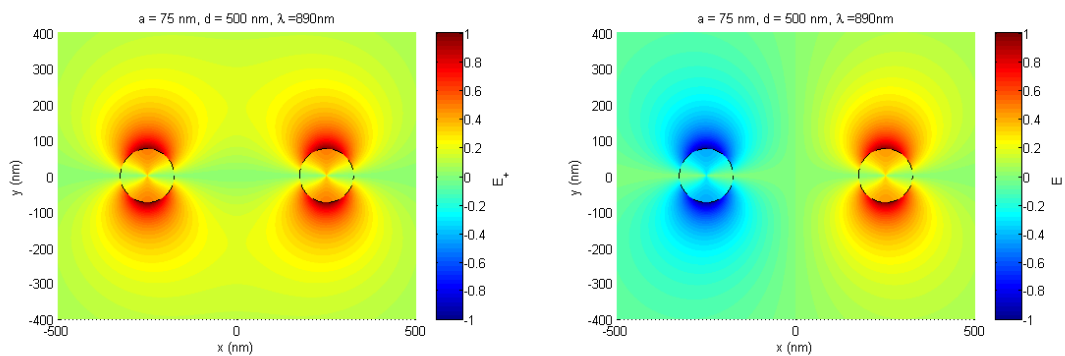
$$\Psi_+ = \bar{\Psi}_1 + \bar{\Psi}_2 \quad (4.20a)$$

$$\Psi_- = \bar{\Psi}_1 - \bar{\Psi}_2 \quad (4.20b)$$

where $\bar{\Psi}_1$ and $\bar{\Psi}_2$ are fundamental solutions for each waveguide in isolation, given by Equations 4.7 to 4.11 in Section 4.2.

Using these equations on a set of common axes, we calculated the fundamental mode profiles of two identical waveguides for the propagation of $\lambda = 890$ nm for our InP nanowire waveguides under a few different nanowire radius and separation. Recall that the refractive indices of the nanowires are $n_c = 3.457$, and the system is submerged in water as the surrounding medium, $n_m = 1.33$. For each set of nanowire radii a and separation d , we calculate and plot the mode profile for the symmetric and antisymmetric modes. The results are shown in the following figures.

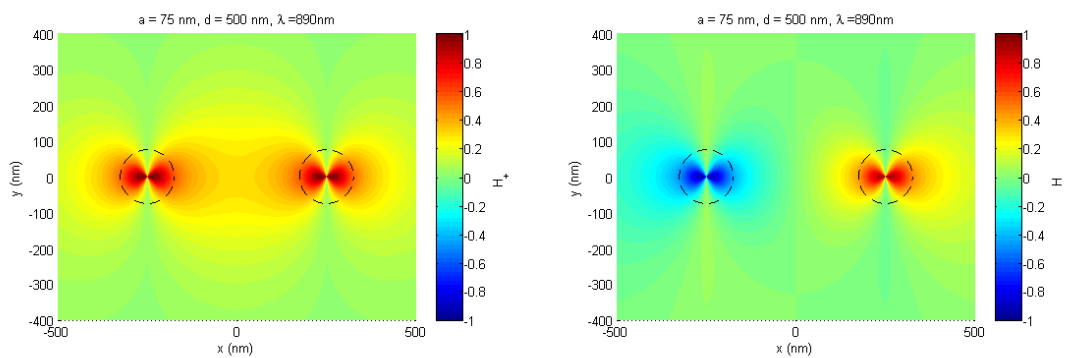
We also compared the electric field intensity E^2 for a composite waveguide system consisting of two 150 nm diameter nanowires separated by 300 nm from our calculations with FDTD simulations, shown in Figure 4.22. The mesh size for the FDTD simulations is 2.5 nm which covers the entire cross section of both nanowires. From the figures we can see that there is good agreement between our calculations and simulated results.



(a) Symmetric mode

(b) Anti-symmetric mode

Figure 4.14: Electric field of the symmetric and anti-symmetric modes at $\lambda = 890$ nm in a pair of coupled 150 nm diameter InP nanowires separated by 500 nm from core to core, with water as the surrounding medium. The black dashed lines indicate the nanowire perimeters.



(a) Symmetric mode

(b) Anti-symmetric mode

Figure 4.15: Magnetic field of the symmetric and anti-symmetric modes at $\lambda = 890$ nm in a pair of coupled 150 nm diameter InP nanowires separated by 500 nm from core to core, with water as the surrounding medium. The black dashed lines indicate the nanowire perimeters.

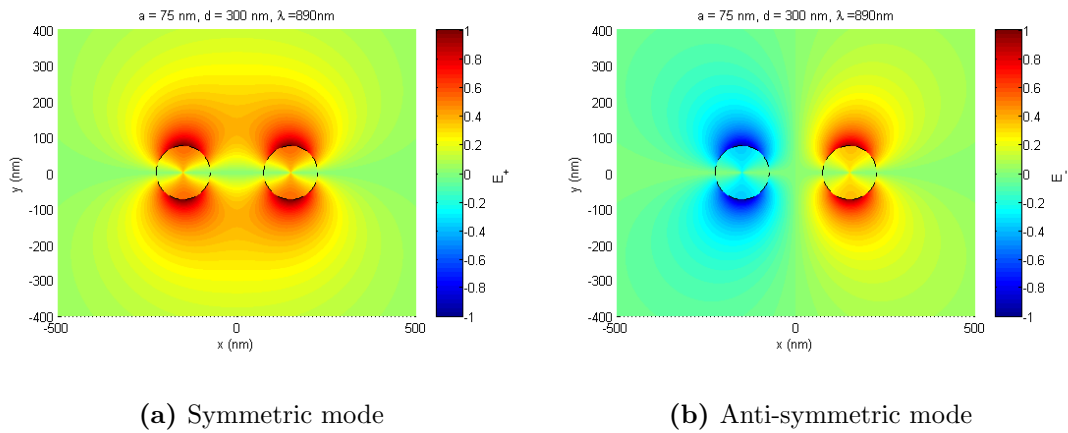


Figure 4.16: Electric field of the symmetric and anti-symmetric modes at $\lambda = 890$ nm in a pair of coupled 150 nm diameter InP nanowires separated by 300 nm from core to core, with water as the surrounding medium. The black dashed lines indicate the nanowire perimeters.

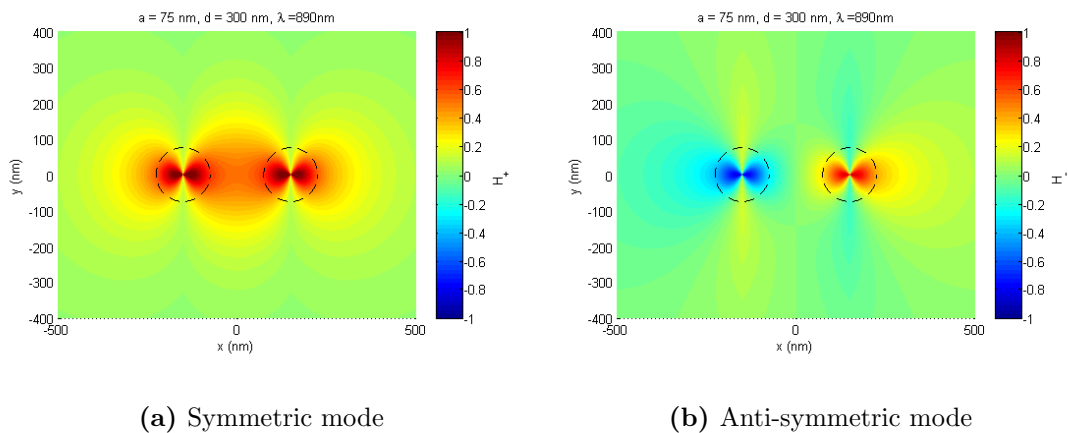
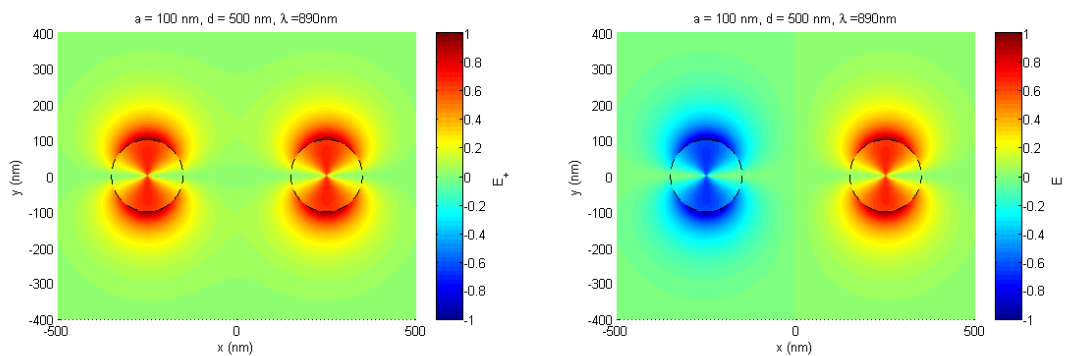


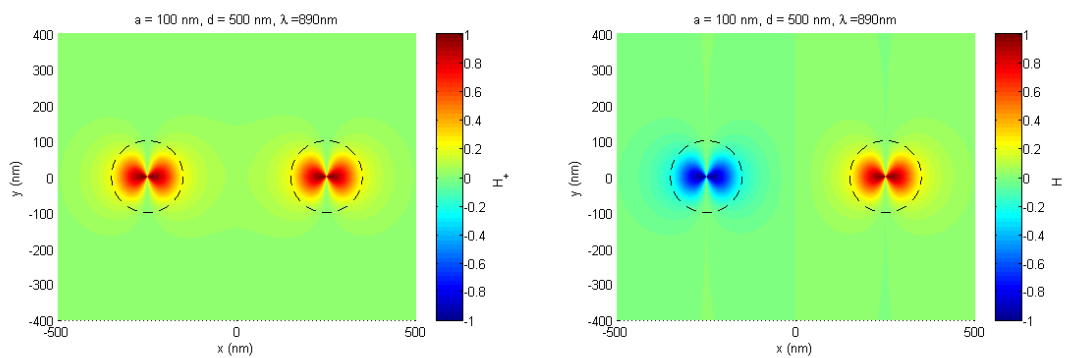
Figure 4.17: Magnetic field of the symmetric and anti-symmetric modes at $\lambda = 890$ nm in a pair of coupled 150 nm diameter InP nanowires separated by 300 nm from core to core, with water as the surrounding medium. The black dashed lines indicate the nanowire perimeters.



(a) Symmetric mode

(b) Anti-symmetric mode

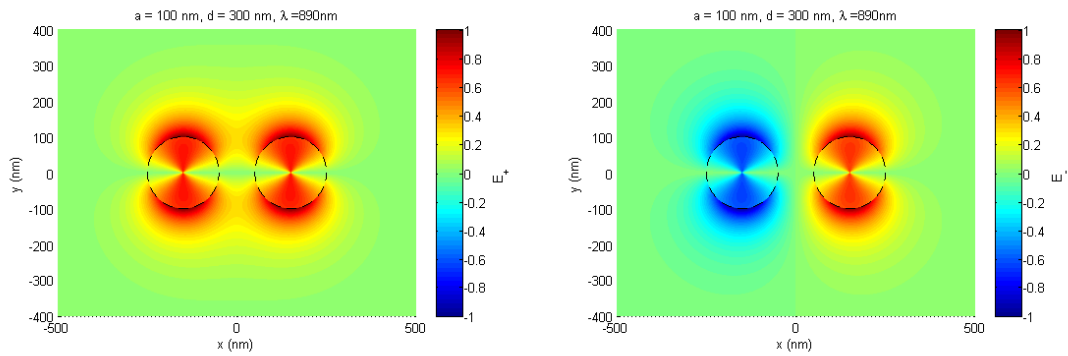
Figure 4.18: Electric field of the symmetric and anti-symmetric modes at $\lambda = 890$ nm in a pair of coupled 200 nm diameter InP nanowires separated by 500 nm from core to core, with water as the surrounding medium. The black dashed lines indicate the nanowire perimeters.



(a) Symmetric mode

(b) Anti-symmetric mode

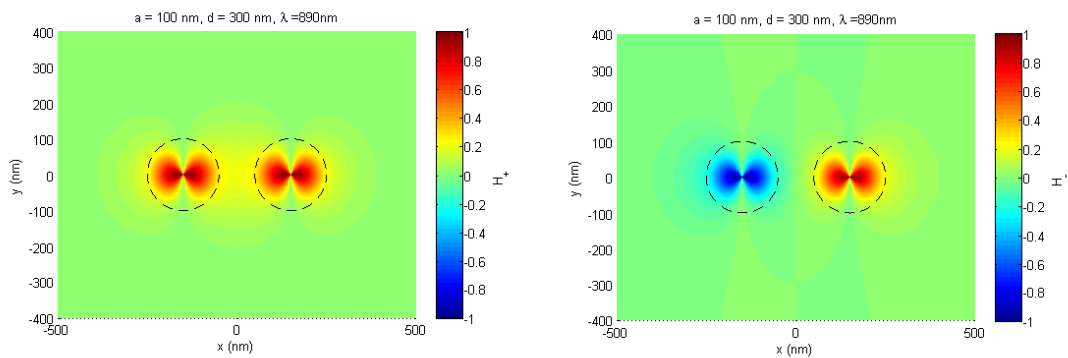
Figure 4.19: Magnetic field of the symmetric and anti-symmetric modes at $\lambda = 890$ nm in a pair of coupled 200 nm diameter InP nanowires separated by 500 nm from core to core, with water as the surrounding medium. The black dashed lines indicate the nanowire perimeters.



(a) Symmetric mode

(b) Anti-symmetric mode

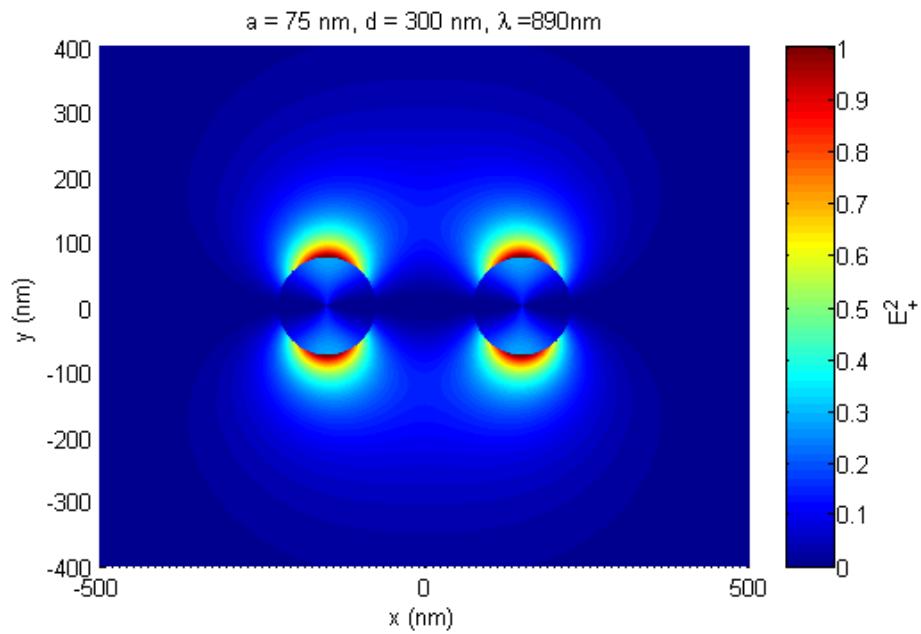
Figure 4.20: Electric field of the symmetric and anti-symmetric modes at $\lambda = 890$ nm in a pair of coupled 200 nm diameter InP nanowires separated by 300 nm from core to core, with water as the surrounding medium. The black dashed lines indicate the nanowire perimeters.



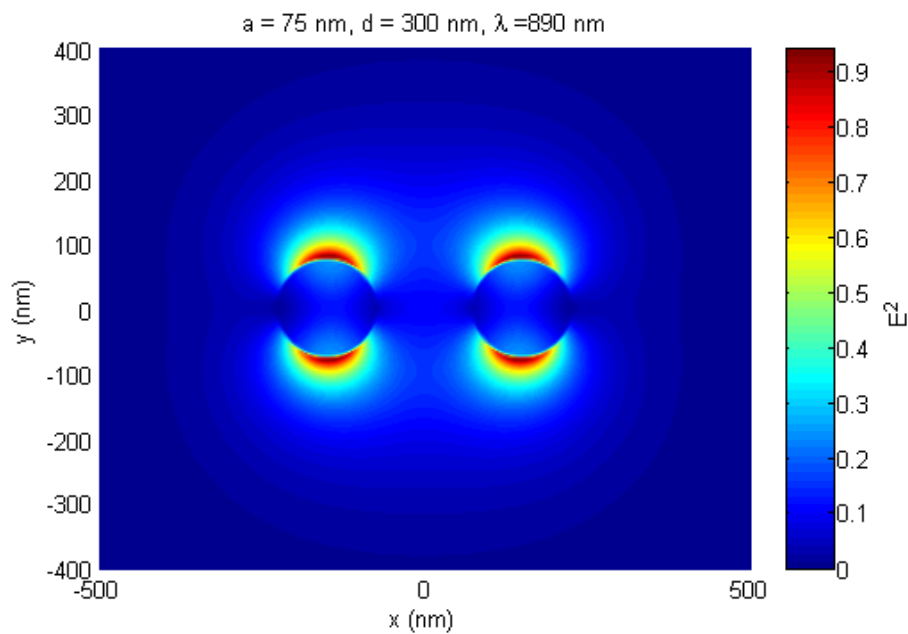
(a) Symmetric mode

(b) Anti-symmetric mode

Figure 4.21: Electric field of the symmetric and anti-symmetric modes at $\lambda = 890$ nm in a pair of coupled 200 nm diameter InP nanowires separated by 300 nm from core to core, with water as the surrounding medium. The black dashed lines indicate the nanowire perimeters.



(a) Our calculations



(b) FDTD simulation results

Figure 4.22: Comparison between analytical calculations and FDTD simulations of the electric field intensity in a pair of coupled 200 nm diameter InP nanowires at $\lambda = 890 \text{ nm}$, separated by 300 nm from core to core with water as the surrounding medium. From the figures we can see that there is good agreement between the two results.

4.8 Optical force calculations from Maxwell's Stress Tensor

In our system of two nanowire waveguides, we are interested in calculating the force experienced by one of the nanowires due to the presence of the other nanowire. One approach is by considering the perturbation in the eigenmode frequency of the waveguide due to changes in the separation between the individual nanowire waveguides, which will be discussed later in Section 4.12. The other approach to calculating the optical forces can be achieved by considering Maxwell's Equations.

Knowledge about the electromagnetic fields of the two-nanowire system as shown in Section 4.7 allows us to calculate the total force due to electromagnetic fields using Maxwell's Stress Tensor. From the Lorentz force law,

$$\mathbf{F} = \int_{\mathcal{V}} \rho (\mathbf{E} + \mathbf{v} \times \mathbf{B}) d^3\mathbf{r} \quad (4.21)$$

$$= \int_{\mathcal{V}} (\rho \mathbf{E} + \mathbf{J} \times \mathbf{B}) d^3\mathbf{r} \quad (4.22)$$

where \mathbf{v} is the velocity of the charge element. The terms in the integral can be expressed entirely using Maxwell's equations [53]:

$$\rho = \epsilon_0 \nabla \cdot \mathbf{E} \quad (4.23a)$$

$$\mathbf{J} = \frac{1}{\mu_0} \nabla \times \mathbf{B} - \epsilon_0 \frac{\partial \mathbf{E}}{\partial t} \quad (4.23b)$$

Substituting Equations 4.23b into Equation 4.22 and rearranging [53], the force becomes

$$\mathbf{F} = \int_{\mathcal{S}} \overleftrightarrow{\mathbf{T}} \cdot d\mathbf{a} - \epsilon_0 \mu_0 \frac{\partial}{\partial t} \int_{\mathcal{V}} \mathbf{S} d^3\mathbf{r} \quad (4.24)$$

where \mathcal{V} is the volume containing the electromagnetic fields, \mathcal{S} is any surface that encloses only the charges and currents within \mathcal{V} , and $\overleftrightarrow{\mathbf{T}}$ is the Maxwell's Stress Tensor with components defined by

$$T_{ij} \equiv \epsilon_0 \left(E_i E_j - \frac{1}{2} \delta_{ij} E^2 \right) + \frac{1}{\mu_0} \left(B_i B_j - \frac{1}{2} \delta_{ij} B^2 \right) \quad (4.25)$$

The full derivation of Equation 4.24 from Equations 4.22 and 4.23b is shown in Appendix A.

In our system of two nanowire waveguides, the force experienced by one of the nanowires can be calculated from the perturbation of the electromagnetic fields due to the presence of the second nanowire using Maxwell's Stress Tensor. Since our nanowire waveguides are illuminated by a continuous wave laser, we can assume that the power flowing through the system is constant over time, so $\partial \mathbf{S} / \partial t = 0$ and

$$\mathbf{F} = \int_S \overleftarrow{\mathbf{T}} \cdot d\mathbf{a} \quad (4.26)$$

In other words, the force experienced by a nanowire is given by the sum of the force density over the surface area of the nanowire. To calculate the force, recall from Figure 4.11 that our nanowires are approximated as cylinders. The surface element $d\mathbf{a}$ of the curved surface of a cylinder is given as

$$d\mathbf{a} = a \, d\phi \, dz \, \hat{\mathbf{r}} \quad (4.27a)$$

$$\hat{\mathbf{r}} = \cos \phi \, \hat{\mathbf{x}} + \sin \phi \, \hat{\mathbf{y}} \quad (4.27b)$$

Due to the symmetry of the system, we only expect the force to be non zero in the direction of separation which is in the x direction, hence we only need to consider $\left(\overleftarrow{\mathbf{T}} \cdot d\mathbf{a} \right)_x$

$$\left(\overleftarrow{\mathbf{T}} \cdot d\mathbf{a} \right)_x = T_{xx} da_x + T_{xy} da_y + T_{xz} da_z \quad (4.28)$$

$$= T_{xx} a \, d\phi \, dz \, \cos \phi + T_{xy} a \, d\phi \, dz \, \sin \phi \quad (4.29)$$

Hence, the force on a nanowire due to the presence of the second nanowire is given by

$$F = F_x = \iint_S (T_{xx} \cos \phi + T_{xy} \sin \phi) a \, d\phi \, dz \quad (4.30)$$

$$= a \int_0^{2\pi} (T_{xx} \cos \phi + T_{xy} \sin \phi) \, d\phi \int_0^L dz \quad (4.31)$$

$$\therefore F = aL \int_0^{2\pi} (T_{xx} \cos \phi + T_{xy} \sin \phi) \, d\phi \quad (4.32)$$

Using Equation 4.32 and the electromagnetic fields calculated in Section 4.7, we calculated the optical forces between 75 nm, 100 nm and 150 nm radius InP nanowire waveguides for a range of waveguide separations. The results are normalised with respect to power by integrating the Poynting vector (Section 4.3) to obtain the normalisation constant. The results are presented in Figure 4.23 in force per μm length of nanowire waveguide per mW of optical power coupled into the system.

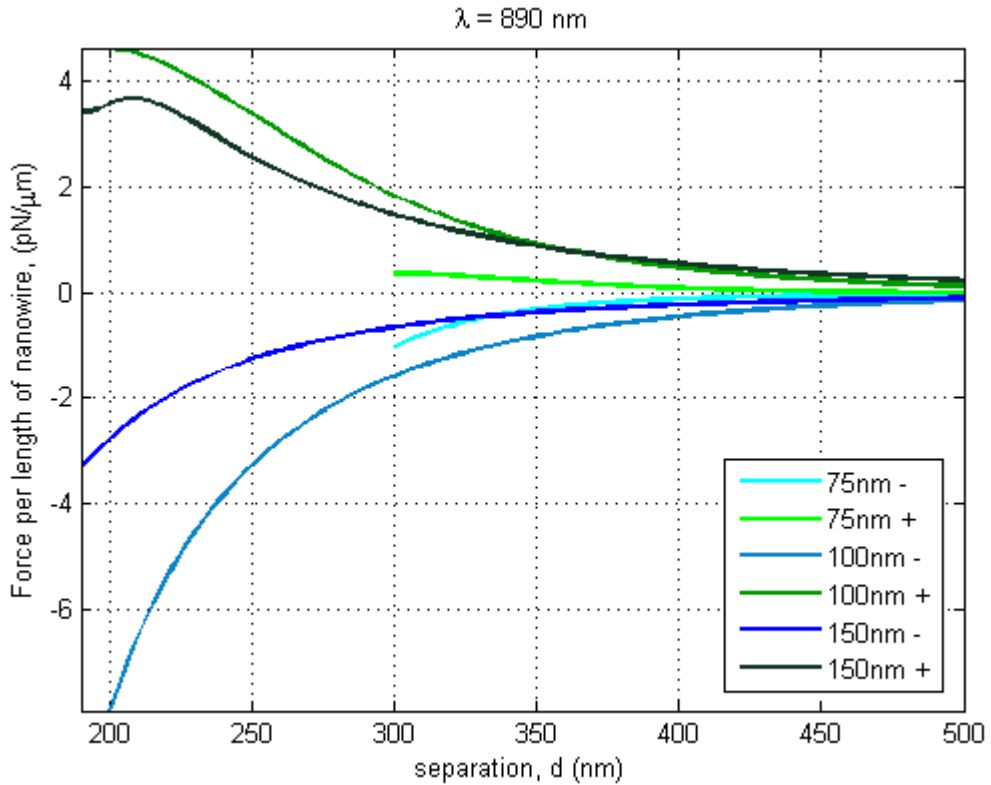


Figure 4.23: Optical forces per length from symmetric (+) and antisymmetric (-) modes of coupled 75 nm, 100 nm and 150 nm InP nanowires as a function of separation d , per mW of optical power coupled into the waveguides. From the figure we see that for all nanowire radii, symmetric modes lead to negative forces which are attractive while anti-symmetric modes lead to positive forces which are repulsive.

4.9 Power transfer between coupled nanowires and beat length

The power flow through each nanowire waveguide $P_1(z)$ and $P_2(z)$ can be obtained by integrating the intensity of the field over the cross section of the nanowire. To achieve this we first consider the magnitude of the total transverse electric field E at any point, given by [30]

$$E = b_+ \Psi_+ e^{i\beta_+ z} + b_- \Psi_- e^{i\beta_- z} \quad (4.33)$$

Where b_{\pm} are modal amplitudes, $\Psi_{\pm} = \bar{\Psi}_1 \pm \bar{\Psi}_2$ are fundamental solutions to the two coupled waveguide system and $\beta_{\pm} = \beta \pm C$ are the propagation constants associated with the fundamental solutions (given in Equation 4.17). We also make the assumption that only the first nanowire is illuminated at the endface $z = 0$, so $E_2(z = 0) = 0$.

Since the waveguides are weakly coupling, in the proximity close to the second nanowire the contribution from the first nanowire is small i.e. $\bar{\Psi}_1 \approx 0$. So $\Psi_+ \approx -\Psi_- \approx \bar{\Psi}_2$. Also at $z = 0$, $b_+ \approx b_-$. If we substitute all of the above into Equation 4.33, E_2 around the second nanowire becomes

$$E_2 = b_+ \bar{\Psi}_2 e^{i(\beta+C)z} - b_+ \bar{\Psi}_2 e^{i(\beta-C)z} \quad (4.34a)$$

$$= b_+ \bar{\Psi}_2 e^{i\beta z} (e^{iCz} - e^{-iCz}) \quad (4.34b)$$

Similarly around the first nanowire $\bar{\Psi}_2 \approx 0$, therefore $\Psi_+ \approx \Psi_- \approx \bar{\Psi}_1$ and E_1 becomes

$$E_1 = b_+ \bar{\Psi}_1 e^{i\beta z} (e^{iCz} + e^{-iCz}) \quad (4.35)$$

Applying Euler's formula on Equations 4.35 and 4.34 gives

$$E_1 = 2b_+ \bar{\Psi}_1 e^{i\beta z} \cos(Cz) \quad (4.36a)$$

$$E_2 = 2ib_+ \bar{\Psi}_2 e^{i\beta z} \sin(Cz) \quad (4.36b)$$

From Equation 4.36 we can then integrate the field intensity for each nanowire waveguide and obtain the power flow along the two nanowire configuration. Assuming no net power loss, the power is given as the following

$$P_1(z) = P \cos^2(Cz) \quad (4.37a)$$

$$P_2(z) = P \sin^2(Cz) \quad (4.37b)$$

Where $P_1(z)$ is the power in one nanowire, $P_2(z)$ is the power along the second nanowire and C is the coupling constant.

A useful quantity from an experimental stand point is the beat length L_0 of coupled nanowire waveguides, which is defined as the length along the waveguide where there is total transfer of power from one waveguide to the other and back [30]. Hence, the beat length L_0 is given as

$$L_0 = \frac{2\pi}{C} \quad (4.38)$$

In Figure 4.24, the beat length is plotted as a function of the radius of the nanowires and the separation between both nanowires. We require the lengths of the nanowire waveguides to be greater than the beat length so that a large power transfer between the two nanowires can occur, and the coupling effects can be observed experimentally. It is evident from the figure that minimising the separation between adjacent nanowire waveguides minimises the beat length and hence the distance for which full power transfer occurs between two waveguides. Larger nanowire radii result in smaller beat length when the separation is small (< 300 nm), but increases much more rapidly with separation.

In terms of proximity sensing applications, nanowires of larger radii have greater sensitivity while nanowires of 75 nm radius can be used to sense larger distances. Since our nanowires are typically 10 μm in length, it can be seen from Figure 4.24 that if the separation between nanowires is greater than 500 nm then the beat length becomes much larger than the length of the nanowires and as a result very little power will be coupled into the unilluminated nanowire.

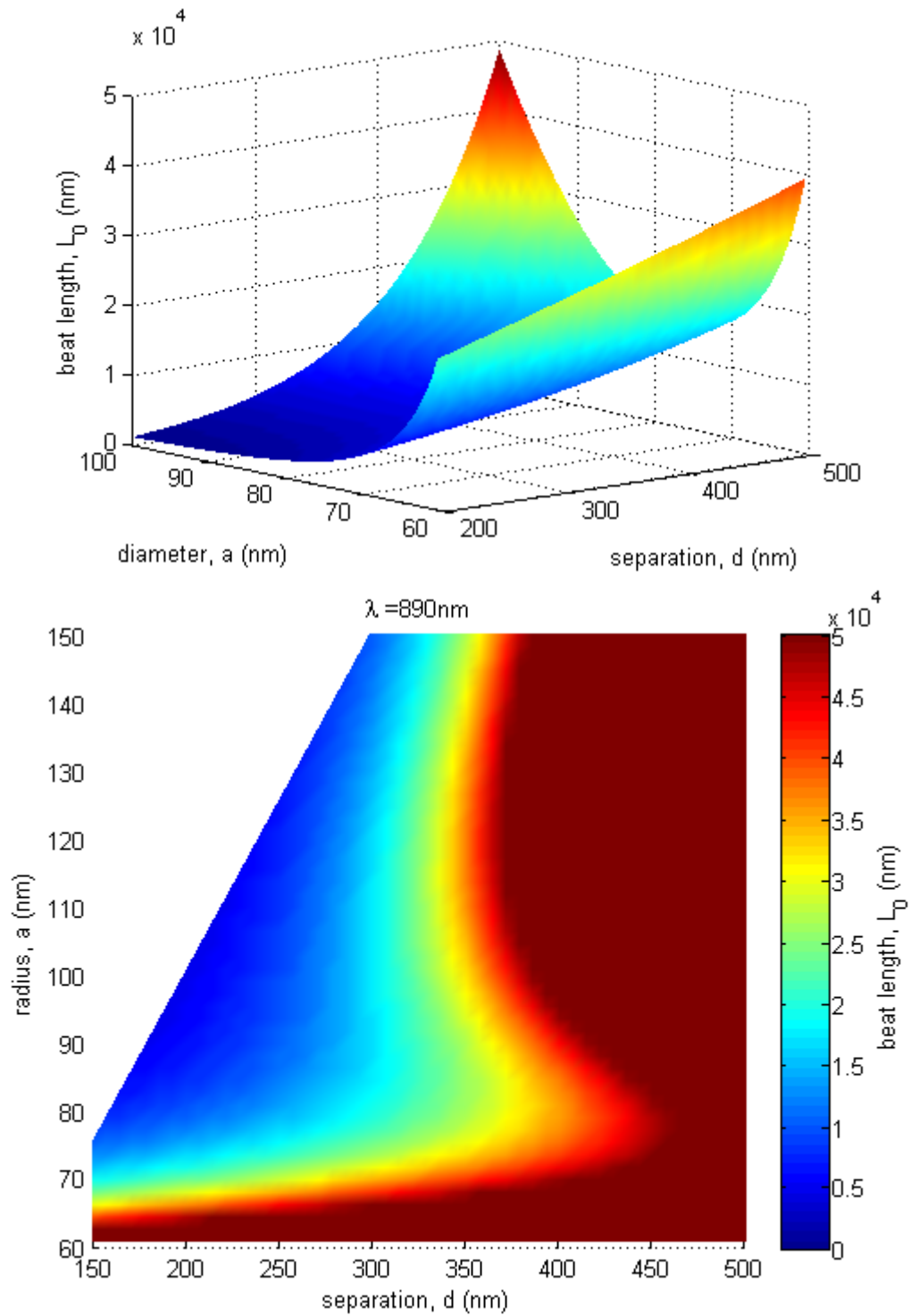


Figure 4.24: Beat length L_0 as a function of nanowire radii a and core-to-core separation d . In the bottom figure, the dark red region on the right side represents beat lengths $L_0 > 50 \mu\text{m}$ which is much larger than the lengths of the nanowires used in our experiments.

4.10 Group velocities of coupled nanowire waveguides

The group velocity, v_g optical waveguides is a useful quantity in many applications. In the context of this work, the group velocity is required for the calculation of the optical forces on coupled waveguides from the eigenmode analysis shown in Section 4.12.

Recall in Section 4.4 we calculated the the group velocity v_g of an isolated InP nanowire waveguide submerged in deionised water.

$$v_g(\lambda) = \frac{-2\pi c}{\lambda^2} \frac{d\lambda}{d\beta} \quad (4.39)$$

where λ is the free space wavelength and β is the propagation constant of a mode in an isolated waveguide. In Section 4.6 we see that when two identical waveguides are coupled, the fundamental mode of the resulting composite waveguide has two fundamental solutions with propagation constants β_+ and β_- given by $\beta_{\pm} = \beta \pm C$ where C is the coupling constant. This allows us to calculate the group velocity of the symmetric and anti-symmetric fundamental modes of the coupled nanowire waveguides.

$$v_{g+}(\lambda) = \frac{-2\pi c}{\lambda^2} \frac{d\lambda}{d\beta_+} \quad (4.40)$$

$$v_{g-}(\lambda) = \frac{-2\pi c}{\lambda^2} \frac{d\lambda}{d\beta_-} \quad (4.41)$$

An example of group velocities of the symmetric and anti-symmetric fundamental modes for coupled 100nm radius InP nanowire waveguides at 300 nm separation are plotted in Figure 4.25. Also shown in the plot is the group velocity of the nanowire in isolation.

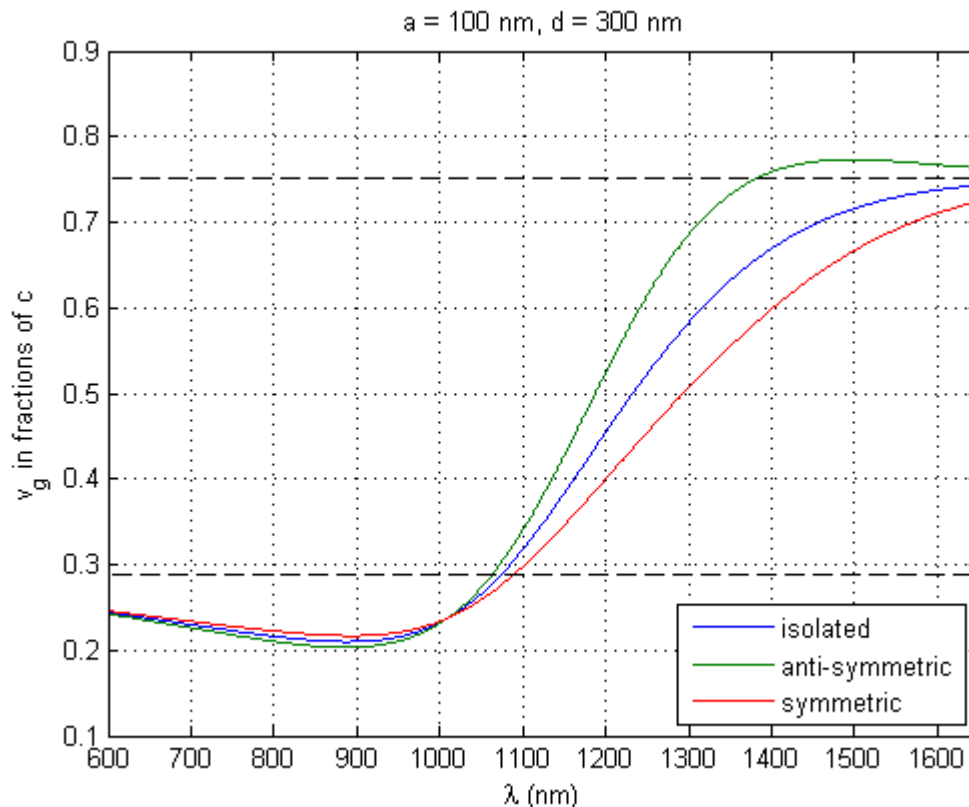


Figure 4.25: Group velocity for the symmetric and antisymmetric modes of coupled 100 nm InP nanowires separated at 300 nm, shown in red and green. Also shown in blue is the group velocity for a single 100 nm InP nanowire waveguide.

4.11 Dispersion relation of coupled nanowire waveguides

It is useful to calculate the dispersion relation for coupled InP nanowire waveguides because the changes in dispersion due to separation can be used to calculate the optical forces. Figures 4.26, 4.27, and 4.28 show the dispersion relation of the symmetric (red curves) and anti-symmetric (green curves) modes for 100 nm radius InP nanowire waveguides at core-to-core separations of 250 nm, 300 nm and 500 nm. Also shown in the figures is the dispersion for an isolated InP nanowire waveguide (blue curves), and the light cone for a plane wave in the surrounding medium i.e. deionised water (dashed lines).

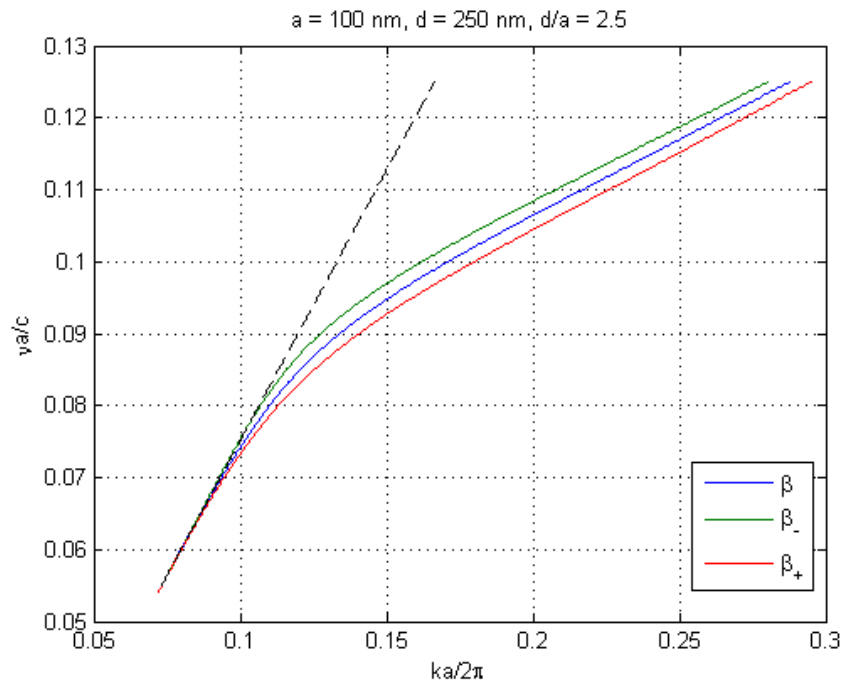


Figure 4.26: Dispersion relation for the unperturbed (blue), symmetric (red) and antisymmetric (green) modes of coupled 100 nm InP nanowires separated at 250 nm.

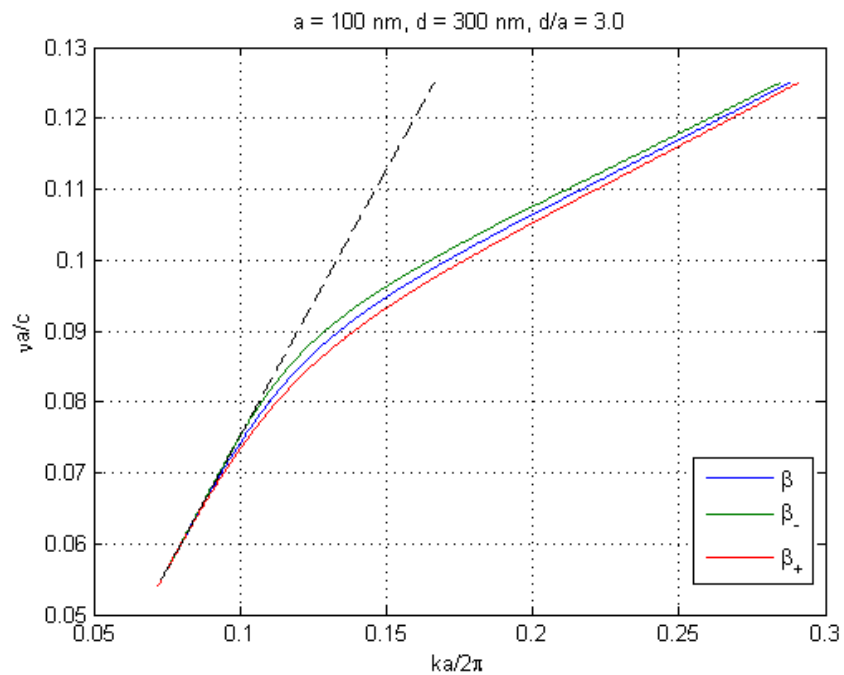


Figure 4.27: Dispersion relation for the unperturbed (blue), symmetric (red) and antisymmetric (green) modes of coupled 100 nm InP nanowires separated at 300 nm.

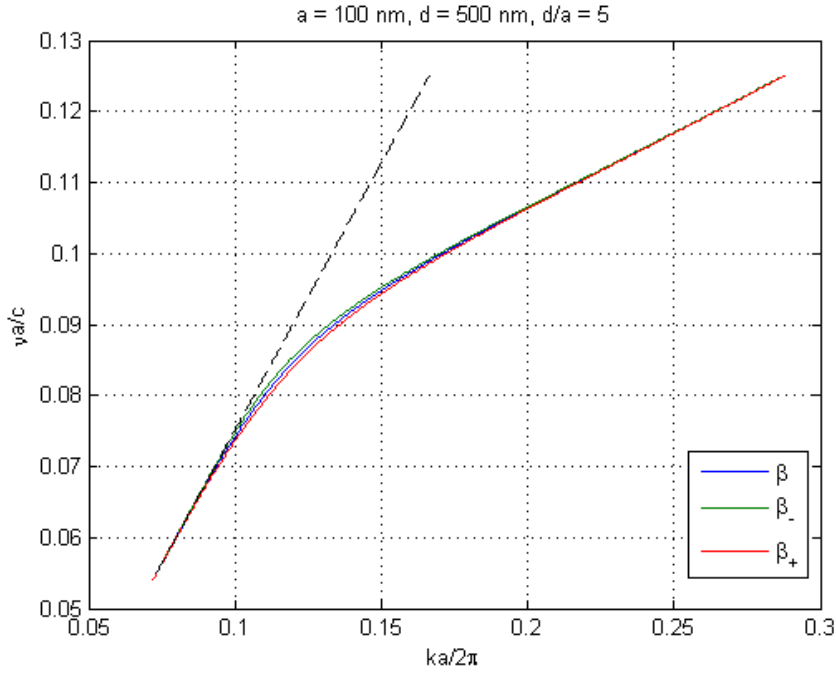


Figure 4.28: Dispersion relation for the unperturbed (blue), symmetric (red) and antisymmetric (green) modes of coupled 100 nm InP nanowires separated at 500 nm.

4.12 Optical forces from eigenmode analysis

Following from Povinelli's analysis of optical forces [6, 54], we consider the system of two parallel waveguides separated by distance d as described in Figure 4.11 earlier in this chapter. Now, assume that energy $U_\omega = N\hbar\omega$ is coupled into an eigenmode of the system with frequency ω , where N is the number of photons and $\hbar\omega$ is the energy per photon. An adiabatic change in the separation Δd will shift the eigenmode frequency by an amount $\Delta\omega$. Conservation of energy then implies that the mechanical force on the waveguides is given by

$$F = -\frac{dU_\omega}{dd} \quad (4.42)$$

with the convention that negative values correspond to attractive forces. Hence,

$$F = -\frac{dU_\omega}{dd} = -\frac{d(N\hbar\omega)}{dd} = -N\hbar\frac{d\omega}{dd} = -\frac{1}{\omega}\frac{d\omega}{dd}U_\omega \quad (4.43)$$

Here $\frac{d\omega}{dd}$ is just the rate of change in the dispersion over waveguide separation for a fixed propagation constant. For the symmetric modes, we see in Figures 4.26, 4.27, and 4.28 that for a fixed propagation constant (hence a fixed \mathbf{k}) the eigenmode frequency ω increases with increasing separation, hence $\frac{d\omega}{dd}$ is positive and the force is attractive. Similarly, the eigenmode frequency for anti-symmetric modes decreases with increasing separation so $\frac{d\omega}{dd}$ is negative and the force is repulsive.

To calculate the energy coupled into the eigenmode U_ω we consider the power transmitted through the coupled waveguides, which is simply given as $P = \sum_{j=\omega} v_{gj} U_j / L$ where v_{gj} and U_j are the group velocity and energy of the j -th mode, while L is the length of the waveguides; the power transmitted through the waveguides comes from the energy of all modes that are coupled through the waveguides. If only a single mode is coupled into the waveguides, then all the power transmitted through the waveguides comes from the energy of that mode and $P = v_g U_\omega / L$ [6]. Hence for single mode coupled waveguides which is the case for our InP nanowire waveguides, the energy coupled into the system is

$$U_\omega = \frac{PL}{v_g} \quad (4.44)$$

Hence, the optical forces due to coupling between two nanowire waveguides is given as

$$F = -\frac{1}{\omega} \frac{d\omega}{dd} \frac{PL}{v_g} \quad (4.45)$$

We calculated the optical forces between 75 nm, 100 nm and 150 nm radius InP nanowire waveguides for a range of waveguide separations and the results are presented in Figure 4.29. These results are presented in force per μm length of nanowire waveguide per mW of optical power coupled into the waveguides. Figure 4.30 shows comparison of forces calculated here with the forces calculated using Maxwell's Stress Tensor (Section 4.8). Both methods show good agreement at large distances but deviates at smaller distances. This is expected because the eigenmode analysis relies on the calculation of the effective propagation constants β_\pm (Section 4.6) using the perturbation theory where the nanowire waveguides are assumed to be weakly coupling, which no longer applies at small distances. However, the eigenmode analysis is useful at large separations because

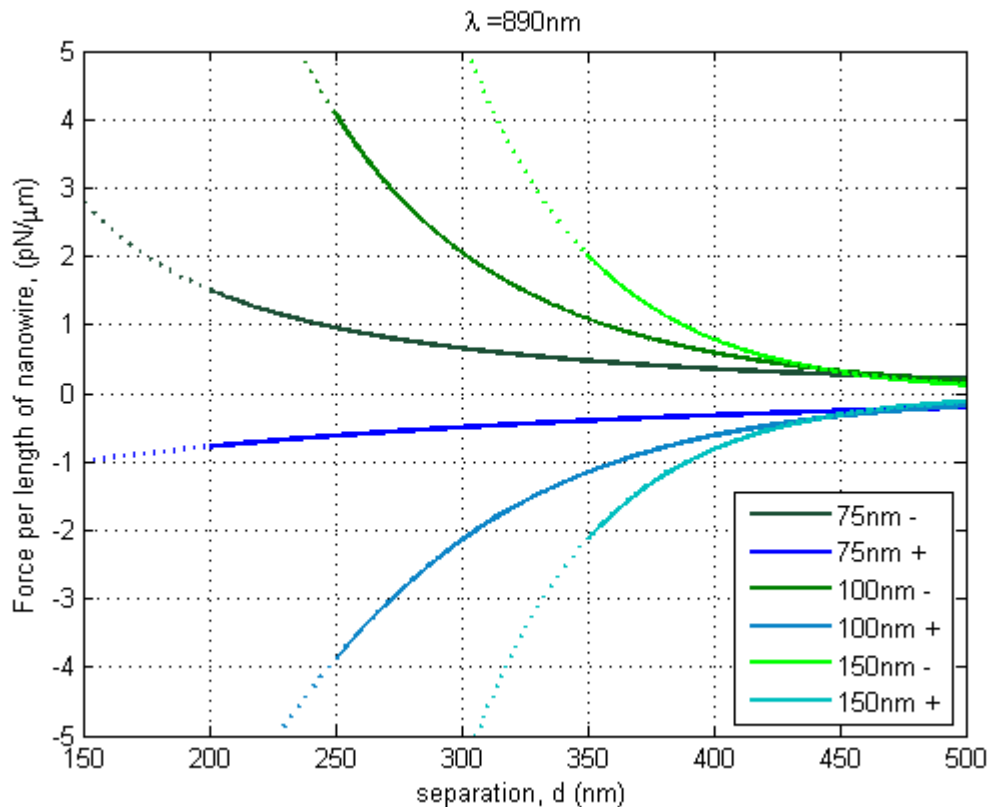


Figure 4.29: Optical forces per length from symmetric (+) and antisymmetric (-) modes of coupled 75 nm, 100 nm and 150 nm InP nanowires as a function of separation d , per mW of optical power is coupled into the waveguides. The dotted lines indicate when the possible deviations between our calculations and the actual result can be significant.

it does not require the full evaluation of the electromagnetic field of the system which can be difficult in some cases.

Based on these results, if we have a system of two coupled 100 nm radius InP nanowire waveguides of 5 μm in length separated by 300 nm and 10 mW of power is coupled into the waveguides, we expect optical forces of about 100 pN acting on the waveguides. This is comparable in magnitude to the trap stiffness of optical tweezers (Section 3.3.5) and is a good indication that it is measurable by optical trapping techniques. In the next chapter I will discuss our attempts at experimentally measuring this optical interaction between coupled InP nanowires.

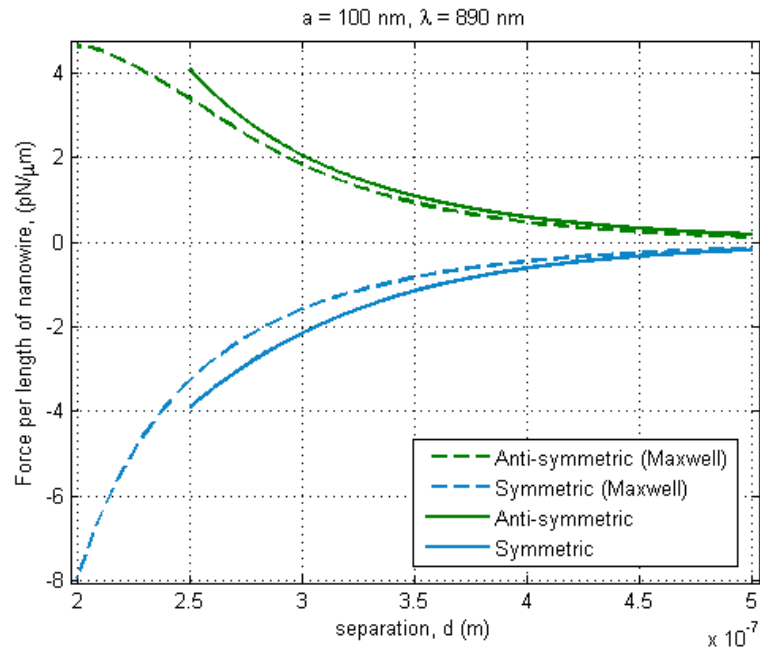
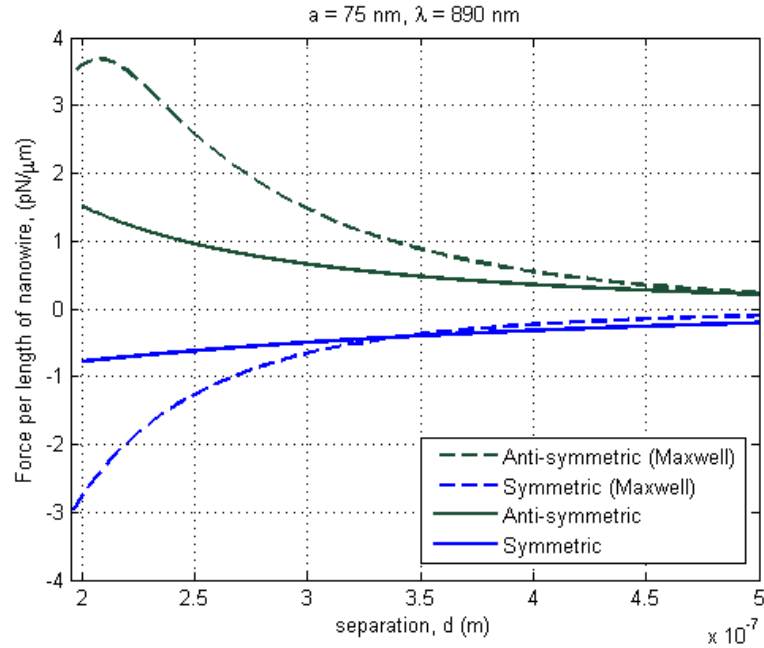


Figure 4.30: Calculated optical forces for (a) 75 nm nanowire pairs and (b) 100 nm nanowire pairs. Dashed lines represent forces calculated using Maxwell's Stress Tensor while solid lines represent forces calculated with the eigenmode analysis. Both methods show good agreement at large distances but deviates at smaller distances. This is expected because at small distances the nanowire waveguides are no longer weakly coupling.

4.13 Conclusion

In this chapter we have studied the waveguiding properties of single and two coupled InP nanowire waveguides. For single InP nanowire waveguides, we have calculated the field profile and poynting vectors, and shown that the field intensity is weak in the core of the nanowires and that significant evanescent fields extend outside the nanowire core. We also calculated the dispersion and group velocity of guided modes in InP nanowire waveguides. These are all critical parameters which have to be taken into account when we examine the coupling between two nanowires.

In the case of two nanowire waveguides, we looked at the coupling effects between waveguides. In particular, we calculated the coupling constant and the field profiles of two coupled InP nanowire waveguides and the beat length. We found conditions for which the beat length is comparable to the length of a typical nanowire waveguide, which implies that the full transfer of power from one nanowire waveguide to the other is possible in the context of experiments. On the other hand, the calculated field profiles enable us to calculate the forces between coupled nanowire waveguides using the Maxwell's Stress Tensor. We also studied the change in dispersion relation and calculated the optical forces between two waveguides via eigenmode analysis. Comparing results from both methods, we found that the forces calculated with the eigenmode analysis show a good agreement with values obtained from calculations using Maxwell's Stress Tensor. We found that the coupling forces due to optical coupling of the guided modes are comparable in magnitude to the gradient forces of the optical tweezers that hold the nanowires in place, which indirectly implies that optical tweezers is the ideal tool for measuring such coupling interactions.

4.14 References

- [1] M. Li, W. H. P. Pernice, C. Xiong, T. Baehr-Jones, M. Hochberg, and H. X. Tang. Harnessing optical forces in integrated photonic circuits. *Nature*, 456(7221):480–U28, 2008. 376FW Times Cited:238 Cited References Count:28.
- [2] D. Van Thourhout and J. Roels. Optomechanical device actuation through the optical gradient force. *Nature Photonics*, 4(4):211–217, 2010. 585OP Times Cited:104 Cited References Count:55.
- [3] H. Li, J. W. Noh, Y. Chen, and M. Li. Enhanced optical forces in integrated hybrid plasmonic waveguides. *Optics Express*, 21(10):11839–11851, 2013. 149RU Times Cited:11 Cited References Count:36.
- [4] M. Eichenfield, C. P. Michael, R. Perahia, and O. Painter. Actuation of micro-optomechanical systems via cavity-enhanced optical dipole forces. *Nature Photonics*, 1(7):416–422, 2007. 188YL Times Cited:137 Cited References Count:39.
- [5] W. H. P. Pernice, M. Li, and H. X. Tang. Theoretical investigation of the transverse optical force between a silicon nanowire waveguide and a substrate. *Optics Express*, 17(3):1806–1816, 2009. 408JX Times Cited:36 Cited References Count:21.
- [6] M. L. Povinelli, M. Loncar, M. Ibanescu, E. J. Smythe, S. G. Johnson, F. Capasso, and J. D. Joannopoulos. Evanescent-wave bonding between optical waveguides. *Optics Letters*, 30(22):3042–3044, 2005. 983UY Times Cited:145 Cited References Count:20.
- [7] J. Ma and M. L. Povinelli. Large tuning of birefringence in two strip silicon waveguides via optomechanical motion. *Optics Express*, 17(20):17818–17828, 2009. 500JP Times Cited:12 Cited References Count:39.
- [8] J. Roels, I. De Vlaminck, L. Lagae, B. Maes, D. Van Thourhout, and R. Baets. Tunable optical forces between nanophotonic waveguides. *Nature Nanotechnology*, 4(8):510–513, 2009. 483DO Times Cited:73 Cited References Count:17.
- [9] R. W. Bowman and M. J. Padgett. Optical trapping and binding. *Reports on Progress in Physics*, 76(2), 2013. 086PI Times Cited:43 Cited References Count:250.
- [10] K. Svoboda and S. M. Block. Force and velocity measured for single kinesin molecules. *Cell*, 77(5):773–784, 1994. Nq123 Times Cited:525 Cited References Count:44.
- [11] J. T. Finer, R. M. Simmons, and J. A. Spudich. Single myosin molecule mechanics - piconewton forces and nanometer steps. *Nature*, 368(6467):113–119, 1994. Na030 Times Cited:1190 Cited References Count:45.
- [12] J. E. Molloy, J. E. Burns, J. Kendrickjones, R. T. Tregear, and D. C. S. White. Movement and force produced by a single myosin head. *Nature*, 378(6553):209–212, 1995. Td759 Times Cited:400 Cited References Count:14.

- [13] K. Visscher, M. J. Schnitzer, and S. M. Block. Single kinesin molecules studied with a molecular force clamp. *Nature*, 400(6740):184–189, 1999. 214JM Times Cited:592 Cited References Count:32.
- [14] D. B. Phillips, M. J. Padgett, S. Hanna, Y. L. D. Ho, D. M. Carberry, M. J. Miles, and S. H. Simpson. Shape-induced force fields in optical trapping. *Nature Photonics*, 8(5):400–405, 2014. Af9cc Times Cited:17 Cited References Count:42.
- [15] C. Doolin, P. H. Kim, B. D. Hauer, A. J. R. MacDonald, and J. P. Davis. Multidimensional optomechanical cantilevers for high-frequency force sensing. *New Journal of Physics*, 16, 2014. Ae1fc Times Cited:6 Cited References Count:36.
- [16] Stephen Simpson, philip jones, Onofrio Marago, and Simon Hanna. Optical binding and synchronisation in arrays of non-spherical particles. In *Optics in the Life Sciences*, OSA Technical Digest (online), page OtM2E.7. Optical Society of America, 2015.
- [17] K. J. Huang, S. Y. Yang, and L. M. Tong. Modeling of evanescent coupling between two parallel optical nanowires. *Applied Optics*, 46(9):1429–1434, 2007. 146PC Times Cited:59 Cited References Count:31.
- [18] W. H. P. Pernice, M. Li, K. Y. Fong, and H. X. Tang. Modeling of the optical force between propagating lightwaves in parallel 3d waveguides. *Optics Express*, 17(18):16032–16037, 2009. 494AO Times Cited:15 Cited References Count:15.
- [19] W. H. P. Pernice, M. Li, and H. X. Tang. Optomechanical coupling in photonic crystal supported nanomechanical waveguides. *Optics Express*, 17(15):12424–12432, 2009. 475XE Times Cited:18 Cited References Count:18.
- [20] L. Zhu. Frequency dependence of the optical force between two coupled waveguides. *Optics Letters*, 34(18):2870–2872, 2009. 498CS Times Cited:5 Cited References Count:11.
- [21] L. M. Tong, J. Y. Lou, and E. Mazur. Single-mode guiding properties of subwavelength-diameter silica and silicon wire waveguides. *Optics Express*, 12(6):1025–1035, 2004. 808UU Times Cited:286 Cited References Count:23.
- [22] Y. Huang, X. F. Duan, Y. Cui, L. J. Lauhon, K. H. Kim, and C. M. Lieber. Logic gates and computation from assembled nanowire building blocks. *Science*, 294(5545):1313–1317, 2001. 491VF Times Cited:1418 Cited References Count:22.
- [23] C. Thelander, T. Martensson, M. T. Bjork, B. J. Ohlsson, M. W. Larsson, L. R. Walenbergh, and L. Samuelson. Single-electron transistors in heterostructure nanowires. *Applied Physics Letters*, 83(10):2052–2054, 2003. 717LJ Times Cited:294 Cited References Count:14.
- [24] X. F. Duan, Y. Huang, R. Agarwal, and C. M. Lieber. Single-nanowire electrically driven lasers. *Nature*, 421(6920):241–245, 2003. 635KG Times Cited:1578 Cited References Count:25.

-
- [25] J. F. Wang, M. S. Gudiksen, X. F. Duan, Y. Cui, and C. M. Lieber. Highly polarized photoluminescence and photodetection from single indium phosphide nanowires. *Science*, 293(5534):1455–1457, 2001. 465XV Times Cited:1135 Cited References Count:17.
- [26] C. M. Lieber. Design, synthesis and properties of programmable nanowire transistors for nanoscale circuits and processors. *Abstracts of Papers of the American Chemical Society*, 243, 2012. 219JX 1039-INOR Times Cited:0 Cited References Count:0.
- [27] H. Yan, H. S. Choe, S. W. Nam, Y. J. Hu, S. Das, J. F. Klemic, J. C. Ellenbogen, and C. M. Lieber. Programmable nanowire circuits for nanoprocessors. *Nature*, 470(7333):240–244, 2011. 718RQ Times Cited:222 Cited References Count:21.
- [28] Y. Nakayama, P. J. Pauzauskie, A. Radenovic, R. M. Onorato, R. J. Saykally, J. Liphardt, and P. D. Yang. Tunable nanowire nonlinear optical probe. *Nature*, 447(7148):1098–U8, 2007. 183HT Times Cited:187 Cited References Count:30.
- [29] F. Wang, P. J. Reece, S. Paiman, Q. Gao, H. H. Tan, and C. Jagadish. Nonlinear optical processes in optically trapped inp nanowires. *Nano Letters*, 11(10):4149–4153, 2011. 830OT Times Cited:5 Cited References Count:28.
- [30] Allan W. Snyder and W. Snyder Allan. *Optical waveguide theory*. London and New York : Chapman and Hall, London and New York, 1983. (John D.) Includes bibliographical references and indexes.
- [31] M. C. Frawley, I. Gusachenko, V. G. Truong, M. Sergides, and S. N. Chormaic. Selective particle trapping and optical binding in the evanescent field of an optical nanofiber. *Optics Express*, 22(13):16322–16334, 2014. Aj9tn Times Cited:4 Cited References Count:25.
- [32] Y. B. Ovchinnikov, S. V. Shulga, and V. I. Balykin. An atomic trap based on evanescent light waves. *Journal of Physics B-Atomic Molecular and Optical Physics*, 24(14):3173–3178, 1991. Fz743 Times Cited:68 Cited References Count:12.
- [33] S. Kawata and T. Sugiura. Movement of micrometer-sized particles in the evanescent field of a laser-beam. *Optics Letters*, 17(11):772–774, 1992. Hu973 Times Cited:200 Cited References Count:19.
- [34] C. D. Mellor and C. D. Bain. Array formation in evanescent waves. *Chemphyschem*, 7(2):329–332, 2006. 013IZ Times Cited:54 Cited References Count:21.
- [35] G. Brambilla, G. S. Murugan, J. S. Wilkinson, and D. J. Richardson. Optical manipulation of microspheres along a subwavelength optical wire. *Optics Letters*, 32(20):3041–3043, 2007. 229BG Times Cited:66 Cited References Count:24.
- [36] A. H. J. Yang, S. D. Moore, B. S. Schmidt, M. Klug, M. Lipson, and D. Erickson. Optical manipulation of nanoparticles and biomolecules in sub-wavelength slot waveguides. *Nature*, 457(7225):71–75, 2009. 389OR Times Cited:309 Cited References Count:30.
-

- [37] B. S. Ahluwalia, P. Lovhaugen, and O. G. Hellesø. Waveguide trapping of hollow glass spheres. *Optics Letters*, 36(17):3347–3349, 2011. 817JC Times Cited:9 Cited References Count:14.
- [38] S. E. Skelton, M. Sergides, R. Patel, E. Karczewska, O. M. Marago, and P. H. Jones. Evanescent wave optical trapping and transport of micro- and nanoparticles on tapered optical fibers. *Journal of Quantitative Spectroscopy & Radiative Transfer*, 113(18):242–250, 2012. Sp. Iss. SI 059DX Times Cited:12 Cited References Count:60.
- [39] A. P. Abel, M. G. Weller, G. L. Duveneck, M. Ehrat, and H. M. Widmer. Fiber-optic evanescent wave biosensor for the detection of oligonucleotides. *Analytical Chemistry*, 68(17):2905–2912, 1996. Ve598 Times Cited:179 Cited References Count:38.
- [40] M. J. Levene, J. Korlach, S. W. Turner, M. Foquet, H. G. Craighead, and W. W. Webb. Zero-mode waveguides for single-molecule analysis at high concentrations. *Science*, 299(5607):682–686, 2003. 640KH Times Cited:646 Cited References Count:30.
- [41] P. Zhu and H. G. Craighead. Zero-mode waveguides for single-molecule analysis. *Annual Review of Biophysics*, Vol 41, 41:269–293, 2012. Bbr09 Times Cited:17 Cited References Count:64 Annual Review of Biophysics.
- [42] A. Hardy and W. Streifer. Coupled mode theory of parallel wave-guides. *Journal of Lightwave Technology*, 3(5):1135–1146, 1985. Atl57 Times Cited:259 Cited References Count:18.
- [43] A. Hardy, S. Shakir, and W. Streifer. Coupled-mode equations for two weakly guiding single-mode fibers. *Opt Lett*, 11(5):324, 1986. Hardy, A Shakir, S Streifer, W eng 1986/05/01 00:00 Opt Lett. 1986 May 1;11(5):324.
- [44] H. A. Haus and W. P. Huang. Coupled-mode theory. *Proceedings of the Ieee*, 79(10):1505–1518, 1991. Gu211 Times Cited:164 Cited References Count:153.
- [45] H. A. Haus, W. P. Huang, S. Kawakami, and N. A. Whitaker. Coupled-mode theory of optical wave-guides. *Journal of Lightwave Technology*, 5(1):16–23, 1987. F7178 Times Cited:198 Cited References Count:15.
- [46] W. P. Huang. Coupled-mode theory for optical wave-guides - an overview. *Journal of the Optical Society of America a-Optics Image Science and Vision*, 11(3):963–983, 1994. Mz514 Times Cited:211 Cited References Count:102.
- [47] W. P. Huang and J. W. Mu. Complex coupled-mode theory for optical waveguides. *Optics Express*, 17(21):19134–19152, 2009. 506HV Times Cited:23 Cited References Count:27.
- [48] A. W. Snyder and A. Ankiewicz. Fiber couplers composed of unequal cores. *Electronics Letters*, 22(23):1237–1238, 1986. E9116 Times Cited:28 Cited References Count:4.

- [49] A. W. Snyder, A. Ankiewicz, and A. Altintas. Fundamental error of recent coupled mode formulations. *Electronics Letters*, 23(20):1097–1098, 1987. K2631 Times Cited:25 Cited References Count:16.
- [50] W. Streifer. Coupled mode theory. *Electronics Letters*, 23(7):315–316, 1987. G9120 Times Cited:5 Cited References Count:16.
- [51] W. Streifer. Fundamental error of recent coupled mode formulations. *Electronics Letters*, 24(11):718–719, 1988. N7144 Times Cited:7 Cited References Count:0.
- [52] Zi Hua Wang and S. R. Seshadri. Asymptotic theory of guided modes in two parallel, identical dielectric waveguides. *Journal of the Optical Society of America A*, 5(6):782–792, 1988.
- [53] David J. Griffiths and David J. Griffiths. *Introduction to electrodynamics*. Upper Saddle River, NJ : Prentice Hall, Upper Saddle River, NJ, 3rd ed. edition, 1999. (David Jeffrey) (David Jeffery) Includes bibliographical references and index.
- [54] M. L. Povinelli, S. G. Johnson, M. Loncar, M. Ibanescu, E. J. Smythe, F. Capasso, and J. D. Joannopoulos. High-q enhancement of attractive and repulsive optical forces between coupled whispering-gallery-mode resonators. *Optics Express*, 13(20):8286–8295, 2005. 973TF Times Cited:108 Cited References Count:28.

Chapter 5

Measurement of Forces by Time Shared Optical Tweezers

5.1	Introduction	144
5.2	Trap multiplexing and multiple particle tracking methods	145
5.2.1	Orthogonally polarised dual beam optical tweezers	145
5.2.2	Trap multiplexing and tracking by holographic optical tweezers	147
5.2.3	Fast tracking by time-shared trap multiplexing	151
5.3	Limits of tracking by time-shared optical tweezers	152
5.4	Hydrodynamic coupling interactions	155
5.5	Tracking of multiple polystyrene particles by time-shared traps . . .	157
5.6	Tracking of multiple gold nanoparticles by time-shared traps	161
5.7	Applicability of time-shared optical tweezers in trapping and tracking two interacting InP nanowires	163
5.8	Conclusion	164
5.9	References	166

5.1 Introduction

In Chapter 4 we calculated the coupling properties and resulting optical forces in two coupled InP nanowire waveguides. In this chapter we propose experimental approaches to physically recreate our hypothetical coupled nanowire waveguides system, and observe the coupling interactions between the two nanowire waveguides. We note that in our system of two nanowires suspended in water, hydrodynamic interactions may play a crucial role on top of optical interactions between the nanowires.

The study of interaction forces between multiple particles requires the trapping and tracking of each interacting particles individually. Optical tweezers is the ideal tool for such studies due to its ability to isolate and track single particles. We will examine the merits and limitations of various trap multiplexing techniques and multiple particle trapping modalities currently within the literature. Current optical tweezers multiplexing techniques such as holographic tweezers enable the trapping of multiple particles quite easily and video methods enable the simultaneous tracking of multiple trapped particles, but monitoring fast dynamics of multiple trapped particles remain a challenge.

In this chapter we demonstrate a technique that do not suffer from the above limitations to simultaneously trap and track multiple particles, and can be easily expanded to more than two trapped particles. It is a generic tool that is suitable for studying various kinds of interaction between multiple micro- and nano-sized objects including electrical, optical and hydrodynamic coupling interactions. Taking into account some necessary compromises, we propose the use of time sharing for trap multiplexing combined with back focal plane interferometry for particle tracking. Using time-shared traps, the tracking of each particle in each trap can be achieved by reading the quadrant photo detector synchronously with the time sharing of the traps. We will then explore the viability of this chosen method for our system by performing measurements on hydrodynamic interactions as it is built into the system and well characterised within the literature.

5.2 Trap multiplexing and multiple particle tracking methods

5.2.1 Orthogonally polarised dual beam optical tweezers

One of the earliest experiments to trap and track two particles is done by Meiners and Quake [1], with the use of a dual beam optical tweezers setup. In this experiment, two separate beams were sent into the high NA objective to generate two gradient force optical trap. In order to track each particle individually, the two traps was orthogonally polarised. The scattered signal collected by the condenser lens from both particles can then be separated using a polarising beam splitter and fed into two separate quadrant photodiodes allowing each particle to be tracked individually. With this technique Meiners and Quake were able to measure the hydrodynamic cross correlation between two optically trapped latex beads.

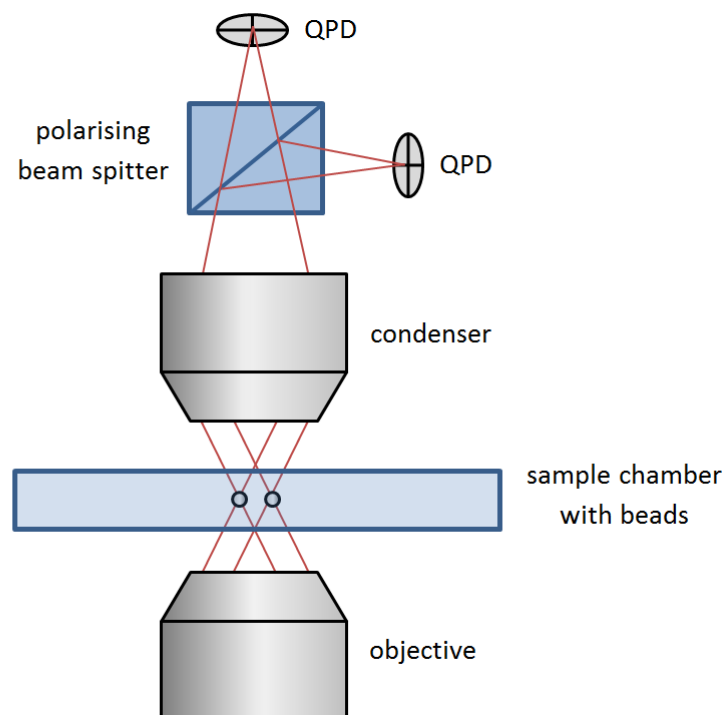
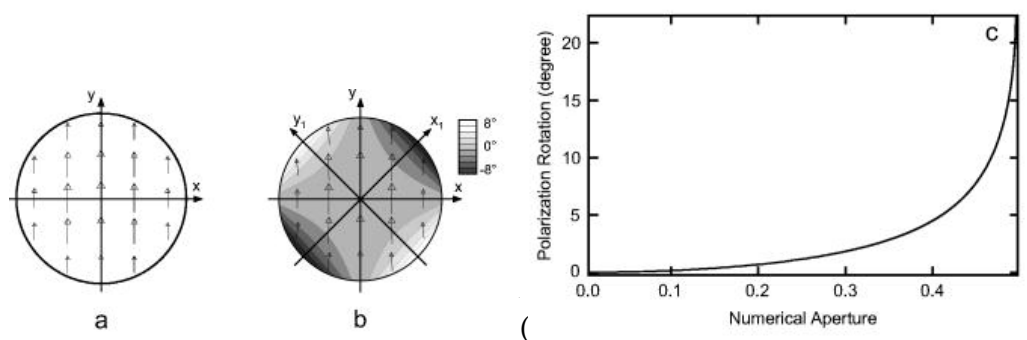


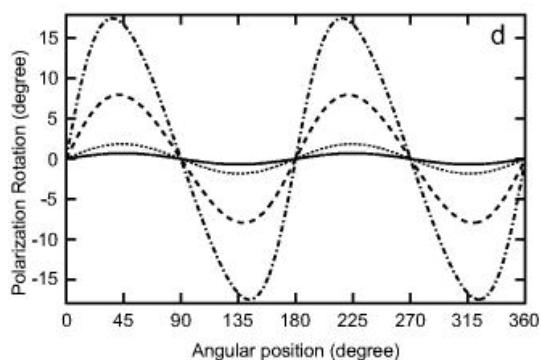
Figure 5.1: Schematic diagram of the apparatus used by Meiners and Quake [1] to measure the cross-correlation of two optically trapped microspheres. Two orthogonally polarised laser beams are focused into the sample cell, each trapping a microsphere. The light scattered from the microspheres are collected with a second objective lens and separated by a polarising beam splitter onto two QPD's.

It is easy to see that this technique is only limited to a maximum of two particles. Apart from that, this technique assumes full conservation of polarisation after

scattering which is not necessarily true. Partial depolarisation after scattering even on homogeneous particles occurs due to the use of high numerical aperture (NA) optics in optical tweezers [2, 3]. This is because for a linearly polarised beam refracting on the surface of a lens, the electric field exhibits different parallel and perpendicular components relative to the plane of incidence depending on the position on the lens. Since the two components are refracted differently, the polarization of the total electric field is rotated as described by the Fresnel equations. Mangeol *et al.* calculated the effects of these partial depolarisation for different NA lenses, shown in Figure 5.2. In particular, they found that there can be a polarisation rotation of up to 20 degrees for lenses with a NA of 0.49 [2]. These depolarisation effects has been verified experimentally [2], and can often reach up to 10% of the integrated intensity of the laser trap [3], causing significant cross-talk and systematic errors in measurements.



(a) Incident electric field. (b) Calculated electric field in the back focal plane of the second lens. (c) The rotation of polarization of the electric field exiting from the two lens system on the y_1 axis for $y_1 > 0$



(d) The rotation of polarization of the electric field exiting from the two lens system on the perimeter of NA = 0.20 (solid), NA = 0.30 (dotted), NA = 0.45 (dashed), and NA = 0.49 (dash-dotted).

Figure 5.2: Rotation of polarization of a Gaussian beam passing a system of two identical lenses. The electric fields are limited to a 3.8 mm disk. Figure from [2]. Reprinted with permission from [2]. Copyright 2008, AIP Publishing LLC.

Several methods has been suggested to address this problem, including polarisation rectification by beam back propagation through the condenser and objective lenses [2], frequency detuning of one of the traps [2], and advanced signal processing using Bayesian inference [4]. But even with these implementations, orthogonally polarised multi-traps cannot be used to track rotating particles or particles exhibiting birefringence [5], as it is known that the scattering of polarised light off rotating or birefringent particles changes the polarisation of the light [6]. All of these considerations has driven the need for more novel methods of generating multiple optical traps. Current trap multiplexing techniques can be divided into two main subclasses, namely spatially modulated trap multiplexing e.g. holographic tweezers, and temporally modulated trap multiplexing e.g. trap multiplexing by acousto-optics.

5.2.2 Trap multiplexing and tracking by holographic optical tweezers

Holographic optical tweezers is currently the most popular trap multiplexing method. It has been widely used in various experiments, including the trapping of multiple particles [7–10] and having multiple traps on a single object for orientation control [11, 12]. Holographic optical tweezers work by adding a phase diagram in the Fourier plane of the focal point of the trapping laser. Details about holographic optical tweezers is presented in Chapter 2 Section 2.6. A phase mask consisting of gratings of different spacings will generate multiple trapping points in the focus of the objective lens.

Since holographic optical tweezers form all traps at the same time from a single coherent laser source, the tacking signal from each individual trap may interfere with one another. Furthermore since all tracking signals are collected by one condenser lens, the decoupling of multiple tracking signals from holographically generated multiple optical tweezers is one of the biggest challenges of using holographic optical tweezers to track multiple particles. A common method of achieving this is by tracking each particle graphically using a video camera and centroid finding algorithms [10, 13]. Polin *et al.* trapped and tracked an array of 10 colloidal spheres dispersed in viscous fluid at a range of interparticle separations from 2.6 to 3.7 μm . However, this experiment is only made possible by the use of a water-glycerol mixture as the solvent to significantly slow down the dynamics to a time scale accessible to the video camera [10].

The drawbacks of video tracking methods include limited spatial and temporal resolutions. Typical frame rates of laboratory cameras can only reach up to 1 kHz compared to the speed of a typical QPD which is capable of reading at hundreds of

kHz. This makes video tracking methods ineffective in measuring features that manifest in timescales less than a millisecond. Furthermore, video tracking relies on the direct imaging of the trapped particles, which becomes more challenging as particle sizes approach the diffraction limit; advanced imaging techniques such as dark field imaging or phase contrast microscopy may become necessary to resolve these low contrast particles. These are added complications which ultimately limits the resolution of video tracking techniques.

To address these limitations, there has been significant advances in video tracking methods such as the development of 'smart cameras' with integrated signal processing and more sophisticated tracking algorithms [13–17]. In a study by Di Leonardo *et al.*, a high speed smart camera with integrated centroid tracking is used to track a ring of eight $2\ \mu\text{m}$ spheres trapped in eight holographically generated optical tweezers [13]. Since only the positional information is captured by this camera rather than the whole image, the bandwidth is sufficiently high to monitor the dynamics of the trapped particles. On the other hand, Conkey *et al.* integrated the double-helix point spread function (DH-PSF) technique with holographic optical tweezers [17]. The DH-PSF works by generating two lobes that trace out a double helix by rotating around the optical axis with image defocus. As a particle moves away from focus in one direction, the lobes rotate clockwise while as the particle moves in the opposite direction, the lobes rotate counter-clockwise. The axial position can be determined through the rotation angle of the two lobes, while the lateral position can be estimated by calculating the centroid of the two lobes. This technique was shown to achieve high precision 3D position estimates of about 10 nm laterally and 30 nm axially.

These developments in smart and high speed cameras achieving frame rates of 10s of kHz has greatly improved the temporal resolution of video tracking methods. However, even the fastest high speed cameras with the most sophisticated tracking algorithms are still inferior to QPD sensing methods in terms of spatial and temporal resolution. Furthermore, such high speed cameras are extremely costly, and the hardware requirements such as memory, bandwidth and processing power for the amount of data generated further increase the cost of this method to the point where it is not feasible in most cases.

A recent approach to high speed particle tracking using holographic optical tweezers and interferometric techniques involving the use of spatial filtering [18]. In typical interferometric detection schemes, the tracking signal is imaged onto the back focal plane by a lens. If multiple traps exist on the trapping plane, the tracking signals from each

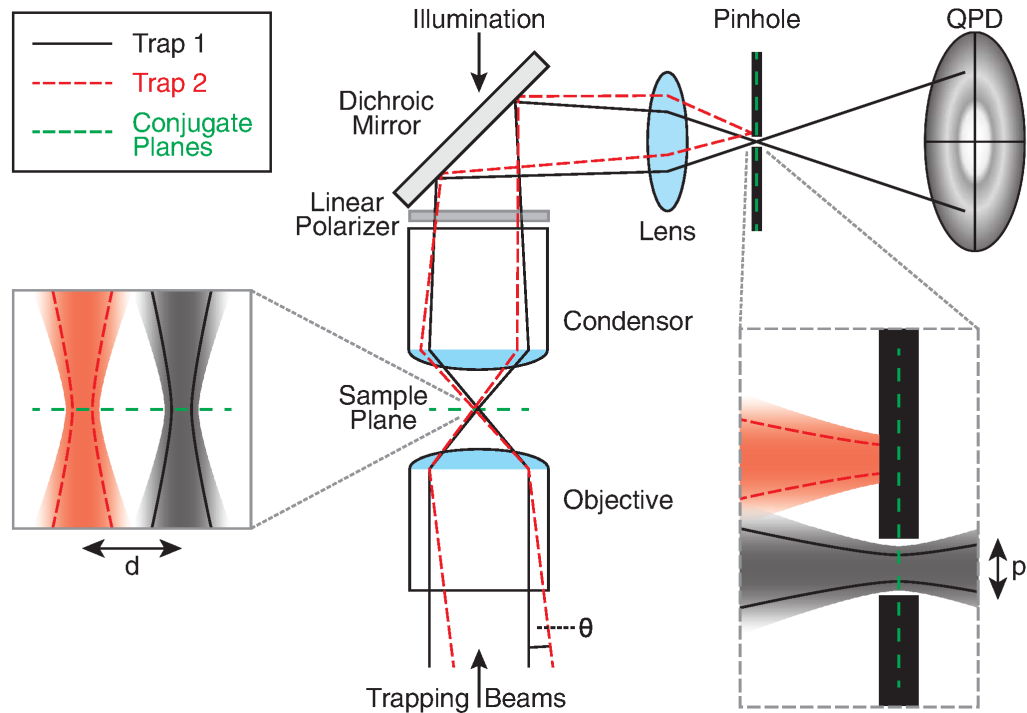


Figure 5.3: Illustration of the spatial filtering method by Ott *et al.* Two independent traps are created in the sample plane by two trapping beams. Trap 2 enters the objective at an angle θ , which translates to a lateral distance d from Trap 1 at the trapping plane. The transmitted light is collected by the microscope condenser. A lens images the back focal plane of the condenser onto a quadrant photodiode for detection of the position of the trapped particle. Blocking the laser beam of Trap 2 by a pinhole located in a plane conjugate to the sample plane, allows for the transmission of Trap 1 to the detector and effectively suppresses crosstalk from Trap 2 [18]. Reprinted with permission from [18]. Copyright 2014, AIP Publishing LLC.

individual particle becomes convoluted in the back focal plane and cannot be separated by the photodiode detector. To overcome this, Ott *et al.* recognised that there exist a phase conjugate plane of the trapping plane in between the QPD and the lens used to image the trapping plane onto the back focal plane. On this intermediate plane which is conjugate to the trapping plane, the trapping beams from multiple traps are spatially well separated as long as they are also well separated in the trapping plane. By placing a spatial filter on this image plane, the tracking signal from one trap can be selected and measured by the QPD while signals from all other traps are blocked (illustrated in Figure 5.3). With appropriately chosen pinhole size, Ott managed demonstrate the removal of crosstalk down to less than 10 % at separations greater than $2 \mu\text{m}$ between traps when $1 \mu\text{m}$ spherical particles are trapped, without distorting the tracking signal

from individual particles [18].

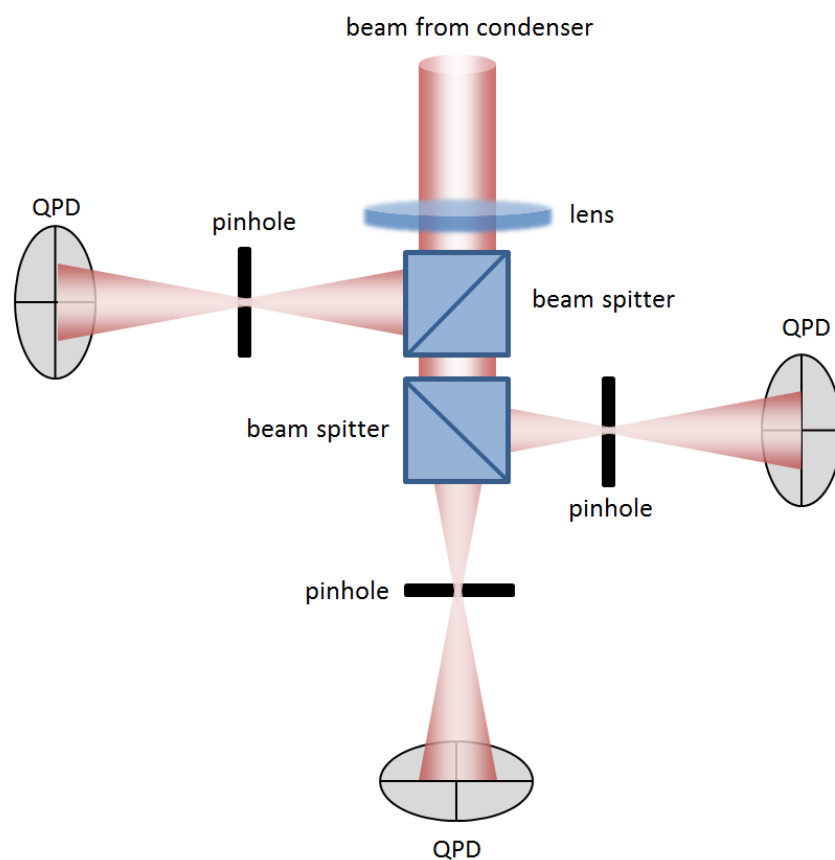


Figure 5.4: Incorporation of beam splitters, additional pinholes and QPD's to track multiple particles in multiple optical tweezers. [19].

Ott *et al.* further demonstrated the expansion of this technique to simultaneously track 3 optically trapped particles by the use of beam splitters and more QPD's, as illustrated in Figure 5.4 [19]. In fact, this technique can be expanded to any number of traps provided the intensity of the signal is sufficiently strong to be split into the number of channels desired and still be detectable after spatial filtering. Conversely, this spatial filtering technique is less feasible when the scattering signal from the trapped particle is weak to begin with, e.g. nanoparticles and nanowires. Moreover, meticulous alignment requirements of the pinholes may reduce the robustness of this method in highly dynamic trapping experiments and experiments involving low symmetry particles such as nanowires.

5.2.3 Fast tracking by time-shared trap multiplexing

In contrast to holographically generated multiple traps which is all created at once, in time-shared optical tweezers the trap is only present in one spot at any particular instant in time. Multiple traps are created when the single trap is scanned rapidly between multiple locations where the traps are desired, at a rate fast enough such that the trapped particles do not have time to diffuse away between visits by the laser [20]. Early forms of time-shared optical tweezers used two axis galvanometer-mounted mirrors to carry out the fast scanning [21] but this was later replaced by non-mechanical beam scanning methods, namely the acousto-optic deflector (AOD) [22, 23] which is still widely used today.

Since time-shared optical tweezers only has one trap present in one spot at any instant in time, it can be used in combination with interferometric techniques to track multiple particles. AOD's can easily scan the trapping laser between multiple trapping sites at up to tens of kHz, while a typical quadrant photodiode (QPD) can track at up to a few MHz; this puts an upper limit on the temporal resolution achievable by this method, although it is still a few orders of magnitude greater than video tracking methods. This high temporal resolution is desirable for probing the fast-dynamics of interacting micro and nano particles, which can occur at nano-second time scales.

Ruh *et al.* demonstrated the use of time-shared optical tweezers with a single QPD to track up to nine particles [24]. In this study, a single beam gradient force optical trap is scanned through nine spots using AOD's. The trap remained on each spot for about 20 μs , and returned to the same spot after 180 μs (after spending 20 μs on each of the other 8 spots). The detector is set to sample at 1 MHz, which amounts to about 20 data points on each one of the nine spots per trap scanning cycle. From these 20 data points, half of them are discarded to remove the contributions from the peaks that arise from beam steering via the AOD's. The remaining points are then averaged and taken as one positional reading of this particular trap. With this method, Ruh *et al.* was able to extract the trajectory of all nine trapped beads of various sizes, and further used these information to study the hydrodynamic interactions between the trapped particles [24].

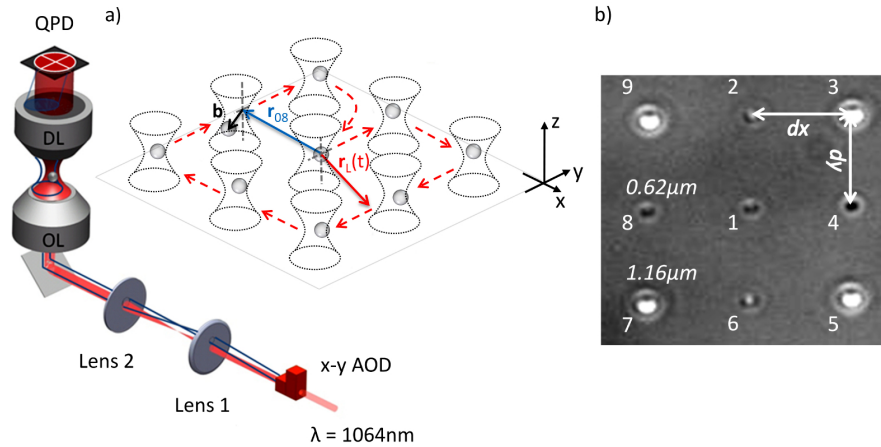


Figure 5.5: (a) The single beam optical tweezers is scanned through 9 locations sequentially by AOD's to generate 9 time-shared optical traps. In each one of the 9 spots, the scattered and unscattered light is projected onto the QPD for a short time ($\sim 20\mu s$). (b) Bright field image of four $1.16\ \mu m$ and five $0.62\ \mu m$ trapped glass beads. The numbers close to each bead indicates the sequence of the scanning of the time-shared optical trap [24].

5.3 Limits of tracking by time-shared optical tweezers

We believe that the use of interferometric particle tracking with time-shared optical tweezers is the best option to be used to measure our InP nanowire system described in Chapter 4. This is because only interferometric methods can achieve sufficiently high data acquisition rates to monitor the fast dynamics of interacting nanowires in our system.

In contrast to Ruh *et al.*'s method of extracting particle trajectory through post processing the QPD readout, we incorporate interferometric sensing using a QPD with time-shared optical tweezers by reading the QPD synchronously with the switching of the trap between locations. The limitations of this method is quantified through calculations presented below. Finally to test the viability of this approach, we tested our system by measuring the hydrodynamic interaction between two $1\ \mu m$ polystyrene spheres (Section 5.5) and two $100\ nm$ gold nanoparticles (Section 5.6).

With the assumption that the sensing of the particle happens synchronously with the switching between time-shared traps, in principle the number of particles that can be simultaneously applied to this method of tracking is limited by the number of particles that can be trapped simultaneously in time shared traps, which we will examine in the following. For the trapped particle to be unaffected by the absence of the trap while time sharing, we require the free diffusion of the particle in the absence of the trap

(while time-shared) to be much smaller than the Brownian displacement of the trapped particle within a single optical trap.

Mathematically, this limit can be written as

$$\langle \Delta x^2 \rangle_{\text{diffusion}} \ll \langle \Delta x^2 \rangle_{\text{trap}} \quad (5.1)$$

If we denote the period in which the time shared trap is present at a particular trapping site as dt , then the period of time when the trap is absent in this same site is $\Delta t = (N-1)dt$ where N is the number of time shared traps. The switching frequency of each trap, which is also synchronous to the sampling of the QPD for each trap is therefore given as $f_{\text{AOD}} = f_{\text{detector}} = 1/N dt$.

Free diffusion is given as $\langle \Delta x^2 \rangle_{\text{diffusion}} \approx 2D\Delta t$ where $D = 2k_B T / \gamma_0$ is the diffusion constant, and only occurs when the trap is absent so

$$\langle \Delta x^2 \rangle_{\text{diffusion}} \approx 2D\Delta t \quad (5.2a)$$

$$= \frac{2k_B T}{\gamma_0} (N-1) dt \quad (5.2b)$$

Using the equipartition theorem on optically trapped particles,

$$\langle \Delta x^2 \rangle_{\text{trap}} \approx \frac{k_B T}{\kappa} \quad (5.3)$$

where κ is the trap stiffness of the optical trap.

Combining Equations 5.1, 5.2b and 5.3, the inequality becomes

$$(N-1) dt \ll \frac{\gamma_0}{2\kappa} \quad (5.4a)$$

$$N \ll \frac{\gamma_0}{2\kappa dt} + 1 \quad (5.4b)$$

From Equation 5.4, we see that in order to increase the number of possible time shared traps, the switching time between each time shared trap dt should be reduced.

The reduction of dt ensures that the switching frequency of each time shared trap is much higher than the roll-off frequency of the trapped particle frequency response, as the particle motion is insensitive to external disturbances faster than this frequency [22]. However, N cannot be increased indefinitely by a reduction in dt due to limits in the trap stiffness κ as we will examine in the following.

Given a fixed trap stiffness, κ in the single beam optical trap without time sharing and N representing the number of time shared traps generated from that single trap, the trap stiffness of each time shared trap becomes κ/N . As the number of time shared traps increases, the trap stiffness in each individual trap diminishes due to the reduced duty cycle in each trap, thus imposing a limit on the maximum number of traps possible [22]. Thus,

$$\frac{\kappa}{N} > \kappa_0 \quad (5.5a)$$

$$N < \frac{\kappa}{\kappa_0} \quad (5.5b)$$

where κ_0 represents the minimum trap stiffness for which a particle can be stably trapped. This means that in order to increase the number of time shared traps, the trap stiffness, κ of the single trap before time sharing should be increased proportionally as well.

Further constraints should be considered when the interaction between particles is of interest. In the case of two hydrodynamically interacting particles, the drift of each particle in the absence of the trap should not exceed the correlation distance between particles. The cross correlation between two identical particles at the fundamental relaxation time, τ is given as [1]

$$\langle x_1(\tau) x_2(0) \rangle \approx -\frac{1}{e} \frac{k_B T}{\kappa} \frac{3a}{2d} \quad (5.6)$$

where a is the radius of the particles, d is the distance between them and the negative sign denotes anti-correlated motion. The magnitude of this correlation distance should be less than the free diffusion in the absence of the trap, i.e.

$$\frac{1}{e} \frac{k_B T}{\kappa} \frac{3a}{2d} > 2D\Delta t \quad (5.7)$$

where τ is the fundamental relaxation time given by $\tau = \gamma_0/\kappa$ [1]. Substituting $D = 2k_B T/\gamma_0$ and $\tau = \gamma_0/\kappa$ in to Equation 5.7 gives

$$\Delta t < \frac{3}{4e} \frac{\gamma_0}{\kappa} \frac{a}{d} = \left(\frac{3}{4e} \frac{a}{d} \right) \tau \quad (5.8)$$

Since $(3/4e) < 1$ and $a/d \leq 1$, it is clear from this inequality that the scanning rate should be sufficiently fast such that the period of time when the trap is absent in a trapping site is shorter than the fundamental relaxation time.

The above findings indicate that as long as we can switch the AOD's fast enough and have sufficiently high trapping laser power to create a high enough trap stiffness, there is no limit to the number of particles that can be trapped and tracked simultaneously by this method. However, the physical capabilities of our equipment imposes a practical limit on this number. For example, the Gooch and Houesgo AOD's used in our experiments have a rise time of 4.5 s, which imposes an absolute limit on how small dt can be.

5.4 Hydrodynamic coupling interactions

The diffusion behaviour of a many particle system can be described by the generalised Langevin equations for many particles (neglecting inertial terms)

$$\dot{\mathbf{R}} = \mathbf{H}(\mathbf{R}) \cdot \mathbf{F} \quad (5.9)$$

Here \mathbf{R} represents the coordinates of N particles with components R_i^α where ($i = 1, \dots, N, \alpha = x, y, z$) i.e. $\mathbf{R} = [\mathbf{R}_1, \mathbf{R}_2, \dots, \mathbf{R}_N]$; $\mathbf{R}_1 = R_{x1}\hat{\mathbf{x}} + R_{y1}\hat{\mathbf{y}} + R_{z1}\hat{\mathbf{z}}$. \mathbf{F} represents an external force and \mathbf{H} is the mobility matrix which can be approximated by the Oseen tensor given by [13]

$$H_{ij}^{\alpha\beta} = \frac{1}{\gamma_0} \delta_{\alpha\beta} \delta_{ij} + \frac{1}{\gamma_0} (1 - \delta_{ij}) \frac{3}{4} \frac{a}{r_{ij}} \left(\delta_{\alpha\beta} + \frac{r_{ij}^\alpha r_{ij}^\beta}{r_{ij}^2} \right) \quad (5.10)$$

where γ_0 is the drag coefficient and $r_{ij}^\alpha = R_j^\alpha - R_i^\alpha$ is the separation between particles. Here δ represents the Kronecker delta function.

For optically trapped particles, we can separate the force term \mathbf{F} in Equation 5.9 into a restoring force component $-\mathbf{K} \cdot \mathbf{R}'$ where \mathbf{K} is the stiffness matrix, ζ represent stochastic forces, and $\mathbf{R}' = \mathbf{R} - \mathbf{R}_0$ is the displacement coordinates of particles from their equilibrium positions \mathbf{R}_0

$$\langle \zeta(t) \rangle = 0 \quad (5.11a)$$

$$\langle \zeta(t) \zeta(t') \rangle = 2\mathbf{H}_{ij}^{-1} k_B T \delta(t - t') \quad (5.11b)$$

Equation 5.9 can then be rewritten as the following [13]:

$$\dot{\mathbf{R}}' = \mathbf{H}(\mathbf{R}) \cdot [-\mathbf{K} \cdot \mathbf{R}' + \zeta] \quad (5.12)$$

Now, if the displacement of each individual particle from its equilibrium is small compared to the interparticle distances, then $r_{ij}^\alpha = R_j^\alpha - R_i^\alpha \approx R_{0j}^\alpha - R_{0i}^\alpha$ and \mathbf{H} is constant to a good approximation [1, 13].

Following calculations from Meiners's study for two spherical particles [1], the correlation functions is given as the following:

$$\langle R_1^\alpha(t) R_1^\beta(0) \rangle = \langle R_2^\alpha(t) R_2^\beta(0) \rangle \quad (5.13a)$$

$$= \delta_{\alpha\beta} \frac{k_B T}{2\kappa_\alpha} \left(e^{-t(1+\varepsilon_\alpha)/\tau_\alpha} + e^{-t(1-\varepsilon_\alpha)/\tau_\alpha} \right) \quad (5.13b)$$

$$\langle R_1^\alpha(t) R_2^\beta(0) \rangle = \langle R_2^\alpha(t) R_1^\beta(0) \rangle \quad (5.13c)$$

$$= \delta_{\alpha\beta} \frac{k_B T}{2\kappa_\alpha} \left(e^{-t(1+\varepsilon_\alpha)/\tau_\alpha} - e^{-t(1-\varepsilon_\alpha)/\tau_\alpha} \right) \quad (5.13d)$$

where $\alpha, \beta = x, y, z$ represents the indices for each direction in 3D, κ_α is the trap stiffness, $\tau_\alpha = \gamma_0/\kappa_\alpha$ is the fundamental relaxation time and $\gamma_0 = 6\pi\eta a$ is the drag coefficient of spherical particles with radius a within fluids with shear viscosity η . δ represents the Kronecker delta function. The dimensionless parameter ε_α describes the ratio between the mobility of the beads and the strength of the hydrodynamic coupling between them, which amounts to $\varepsilon_y = 3a/2d$ for motion in the longitudinal axis of the

two particles and $\varepsilon_x = \varepsilon_z = 3a/4d$ for the transverse axis where $d = |\mathbf{r}_{1,2}| = |\mathbf{R}_2 - \mathbf{R}_1|$ is the distance between the two particles [1].

If we take the derivative of the cross correlation function $\langle R_1^\alpha(t) R_2^\alpha(0) \rangle$, we find a turning point at $t_{\min} = (\tau_\alpha/2\varepsilon_\alpha) \ln[(1 + \varepsilon_\alpha)/(1 - \varepsilon_\alpha)] \approx \tau_\alpha$, which indicates that the cross correlation curves exhibit a time-delayed anti-correlation with a minimum at t_{\min} [1]. The depth of the minimum is then given as

$$\langle R_1^\alpha(\tau_\alpha) R_2^\alpha(0) \rangle \approx -\frac{1}{e} \frac{k_B T}{\kappa_\alpha} \sinh(\varepsilon_\alpha) \quad (5.14a)$$

$$\approx -\frac{1}{e} \frac{k_B T}{\kappa_\alpha} \varepsilon_\alpha \quad (5.14b)$$

This quantity also represents the correlation distance, which provides a measure of the strength of the hydrodynamic interactions. It is clear from Equation 5.14b that the correlation distance scales inversely with inter particle separation d .

5.5 Tracking of multiple polystyrene particles by time-shared traps

To test our particle tracking system, we trapped and tracked two 1 μm polystyrene spheres as a test system to compare against known results [1, 24]. Our experimental setup is described in detail in Chapter 2. As an overview, a 1064 nm Nd:YAG laser is passed through a two-axis acousto-optic deflector (AOD), expanded to overfill a spatial light modulator (SLM), and then contracted to just overfill the back aperture of a 100x oil immersion microscope objective lens. Trapped particles are tracked using back focal plane interferometry. The interference between the trapping laser and laser scattered by the trapped particles is collected by a 0.65 NA condenser lens (Olympus S Plan Fluor 40x 0.65NA ELWD) and projected onto a quadrant photodiode (QPD) placed in the back focal plane.

We switch the input frequency to the y -axis AOD between two values and keep the input frequency of the x -axis AOD constant. The difference between the two input frequency values is converted to real distance d in the trapping plane by the calibration procedure presented in Chapter 3 Section 3.3.3. The y -axis AOD is switched every 50 μs , and the QPD is read synchronously. This creates two time-shared optical traps

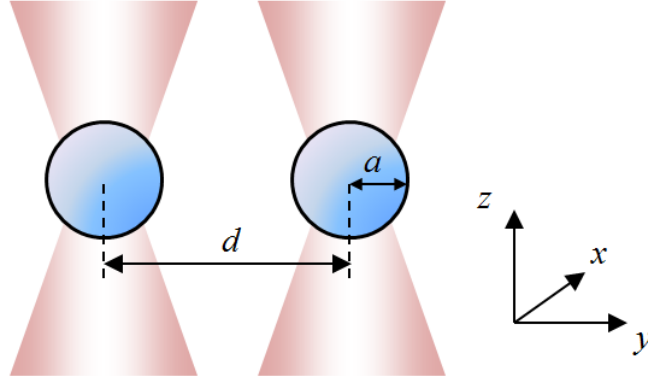


Figure 5.6: Nomenclature and coordinates for describing our system of two optically trapped spheres.

where each trap is sampled at 10 kHz. Each trap is loaded with a single polystyrene sphere with a diameter of $1.0 \pm 0.01 \mu\text{m}$ as illustrated in Figure 5.6. The concentration of spheres in the sample is 0.1 ppm, which is low enough such that no additional spheres are present within at least $20 \mu\text{m}$ of the traps (visually determined from the field of view of the CCD camera) over the duration in which QPD measurements are taken. The trajectories of both spheres are measured by reading the QPD synchronously with the switching of the AOD. Data is collected at a sampling frequency of 10 kHz over a total duration of 60 seconds (10 sets of 6-second measurements). This is repeated for 5 different inter-particle separations, d .

Correlation analysis is performed by numerically calculating the cross correlation between the trajectories of the particles from both traps and the resulting curve is fit with the cross correlation functions (Equations 5.15 and 5.16b).

In the longitudinal direction along the particle separation,

$$\langle R_{y1}(t) R_{y2}(0) \rangle = \frac{k_B T}{2\kappa_y} \left(e^{-t(1+\varepsilon_y)/\tau_y} - e^{-t(1-\varepsilon_y)/\tau_y} \right) \quad (5.15)$$

and in the transverse directions,

$$\langle R_{x1}(t) R_{x2}(0) \rangle = \frac{k_B T}{2\kappa_x} \left(e^{-t(1+\varepsilon_x)/\tau_x} - e^{-t(1-\varepsilon_x)/\tau_x} \right) \quad (5.16a)$$

$$\langle R_{z1}(t) R_{z2}(0) \rangle = \frac{k_B T}{2\kappa_z} \left(e^{-t(1+\varepsilon_z)/\tau_z} - e^{-t(1-\varepsilon_z)/\tau_z} \right) \quad (5.16b)$$

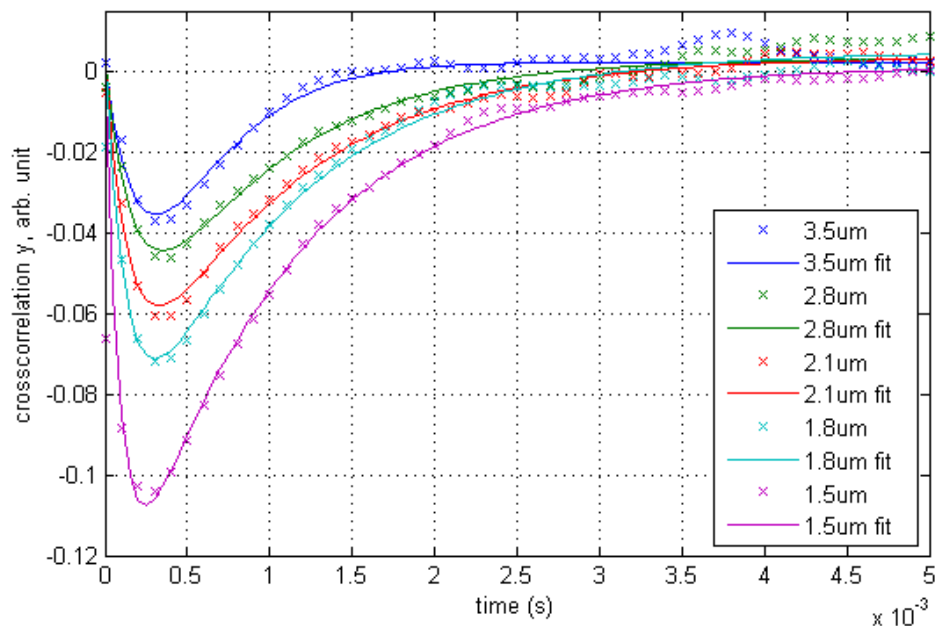


Figure 5.7: Cross correlation functions in the longitudinal y direction of two optically trapped $1 \mu\text{m}$ polystyrene spheres at various inter-particle separations d in the y -direction.

where $\varepsilon_y = 3a/2d$ and $\varepsilon_x = \varepsilon_z = 3a/4d$. Here $\tau_\alpha = \gamma_0/\kappa_\alpha$ is the fundamental relaxation time and κ_α is the trap stiffness for the respective direction ($\alpha = x, y, z$). The results for cross correlation in the y direction (longitudinal), x and z directions (transverse) with fitted curves are presented in Figure 5.7 and 5.8. It should be noted that the vertical axis of the experimental data for the z direction is uncalibrated. From the figures we see that the longitudinal cross correlation of the measured trajectories fits well with theory. On the other hand, the transverse cross correlation of the experimental data shows significant reductions in signal to noise ratio which is more pronounced in cases where the inter particle separations are large. This is because hydrodynamic interaction scales inversely with inter-particle separations, and is weaker in the transverse directions compared to the longitudinal direction. Similar behaviours have also been observed in Ruh *et al.*'s work [24].

From the fits we extracted the fundamental relaxation time in all 3 axes, τ_x , τ_y and τ_z . From these we calculated the trap stiffness for each direction and found them to be $\kappa_x = 40 \pm 2 \text{ pN}/\mu\text{m}$, $\kappa_y = 78 \pm 5 \text{ pN}/\mu\text{m}$ and $\kappa_z = 21 \pm 1 \text{ pN}/\mu\text{m}$. We observe that τ_z is significantly larger than τ_x and τ_y due to the weaker optical confinement along the

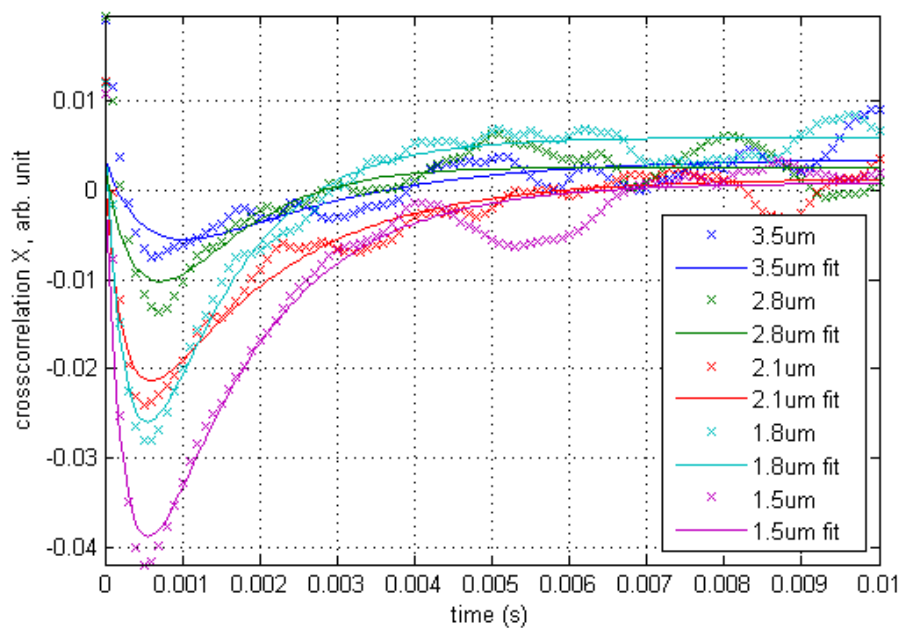
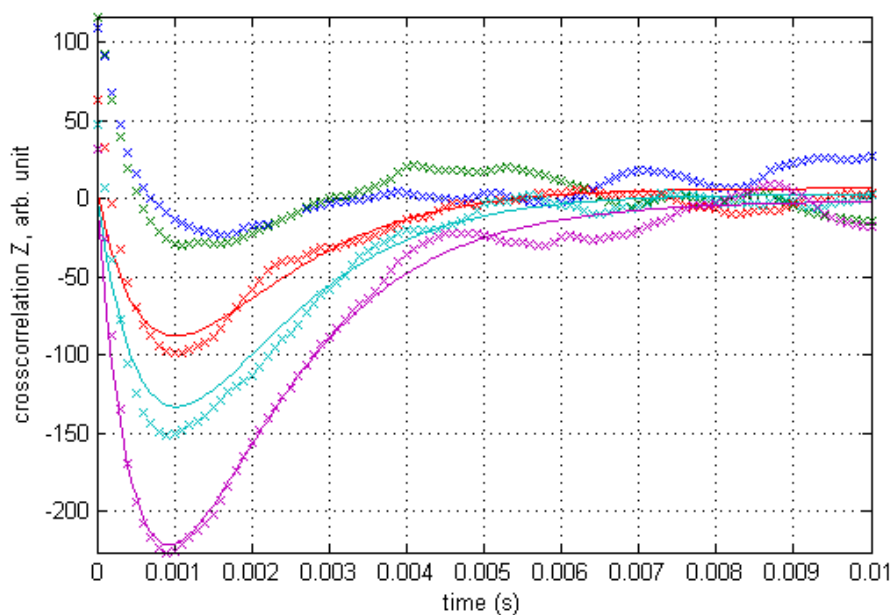
(a) Cross correlation function in the transverse x -direction(b) Cross correlation function in the transverse z -direction

Figure 5.8: Cross correlation functions in the transverse x and z directions of two optically trapped 1 μm polystyrene spheres at various inter-particle separations d in the y -direction.

optical axis as a result of a weaker axial trap stiffness compared to the transverse trap stiffness in the optical trap.

We also plot the depth of the minimum of the cross correlation curves against a/d . A linear relationship is found as predicted by Equation 5.14b. These results are in good agreement with literature [1], showing the applicability of our new technique of measurements.

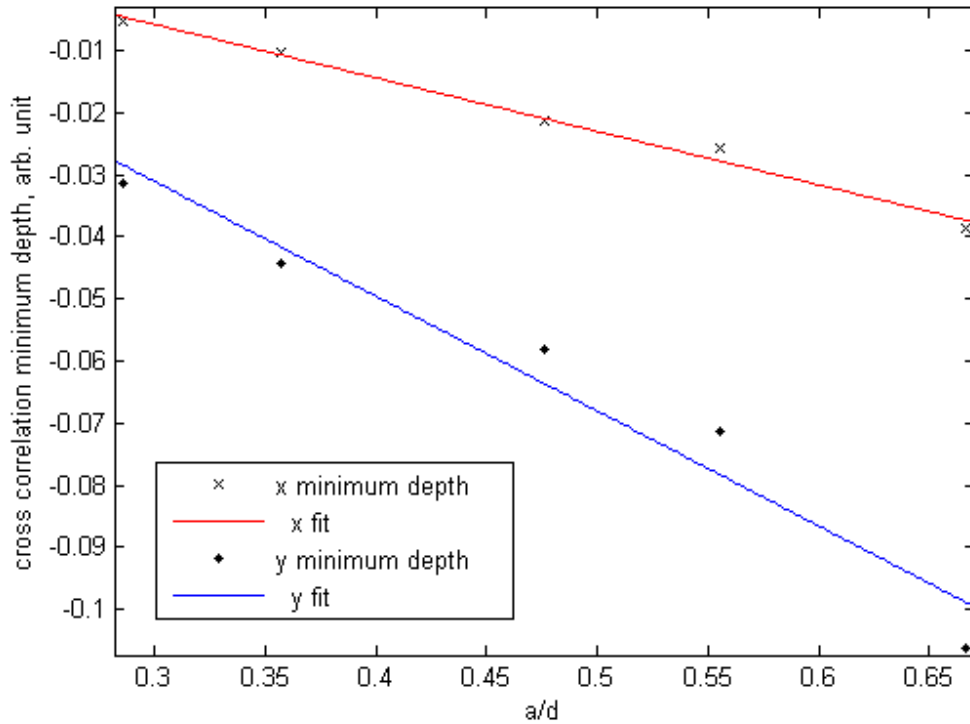


Figure 5.9: Depth of the minimum in the cross correlation functions versus ratio of radius a and inter particle separation d . The fit shows a linear relation as predicted by Equation 5.14b.

5.6 Tracking of multiple gold nanoparticles by time-shared traps

We repeated the experiment in Section 5.5 on 100 nm spherical gold nano particles. The same procedure as outlined in Section 5.5 is used. However, the measurement results we obtained showed no correlation, as shown in Figure 5.10.

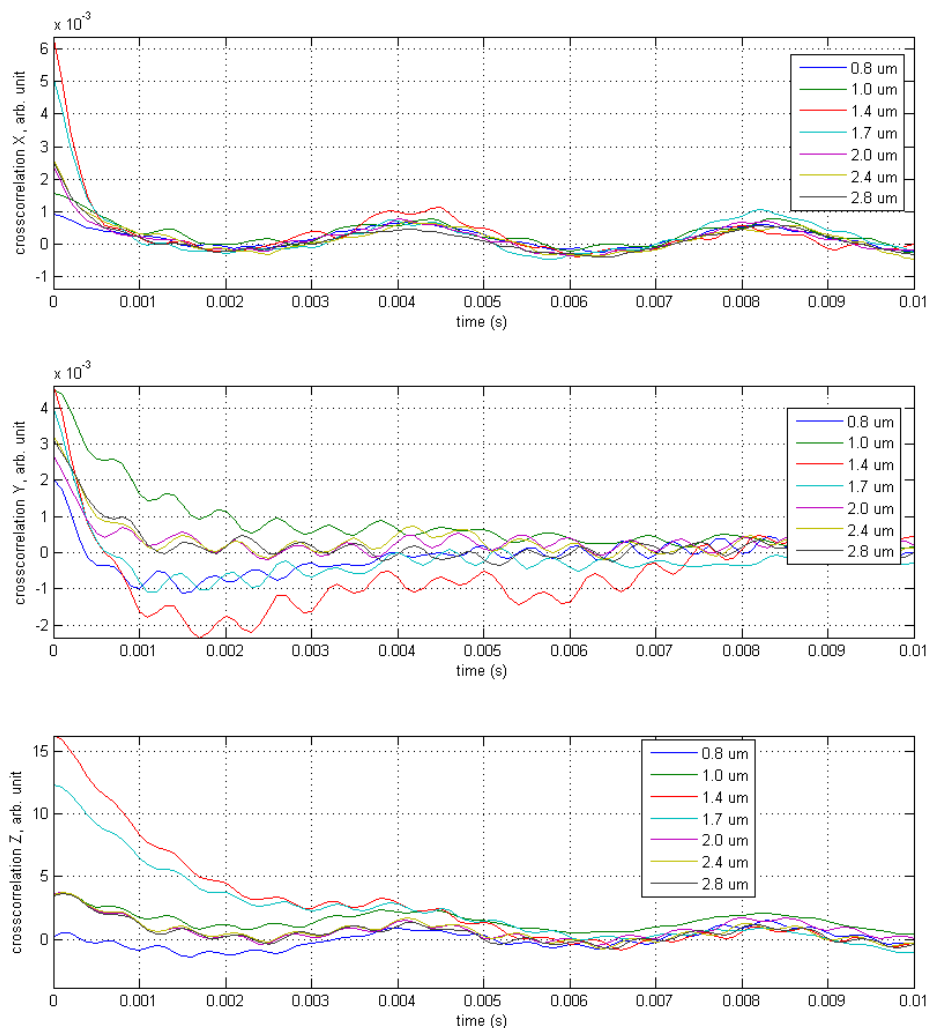


Figure 5.10: Attempt at measuring cross correlations between two optically trapped 100 nm spherical gold nanoparticles.

We believe this is due to the limitations in our instruments, as explained in Section 5.3 above. From Equation 5.8 we can calculate the sampling frequency of our optical tweezers in order to detect hydrodynamic effects between two 100 nm nanoparticles separated by 1 μm :

$$\begin{aligned}
 \Delta t &< \left(\frac{3}{4\epsilon} \frac{a}{d} \right) \tau \\
 &< \left(\frac{3}{4\epsilon} \frac{a}{d} \right) \frac{6\pi\eta a}{\kappa} \\
 &< \sim 1.5\mu s
 \end{aligned}$$

This means in order to be able to measure the hydrodynamic effects between these nanoparticles, the time-sharing and sampling of the optical traps will have to be less than $1.5 \mu s$ which is beyond the capabilities of our instruments. This is an order of magnitude faster than the requirements for measuring $1 \mu m$ spheres because the smaller nanoparticles have a smaller hydrodynamic drag $\gamma_0 = 6\pi\eta a$ and hence a shorter relaxation time τ . Furthermore, for a fixed inter-particle separation a smaller particle brings down the ratio between the mobility of the particles and the strength of hydrodynamic coupling between them, which is directly proportional to the ratio between particle size and separation, $\epsilon_y = 3a/2d$ as mentioned in Section 5.4. We are also unable to bring the two nanoparticles any closer than $0.8 \mu m$ due to the diffraction limited spot size of the trap focus, which is calculated to be $0.8 \mu m$. Moreover, we also observed Kremer's hopping effects of the nanoparticles between the two optical traps at separations up to $1.2 \mu m$, which is beyond the scope of this work.

5.7 Applicability of time-shared optical tweezers in trapping and tracking two interacting InP nanowires

From our measurements of single trapped InP nanowires we have discovered anomalous trapping dynamics as presented in Chapter 3. In particular, we've observed resonant behaviours in the form of resonance peaks using interferometric tracking methods with photodiode detectors (Section 3.6); it should be noted that these peaks occur at hundreds to two thousand Hz, which is beyond the temporal resolution of standard video tracking methods. These effects could contribute significantly to the dynamics of two interacting nanowires, and we believe fast particle tracking using interferometric techniques with QPD's is the most feasible way to probe these behaviours.

In Section 5.3 we explored the limits of tracking by time-shared optical tweezers. We now show that the the system of two interacting InP nanowires discussed in Chapter

4 Section 4.5 is within the constraints of this measurement technique. Applying Equation 5.4 to our system of two nanowires we have

$$\frac{\gamma_{\perp}}{2\kappa dt} \gg 1 \quad (5.17a)$$

$$\therefore dt \ll \frac{1}{2} \frac{\gamma_{\perp}}{\kappa} \quad (5.17b)$$

where we have taken $N = 2$ for two time-shared traps, dt is the switching interval of the AOD's, κ is the trap stiffness and γ_{\perp} is the drag coefficient of the nanowires given by [25, 26]

$$\gamma_{\perp} = \frac{4\pi\eta_0 L}{\ln(L/2a) + \delta_{\perp}} \quad (5.18)$$

The inequality 5.17b also signifies that the duration when the trap is absent at a trapping site should be less than half of the fundamental relaxation time of the nanowire within the trap.

Based on our InP nanowire system in Chapter 4.5, with typical nanowire radii of $a = 100$ nm, length $L = 5$ μm , and trap stiffness $\kappa = 50$ pN/ μm , we require

$$dt \ll \frac{1}{2} \frac{\gamma_{\perp}}{\kappa} = 155\mu\text{s} \quad (5.19)$$

Since our setup can achieve $dt = 50\mu\text{s}$, we believe that time-shared optical tweezers is a possible way to study the system of two interacting InP nanowires discussed in Chapter 4. Furthermore, if we look at the diffusion of nanowires in the absence of the trap, we find that the mean squared displacement of these nanowires are $\langle \Delta x^2 \rangle_{\text{diffusion}} \approx 50$ nm², which is well within the Brownian fluctuations of these nanowires within the optical trap.

5.8 Conclusion

In order to experimentally realise the system that we simulated in the last chapter, we require a method of optically trapping and tracking multiple particles. Optical

tweezers is a viable option and in this chapter we explored various multi-particle trapping and tracking methods using optical tweezers currently available in the literature. We discounted the use of holographic optical tweezers due to its general incompatibility with interferometric particle tracking methods, which is able to achieve much higher sampling rates than video tracking methods commonly used with holographic tweezers. This is because video tracking has a limited sampling rate which is not fast enough to resolve the fast dynamics of interacting particles.

We then demonstrate a novel particle trapping and tracking method using time-shared optical tweezers and explored the limitations of this approach. As a test system we successfully measure the hydrodynamic coupling between two $1\ \mu\text{m}$ polystyrene spheres. However, measurements performed on $100\ \text{nm}$ spherical gold nanoparticles remain unsuccessful due to the limitations in the switching and sampling frequency of our apparatus. Finally, we show through calculations that the required conditions to study the two parallel InP nanowires system that we have simulated in Chapter 4 are within the limits of our time-shared optical tweezers.

5.9 References

- [1] J. C. Meiners and S. R. Quake. Direct measurement of hydrodynamic cross correlations between two particles in an external potential. *Physical Review Letters*, 82(10):2211–2214, 1999. 173AX Times Cited:140 Cited References Count:14.
- [2] P. Mangeol and U. Bockelmann. Interference and crosstalk in double optical tweezers using a single laser source. *Review of Scientific Instruments*, 79(8), 2008. 350SX Times Cited:10 Cited References Count:13.
- [3] M. Atakhorrani, K. M. Addas, and C. F. Schmidt. Twin optical traps for two-particle cross-correlation measurements: Eliminating cross-talk. *Review of Scientific Instruments*, 79(4), 2008. 295EC Times Cited:15 Cited References Count:34.
- [4] Y. von Hansen, A. Mehlich, B. Pelz, M. Rief, and R. R. Netz. Auto- and cross-power spectral analysis of dual trap optical tweezer experiments using bayesian inference. *Review of Scientific Instruments*, 83(9), 2012. 015DW Times Cited:12 Cited References Count:48.
- [5] M. C. Zhong, J. H. Zhou, Y. X. Ren, Y. M. Li, and Z. Q. Wang. Rotation of birefringent particles in optical tweezers with spherical aberration. *Applied Optics*, 48(22):4397–4402, 2009. 490BC Times Cited:6 Cited References Count:31.
- [6] S. J. Parkin, T. A. Nieminen, N. R. Heckenberg, and H. Rubinsztein-Dunlop. Optical measurement of torque exerted on an elongated object by a noncircular laser beam. *Physical Review A*, 70(2), 2004. 851WO Times Cited:21 Cited References Count:28.
- [7] J. E. Curtis, B. A. Koss, and D. G. Grier. Dynamic holographic optical tweezers. *Optics Communications*, 207(1-6):169–175, 2002. 569WQ Times Cited:669 Cited References Count:22.
- [8] J. Liesener, M. Reicherter, T. Haist, and H. J. Tiziani. Multi-functional optical tweezers using computer-generated holograms. *Optics Communications*, 185(1-3):77–82, 2000. 371JL Times Cited:248 Cited References Count:11.
- [9] D. G. Grier. A revolution in optical manipulation. *Nature*, 424(6950):810–816, 2003. 711HQ Times Cited:1817 Cited References Count:85.
- [10] M. Polin, D. G. Grier, and S. R. Quake. Anomalous vibrational dispersion in holographically trapped colloidal arrays. *Physical Review Letters*, 96(8), 2006. 018AX Times Cited:49 Cited References Count:22.
- [11] D. B. Phillips, J. A. Grieve, S. N. Olof, S. J. Kocher, R. Bowman, M. J. Padgett, M. J. Miles, and D. M. Carberry. Surface imaging using holographic optical tweezers. *Nanotechnology*, 22(28), 2011. 775NX Times Cited:16 Cited References Count:28.
- [12] D. B. Phillips, S. H. Simpson, J. A. Grieve, G. M. Gibson, R. Bowman, M. J. Padgett, M. J. Miles, and D. M. Carberry. Position clamping of optically trapped microscopic non-spherical probes. *Optics Express*, 19(21):20622–20627, 2011. 835VV Times Cited:23 Cited References Count:16.

- [13] R. Di Leonardo, S. Keen, J. Leach, C. D. Saunter, G. D. Love, G. Ruocco, and M. J. Padgett. Eigenmodes of a hydrodynamically coupled micron-size multiple-particle ring. *Physical Review E*, 76(6), 2007. Part 1 246CR Times Cited:23 Cited References Count:28.
- [14] C. D. Saunter, G. D. Love, M. Johns, and J. Holmes. Fpga technology for high speed, low cost adaptive optics - art. no. 61081g. *5th International Workshop on Adaptive Optics for Industry and Medicine*, 6018:G1081–G1081, 2005. Beu93 Times Cited:10 Cited References Count:6 Proceedings of the Society of Photo-Optical Instrumentation Engineers (Spie).
- [15] K. Kepa, D. Coburn, J. C. Dainty, and F. Morgan. High speed optical wavefront sensing with low cost fpgas. *Measurement Science Review*, 8(4):87–93, 2008. 390OQ Times Cited:8 Cited References Count:15.
- [16] F. C. Cheong, B. J. Krishnatreya, and D. G. Grier. Strategies for three-dimensional particle tracking with holographic video microscopy. *Optics Express*, 18(13):13563–13573, 2010. 613VG Times Cited:72 Cited References Count:31.
- [17] D. B. Conkey, R. P. Trivedi, R. P. Pavani, I. I. Smalyukh, and R. Piestun. Three-dimensional parallel particle manipulation and tracking by integrating holographic optical tweezers and engineered point spread functions. *Optics Express*, 19(5):3835–3842, 2011. 741NL Times Cited:20 Cited References Count:30.
- [18] D. Ott, S. N. S. Reihani, and L. B. Oddershede. Crosstalk elimination in the detection of dual-beam optical tweezers by spatial filtering. *Review of Scientific Instruments*, 85(5), 2014. Ai7ud Times Cited:3 Cited References Count:25.
- [19] D. Ott, S. N. S. Reihani, and L. B. Oddershede. Simultaneous three-dimensional tracking of individual signals from multi-trap optical tweezers using fast and accurate photodiode detection. *Optics Express*, 22(19):23661–23672, 2014. Aq4ib Times Cited:0 Cited References Count:40.
- [20] R. W. Bowman and M. J. Padgett. Optical trapping and binding. *Reports on Progress in Physics*, 76(2), 2013. 086PI Times Cited:43 Cited References Count:250.
- [21] K. Visscher, G. J. Brakenhoff, and J. J. Krol. Micromanipulation by multiple optical traps created by a single fast scanning trap integrated with the bilateral confocal scanning laser microscope. *Cytometry*, 14(2):105–114, 1993. Kk319 Times Cited:113 Cited References Count:26.
- [22] K. Visscher, S. P. Gross, and S. M. Block. Construction of multiple-beam optical traps with nanometer-resolution position sensing. *Ieee Journal of Selected Topics in Quantum Electronics*, 2(4):1066–1076, 1996. Xd616 Times Cited:262 Cited References Count:32.
- [23] G. J. Brouhard, H. T. Schek, and A. J. Hunt. Advanced optical tweezers for the study of cellular and molecular biomechanics. *Ieee Transactions on Biomedical Engineering*, 50(1):121–125, 2003. 645MB Times Cited:42 Cited References Count:13.

- [24] D. Ruh, B. Trankle, and A. Rohrbach. Fast parallel interferometric 3d tracking of numerous optically trapped particles and their hydrodynamic interaction. *Optics Express*, 19(22):21627–21642, 2011. 842DC Times Cited:8 Cited References Count:38.
- [25] M. M. Tirado and J. Garciadelatorre. Translational friction coefficients of rigid, symmetric top macromolecules - application to circular-cylinders. *Journal of Chemical Physics*, 71(6):2581–2587, 1979. H1466 Times Cited:278 Cited References Count:25.
- [26] M. M. Tirado, C. L. Martinez, and J. G. Delatorre. Comparison of theories for the translational and rotational diffusion-coefficients of rod-like macromolecules - application to short dna fragments. *Journal of Chemical Physics*, 81(4):2047–2052, 1984. Tg208 Times Cited:278 Cited References Count:28.

Chapter 6

Conclusion

In this final chapter I will summarise the important findings presented throughout this thesis. Possible future work that leads on from this thesis will be discussed briefly as well.

To summarise, we have examined some advanced trapping dynamics of single and multiple high refractive index, high aspect ratio nanowires. In Chapter 3, the higher order dynamics on an optically trapped InP nanowire due to coupling between rotational and translational degrees of freedom is examined. We found that the influence of non-conservative coupling between translation and rotational modes in optically trapped nanowires leads to a distinct resonance peak in the power spectrum and an accompanying winding of the particle trajectories, which suggests that the trapped nanowires undergo cyclic motion. These complex dynamics are indeed richer than initially anticipated, and leaves more to be understood than the current standard picture of an optically trapped sphere.

In Chapter 4 we studied the coupling of the trapping laser into the waveguiding modes of the trapped nanowire. We showed that the field intensity is weak in the core of the nanowires and that significant evanescent fields extend outside the nanowire core. In this chapter we also looked into the coupling interactions between multiple trapped nanowires. We found that the beat length is comparable to the length of a typical nanowire waveguide, which implies that the full transfer of power from one nanowire waveguide to the other is possible. We also discovered that the coupling forces due to optical coupling of the guided modes are comparable in magnitude to the gradient forces of the optical tweezers that hold the nanowires in place. These findings,

combined with the results from Chapter 3 suggest the occurrence of complex dynamics when multiple nanowires interact. Although we have only examined one particular type of interaction i.e. optical coupling, we acknowledge the existence of other forms of coupling such as hydrodynamic coupling [1] and Casimir forces [2], which opens up many questions for future research. These results also have profound implications on nanowire applications involving interaction forces, such as the self-assembly of nano-structures or the development of nano-sensors.

Finally in Chapter 5, in order to experimentally probe the coupling interactions between multiple nanowires we demonstrated a novel particle trapping and tracking method using time-shared optical tweezers and explored the limitations of this approach. We show through calculations that the required conditions to study the two parallel InP nanowires system that we have simulated in Chapter 4 are within the limits of our time-shared optical tweezers. As a test to our system we successfully measured the hydrodynamic coupling between two $1\ \mu\text{m}$ polystyrene spheres. Future work include improving this measurement technique and using it to conduct measurements on multiple trapped nanowires to quantify interacting forces between coupled nanowires.

6.1 References

- [1] J. C. Meiners and S. R. Quake. Direct measurement of hydrodynamic cross correlations between two particles in an external potential. *Physical Review Letters*, 82(10):2211–2214, 1999. 173AX Times Cited:140 Cited References Count:14.
- [2] A. Larraza, C. D. Holmes, R. T. Susbilla, and B. Denardo. The force between two parallel rigid plates due to the radiation pressure of broadband noise: An acoustic casimir effect. *Journal of the Acoustical Society of America*, 103(5):2267–2272, 1998. 1 Zm942 Times Cited:12 Cited References Count:13.

Appendix A

Derivation of force in terms of Maxwell's Stress Tensor and Poynting Vector

Here I will show the derivation of force expressed in terms of the Maxwell's Stress Tensor and Poynting Vector (Equation 4.24) from Maxwell's Equations (Equations 4.22 and 4.23b) [1].

We start the derivation by the calculation of the total force due to electromagnetic fields on the charges and currents within some volume \mathcal{V} . From the Lorentz force law, we have

$$\mathbf{F} = \int_{\mathcal{V}} \rho (\mathbf{E} + \mathbf{v} \times \mathbf{B}) d^3\mathbf{r} \quad (\text{A.1})$$

$$= \int_{\mathcal{V}} (\rho \mathbf{E} + \mathbf{J} \times \mathbf{B}) d^3\mathbf{r} \quad (\text{A.2})$$

We can think of the integrand as a force density, or force per unit volume \mathbf{f} :

$$\mathbf{f} \equiv \rho \mathbf{E} + \mathbf{J} \times \mathbf{B} \quad (\text{A.3})$$

This can be expressed entirely in terms of fields by using Maxwell's equations:

$$\rho = \epsilon_0 \nabla \cdot \mathbf{E} \quad (\text{A.4})$$

$$\mathbf{J} = \frac{1}{\mu_0} \nabla \times \mathbf{B} - \epsilon_0 \frac{\partial \mathbf{E}}{\partial t} \quad (\text{A.5})$$

Hence we get

$$\mathbf{f} = (\epsilon_0 \nabla \cdot \mathbf{E}) \mathbf{E} + \left[\frac{1}{\mu_0} \nabla \times \mathbf{B} - \epsilon_0 \frac{\partial \mathbf{E}}{\partial t} \right] \times \mathbf{B} \quad (\text{A.6})$$

Now, from the product rule

$$\frac{\partial}{\partial t} (\mathbf{E} \times \mathbf{B}) = \frac{\partial \mathbf{E}}{\partial t} \times \mathbf{B} + \mathbf{E} \times \frac{\partial \mathbf{B}}{\partial t} \quad (\text{A.7})$$

and from Faraday's law

$$\frac{\partial \mathbf{B}}{\partial t} = -\nabla \times \mathbf{E} \quad (\text{A.8})$$

Combining Equation A.7 and Equation A.8 we get

$$\frac{\partial \mathbf{E}}{\partial t} \times \mathbf{B} = \frac{\partial}{\partial t} (\mathbf{E} \times \mathbf{B}) - \mathbf{E} \times \frac{\partial \mathbf{B}}{\partial t} \quad (\text{A.9})$$

$$= \frac{\partial}{\partial t} (\mathbf{E} \times \mathbf{B}) + \mathbf{E} \times (\nabla \times \mathbf{E}) \quad (\text{A.10})$$

We can insert this into Equation A.6. We also have to perform a mathematical trick of adding on a term $\frac{1}{\mu_0} (\nabla \cdot \mathbf{B}) \mathbf{B}$. This is always zero because $\nabla \cdot \mathbf{B} = 0$, but it gives the equation a symmetry that will be useful. We then obtain the force density:

$$\mathbf{f} = \epsilon_0 (\nabla \cdot \mathbf{E}) \mathbf{E} + \frac{1}{\mu_0} (\nabla \cdot \mathbf{B}) \mathbf{B} + \frac{1}{\mu_0} (\nabla \times \mathbf{B}) \times \mathbf{B} - \epsilon_0 \frac{\partial \mathbf{E}}{\partial t} \times \mathbf{B} \quad (\text{A.11})$$

$$= \epsilon_0 (\nabla \cdot \mathbf{E}) \mathbf{E} + \frac{1}{\mu_0} (\nabla \cdot \mathbf{B}) \mathbf{B} + \frac{1}{\mu_0} (\nabla \times \mathbf{B}) \times \mathbf{B} - \epsilon_0 \frac{\partial}{\partial t} (\mathbf{E} \times \mathbf{B}) - \epsilon_0 \mathbf{E} \times (\nabla \times \mathbf{E}) \quad (\text{A.12})$$

Now, we use another identity from vector calculus which says

$$\nabla (\mathbf{A} \cdot \mathbf{B}) = \mathbf{A} \times (\nabla \times \mathbf{B}) + \mathbf{B} \times (\nabla \times \mathbf{A}) + (\mathbf{A} \cdot \nabla) \mathbf{B} + (\mathbf{B} \cdot \nabla) \mathbf{A} \quad (\text{A.13})$$

If $\mathbf{A} = \mathbf{B} = \mathbf{E}$, we get

$$\nabla (E^2) = 2\mathbf{E} \times (\nabla \times \mathbf{E}) + 2(\mathbf{E} \cdot \nabla) \mathbf{E} \quad (\text{A.14})$$

thus

$$\mathbf{E} \times (\nabla \times \mathbf{E}) = \frac{1}{2} \nabla (E^2) - (\mathbf{E} \cdot \nabla) \mathbf{E} \quad (\text{A.15})$$

$$\mathbf{B} \times (\nabla \times \mathbf{B}) = \frac{1}{2} \nabla (B^2) - (\mathbf{B} \cdot \nabla) \mathbf{B} \quad (\text{A.16})$$

Substituting these into Equation A.12 we obtain

$$\begin{aligned} \mathbf{f} = \epsilon_0 (\nabla \cdot \mathbf{E}) \mathbf{E} + \frac{1}{\mu_0} (\nabla \cdot \mathbf{B}) \mathbf{B} - \epsilon_0 \frac{\partial}{\partial t} (\mathbf{E} \times \mathbf{B}) \\ - \frac{1}{\mu_0} \mathbf{B} \times (\nabla \times \mathbf{B}) - \epsilon_0 \mathbf{E} \times (\nabla \times \mathbf{E}) \quad (\text{A.17}) \end{aligned}$$

$$\begin{aligned} = \epsilon_0 (\nabla \cdot \mathbf{E}) \mathbf{E} + \frac{1}{\mu_0} (\nabla \cdot \mathbf{B}) \mathbf{B} - \epsilon_0 \frac{\partial}{\partial t} (\mathbf{E} \times \mathbf{B}) \\ - \frac{1}{2} \nabla \left(\epsilon_0 E^2 + \frac{1}{\mu_0} B^2 \right) + \epsilon_0 (\mathbf{E} \cdot \nabla) \mathbf{E} + \frac{1}{\mu_0} (\mathbf{B} \cdot \nabla) \mathbf{B} \quad (\text{A.18}) \end{aligned}$$

$$\begin{aligned} = \epsilon_0 [(\nabla \cdot \mathbf{E}) \mathbf{E} + (\mathbf{E} \cdot \nabla) \mathbf{E}] + \frac{1}{\mu_0} [(\nabla \cdot \mathbf{B}) \mathbf{B} + (\mathbf{B} \cdot \nabla) \mathbf{B}] \\ - \frac{1}{2} \nabla \left(\epsilon_0 E^2 + \frac{1}{\mu_0} B^2 \right) - \epsilon_0 \frac{\partial}{\partial t} (\mathbf{E} \times \mathbf{B}) \quad (\text{A.19}) \end{aligned}$$

Here we introduce the Maxwell stress tensor $\overleftrightarrow{\mathbf{T}}$ which is a 3×3 matrix with components defined by

$$\boxed{T_{ij} \equiv \epsilon_0 \left(E_i E_j - \frac{1}{2} \delta_{ij} E^2 \right) + \frac{1}{\mu_0} \left(B_i B_j - \frac{1}{2} \delta_{ij} B^2 \right)} \quad (\text{A.20})$$

Note that the tensor is symmetric: $T_{ij} = T_{ji}$. If we define the scalar product of the tensor with an ordinary vector to be another vector:

$$\left[\mathbf{a} \cdot \overleftrightarrow{\mathbf{T}} \right]_j = \sum_i a_i T_{ij} \quad (\text{A.21})$$

where the subscript j indicates the j th component of the resulting vector, then the divergence is

$$\left[\nabla \cdot \overleftrightarrow{\mathbf{T}} \right]_j = \sum_i \partial_i T_{ij} \quad (\text{A.22})$$

Substituting in Equation A.20, we get

$$\begin{aligned} \left[\nabla \cdot \overleftrightarrow{\mathbf{T}} \right]_j &= \epsilon_0 \sum_i \left((\partial_i E_i) E_j + E_i (\partial_i E_j) - \frac{1}{2} \delta_{ij} \partial_i E^2 \right) \\ &\quad + \frac{1}{\mu_0} \sum_i \left((\partial_i B_i) B_j + B_i (\partial_i B_j) - \frac{1}{2} \delta_{ij} \partial_i B^2 \right) \end{aligned} \quad (\text{A.23})$$

$$\begin{aligned} &= \epsilon_0 \left((\nabla \cdot \mathbf{E}) E_j + (\mathbf{E} \cdot \nabla) E_j - \frac{1}{2} \partial_j E^2 \right) \\ &\quad + \frac{1}{\mu_0} \left((\nabla \cdot \mathbf{B}) B_j + (\mathbf{B} \cdot \nabla) B_j - \frac{1}{2} \partial_j B^2 \right) \end{aligned} \quad (\text{A.24})$$

Comparing this with Equation A.19, we see that we can write \mathbf{f} in terms of $\overleftrightarrow{\mathbf{T}}$ and the Poynting vector as

$$\boxed{\mathbf{f} = \nabla \cdot \overleftrightarrow{\mathbf{T}} - \epsilon_0 \mu_0 \frac{\partial \mathbf{S}}{\partial t}} \quad (\text{A.25})$$

The total force on the volume then becomes

$$\mathbf{F} = \int_{\mathcal{V}} \mathbf{f} d^3\mathbf{r} \quad (27) \tag{A.26}$$

$$= \int_{\mathcal{V}} \left(\nabla \cdot \overleftrightarrow{\mathbf{T}} - \epsilon_0 \mu_0 \frac{\partial \mathbf{S}}{\partial t} \right) d^3\mathbf{r} \quad (28) \tag{A.27}$$

From the Equation A.22 for the divergence, we can see that the vector resulting from the divergence has as its components the divergences of each column of $\overleftrightarrow{\mathbf{T}}$. Therefore we can apply the divergence theorem to the first term in the integrand to get

$$\boxed{\mathbf{F} = \int_{\mathcal{S}} \overleftrightarrow{\mathbf{T}} \cdot d\mathbf{a} - \epsilon_0 \mu_0 \frac{\partial}{\partial t} \int_{\mathcal{V}} \mathbf{S} d^3\mathbf{r}} \tag{A.28}$$

where \mathcal{S} is any surface that encloses only the charges and currents within \mathcal{V} .

A.1 References

- [1] David J. Griffiths and David J. Griffiths. *Introduction to electrodynamics*. Upper Saddle River, NJ : Prentice Hall, Upper Saddle River, NJ, 3rd ed. edition, 1999. (David Jeffrey) (David Jeffery) Includes bibliographical references and index.

